RecA-templated DNA scaffolds for selective site-specific assembly of nanoparticles for electronic devices

Mindaugas Dzikaras

School of Electronic and Electrical Engineering

University of Leeds

Submitted in accordance with the requirements for the degree of

Doctor of Philosophy

September 2017

The candidate confirms that the work submitted is his/her own and that appropriate credit has been given where reference has been made to the work of others.

Acknowledgements

I would like to express my uttermost gratitude to Prof. Christoph Wälti for his guidance and supervision. His everyday support, constant encouragement, patience and unconditional dedication made this work possible to achieve. I would also like to thank Prof. Alexander Giles Davies for his supervision, support and advices throughout the project.

I would like to thank Dr. Rajan Sharma for his extensive help on all aspects of this project, from basic lab training, input on experimental design and result evaluation to stimulating discussion and extensive psychological support. His input to this work is irreplaceable and deeply appreciated. I want to thank Dr. Michal Szymonik for helpful discussions, lab training, technical help on thesis writing and moral support and Dr. Simon White for advices on specific problems and help using fluorospectrophotometric equipment and purification techniques.

I would also like thank Dr. Irene Zaccari, Andrew Lee, William Morton, Sybilla Corbett and all the other fellow researchers in the Bioelectronics group for their help, advice, encouraging consultations and friendly time in the office. They invigorated my interest in the field, helped to see the project in a larger picture and kept the everyday work pleasant and stimulating.

I reserve special thanks to my mother, father and sister, who provided me with the possibility to pursue this degree and supported me throughout and Dean Leyland and many other friends, who made my time as a PhD student happy and memorable.

Abstract

With today's challenges in the electronic industry, novel alternative approaches for manufacturing devices at nanoscale are being investigated. Using self-assembly, arguably has the best potential for nanostructures.

DNA and proteins - some of the most important biomolecules use self-assembly extensively for natural functions. Chemical and structural predictability of DNA and specificity of proteins promise a big potential for novel materials and could allow creation of structures controlled at nanoscale level.

RecombinaseA - a DNA-binding protein has been used for controllable and predictable patterning of selected DNA sequences, opening the way to nanometre-scale DNA marking. However, protein patterning alone does not add any electric or other desired functionality to the DNA, therefore additional modifications are neccessary. Furthermore, since biological molecules have transient functionality, system stability investigation is crucial for needed modification and subsequent usage.

This project focused on RecA-patterned DNA modification for electric property addition. Thiolation and subsequent attachment of gold or magnetic nanoparticles to RecA protein present on DNA were investigated as a method for creating electrically conductive nanoscale objects. More specifically, attachment of gold nanoparticles throughout the whole patterned region of DNA and attachment of single nanoparticles at precise positions were looked into. The work successfully demonstrated that both nanoparticle deposition along the full length of RecA-coated DNA and specific single nanoparticle positioning is feasible.

For investigating RecA-DNA stability, a system based on FRET was devised and used to analyse interaction kinetics. It was found that RecA-DNA complexes are fully formed in minutes and stay bound for hours. Specific configurations of the set-up showed distinct lack of signal, suggesting complicated interactions between the protein and patterned DNA.

The project demonstrated through binding of NPs at specific locations and on the whole filament length that the system has potential for electronic applications and its stability is sufficient for processing times.

Abbreviations

ssDNA	Single-stranded DNA
dsDNA	Double-stranded DNA
bp	Base pairs
kbp	kilobase pairs
kDa	kiloDalton
dNTP	Deoxynucleoside Triphosphate
MgAc	Magnesium Acetate
AFM	Atomic Force Microscopy
MFM	Magnetic Force Microscopy
SPR	Surface Plasmon Resonance
SATA	N-succinimidyl S-acetylthioacetate
2-IT	2-iminothiolane
SPDP	Succinimidyl 3-(2-pyridyldithio)propionate
DTNB	5,5'-dithiobis-(2-nitrobenzoic acid (Ellman's reagent)
TNB^-	2-nitro-5-thiobenzoate
DTDP	4,4'-dithiodipyridine
HEPES	4-(2-hydroxyethyl)-1-piperazineethanesulfonic acid
BSA	Bovine Serum Albumin
NP	Nanoparticle
FRET	Fluorescence Resonance Energy Transfer
MCH	6-mercapto-1-hexanethiol
DTT	Dithiothreitol
TCEP	tris(2-carboxyethyl)phosphine
DNA	Deoxyribonucleotic Acid
PCR	Polymerase Chain Reaction
RecA	Recombinase-A
ATP	Adenosine triphosphate
ATPγs	Adenosine-5'-O-thiotriphosphate

Contents

List of Figures

LIST OF FIGURES

Chapter 1

Introduction

1.1 The possibilities of matter engineering at the nanoscale

The advancement in natural sciences has consistently led to more complex and sophisticated discoveries and engineering achievements. The first endeavours in physics, chemistry and biology were performed with limited toolsets and at scales where eyesight and hand manipulation could be used without any enhancing utilities. The relatively simple discoveries led to utilisation of the found principles in the form of new and improved tools, which led to more advanced research. Gradually, the work led to realisation that matter in its diverse types and collections took a pivotal role in all three natural sciences and that human manipulation of matter at ever smaller scale can yield novel materials and devices. In contemporary science, material physics, biology and chemistry are probed at a scale close to atoms – the most basic matter constituent. By reaching the such scale, researchers are working at the foundational level for the natural sciences, which opens the possibilities of combining the traditional field elements, such as bulk materials, organic and biological molecules, into novel arrangements and networks.

Current biotechnology already works at single biomolecule level. Protein modification and expression, DNA sequence manipulation and novel antibody construction are performed daily with important applications in medicine, agriculture, industry and history. Contemporary material and chemical research is working at nanoscale – dealing with sizes in the order of molecules – too, leading to improved materials, novel pharmaceuticals and industrial applications. However, the engineering potential is still

not fully realised.

A full control of matter at nanoscale could eventually lead to integration of chemistry, material science and biology at the most fundamental level. There is strive to produce superior materials with such properties as self-repair, self-assembly and fine-tuned response to external stimuli, such as light, environmental gasses and liquids or physical force. Integration of biological molecules with traditional materials should unlock such options because biomolecules are evolved to interact with and are reactive to environmental changes.

Contemporary medicine excels in pharmaceuticals that selectively treat a specific illness. However, the drugs typically have undesired side effects and affect the whole patient body. Integrating pharmaceuticals with novel nanoscience materials such as nanoparticles, could deliver drugs to specific organs and tissues that are in need of treatment, minimising any side effects on other parts of the body. Furthermore, such targeted delivery systems would allow for new treatments of specifically localised conditions such as cancer. In the long term, unification of biological and non-biological materials has the potential of monitoring and manipulating patient health at a single cell level via signal inputs and outputs through simple electric, light or other conventional methods.

Use of biomolecules specific to certain molecules could also work as environmental sensors. By integrating such molecules with conventional materials, large array of nanoscale monitoring devices would allow for cheap and detailed pollution or production quality observation.

The relatively small size of nanodevices and the "bottom-up" approach of nanomaterial construction comes with certain intrinsic advantages. The "bottom-up" approach championed in nanoscience describes manufacturing of a functioning device or material by taking the smallest building blocks and assembling them in the right way to achieve the final product. That is in contrast to the traditional "top-down" approach, where basic materials are reduced by milling, sawing, etching and other ways to the right sizes and combined as building blocks to create the final device. Since the manufacturing tools are designed to be both interacted by engineers and reach as small manipulation scales as possible, the device created will have smallest features that are defined by the tool's smallest parts. Nanoscale device size is defined by its complexity and number

of parts and most crucially, by the size of parts. Nanodevices are created by combining naturally-small molecules, atoms and other similar-sized entities as opposed to being-dependent on a relatively large manipulation tool. Since the building blocks are usually brought together by natural forces interacting between them, their positioning is very precise, down to single-nanometre resolution or less. This allows to achieve very small tolerances and great device characteristics. Furthermore, even though the initial building blocks are of the single nanometre order-size, the final assembled constructs are not limited in size. This unlocks the ability not just for the nanoscale devices, but also for novel materials where the material properties arises from the assembled component placement relative to each other and their interaction and preserved long range order in the final structure.

Secondly, there is small to no material wastage in the "bottom-up" approach. Any unused building block in this method is typically ready to be used in a different product, whereas any excess material that is removed in traditional manufacturing is often not salvageable and discarded. This considerably saves on production costs.

Another advantage saving in production costs is the manufactured device size itself. A nanoscale equivalent of a microscale device is not small enough to integrate with other systems, it also costs less in materials to produce. Alternatively, many more devices can be created with for a comparable price of aforementioned microscale device. This leads to ubiquity of produced nanodevices and their potential liberal integration to organism tissue cells, traditional materials and surfaces resulting in device networks.

The nanoscale materials are also welcomed in electronic engineering, because of their flexibility and ability to access the smallest elements. The electronics industry is one of the fastest progressing fields contemporary human life with high commercial demand, but the fast progress is slowing down and new avenues are being explored. Arguably, nanoscience is already making an impact to electronics as its one of the first major commercial areas and will continue to affect it.

1.2 The current state of the electronics industry

With today's wide and ubiquitous spread of electronic devices used in general and specialised computing, imaging components for photography or medical systems, thermal

and light sensors and other applications, there is an ever-growing demand for manufacture and integration of electronic components. A typical modern device is composed of up to billions of electronic elements requiring enormous engineering and financial efforts to achieve a pre-designed assembly of micro- and nano-scale constituents. Even though electronics prove irreplaceable in many diverse fields today, the consumer demand for more powerful devices which requires even smaller components is proving hard to satisfied. The electronics industry is starting to struggle with device manufacture since device elements are already in the nanoscale regime and experiencing size-related production issues. The iterative improvements are continuously being applied to each new generation of manufacturing processes to improve the device characteristics, however the unavoidable approach of device element size to the fundamental physical limits calls for novel manufacturing techniques.

Arguably the most important part of any electronic device is a transistor: a fast switch for electric conduction driven by change in electrical current or voltage. This switch is partially produced from a semiconducting material (or a 'semiconductor' for short) whose conductivity can be modified. Even though transistors became one of the favoured constructing elements, there was a practical limit to the size of transistors and other elements since each component needed to be manually wired and assembled together to produce functional electronic circuits and devices. Although there were some ideas to produce devices requiring no assembly, this was not realised until 1958–1959 by Jack Kilby from Texas Instruments and Robert Noyce from Fairchild Semiconductors [1]. This marked the invention of the integrated circuit (IC): a device that has a set of interconnected constituents (as specified by a device design) produced from a single piece of material and wired together simultaneously without the need for post-fabrication assembly, drastically reducing labour time, cost and material resources needed.

Having fast-switching transistors produced in parallel and in massive numbers in a single IC established the modern electronic industry, and most importantly, enabled the exponential growth of electronics industry. The main drive for such achievements is essentially the trend of miniaturisation: the shrinking size of transistors allows more of them on a single integrated chip increasing device's computational performance, image sensor resolution, etc. Conventional modern transistors in devices are typically produced as metal–oxide–semiconductor field-effect transistors (MOSFETs) using

complementary metal–oxide–semiconductor (CMOS) technology [2]. The technology fully relies on (photo-)lithography as a device production method [3] [4]. New photolithographical techniques are constantly being developed with each new generation of devices to allow for higher numbers of MOSFETs per electronic chip. This iterative scaling was noticed and quantified by Gordon E. Moore [5]. According to the popular "Moore's Law", each fixed amount of time (typically every 18 months) the advantageous characteristics of an electronic device—number of transistors on an IC, size of the transistor, hard disk drive memory capacity, imaging sensor resolution—tends to double. To this day, each new generation of devices produced followed the trend.

However, IC scaling is gradually becoming a more and more difficult task. The latest techniques are pushing MOSFET sizes below 20 nanometres (nm) but come with high financial and device performance costs [6] [7]. Development of each new next-generation processing technology costs more than the previous and, most importantly, the devices are reaching fundamental physical limits [8]. Besides manufacturing issues, such small-scale transistors are challenged by other problems, such as current leakage due to quantum tunnelling and suboptimal heat dissipation characteristics [9] [8]. With ever-increasing consumer market demand for more powerful computing devices, there's clearly a demand for novel approaches to electronic device manufacturing.

Some of the proposed solutions to the aforementioned problem involve use of novel materials, such as graphene or nanowires. Graphene is typically hailed as a future electronic device material due to its unique properties [10]. Graphene's structure of only a single layer of atoms, gives rise to ballistic charge transport (conductivity with minimal losses due to electron scattering), orientation-dependent electrical conductivity, thermal conductivity higher than diamond and mechanical strength 100 times higher than steel [11] [12] [10] [13]. Because of these properties, graphene is considered to have potential applications in electronics: from replacing MOSFETs to better touch screens and Hall effect sensors [14] [15] [16]. However, although significant resources are dedicated to it, there are still no large scale commercial applications making use of it [10] [11]. As for inorganic nanowires, they are typically produced through nucleation and growth processes which do not guarantee exactly defined length [17]. Furthermore, nanowire positioning after production will typically be random and they will not be integrated into hierarchical structure needed for a working device [18].

With today's chemical and biochemical techniques able to produce a vast selection of nanometre-scale objects, such as the aforementioned nanowires, it would be advantageous to have a system to position and interconnect them precisely as desired. This would enable production of ICs, assembled from components smaller than a modern transistor in a controlled hierarchical structure with nanometre order precision to the final device and saving material and production time costs. The added benefit of fully utilising the third dimension for component population (as opposed to today's lithographical use of it for just hierarchical integration), would open up possibilities for even more complex ICs and more powerful devices. Furthermore, since basic constituents are produced chemically in mole quantities, it would be trivial to scale device production to large quantities. The chemical and biochemical nature of the building blocks would also allow for easier integration with the biological world – a frontier sought after by the current industry with little success. Also, interaction with various chemical compounds would unlock opportunities for flexible and diverse ways of exploiting optic, magnetic, mechanical and other material properties. A system with such properties would most definitely be considered the next major step in electronic engineering since the invention of the IC. However, no such alternative to ICs and related aspects of them, such as photolitography, compatible materials and fully developed workflows have been yet developed and the best approach is still yet to be found.

1.3 Self-assembly as the new manufacturing method

The natural world seems to have solved a similar problem of massive parallelisation at nanoscale in a graceful manner, refined by many years of evolution. Biological molecules with sizes comparable to modern electronic components arrange themselves by well defined rules which are coded intrinsically in their structure [19]. The concept is known as 'self-assembly' and can be defined as reversible and spontaneous association of molecules into thermodynamically stable and structurally well-defined compounds, held together by non-covalent forces [19]. These molecules join through a number of non-covalent bonds in site-specific, sequential manner. Although the non-covalent forces such as hydrogen and van der Waals bonds are weak compared to covalent bonds, the sum of numerous such interactions lead to stable higher order structures of sizes in the range of few nanometres to micrometers.

Electrostatic characteristics of biomolecules, such as proteins, DNA (deoxyribonucleic acid), RNA (ribonucleic acid) and lipids, allow them to interact with very high specificity and efficiency, whereas reversibility of self-assembled compounds ensures ephemeral structures and molecule mobility. The end result is the highly sophisticated molecular machinery found in every living cell, enabling fully autonomous functioning of the cell through biomolecular signalling, transport, structural building and material take-up and release. And all is driven by specific molecular interactions happening in parallel and at rates high enough to sustain life [20]. Natural world uses self-assembly extensively from small protein complexes, to viral RNA assembly with proteins to form final virions and, arguably, full cell formation. A good example of that is the tobacco mosaic virus (TMV) assembly [21]. The structural virus proteins come together and form a cylindrical screw only in the presence of its own RNA that becomes encapsulated in the middle of the formed structure.

Amid various biomolecules, DNA and proteins stand out in their self-assembly abilities. DNA with its relatively simple structure of four types of repetitive units interspersed among themselves is easily predictable in its properties and behaviour [20]. Since DNA–DNA interactions happen solely through DNA's own structural building units, it is relatively simple to design and self-assemble many DNA fragments to create complex two- and three-dimensional geometric structures much larger than the original DNA with minimal cost [22] [23] [24] [25] [26]. The first artificial DNA structures were demonstrated by Seeman in the early 1980s as repeat DNA motifs capable of self-assembling into large-scale lattices [27]. Rothemund textitet al. demonstrated folding of some of the most complex 2D shapes constructed from viral ssDNA folded by shorter 'staple' ssDNA with strategically selected sequences [24]. The staple ssDNA brought together different regions of viral ssDNA and held them together, forming pre-designed 2D shapes. This work showed Other DNA structures have been used for trapping other molecules, demonstrating switchable structural states, performing simple computations and for constructing molecular motors for molecular transport capable of walking on one-dimensional tracks and two-dimensional surfaces [28] [29] [30] [31] [32] [33] [34]. As for proteins, their very high specificity for other biomolecules allows to them to carry out their work in the presence of other proteins without side interactions [20]. Protein-based self-assembled structures are present as well, including artificial ones, like fibrous

biomaterials developed by various groups [35]. This property can be utilised to impart order to a solution-based system when possibly interfering molecules are present.

The phenomenal mechanism of biological self-assembly is the reason why research interest in using it for electronics is increasing [36] [37]. The ability to organise primitive building blocks into complex three-dimensional shapes with sub-nanometre precision in a parallel fashion with little or no intervention would allow for a novel manufacturing process surpassing lithography in many aspects. However, biomolecules on their own do not posses any electronic properties exploitable for more advanced engineering [38] . Hence, for the designed biomolecular large-scale structures to be useful, additional modifications need to be considered.

1.4 Nanoparticles for imparting electronic properties

Since organic compounds such as biomolecules generally have limited electronic characteristics, when such abilities are desired, electrically conductive inorganic compounds such as metals or semiconductors need to be bound to the molecules of interest. This can be achieved by anchoring molecules onto inorganic surfaces, forming metal ion–ligand complexes, electrostatic binding of metal ions to negatively-charged biomolecules , or seeding, nucleating and developing metals onto biomolecules [39] [40] [41] [42] [43] [44] [45] [46] [47] [48]. Often these methods are combined to achieve a better level of metallisation. Another well-established technique is the use of metallic nanoparticles. Nanoparticles (NPs) are (typically) spherical crystalline clusters of atoms, with a radius of up to 100nm, possesing properties unique to their size, such as a surface plasmon resonance peak or controllable aggregation, as well as properties similar to the bulk material [49] [50]. Extensive research has been carried out on NP–biomolecule conjugation developing novel nanoscale systems [51] [52] [53] [54]. Due to their relevant size, controllable behaviour, flexible attachment chemistry, ease of synthesis and, most importantly, electronic properties, nanoparticles are a primary choice for imparting different electronic properties to biomolecules or structures thereof.

By utilising DNA as structural and 'scaffolding' material, proteins for site-specific binding and position marking and nanoparticles for inducing metallic, semiconducting or magnetic behaviour, one could create exciting molecular electronic devices with superior or even unprecedented behaviour, and of extremely small scale, possibly stepping

into the regime and exploitation of quantum mechanical phenomena. The developed process itself would rival conventional lithographical processes in performance, feature-size, financial and ease-of-use terms.

1.5 Objective

The objective of this PhD project is to explore and evaluate methods for imparting metallic and magnetic behaviour through nanoparticle attachment to a specific DNA–protein structure technology. This is carried out through site-specific DNA metallisation using nanoparticles in two different ways: by attaching single nanoparticles in specified locations throughout the whole length of DNA, and by fully covering a specific linear fragment of DNA with nanoparticles. The nanoparticle binding along the DNA is controlled by a protein binding on DNA in a specific, controlled fashion.

The technology used to achieve these goals is based on interactions of different lengths and types of DNA and a protein called RecA. Research has shown that the DNA-binding protein RecA can be used to selectively 'pattern' DNA to a high precision by firstly polymerising on relatively short single-stranded DNA and forming what is called a nucleoprotein filament ('filament' for brevity) and afterwards invading a longer double-stranded DNA (dsDNA) with filament binding in a parallel fashion on this dsDNA [55] (Figure 1.1). The section of dsDNA that the filament will bind depends on the composition and sequence of the aforementioned structural building units of the ssDNA in this filament. If ssDNA sequence has same or very similar sequence to that of a particular region on dsDNA, the binding will occur and the region will contain a triple-stranded fragment with RecA wound around it.

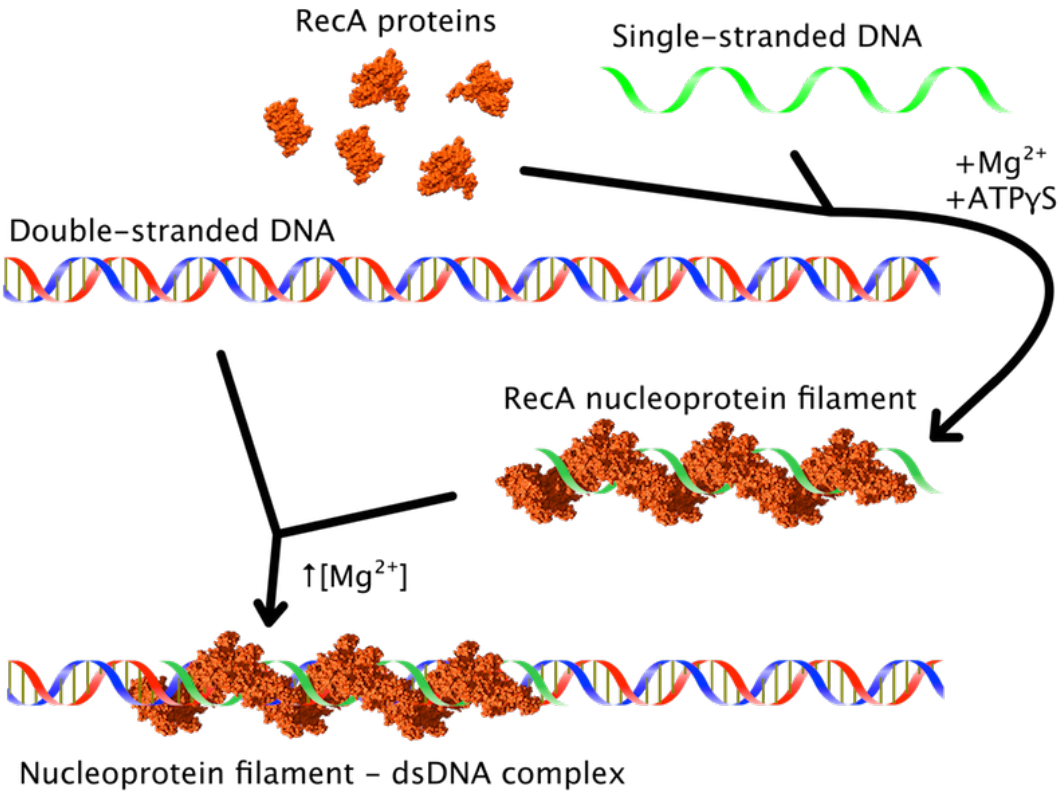

Figure 1.1: The mechanism of selective RecA nucleoprotein filament formation and patterning on double-stranded DNA based on DNA sequence recognition.

Multiple-patterning of two or more dsDNA fragments has been shown to be possible [56]. This is a powerful tool for patterning site-specific length-specific regions of dsDNA – the most common type of DNA – in a controlled and precise way. The bound protein can be used as a target for binding nanoparticles and metallising specific extents of DNA scaffold. Alternatively, one of the ends of the bound ssDNA can be used as a target for a single nanoparticle binding.

Nucleoprotein filaments can also be formed directly on dsDNA throughout its full length [57]. This does not allow for site-specific patterning but simplifies the system and would allow for basic nanowire fabrication if metallic NPs were conjugated to the RecA protein throughout full length of the filament.

The structural stability of these DNA–protein complexes should be good enough for

subsequent nanoparticle binding and so the time-based stability of the made structures and relevant reaction rates for forming them are investigated in this project.

1.5.1 Protein thiolation and nanoparticle conjugation

A nucleoprotein filament patterned on long 'template' dsDNA can be modified to accommodate the binding of NPs. Typically, NPs will not have any preference for site-specific attachment throughout the whole patterned structure, but if proteins for example, are modified to contain a certain chemical group that has high affinity for NP material, NPs will will deposit selectively onto protein surfaces. A simple and an established method is the use of gold–thiol (chemical group $-SH$) chemistry [58] [59]. Gold nanoparticles (Au NPs) are the most widely synthesised and utilised type of NPs and protein thiolation (modification to incorporate thiols) is also well established [49] [60]. Protein thiolation is typically performed by reacting an external thiolating reagent such as 2-iminothiolane with the primary amines (chemical group $-NH_2$) abundantly available on the protein surface [60] in lysine amino acids – one of the protein building blocks. When the filament surface is thiolated through modification of RecA, Au NPs can be introduced to form site-selective electrically conductive gold-coated regions on template dsDNA or, alternatively, a metallic nanowire throughout the full extent of the filament (Figure 1.2).

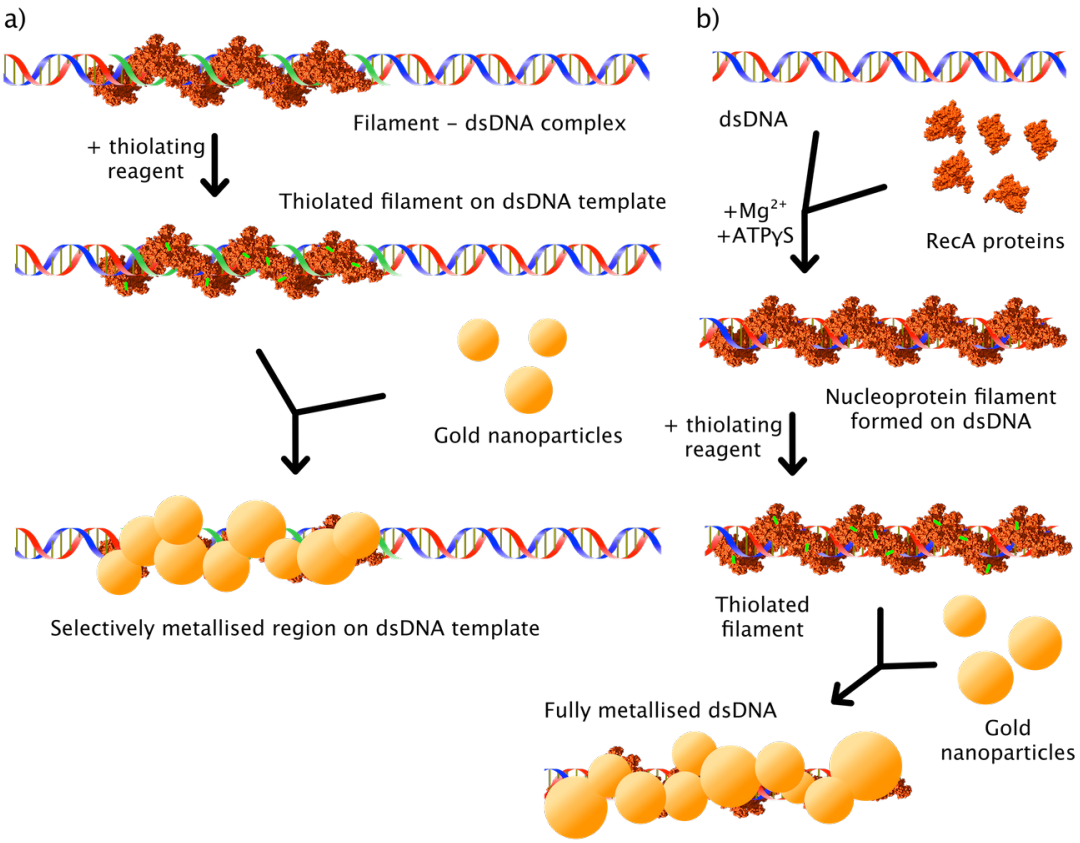

Figure 1.2: Two systems for metallising DNA: a) specific metallisation using nucleoprotein filament patterning on template dsDNA using gold–thiol chemistry; b) non-specific dsDNA metallisation using the same RecA protein and attachment chemistry.

Additionally, magnetic nanoparticles can be conjugated to impart magnetic properties to regions of the structure. The project work deals with superparamagnetic magnetite (F_3O_4) nanoparticles which have a gold shell around the magnetite core. This particular composition gives magnetic properties whilst retaining the same gold–thiol chemistry for NP conjugation. The described metallisation process can be scaled up to site-specific metallisation of large and complex DNA structures, creating transistors, capacitors, inductors, interconnects and other components – fully realising conventional electronic devices.

1.5.2 Selective site-specific single nanoparticle placement on patterned DNA structures

For novel devices exploiting quantum mechanical phenomena, the electronic components on the DNA scaffold need to scale down below about 10nm [49]. This typically means a single nanoparticle with a diameter below 10nm. The previously described system is not able to achieve this since the shortest possible filament involves two RecA proteins and the protein surface is thiolated non-specifically, yielding numerous thiols per filament. The exposed thiols will be able to accommodate more than one <10nm-sized NP, preventing the ability to produce quantum devices. A way to achieve single nanoparticle placement is to avoid protein modification and use thiol-terminated ssDNA for nucleoprotein filament formation. Such ssDNA can be easily synthesised with a thiol at the end of the DNA chain [61] [62]. After filament patterning on template dsDNA is finished, the incorporated ssDNA will have a flanking thiol at one end of the patterned region, allowing the conjugation of only a single NP. Such an approach of single nanoparticle placement may yield the ability to build quantum entities such as quantum bits or electron spin filtering devices [63] [64].

Both of the aforementioned metallisation strategies are examined in this project for manufacturing molecular electronic devices.

1.5.3 Template dsDNA–nucleoprotein filament stability investigation

Since nanoparticle positioning depends on a filament staying in a fixed location with respect to the template DNA, there is a need to ensure that filaments stay bound to their respective template position until metallisation is fully performed and the structures are safely deposited from solutions onto dry surfaces. To investigate this, Förster resonance energy transfer (FRET) is used.

FRET is an optical technique based on fluorescence – an optical phenomenon where a molecule, called fluorophore, absorbs a specific wavelength of light and emits a longer wavelength [65]. In this work, FRET is used by having one fluorophore attached to the end of the binding ssDNA and a different fluorophore attached to the end of the template dsDNA (Figure 1.3). The patterning region is designed so that when the filament formed on ssDNA binds onto the template dsDNA, both of the fluorophores come close to each other and their interaction can be measured optically.

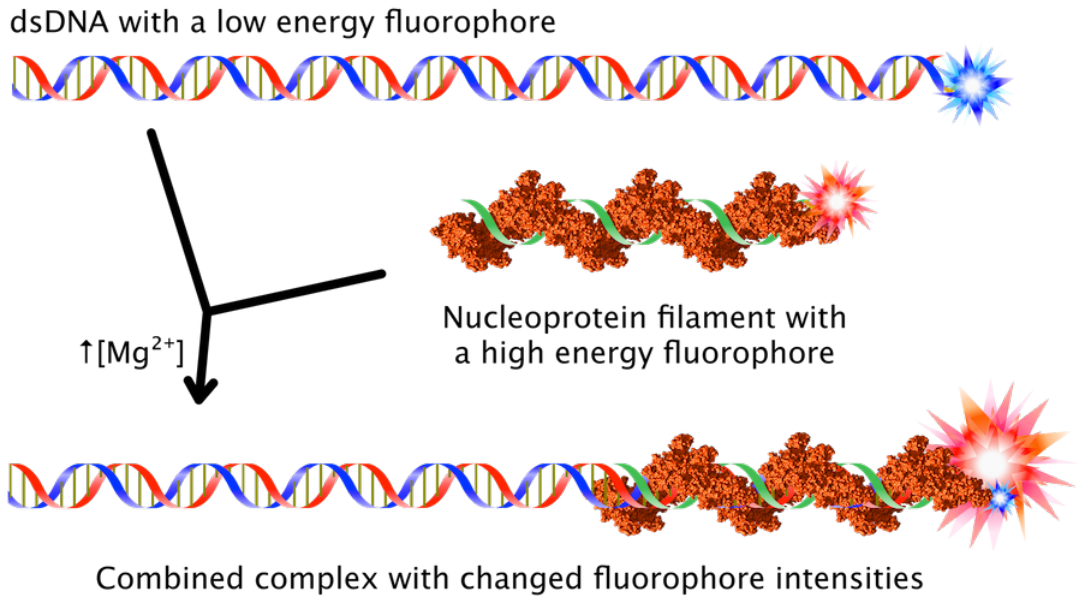

Figure 1.3: The method of measuring template DNA–filament interaction. dsDNA and the filament, both having a fluorophore each, interact by filament patterning mechanism and bring the fluorophores into proximity. Fluorophore intensities change due to FRET, which can be registered.

This allows the binding rate of the filament to template dsDNA to be measured. To measure the unbinding (or dissociation) rate of filament-dsDNA, an excess amount of template dsDNA without a fluorophore attached can be introduced into the system. If filaments are bound tightly to their template dsDNA, the optical interaction will not change and the structure can be considered stable. If, however, filaments tend to unbind from the template dsDNA and bind again over time, the introduced excess dsDNA without a fluorophore will outcompete the original dsDNA for filament binding. Since now the fluorophores are separated again, the optical properties should change and that would indicate unstable filament-dsDNA structures.

This is the technique used in this work to determine the stability of nucleoprotein filament-dsDNA templates and therefore the suitability for subsequent modification, such as metallisation.

1.6 Overview of the chapters

Here is given a summary of the following chapters and their content.

1.6.1 Chapter 2 Project background

Introductory knowledge is supplied on proteins and DNA, their structure, self-assembly properties and natural purpose in cells. Structure, stability and other properties of protein RecA and RecA–DNA complexes called nucleoprotein filaments are described. Additionally, background on protein thiolation and other modifications as well as nanoparticles and their conjugation is provided for understanding of the chemistry used in this work.

1.6.2 Chapter 3 Literature review

This chapter overviews the relevant work that has already been carried out on creating two- and three-dimensional artificial DNA structures and exploiting them for any applications, attempts at metallisation of such DNA-based structures or DNA itself, and use of RecA for selective DNA patterning. The chapter also reviews alternative methods of building large scale objects from any other nanoscale components suitable for electronic applications.

1.6.3 Chapter 4 Experimental Techniques

The reader is introduced to experimental techniques used in this work, namely polymerase chain reaction, gel electrophoresis, atomic force microscopy, (fluoro-)spectrophotometry, confocal microscopy, and Förster resonance energy transfer.

1.6.4 Chapter 5 Nucleoprotein filament formation, thiolation, purification and metallisation

Here work on RecA nucleoprotein filament formation and thiolation with three different thiolating reagents under various conditions is described. Different methods attempted for purifying both thiolated nucleoprotein filaments or just thiolated RecA including protein spin columns, dialysis and magnetic bead purification are included. Methods used in quantifying protein thiolation levels, namely through use of Ellman's

reagent, 2,2'-Dithiodipyridine or binding of gold nanoparticles are discussed. Afterwards, the chapter focuses on thiolated nucleoprotein filament metallisation using gold and magnetic gold-coated nanoparticles and the dependence on different variables such as incubation time or salt concentration. Two different methods of nucleoprotein filament thiolation and metallisation – solution-based and surface-bound filament – are compared. Atomic force microscopy images given in this chapter show the extent of metallisation and regularity of nucleoprotein filaments.

1.6.5 Chapter 6 Selective site-specific single nanoparticle placement on patterned DNA structures

A system of positioning single nanoparticles along double-stranded DNA–nucleoprotein filament complexes with single base precision is introduced and work to realise it is described. Two different approaches for having such a system with interspaced nanoparticles are documented. The formation of double-stranded DNA–nucleoprotein filament complexes is quantified through restriction enzyme gel assays.

1.6.6 Chapter 7 FRET and gel time snapshots for measuring kinetics and stability of filament–dsDNA interaction

To evaluate formation rates and stability of nucleoprotein filament structures, FRET was used and followed with a confocal microscope and a fluorospectrophotometer. FRET analysis was done on two similar double-stranded DNA–nucleoprotein filament complex systems with significantly different results which are explained with current DNA–filament interaction models. Furthermore, restriction enzyme gel assays were used to confirm the reaction kinetics observed via FRET.

1.6.7 Chapter 8 Conclusion and future work

The reader is given a short summary and conclusion of the project work done, and insights into potential future directions.

1.7 Conclusion

This chapter established the potential of nanoscale materials and devices and reviewed the current state of electronic industry, lithographical manufacturing processes and the

challenges the industry faces. Biomolecules with their unique ability to recognise other molecules, and, most importantly, self-assemble from single entities to much larger sophisticated compound structures were introduced and evaluated as a replacement for lithographical processes. It was concluded that some form of electronic character needs to be imparted to these structures before they can be used in electronic applications and nanoparticles were suggested as a way forward. The project description with a working mechanism outline was given for building nanoscale molecular electronic ICs. Finally, the objective of the whole project was summarised and brief description of each chapter was given.

Chapter 2

Project background

The last chapter established the idea and the potential of nanoscale engineering and suggested the use of biological molecules and inorganic nanoparticles for constructing a framework for novel devices and materials. This chapter introduces the basic information on biomolecules proteins and DNA, their chemical composition, structure and natural functionality. In particular, protein RecA and the RecA–DNA structure called nucleoprotein filament are described extensively since they are the main structural component of this project work. Finally nanoparticles and their characteristics are presented. All this information is given for good foundational knowledge of specific molecules and processes used in experimental work, described in later chapters.

2.1 DNA

Deoxyribonucleic acid or 'DNA' for short is a biomolecule found in majority of living cells. It is located in cell's cytosol in prokaryotic cells and in its nucleus in eukaryotic cells. The natural function of DNA is to contain the information needed to create the organism in which the DNA is in. With help of selected proteins, information coded in the DNA gets transformed into connected amino acid peptides, which ultimately become new proteins – a process known as protein expression. Alternatively, DNA also codes for levels of protein expression and the synthesis of biomolecules that regulate the expression.

Although DNA was first extracted in 1869, its actual structure remained unknown for a while [66]. Only in 1953 James Watson and Francis Crick determined the complex

DNA structure [67], based on the work done by Rosalind Franklin, Raymond Gosling and Maurice Wilkins.

The structure of DNA is a linear polymeric chain consisting of alternating monosaccharide deoxyriboses and phosphates. One of four subunits known as nucleic acid bases or nucleobases: adenine ('A'), guanine ('G'), cytosine ('C') and thymine ('T') – branches off of each deoxyribose [68] (Figure 2.1). Only one nucleobase (or 'base') is present at each deoxyribose and any one of the four nucleobases can take the place. Cytosine and thymine are classified as pyrimidines – organic compounds with a six-membered heterocyclic carbon atom ring where two of the carbons are replaced by nitrogen. Adenine and guanine are classified as purines – another organic compound where a pyrimidine ring is fused with a five-membered ring, in which 2 of the carbon atoms are replaced by nitrogens.

A collection of a phosphate, a deoxyribose and one nucleobase comprise a single nucleotide or a 'base'. Nucleotides are connected together through the aforementioned alternating deoxyriboses and phosphates of each nucleotide. Such a strand of nucleotides connected in a linear manner create a single-stranded DNA (ssDNA). The repeating structure of deoxyriboses and phosphates without the corresponding bonded nucleosides is named the phosphate deoxyribose backbone. The length of a ssDNA can typically range from single-digit nucleotides (or 'bases') to thousands and tens of thousands of nucleotides. Each DNA strand has directionality. Since all the nucleotides in DNA are connected through a phosphate deoxyribose backbone, at the end of the DNA, either a phosphate or a deoxyribose will be terminal. Deoxyribose has its carbon atoms labeled sequentially in its five-membered ring including one carbon atom outside the ring 1' - 5' (pronounced "one prime" to "five prime") The end of the ssDNA strand, that has the deoxyribose exposed is called the 3' end, because the next phosphate would attach to the 3' carbon atom of that deoxyribose. The opposite end of the ssDNA that has the terminal phosphate is named the 5' end, because 5' carbon in the last deoxyribose has the terminal phosphate bound to it. 5' to 3' is considered the conventional DNA direction.

A ssDNA can interact with another ssDNA if they have specific sequence of bases. Each adenosine can interact with a thymine (forming an 'AT' pair) and each cytosine can interact with a guanine (forming a 'CG' pair) via hydrogen bonding [68]. The specific hydrogen binding of AT and CG pairs is called Watson-Crick base-pairing. For

ssDNAs to interact properly, they need to be aligned antiparallel to each other – that is, one ssDNA will be aligned in parallel to the second ssDNA with respect to their phosphate deoxyribose backbones, but with ssDNA directionality running opposite of each other. In such arrangement, the sequence of bases in one strand will interact with the other strand forming hydrogen bonds and bringing the strands close together, as long as the sequence of bases on the second strand has the corresponding nucleobase for each nucleobase in the first strand. The binding of two DNA strands being specific only to the aforementioned conditions is known as the principle of complementarity and such two strands are considered complementary if they interact throughout their whole lengths [68]. Two fully interacting ssDNAs form a double-stranded DNA (dsDNA).

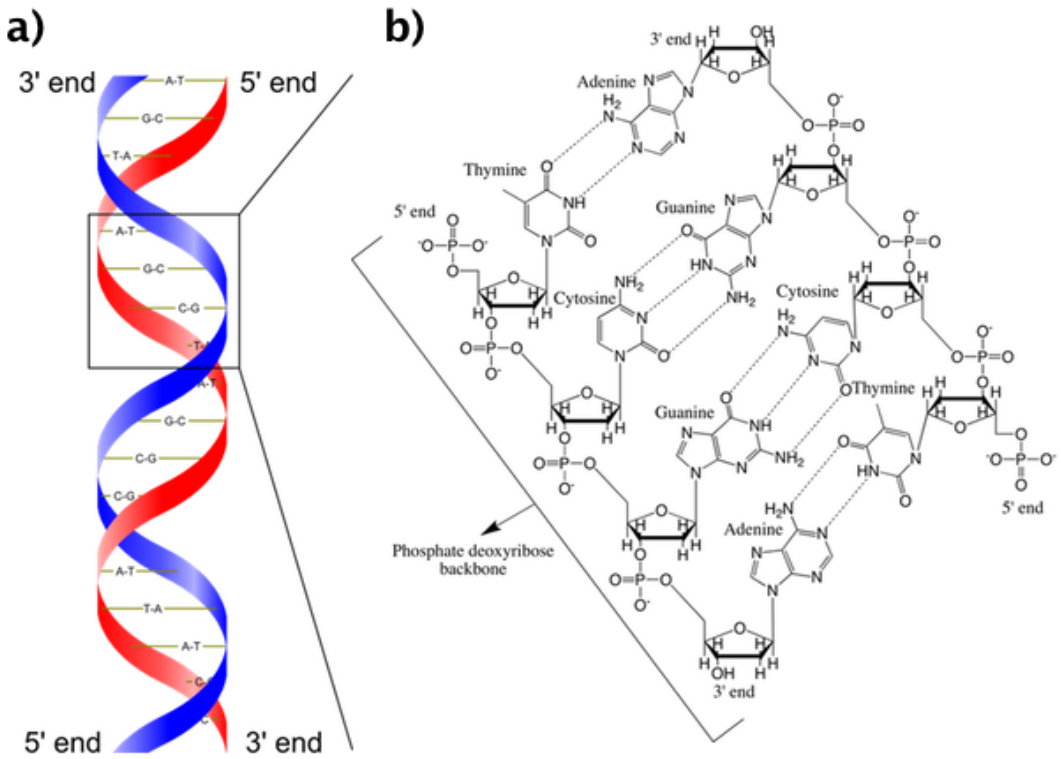

Figure 2.1: a) A large scale structure overview of a double-stranded DNA molecule: nucleobases are marked with letters 'A', 'C', 'G' and 'T', two separate phosphate deoxyribose backbones are depicted in red and blue; b) a detailed chemical illustration of structural elements of DNA: the phosphate deoxyribose backbone is marked separately, and the complementary nucleobases are forming hydrogen bonds.

The formed dsDNA is helical: both of the strands twist around a common rotational axis present along the length of the DNA [68]. The helical nature of the dsDNA is an energetic compromise on two repelling negatively charged phosphate deoxyribose backbones coming close together and the attractive forces in the form of hydrogen bonds between the bases stacked vertically throughout the rotational axis. The helical twist introduces to dsDNA two distinct grooves over a helical turn between the edges of the phosphate backbone on the same side: the major and the minor grooves. Different groove binds different molecules because of geometrical restrictions.

While ssDNA length is typically referred by the number of bases (b) present, the

length of dsDNA is referred by the number of base pairs (bp), since each strand contributes a nucleotide for the length of dsDNA. A single turn – also known as the helical pitch – of the B-DNA (the most common type of dsDNA) helix is 3.4nm and contains 10.5bp [68]. The diameter of such DNA is 2nm [20].

Besides B-DNA, which is the most prevalent form in cells, there exist two other conformations (structural varieties) of dsDNA. Z form of dsDNA (Z-DNA) can occur when the cell DNA is chemically modified through methylation (introduction of methyl chemical groups on cytosines). Z-DNA has a considerably longer helical pitch (4.6nm) compared to B-DNA and most importantly, the rotation of the DNA twist is reversed. B-DNA is a right-handed helix, whereas Z-DNA is left-handed. A-DNA is the third DNA form. It is wider (2.3nm) than B-DNA, right-handed and is found in partly dehydrated environments and in protein-DNA complexes. Also, DNA-RNA strand hybrids, which can achieved by manipulating normal DNA with temperature changes have a degree of similarity to A-DNA.

A dsDNA can be converted into two constituent ssDNAs by heating the dsDNA above a certain temperature known as the melting temperature (T_m). This gives the molecule enough energy to disrupt the hydrogen bonding between the complementary bases and separates the dsDNA. This process is called thermal denaturation. T_m is mainly dependent on the length of dsDNA, ion concentration in the solution and the ratio of CG pairs over AT pairs in the dsDNA of interest. Conversely, if two complementary ssDNAs are brought together whilst under T_m, they will spontaneously assemble into dsDNA. This process is called hybridisation [20]. A cycle of thermal DNA denaturation and rehybridisation is called annealing. The ability to separate dsDNA into its constituent ssDNAs and hybridise them back into dsDNA is a powerful tool and is used in polymerase chain reaction (PCR) and building of complex branched DNA structures.

A ssDNA can also interact with itself, without the need for a second ssDNA. If any part of ssDNA is complementary to another remote part, they can bind together and form secondary structures such as hairpins and pseudoknots [68].

Even though two strands of DNA are held together by Watson-Crick base-pairing, there can be an alternative hydrogen bond-based interaction between the bases called Hoogsteen base-pairing. In such case, one of the interacting bases is flipped with respect to its complementary base in the plane of interacting bases when comapred to the

Watson-Crick base-pairing. Both AT and CG base-pairs form 2 hydrogen bonds each in Hoogsteen base-pairing. Since the bases are flipped with respect to the complementary ones, Hoogsteen base-pairing can be found in certain cases of parallel DNA strands. Triple-stranded DNA (tsDNA) can be formed with a third strand of DNA inserting itself into the major groove of an already present dsDNA and interacting through Hoogsteen base-pairing with one of the dsDNA strands. The tsDNA is energetically unfavourable therefore it can only form under certain specific conditions.

If one of the dsDNA strands is rich in purines and consequently, the complementary strand is rich in pyrimidines, a third strand that is composed of complementary pyrimidines can bind the first strand through Hoogsteen base-pairing in the major groove. This is found in portions of genomic DNA known as H-DNA. tsDNA is also used for medical applications by developing triplex-forming oligonucleotides (TFOs) that bind specific regions of dsDNA and suppress DNA expression. If the dsDNA strands are not composed primarily of just the purines or the pyrimidines, tsDNA cannot form on its own. It can be formed in a complex with protein RecombinaseA for exchanging DNA strands, which is the phenomenon, that is the basis of this project. Quadruple strand DNA (qsDNA) are possbile as well. G-quadruplexes are qsDNA structures formed from DNA that has only guanine it its sequence. In such case, the DNA folds in such a way, that parts of it make 4 parallel and antiparallel strands that all interact with each other via Hoogsteen base-pairing. The G-quadruplex is further stabilised by a cation such as sodium or potassium in the centre of the paired bases plane. These qsDNA structures are found in the repeating sequences of telomeric genomic DNA and also lengths of DNA, responsible for protein expression regulation.

Even though DNA is typically portrayed as a double-stranded linear molecule, often it is found in a circular form. In such case, the dsDNA is in a ring shape and has no exposed 3' and 5' ends.

Circular dsDNA has the property of supercoiling, which is typically not present in the linear form of DNA. Supercoiling describes the geometric changes circular dsDNA undergoes when it is overwound or underwound, compared to its helical pitch. If overwinding of the DNA occurs, supercoiling is considered positive, whereas underwinding produces negative supercoiling. The winding produces twist and stress on the DNA which can transform itself to writhe – a loop of DNA that reduces the shear stress on it. For sufficiently long DNA, looping can occur naturally due to DNA's flexibility.

Topoisomerases are proteins, which responsible for the unwinding of the DNA. When a topoisomerase interacts with the dsDNA by unwinding and moving along it, the dsDNA is overwound in front of the protein and underwound behind it.

Besides topoisomerases and RecombinaseA, there are other proteins that interact with ssDNA and dsDNA in various ways. Examples are polymerases and nucleases that are responsible for multiplication and degradation of DNA, single-stranded DNA-binding protein prevents ssDNA hybridisation to dsDNA when needed and histone proteins pack the genomic DNA and control its expression.

2.2 Proteins

Expand protein interaction with water and other surrounding molecules, pH influence on protein surface charge

Expand on protein – protein interactions and conformational changes

Proteins are biomolecules present in all cells and are responsible for variety of crucial functions [68]. They bind other proteins and biomolecules and maintain cell's structural integrity and metabolic activity. Proteins are polymers composed of different amino acids linked together in a linear fashion through peptide bonds [68]. An amino acid is an organic molecule consisting of a primary amine (chemical group $-NH_2$), a carboxylic acid ($-COOH$) and a side chain (or a 'side group' denoted as 'R') – all linked through a carbon atom named alpha carbon (C_α) [68]. The peptide bond between each amino acids is formed by reaction of the primary amine on one amino acid and the carboxylic acid of the subsequent amino acid. The side chain determines the type of amino acid [68]. The only exception to the described binding model is the amino acid proline (Pro, P) which has a side chain that connects to both (C_α) and the amine group, making it a secondary amine [68]. There are 23 natural amino acids used as precursors for proteins and 20 of them are coded for by the DNA in the organisms which makes them the main amino acids [68] [69] [70]. Each side chain confers unique properties to its respective amino acid which is crucial for the final structure of the protein [68]. The amino acids are categorised into three groups depending on their side group main property: hydrophobic, hydrophilic and amphiphilic. Additional characteristics such as presence of positive or negative charge, the size of amino acid and the presence of

specific chemical groups, like thiols in cysteine amino acids affect. All of these properties determine the final shape and function of the protein.

When proteins are synthesised, other, already formed proteins catalyse the production by joining amino acids one by one by a peptide bond ($-$C(O)NH$-$) formed between the current amino acid's amino group and next amino acid's carboxyl group [68]. In terms of cell biochemistry, this process is named translation and is one of the steps in creating a functional protein from the information encoded in the cell DNA. The chaining of amino acids in translation leads to a formation of a polypeptide: a sequence of linearly connected amino acids [68]. The beginning of a polypeptide is called the N-terminus and the end of the polypeptide is called the C-terminus because they are terminated with an amine and carboxylic acid respectively [68]. Proteins have primary, secondary, tertiary and sometimes quaternary structure which all represent different perspectives for looking at the same protein [68] 2.2. The polypeptide with its unique sequence of amino acids is considered to be the primary structure of a protein [68].

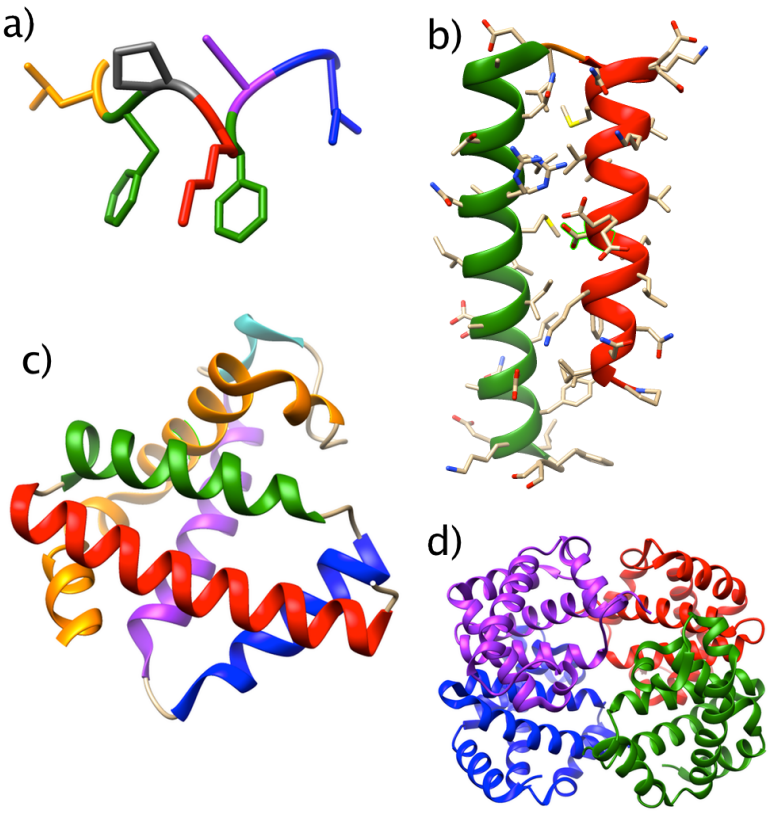

Figure 2.2: Different levels of protein structure: a) primary protein structure (a polypeptide) – a sequence of amino acids connected together (each amino acid is coloured differently); b) (α-helices and β-sheets) – amino acids interact with neighbouring amino acids forming stable structures (two α-helices are coloured differently; amino acid side chains are visible protruding from α-helices backbone); c) tertiary protein structure (folded protein) – α-helices themselves interact forming a globular protein (α-helices coloured differently); d) quaternary protein structure (subunit interaction) – some globular proteins interact with each other, forming larger final protein structure (each subunit is coloured differently). a) - c) uses myoglobin structure as an example (PDB entry: 1MBN and d) uses bovine haemoglobin as an example (PDB entry: 1G09).

The polypeptide chain is flexible enough to allow interaction of the side groups in the polypeptide. Depending on the sequence, some regions of the protein interact in a parallel or antiparallel fashion, forming β-sheets, or the side groups can interact with neighbouring amino acid side groups forming α-helices [68]. This interaction is based

on hydrogen-bonding and brings regions of the protein into certain three-dimensional conformational shapes and the α-helices and β-sheets are considered to be the secondary protein structure. β-sheet interactions result in a planar sheet of aligned polypeptide fragments, which is often bent and perturbed to minimise the total protein energy. α-helix interactions produce a right-handed helical shape of a single polypeptide region.

Certain other secondary protein structures exist, such as polyproline helices, α-sheets, π-helices and 3_10-helices, but they are rarer than the prevalent α-helices and β-sheets.

The formed α-helices and β sheets are brought closer together by weaker attraction forces, compacting the protein and giving its unique internal three-dimensional structure. This is called the tertiary protein structure and for a single polypeptide protein, the highest order one [68]. Some tertiary protein structures can be further stabilised internally by disulfide bonds (S−S) formed between two thiols present on cysteine (Cys, 'C') amino acids [68].

Some tertiary protein structures interact to a relatively high degree and spend majority of the time bound to each other. In this case, such tertiary structures are considered protein sub-units and the final quaternary protein structure is comprised of two or more same or different protein sub-units, each originating from their own polypeptide [68].

The hierarchical protein structure organisation shows how a linear polymeric polypeptide chain folds into the final protein shape which is determined only by the amino acid side groups and their sequence in the polypeptide. Only a single change in the sequence can lead to different protein folding, typically either improving or decreasing protein function.

Hydrophobic amino acids have side groups with no full or partial electric charge (apolar). Since proteins typically reside in aqueous solutions and water is partially charged, the hydrophobic amino acids tend to avoid being exposed to water and hence majority of them end up being buried inside the protein structure instead of exposed on the protein surface [20]. Hydrophobic amino acids do, however, interact weakly with themselves through van der Waals attraction forces. Both the van der Waals attraction and water avoidance contributes to partial protein structure stabilisation.

Hydrophilic amino acids are either partially or fully charged with a negative or positive charge (polar) enabling interactions with other water, polypeptide backbone

and other polar side chains. This too contributes to protein stabilisation.

Amphiphilic amino acids have both polar and apolar characteristics and tend to position themselves on the interface between polar hydrophobic and hydrophilic amino acids.

The surface-exposed amino acids determined the protein charge and interaction with other biomolecules. However, proteins do not have a static surface charge: depending on the pH of the solution, exposed side groups can loose or gain charge, changing protein surface charge and protein characteristics [68]. The pH at which the specific protein has a net zero charge is known as the isoelectric point (pI) [20]. Additionally, proteins might have certain post-translational modifications. These involve addition of certain chemical groups (acetates, methylation, etc.) or biochemical molecules (sugars or lipids) to the amino acids after the polypeptide is fully synthesised [20]. This further changes the protein characteristics.

The basic biochemical functions of proteins are binding, reaction catalysis, performing a structural function and state switching [71]. These functions build up to satisfy more sophisticated cellular needs. Binding is the highly specific protein recognition and interaction with other proteins, lipids, sugars and any other molecules through the charge distribution on the protein surface. It allows to make order in a cell system with thousands of different proteins, utilise biochemical cascades for signalling and recognise foreign to the cell entities via antibody–antigen interactions [71]. Reaction catalysis is performed by proteins called enzymes which allow to increase reaction rates by orders of magnitude and control the organism's metabolism [71]. When protein subunits bind to itself, this can lead to long range structural components such as actin filaments, microtubules or collagen, which act as a structural component and give the cell its shape or facilitate material transport. Protein switching is the conformational change in protein structure, allowing to register events such as pH or electrolyte concentration change or binding of another molecule, and trigger responses to them [71].

Building from simple variation of amino acids in the polypeptide sequence, vast selection of proteins are synthesised allowing for advanced functionality from cellular to organism level.

2.3 Protein RecA

Protein RecombinaseA (RecA) of *E. Coli* (*Escherichia coli*) is an enzymatic DNA-binding protein naturally involved in recombination and repair of DNA [72]. Its main function is homologous recombination of DNA strands: the facilitation of strand exchange between two DNA molecules [72]. Homologous recombination can occur over the entire length or certain fragments of two DNAs as long as one of the DNAs has a strand that is identical in sequence or similar to the other one. RecA is contains 352 amino acids (residues), has a calculated molecular weight of 37.842 kilodaltons (kDa) and a pI of 5.0 [73]. RecA is also classed as an ATPase: it needs ATP or an analogue to perform its function [72].

RecA X-Ray crystallographic structures have been reported for five different species. Story *et al.* showed the first structure of *E. Coli* RecA protein and its polymer form in presence of adenosine diphosphate (ADP) (protein database (PDB) entries '1REA' and '2REB') [72]. Chen and co-workers published the *E. Coli* RecA structure in the presence of DNA and non-hydrolysable version of ATP called ADP-aluminium fluoride-Mg (PDB entry '3CMT') [74]. Datta *et al.* revealed the RecA monomeric structures for *Mycobacterium Tuberculosis* in the presence of ADP–AlF4 (PDB entry '1G19') and *Mycobacterium smegmatis* in the presence of ADP, ATPγS, and dATP (PDB entry '1UBC') [75]. Prabu and co-workers later provided more structural data for *Mycobacterium smegmatis* RecA mutants, elucidating more on the monomeric structure of RecA (PDB entries '2ZR7', '2ZRP' an many others, all of them given in the original publication) [76]. A *E. Coli* RecA mutant with additional residues at N-terminus was also investigated by Xing and Bell [73]. Rajan and Bell reported a version of RecA found in an extremophile *Deinococcus radiodurans* with somewhat different structure to *E. Coli* (PDB entry '1XP8') [77]. A crystal structure for *Thermotoga maritima* RecA was also published (PDB entry '3HR8') but no associated publication was declared.

All of the published RecA structures reveal that RecA consists of three domains: a large central domain (M) and two smaller domains: 'amino' (N) and 'carboxy' (N), present at N-terminus and C-terminus of the protein respectively 2.3. The large central domain (M) in *E. Coli* spans from residue 34 to 269 and is mainly responsible for binding DNA and ATP or an analogue of ATP. The central domain involves a twisted β-sheet with 8 β-strands and 4 α-helices. The M domain contains two binding

loops: one (residues 156-165) for binding dsDNA and the second (residues 194-210) for binding ssDNA. The ATP binding pocket in the central domain (47-74) binds only the phosphate ($-PO_4$) part of the ATP. The small amino (N) domain is between amino acids 1 and 33, contains an α-helix and a β-strand and flanks from the rest of RecA. This domain has been shown to be important in stable formation of RecA polymer and ssDNA nucleoprotein filament. Residues 270-352 contain small carboxy (C) domain. It contains high concentration of negatively-charged amino acids and has been proposed as a controlling region for binding and unbinding of dsDNA [72]. The position of C domain with respect to M domain has also been shown to determine whether formed nucleoprotein filament is 'active' or 'inactive'. An 'active' RecA binds to DNA in the presence of ATP or ATPγS whereas the 'inactive' form of RecA binds onto DNA in the presence of ADP [72].

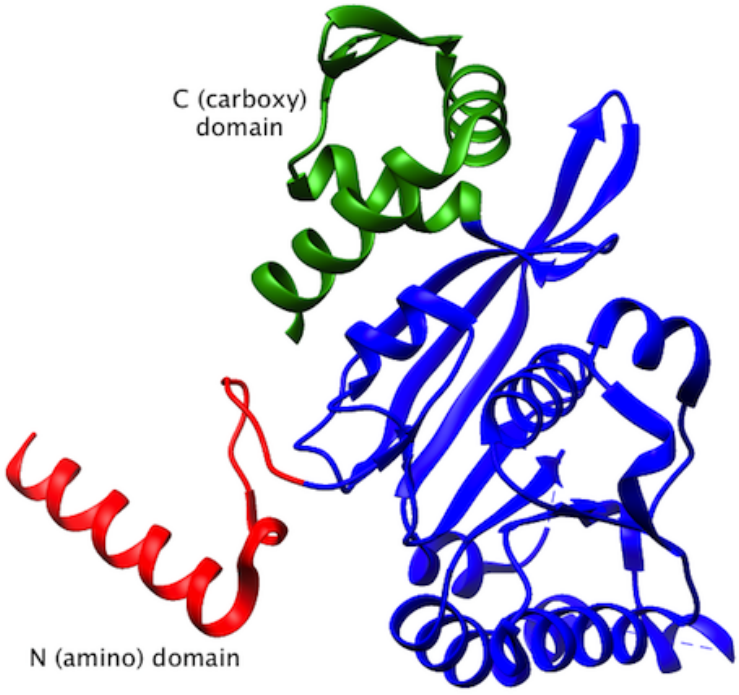

Figure 2.3: RecA protein structure with identified N-terminus and C-terminus domains.

RecA significance in nature comes from its ability to polymerise and interact with DNA. In presence of DNA and co-factors or in some conditions even without DNA, RecA polymerises with itself forming fibrous structures. [74] In presence of ADP, the

crystal structure of *E. coli* RecA protein, reported by Story *et al.* showed a helical polymer with a pitch of 8.3 nm [72]. The reported crystal structure was ceveloped without any ATP and DNA. A similar feature of 7.3 nm pitch was reported by Egelman and Stasiak using electron microscope, when the nucleoprotein filament was formed on a DNA molecule in the presence of ADP [78] [57]. With ATP or γ was used by them to form the nucleoprotein filament on ssDNA or dsDNA, more extended filaments with a 9.5 nm pitch were found. The RecA helix is approximately 1.2 nm wide, with a central diameter of 0.25 nm. ATP is bound near the center of the helix. The amino domain of each RecA monomer is involved in maintaining the RecA polymer bonds.

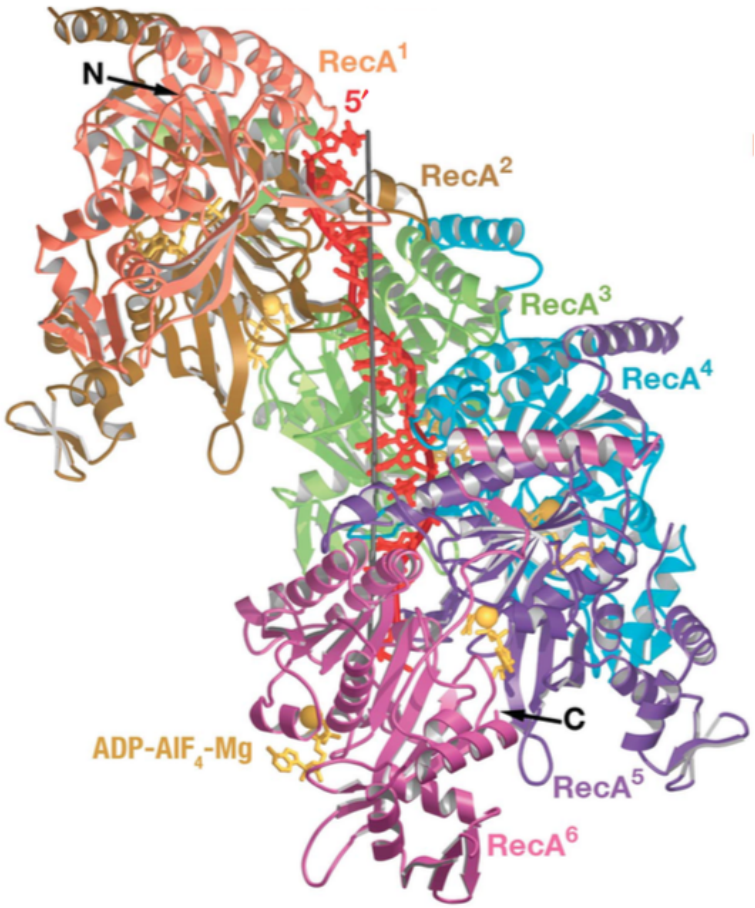

Figure 2.4: A RecA-DNA presynaptic nucleoprotein filament. Six RecA monomers depicted in different colours and labelled. Exposed N and C termini marked on the ending RecA monomers. Yellow colour depicts a non-hydrolysable ATP analog ADP-AlF4-Mg co-factor. Red colour depicts the central ssDNA . Reproduced from[78].

RecA has at least three distinct functions in biology: a) DNA strand exchange in homologous recombination, b) regulatory role in induction of SOS response to DNA damage and c) participation in SOS mutagenesis as a LexA coprotease. The most important one is the strand exchange which is the exchange of the strand between two DNA molecules containing a region of matching sequence and was initially proposed by Paul Howard-Flanes [79]. The strand exchange occurs between two DNA molecules when the following two criteria's are met: (1) one of the DNA molecules contains a region of ssDNA; and (2) the other dsDNA molecule contains a site homologous

to the ssDNA region. The strand exchange could either be a three-strand exchange (one of ssDNA and two strands of dsDNA) or four strand exchange (between two strands of two dsDNA). During the process, the two homologous strands of DNA are exchanged. The process of strand exchange can be divided into these steps: DNA binding, with a nucleation substep, where RecA monomer binds and nucleates onto the ssDNA in the presence of relevant cofactors, and extension substep, where additional RecA monomers bind onto ssDNA and already-bound RecA monomer; DNA alignment, where the formed nucleoprotein filament aligns to and binds a dsDNA; and finally, the exchange of strand, where ATP is hydrolysed that triggers exchange of DNA strands and disassembly of RecA (Figure 2.5).

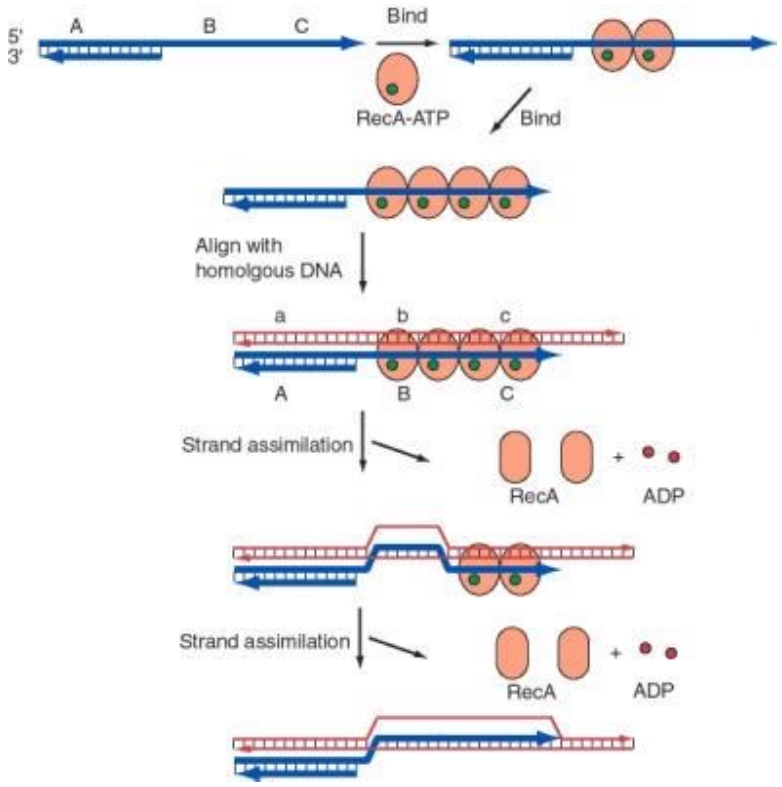

Figure 2.5: The mechanism of RecA-mediated DNA strand exchange.

In addition to its role in homologous recombination, RecA functions as a coprotease for the LexA protein. In a healthy cell, LexA represses the expression of genes encoding DNA repair proteins (the SOS genes). When DNA is damaged, LexA catalyzes its own digestion, thereby allowing synthesis of necessary SOS proteins. However, LexA can

only induce self-catalysis when activated by a ssDNA-RecA filament. A single filament will bind and activate several LexA proteins, each of which then cleaves other bound proteins. Therefore, ssDNA-RecA, a product of DNA injury, stimulates DNA repair.

Since RecA modification in this project depends on the availability of primary amines, it is appropriate to look into lysine – the only amino acid containing primary amines – availability and distribution. A single RecA monomer contains 27 surface-exposed lysines. A recA monomer in polymeric form, bound to DNA, other RecA monomers and cofactors, retains around half of those lysines available. That should be a suitable source of primary amines for thiolation, however impact of lysine modification on RecA stability is currently unknown and is to be investigated.

2.4 Nanoparticles

Nanoparticles are nanoscale crystalline clusters of inorganic material atoms. They can be synthesised as nanorods, cubes or other shaped objects, but spherical nanoparticles are the simplest and the most common [80]. There are two broad categories for nanoparticle synthesis methods: "top-down" approach and "bottom-up" approach [50]. The "top-down" approach uses photolithography, electron beam lithography or other semiconductor-processing technique to remove unneeded material and form desired nanostructures, whereas the "bottom-up" approach is wet chemistry-based: precursor salts are chemically reduced, assembling the material of interest as atoms into clusters. The lithographical methods have the advantage of producing any shape nanoparticles with tightly controlled size distribution, however, they suffer from typical lithography-based processing disadvantages: resolution limits or no ability to parallelise the manufacturing and need for expensive equipment. Additionally, the produced nanoparticles are attached to the surface and further processing might be needed to detach them. In contrast, the more popular "bottom-up" approach involves only the precursor chemical reagents, synthesise the nanoparticles in solutions and can easily scale to large volume production.

The materials that nanoparticles are synthesised of include noble metals, metal oxides and semiconductor materials. Due to their unique fluorescent properties, semiconductor nanoparticles are also named quantum dots [50] [81].

Nanoparticle size (usually 2nm - 50nm), makes them subject to attractive van der Waals forces. Van der Waals forces are relatively weak forces between molecules, atoms and nanoscale objects that come about from electrostatic interaction other than covalent, ionic or metallic bonds. Some of the molecules, even though they are not ionically charged, can have residual charge due to geometrically uneven distribution of electrons in them. They are called molecular dipoles. Such dipoles interact between each other and can also induce dipoles in other molecules with evenly and symmetrically distributed charge. All of these interactions are considered van der Waals forces. An interaction of two permanent dipoles is typically the strongest type of van der Waals forces and is named Keesom force. Forces arising between a permanent dipole and an induced dipole are named Debye forces, and forces between two neutral molecules, atoms or nanoscale objects that induce dipoles to each other are called London dispersion forces. Nanoparticle science is most concerned with London dispersion forces and their role in nanoparticle interactions in solutions. The surface of bare nanoparticle is neutral and two nanoparticles can induce dipoles to each other resulting in attractive force between them. This London dispersion force manifests as nanoparticle affinity to agglomerate into larger, less-defined structures, modifying their properties such as dispersibility and solution colour.

The interaction of neutral nanoscale objects is summarised by the Lennad-Jones potential (2.6). The Lennard-Jones potential quantifies the attraction and repulsion forces of two neutral molecules or atoms with respect to the distance between their centres. It can be mathematically described as

$$V(r) = 4\epsilon \left(\left(\frac{\sigma}{r} \right)^{12} - \left(\frac{\sigma}{r} \right)^{6} \right), \tag{2.1}$$

where V is the intermolecular potential between the two atoms or molecules, ϵ is the well depth, that describes how strong the objects interact, r is the distance between the centres of the objects, and σ is the distance between the objects, at which the intermolecular potential would be zero. The r^{12} term comes from the Pauli exclusion principle, implying that no two objects can have the same position and state at the same time. This results in a strong repulsion between the electron orbitals in the two objects of interest if they are brought together closer via external forces than the minimum energy distance σ. The r^6 term arises from the London dispersion forces and it describes the attractive interaction between the induced dipoles. The steep

curve produced because of the r^{12} term results in repulsion at relatively short distances (subnanometre range) whereas the more gradual decrease of the r^6 term affect the dipoles at nanometres to tens of nanometres. The potential well depth, ϵ is the lowest energy minimum and therefore the most stable distance for the two interacting objects to be at. This is the position at which the attraction and the repulsion balance out.

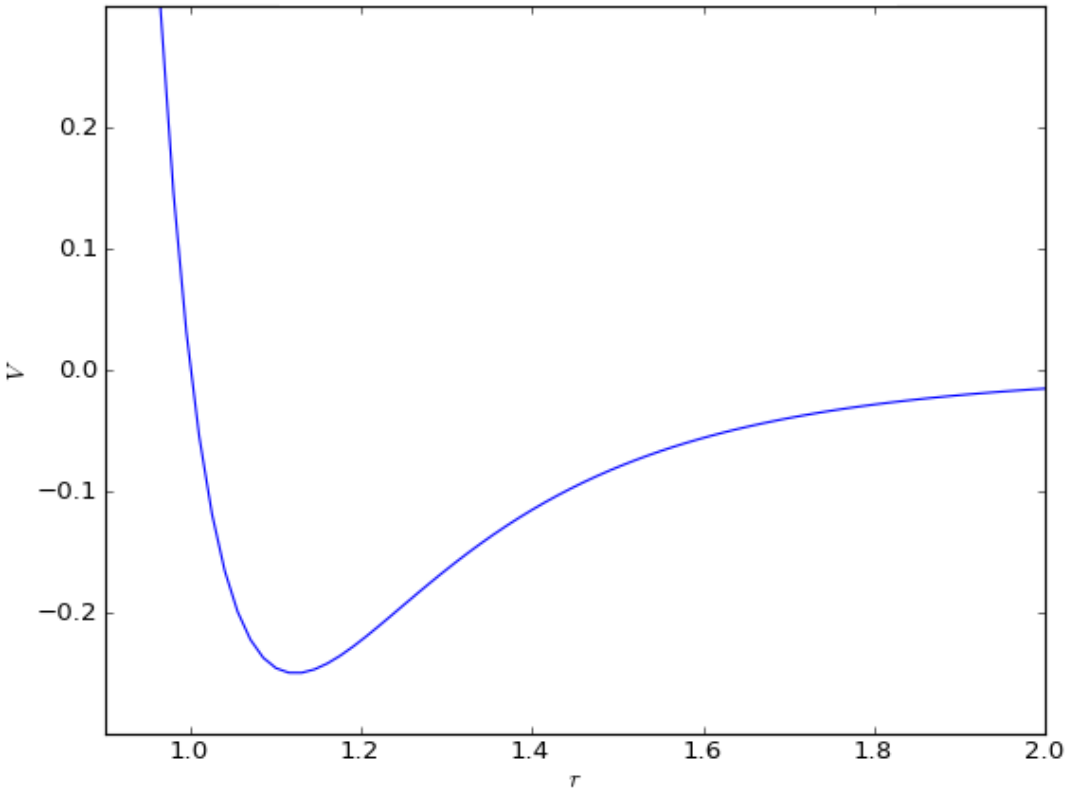

Figure 2.6: A typical graph of a Lennard-Jones potential well.

As mentioned before, nanoparticles will agglomerate because of the London dispersion forces. To retain them in a dispersion form for indefinite time periods, nanoparticles need to be stabilised. Nanoparticles can be stabilised either sterically or electrostatically [49]. Both methods involve nanoparticle surface modification by chemical modification. Electrostatic nanoparticle stabilisation involves adsorption of ionic compounds onto the nanoparticle surface, resulting in nanoparticle surface charge development. This leads to stable nanoparticle solutions due to nanoparticles being charged same way and re-

pelling each other. The electrostatic stabilisation is typically used in polar solvents, including water and utilises citric acid, ascorbic acid or phosphine as the stabilising agent.

The steric stabilisation method involves using long hydrocarbon-based molecules. The bound shell of such long molecules present a physical barrier via steric hindrance for nanoparticle–nanoparticle surface interaction. Due to hydrocarbon nature of these stabilising agents, steric stabilisation is typically reserved for non-polar solvents. Even though steric stabilisation is superior to electrostatic, its limitation of use in non-polar solvents makes it less useful due to main applications of nanoparticles being in applications which require aqueous environment.

In terms of the Lennard-Jones potential, both electrostatic and steric stabilisation introduce a potential barrier between the r^6 term attractive regime and the potential energy well, ϵ. The taller the barrier, the more energy – typically in the form of heat – is needed to be put in the system for nanoparticles to agglomerate.

One of the first type of nanoparticles produced were gold nanoparticles [49]. The most popular method of synthesising gold nanoparticles is through the Turkevich method [49] [82] where gold hydrochlorate solution is reduced using citrate ions.

The most unique property of gold nanoparticles is the cherry-red colour of the nanoparticle solution [50]. This is due to the metallic and nanoscale size nature of the gold nanoparticles. A plasmon resonance (PR) – a collective oscillation of electrons inside the nanoparticle is achieved when nanoparticles are irradiated with light. Only the resonance wavelengths are absorbed and transferred into electron motion, leading to the selective solution colour.

Quantum dots (QDs) - the semiconductor equivalent of metal NPs behave similarly to NPs, but they typically have more discrete levels of energy than NPs and therefore posses different electronic properties. Since electronic excitation and relaxation energies for QDs are similar to visible light photon energy, often QDs show strong fluorescence properties.

The Au NPs used in this work are of 5 nm - 20 nm in diamater. Even though the used NPs are metallic, the smaller size NPs of this range also start exhibiting certain level of energy level discreteness. This behaviour does not manifest in fluorescence, however, if the NPs are to be used as an electrically conducting material, it might affect conduction characteristics. This would have important implications for devices when

NPs are isolated from each other and conduction works through electron ”hopping”, but same effect would be decreased to insignificant levels when NPs would cover an extent of a nucleoprotein filament. High packing and physical touching of NPs rapidly negate the size effects for electronic energy levels and energy levels become continuous, forming a conduction band.

Nanoparticles are mostly used for biomedical, biochemical and sensor applications. Due to gold nanoparticle PR signal being sensitive on nanoparticle agglomeration state, deliberate nanoparticle destabilisation through species of interest is a common technique in nanoparticle sensor use [54] [83] [84] [85].

2.5 Conclusion

This chapter reviewed the main chemical molecules and their properties used in this PhD project. An in-depth description was given of DNA and proteins and their unique structure, function, properties and significance. Additional attention was given to RecA protein, to describe its specific structure in monomeric and polymeric forms and natural functions since it is the main protein used in this work. The element for system metallisation – nanoparticles were also reviewed by looking into their types, synthesis, stability and properties. All of these entities have a significant role in the project and come together to create the aforedescribed system of molecular assembly for electronics.

Chapter 3

Literature Review

This chapter looks into previously done studies on self-assembled DNA nanostructures, and construction of DNA-based devices, attempts to metallise DNA or bind it to nanoparticles and patterning DNA.

3.1 Self-assembling structures

Scientists have great interest in DNA for assembling nanoscale structures due to DNA's property of structural programmability through self-assembly. DNA-based nanostructures are molecular complexes consisting of different ssDNA strands designed to hybridise with themselves at the complementary regions, spontaneously forming desired nanostructures. Self-assembly being prominent at nano- and microscales is an extensively used technique for producing such higher order structures. DNA is tool of the trade for biomolecular self-assembly, because it is relatively simple in structure, yet powerful in diversity of structures it can take, has a diameter of only 2 nm, yet is able to span micrometers in length, is one of the most studied and best understood biomolecules and is cheap to obtain, synthesise in any desired sequence and manipulate with various available molecular biology equipment. The first prominent work on DNA structures was carried out by Seeman and co-workers [86], [27]. Using different ssDNA with complementary regions they produced three- [87] and four-armed [88] branched DNA structures, three dimensional cubes defined by DNA edges [89], two- [90] and three-dimensional DNA crystals [91]. The self-assembled rhombohedral three-dimensional crystals produced by Seeman's group utilised a DNA tensegrity triangle

motif previously used for producing two-dimensional crystal by Liu *et al.* [92]. Seeman's group modified the motif so that protruding 'sticky ends' would allow hybridisation of triangles in three-dimensional space (figure 3.1). The 250 μm-sized crystals illustrate to how large an extent DNA self-assembled structures can grow.

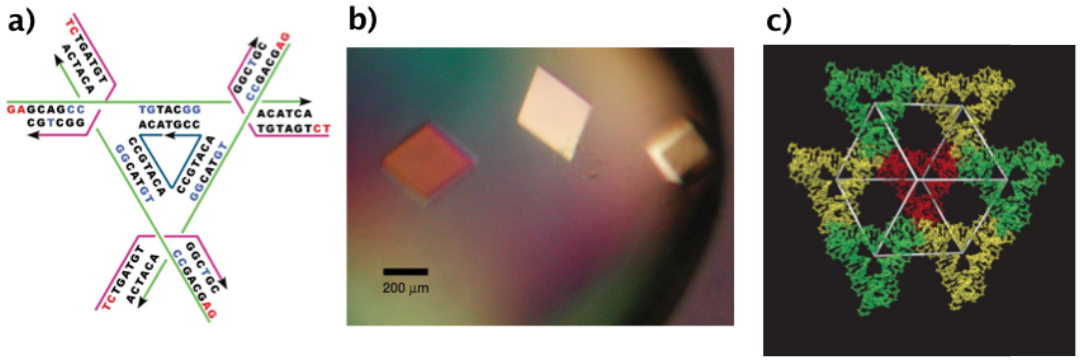

Figure 3.1: a) Tensegrity triangle used by Seeman's group to synthesise microscopic DNA crystals; b) Microscopic DNA crystals imaged with an optical microscope; c) a diagram showing tensegrity triangle spatial self-assembly. Reproduced from reference [96].

Other groups also produced unique DNA structures. Rothemund used one long ssDNA and folded it using short 'stapling' ssDNA strands that are complementary to two different regions on the long ssDNA, making it bend and take up distinctive shape [24]. The technique was used to self-assemble various two dimensional patterns (figure 3.2).

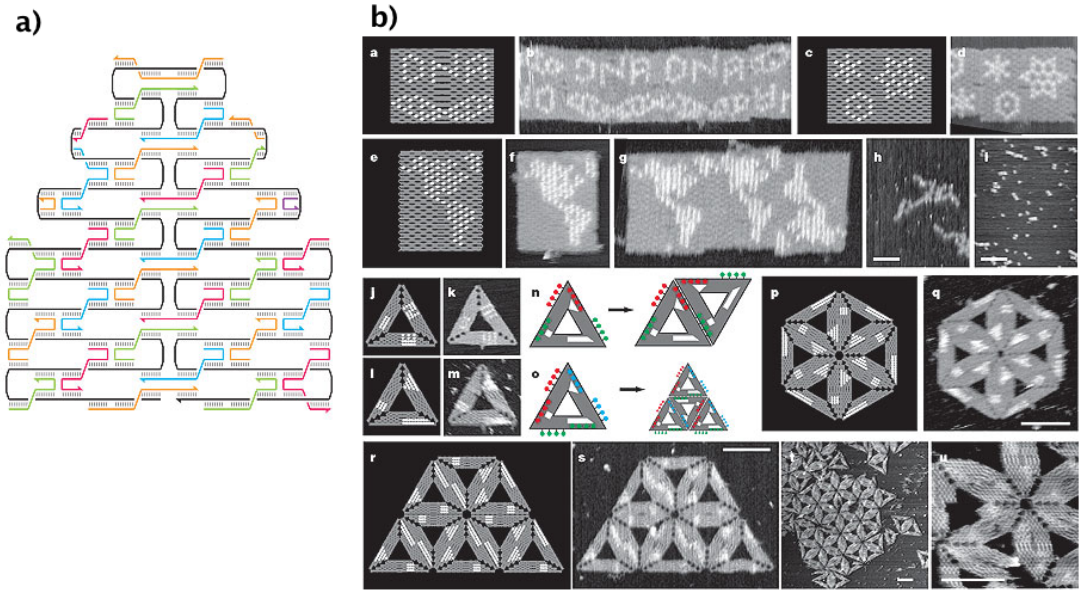

Figure 3.2: a) Diagram, illustrating a technique of "stapling" long ssDNA with short ssDNA fragments used by Rothemund; b) various patterns designed by Rothemund with "stapling" technique and respective self-assembled DNA structures visualised with atomic force microscopy. Reproduced from reference [97].

Formation of three-dimensional structures was also previously shown in literature, such as polyhedra [93], [94], hemispheres and ellipsoids with complex surface curvatures [26] and DNA boxes [28]. Turberfield and co-workers designed DNA tetrahedra and used them to measure structure's stiffness by applying pressure [95]. The structures deformed by 2 nm and withstood on average 170 pN force before collapsing irreversibly. This method allows for measuring mechanical DNA properties, as well as optimising the design for best possible rigidity. The DNA box produced by Andersen *et al.* had dimensions of 42 x 36 x 36 nm^3 and one side attached only by one edge, acting as a lid [28]. The box lid was controllable by several additional protruding ssDNA strands, which 'lock' the box by hybridising to externally added 'key' short ssDNAs. The researchers speculated that the box could be used for such applications as a logic sensor for multiple-sequence signals or for the controlled release of nanocargos. Due to potential for functional applications, DNA box could be considered a nanodevice.

Others have produced nanodevices such as tweezers-shaped controllably opening

and closing DNA machine [96], unidirectional walking DNA machines moving on one-dimensional track, inspired by kinesin 'walking' on microtubules, useful for nanoscale directed cargo delivery [33], [97], devices, 'walking' on two-dimensional landscapes [34], DNA device for programmable chemical reactions [98], and for directing chemical single chemical reagents to avoid any side reactions [99]. All of these devices are fuelled by ssDNA, which competes against other fragments for binding to the DNA structure at the complementary region [23]. As the introduced ssDNA structures usually have longer complementary sequence than the region it competes against, eventually all 'fuel' ssDNA binds to the structure and leads to an expected change.

Attempts at producing DNA logic gates and computing DNA devices were made as well [100–103]. The produced calculating devices were solution based and required addition of ssDNA as input and gave fluorescence signal as output [102], [103]. However, the system was not continuous - it involved nine different tubes representing nine different field in a tic tac toe game. A DNA system, which mimics a neural network has been demonstrated by Qian *et al.* [32]. The model for it was based on artificial neural networks used for modeling on conventional computers.

The DNA structures and devices demonstrate exciting potential for DNA in computing, translational motion, caging reagents, directing reactions and producing large-scale supramolecular structures. However, the demonstrated computational devices are solution-based and statistical instead of more desired deterministic and do not use electrical conduction which would allow faster information transfer. For that, DNA needs to be modified.

3.2 DNA as a conducting wire

The electrical conductivity of DNA has been a controversial topic for many years [104, 105]. In separate studies, DNA was found to be an insulator [38, 106], a conductor [107], a semiconductor [108] and even a superconductor [109]. The high variation in results has been attributed to surface properties, humidity, residual salt bridges and contact formation [104, 105, 110]. A recent study demonstrated DNA conductivity over 34 nm (100 bases) [111]. It was found, that even a single base mismatch results in significant signal attenuation. Nonetheless, majority of the studies conclude that it is

safe to consider DNA as a non-conducting biomolecule as the long-range conductivity is not preserved sufficiently enough for electronic applications [112].

To improve DNA conductivity different approaches were taken. The most common one is modifying the DNA for metallic nanoparticle or metal-producing chemical reagent affinity and subsequently conjugating the reagents to the DNA [42, 45, 48, 113–115]. Other methods include exploiting negatively charged DNA sugar-phosphate backbone for binding cationic nanoparticles or modifying nucleotide bases to act as coordination sites for metal atoms.

Tanaka *et al.* synthesized DNA with custom-modified nucleotides acting as chelators and binding Cu^{2+}, Pd^{2+}, Pt^{2+} or Ni^{2+} ions [114], [40]. Self-assembly of Cu^{2+} and Hg^{2+} ions into an array in between the modified DNA was demonstrated with 0.37 nm distance between metal ions. A similar work was done by Weizman *et al.*, showing binding of Cu^{2+} ions in the interior of DNA having different modified nucleotides [116]. Incorporation of Zn^{2+}, Co^{2+}, or Ni^{2+} in-between DNA nucleotides without any prior nucleotide modification was also demonstrated [116]. These formed complexes were also indirectly shown to transfer electric charge.

The previously described DNA nanowires had metal ions buried in the interior. This has an advantage over other techniques of retaining smallest possible dimensions - the original DNA size. However, the buried metal ions do not form a continuous nanowire and probably do not posses best conductivity. Furthermore, in some cases the technique requires use of non-natural nucleotides, which greatly restricts the use of conventional DNA enzyme-based manipulation tools (polymerase chain reaction (PCR), digestion, ligation, etc.). The method does not have a clear way of introducing metal ions only into desired DNA regions.

An alternative approach of depositing conductive species on the outer surface of DNA allows continuous metal layer formation with varied thickness. The typical reaction involves mixing DNA with a solution of a metal salt and then adding a reducing agent. The DNA may be dissolved in solution, or immobilised on a solid substrate. Metal templating on DNA usually involves aqueous reactions, however organic solvents may be used if the DNA is first aligned by molecular combing on a solid substrate. Metal ions bind strongly to DNA at a variety of sites by electrostatic interaction with the phosphate groups and by coordination to the nucleobases. The metal nuclei can therefore form on the template and growth occurs to produce larger metal NPs, which

under appropriate conditions will eventually coalesce to produce a conductive nanowire. It should be noted that this process is distinct from the interaction of pre-formed metal nanoparticles with a DNA molecule, which is a common, but distinct, strategy for the formation of assemblies of individual nanoparticles. Burley *et al.* used chemically derivatised DNA to reduce metallic form of silver using Tollen's chemistry [115]. The DNA was synthesized with artificial acetylene-containing nucleotide substituting thymine. After the artificial DNA synthesis, a click reaction with glutaraldehyde was done. That yielded aldehyde-modified DNA which was susceptible to subsequent silver reduction from $Ag(NH_3)_2OH$.

Kudo *et al.* produced copper-coated DNA nanowires using a two-step process [42]. Firstly, Pd^{2+} ions were electrostatically adsorbed onto negatively charged DNA backbone and chemically reduced to Pd^0. Resulting Pd nanowires were 6 nm in diameter and were subsequently dipped into copper electroless plating bath. The resulting Cu wires varied in thickness, depending on plating time. 20 s incubation in plating bath resulted 20 nm thick nanowire.

Liu *et al.* also utilised electroless plating for metallising three-armed DNA braching structure [45]. The branched asymmetrical structure initially was exposed to a glutaraldehyde solution and seeded with silver, followed by electroless plating with gold. Continuous metallisation was achieved with average structure height being as small as 32 nm.

Fischler *et al.* preliminarily modified DNA with reducing sugar and metallized the DNA by the reduction of metal ions. Al-Said *et al.* formed uniform conductive nanowires by metallizing DNA/conducting polymer hybrid nanowires. Harb et al. demonstrated a silver seeding method to metallize branched DNA origami structures, which might be a key step toward the realization of DNA-templated nanocircuits. In addition, Tao *et al.* recently reported that the metallized DNA could be used to selectively determine dopamine or the thiol-containing biomolecules in a biological fluid. Metallization of DNA toroids using gold was performed by trivalent cations of bis(ethylenediamine) gold(III) chloride, serving as both a condensing agent and a metal source, during which the DNA template was initially condensed into toroids, while subsequent reduction of gold led to the formation of small gold particles on the surface of the toroids

Glutaraldehyde as a precursor for metallisation was also used for self-assembled DNA nanotubes [117]. Two DNA folding motifs were designed which self-assemble into two-dimensional lattice. However, because one of the motifs include thiol groups, the lattice folds into a tube, stabilised by disulphide bonds formed by the thiols groups on the inner side of the tube. The nanotubes were treated with glutaraldehyde and silver-seeded using $AgNO_3$. The formed nanowires showed linear I-V characteristics.

As an alternative to glutaraldehyde treatment, Braun *et al.* used hydroquinone to reduce silver ions electrostatically adsorbed to negatively charged λ-DNA (16 μm long viral DNA) to metallic silver [48] (figure 3.3). Before treatment, DNA ends were immobilised through sticky end hybridisation to electrode-fixed oligonucleotides. This allowed obtaining I-V characteristics, which indicated linear response and, therefore a successfully formed nanowire.

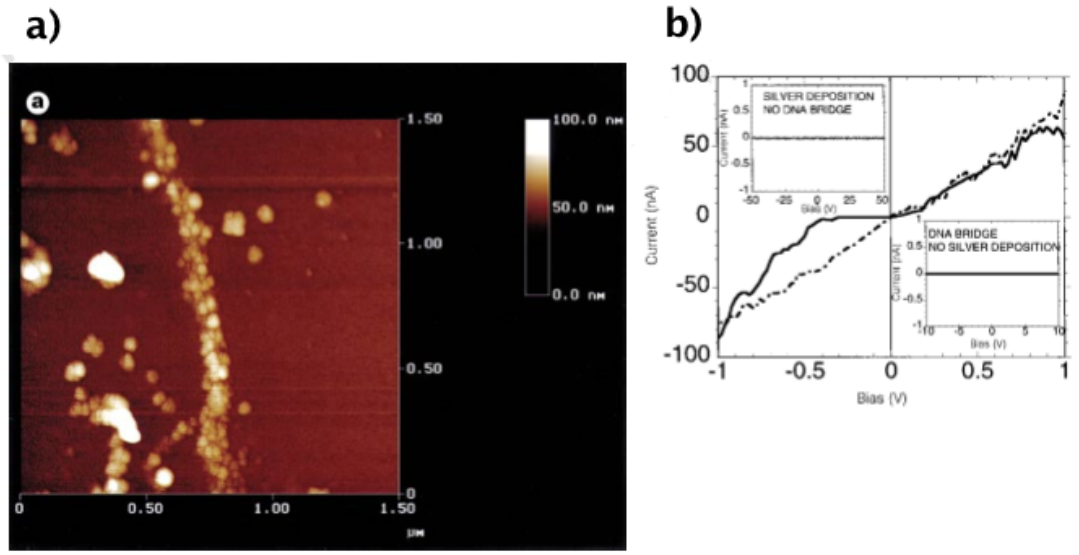

Figure 3.3: a) Silver DNA-templated nanowire synthesised by Braun et al. imaged with atomic force microscopy; b) silver nanowire I-V characteristics showing linear response; two inlets show control samples (one is without silver deposition, [122].

Other DNA-templated nanowires were formed using Co [118], Ni [119, 120] and Pd [121] metals, as well as Fe_2O_3 and $CoFe_2O_3$ [122], [123] magnetic nanoparticles.

3.3 Selective DNA metallisation

Keren *et al.* from Braun's group investigated two ways for producing selectively metallised DNA [124], [125]. Firstly, λ-DNA was treated with glutaraldehyde to introduce aldehyde groups for silver binding and exposed to a silver solution leading to silver cluster formation on the DNA. To reduce silver cluster inhomogeneities additional gold deposition was done (already formed silver aggregates catalysed gold nucleation) resulting in a continuous granular wire. After the successful nanowire formation, Keren *et al.* continued investigating two methods for selective DNA metallisation. In the first method, two different DNA fragments were synthesised using PCR. Using restriction enzyme, complementary overhangs (non-hybridised residual ssDNA) at both ends of these fragments were generated. First set of fragments was treated with glutaraldehyde, whereas the second was left intact. Due to complementary sticky ends, the fragments self-assembled into a long dsDNA with alternating regions of aldehyde-derivatised and non-derivatised regions. Molecules were incubated with silver solution and subsequent SEM (scanning electron microscopy) imaging revealed alternating metal wire and bare DNA regions (figure 3.4).

In the second method, RecA was used as a molecular masking method. A nucleoprotein filament was localised on λ-DNA by homologous region binding. λ-DNA was treated with glutaraldehyde. Before the structure was exposed to silver solution, nucleoprotein filaments were disassembled from the dsDNA and excess glutaraldehyde removed. Nucleoprotein filaments formed by RecA worked as a protecting mask from metallisation stopping glutaraldehyde from reacting with the protected λ-DNA region. The final imaged structure showed a bare DNA gap where nucleoprotein filament was previously bound (figure 3.4).

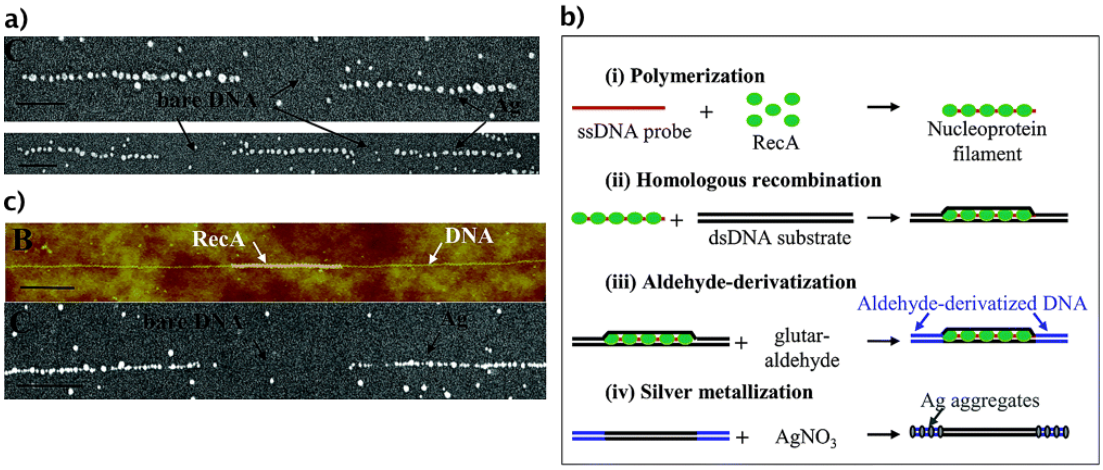

Figure 3.4: a) two transmission electron microscopy images of patterned DNA with alternating silver-metallised regions produced by Keren et al.; b) a diagram explaining how same group used RecA nucleoprotein filament patterning on dsDNA for protection from aldehyde derivatisation and therefore silver metallisation; c) top image - dsDNA patterned with RecA filament before aldehyde derivatisation and metal deposition imaged with atomic force microscopy, bottom image - templated dsDNA after metallisation and RecA filament removal imaged with transmission electron microscope. Reproduced from reference [128]

In the studies reported by Keren and co-workers, the DNA-glutaraldehyde reactions were either carried at room temperatures or lower temperatures for a longer period of time [124]. However, another study to find the kinetics of reaction between glutaraldehyde and DNA by Hopwood suggests that glutaraldehyde reacts with nucleotides only at higher temperatures when DNA is partially or fully melted [126]. It was found that up to 64 °C no reaction starts between glutaraldehyde and DNA and above 75 °C the reaction followed pseudo-first order kinetics, becoming faster at higher temperatures. If Hopwood's findings are correct, the aldehyde derivatisation of λ-DNA by Keren *et al.* was apparently successful.

Furthermore, gluteraldehyde is known to cross-link protein at lower temperatures far better than crosslinking regions of bare dsDNA (if that happens at all) [126]. Crosslinking of proteins at lower temperature or room temperature is a standard protocol in molecular biology to fix the protein sample for TEM (transmission electron

microscopy) and cryoTEM. So treatment of patterned DNA complex with gluteraldehyde can potentially lead to a cross-linked structure resulting in their aggregation, if done the solution. On surface, only a portion of dsDNA or proteins is accessible for aldehyde derivatisation. From the available material, it is not clear how Keren *et al.* overcome these factors.

The way forward is to utilise the patterned region as the nanoparticles nucleation site. One way to achieve that without crosslinking the structure as discussed above, is through the introduction of functionally active sites, such as thiols on the surface, to which a gold nanoparticle can readily bind, which is exploited in this PhD project.

Selective region DNA metallisation is an important tool for nanodevices. However, precise, single nanoparticle placement is needed for full application potential. Many different approaches to attaching a nanoparticle to a DNA framework have been developed for various conditions and having different limitations. One of the first DNA-nanoparticle structures were produced by Loweth *et al.* (figure 3.5)[127].

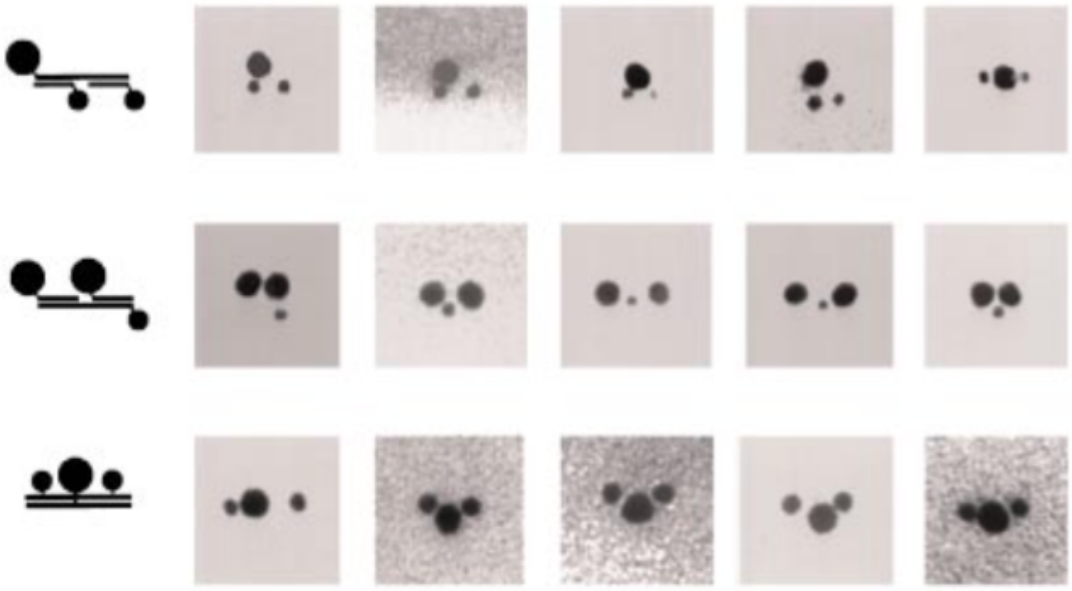

Figure 3.5: Left: schematic of two differing sizes of nanoparticles (5 nm and 10 nm) and their attachment points on a simple dsDNA system. Right: resulting structures as imaged with a TEM. Reproduced from [129].

.

Thiols were incorporated into ssDNA which were allowed to react with selected-size Au NPs in sequential manner. The Au NPs were attached to either thiolated terminal end of 19 bases long ssDNA molecules. The complex was then assembled into dimers or trimers structures, by adding additional complementary 37 base-long ssDNA which was linked to Au NPs on its own. It was demonstrated that, by choosing the right length ssDNA, the Au NPs could be placed at defined positions from each other.

Schreiber *et al.* showed that rigid DNA scaffolds can be used to assemble metal nanoparticles, quantum dots and organic dyes into hierarchical nanoclusters that have a planet?satellite-like structure [128]. The produced nanostructures have a predictable stoichiometry and defined distances of 5 nm - 200nm between conponents (figure 3.6). They also demonstrated that the nanoscale components can be positioned along the radial DNA spacers of the nanostructures, which allows short- and long-range interactions between nanoparticles and selected dyes to be studied in solution.

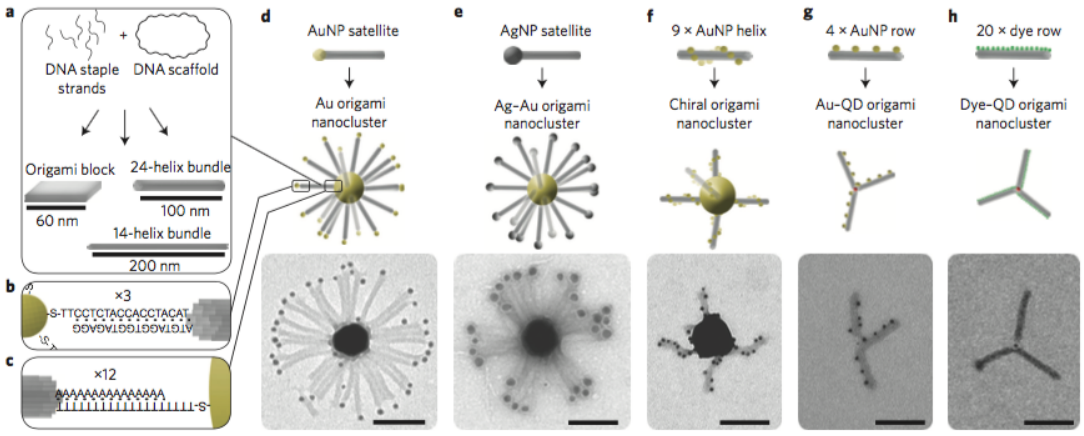

Figure 3.6: a) The set-up for creating DNA scaffold. b) - c) Sequences at the ends of DNA structures that interact with the nanoparticles or other entities. d) - h) Different designs and resulting structures for DNA scaffold - NP (or other nanoscale entity) assembly. Reproduced from reference [130].

.

Using these structures, fluorescence quenching by Au NPs was studied, as well as field-enhanced plasmonic circular dichroism was observed. According to authors, use

of these structures could be adopted for plasmon-based nanolenses or metamaterials. The work has showed potential for assembling other objects than Au NPs in a similar and easy fashion, as well as interactions of Au NPs at nanoscale level with other objects when assembled on the same framework.

Another method of assembling Au NPs at precise locations on DNA uses enzyme-based automation [129]. Russell *et al.* created electrical sensor that uses rolling circle amplification of DNA to stretch across the gap between two electrodes, interact with metal nanoparticle seeds to generate an electrically conductive nanowire, and produce electrical signals upon detection of specific target DNA sequences. This way long ssDNA with simple repetitive sequences are produced that later attach single Au NPs at specific repetitive and equidistant locations (figure 3.7).

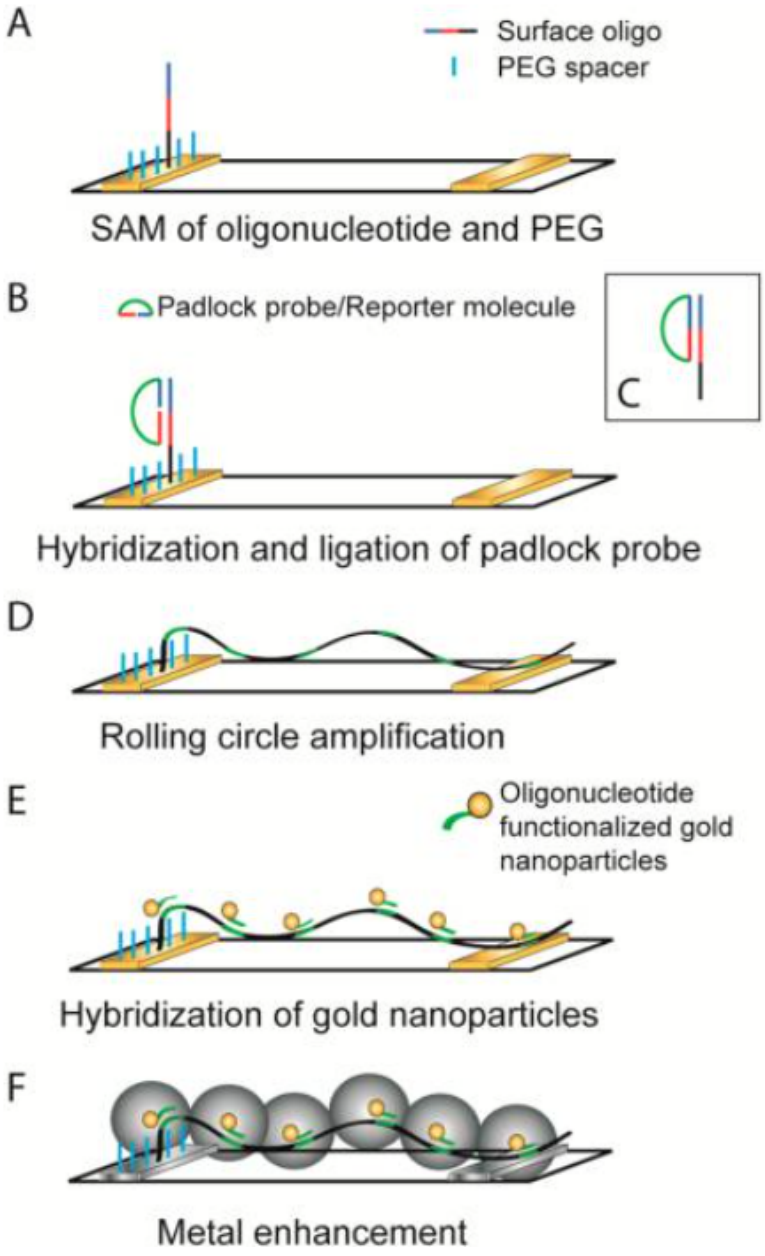

Figure 3.7: The schematic of the system used for rolling circle amplification of DNA for attaching single NPs at specific repetitive locations [131].

This shows the potential for easy management of long, repetitive regions when quality of the manufactured device and precision should not be compromised.

Xiao *et al.* reported self-assembly of metallic nanoparticle arrays onto DNA scaf-

folds, utilising earlier work by Seeman that used double-crossover DNA structures. They were able to assemble an array of 1.4 nm diameter gold nanoparticles with inter-particle spacing of 4 nm and 64 nm. Recently, Sharma *et al.* used four double-cross over DNA nanostructure as a scaffold for the quantum dot assembly. The DNA nanoarrays were used to direct the assembly of streptavidin-conjugated CdSe/ZnS core/shell quantum dot at locations determined by the locations of biotin molecules bound at specific locations of the array.

The abundant examples of DNA metallisation found in previous studies show the interest of DNA metallisation and subsequent use for nanoscale electronics. Some evidence for selective DNA metallisation is also available. However, the used methods for selective metallisation either require separate preparation for individual type of DNA strands or use nucleoprotein filament as a protecting agent. This PhD project is concerned about using the filaments as a target for metal binding on DNA scaffolds. This has an advantage of allowing the DNA junctions remain metal-free if needed for certain applications. As well as region-based metallisation, single nanoparticle placement has been shown to be viable and achievable in many different methods. This is needed for fine-tuning the device functioning.

Chapter 4

Experimental techniques

4.1 Polymerase chain reaction

All of the experiments that required DNA were performed on a 3.5kbp (kilobase-pair) DNA fragments generated from λ-phage DNA (known as λ-DNA) by polymerase chain reaction (PCR). PCR is a method used in molecular biology for exponential multiplication of DNA in vitro (figure 4.1). PCR working principle is based on a family of enzymes called polymerases which purpose is to create a complementary strand for ssDNA using nucleotides. Besides the DNA polymerase, other essential parts for PCR are template DNA, possessing the target DNA fragment sequence, pair of short oligonucleotides known as "primers" which are complementary to and mark two ends of the target DNA, deoxynucleoside triphosphates (dNTP), divalent cations such as Mg2+ and a suitable buffering agent for optimal polymerase activity. The whole PCR procedure can be divided into following steps: Denaturation step: In this first step the template dsDNA is denatured to ssDNA by heating the sample to higher than its melting temperature (for λ-DNA 95 °C is used) for 20-30 seconds that causes hydrogen bond disruption between complementary DNA base pairs and results in two ssDNA. Annealing step: The temperature is then lowered to 3-5 °C below melting temperature of the primers (50-65 °C) at which primers hybridise to the 5' end of the target sequence on the template DNA. Extension (elongation) step: A new complementary DNA strand is synthesized by polymerase, which fills in dNTPs that are complementary to target sequence in 5' to 3' direction starting from the hybridised primer. The temperature for this step is polymerase-dependent and the extension time depends on the target DNA

fragment length. The "denaturation" to" elongation" cycle is usually repeated 10-30 times, doubling the number of DNA strands with each cycle and therefore amplifying the total number of DNA exponentially. The initial cycles are saturated with template DNA but after four cycles target DNA starts to dominate in number and quickly surpasses template DNA.

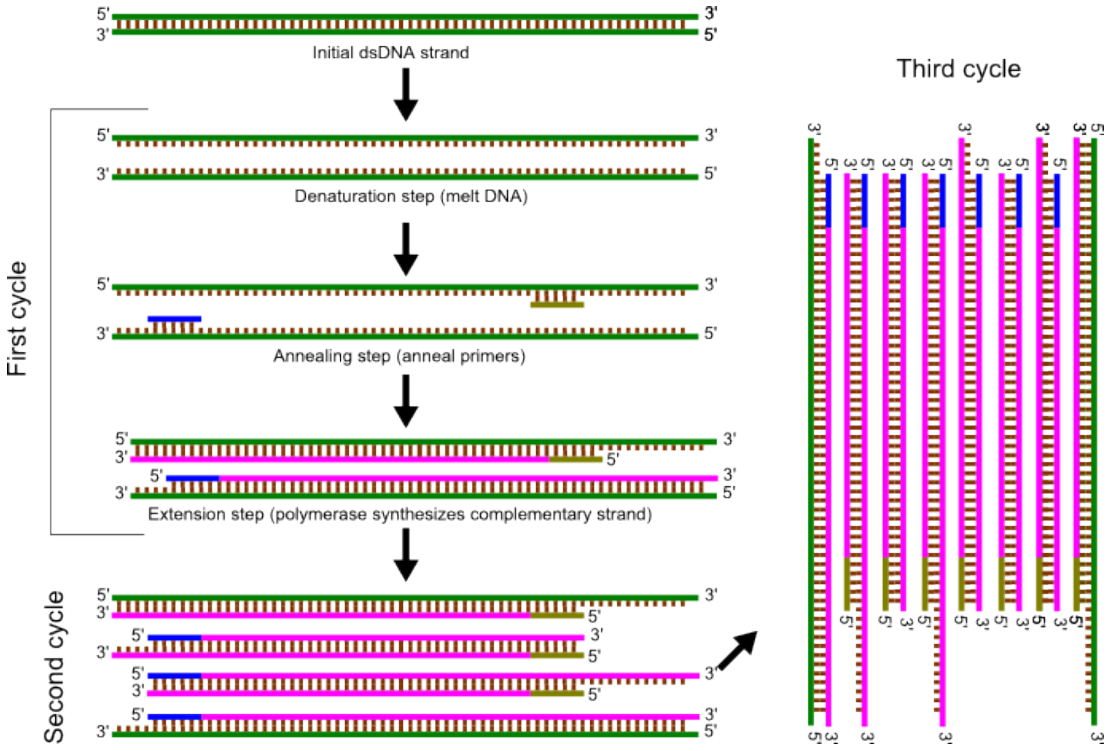

Figure 4.1: Working principle of polymerase chain reaction

Final elongation step: Polymerase finishes polymerising any remaining ssDNA to full dsDNA at 70-74 °C for 5mins – 15mins. Final hold step for any needed time allows temporal storage of PCR products at 4 °C. The enzyme used is thermostable Taq polymerase which was originally extracted from bacterium Thermus aquaticus and is widely used for PCR. Amplification was done using eppendorf "Mastercycler ep gradient S" thermal cycler. After PCR synthesis, products were purified using PCR purification kit.

4.2 Atomic force microscopy

Atomic force microscope (AFM) is a type of scanning probe microscope with high resolution, which uses sharp probe to analyse morphological surface features. AFM images are obtained by scanning a few nanometer wide probe called tip across the sample surface. While scanning, atomic or other interaction forces between surface and the tip are monitored. Any change in force due to surface change is detected by feedback electronics and compensated by adjusting the tip height. The tip is a part of a larger cantilever, which becomes deflected when the tip is attracted or pushed away by the surface (figure 4.2). The signal is detected and amplified by a laser-emitted beam, which reflects from the cantilever to a photodetector. The AFM electronic feedback loop connected to the photodetector keeps the tip at a constant distance from the surface. This height change and sample movement in xy plane under the tip is achieved using a piezoelectric element. The distance the scanner moves in the z direction relative to lateral variation in the x-y plane is used to generate the topographic image of the sample surface.

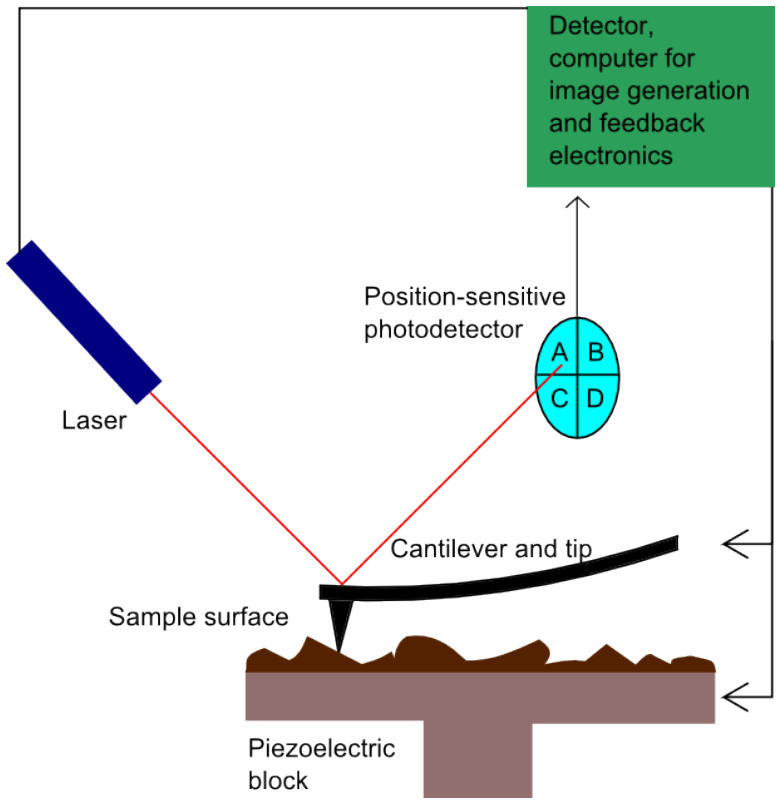

Figure 4.2: Working principles of an atomic force microscope

Two most used AFM imaging modes are contact and tapping modes. In contact mode, the image is produced by measuring the cantilever deflection while it is being dragged across the sample surface. Although contact mode operation gives best resolution, the constant downward force on the tip tends to damage many softer samples such as polymers and biological samples. These disadvantages are avoided by the tapping mode. In tapping mode, cantilever oscillates over the sample surface while scanning takes place. This way, the tip lightly touches the sample at the bottom of each oscillation cycle. This prevents soft sample damage or displacement. Constant tip-sample distance is maintained by using constant oscillation amplitude. Veeco Instruments "Dimension 3100" atomic force microscope set to tapping mode was used for imaging DNA, nucleoprotein filament and nanoparticles samples deposited on mica surface.

An important aspect of the AFM system is the cantilever/tip (probe) assembly which consists of a very sharp tip (typical radius of curvature at the end for commercial tips is 5 nm -10 nm) that protrudes off the bottom of a long and narrow cantilever.

The cantilever/tip assembly is also referred to as the probe. The two most common geometries for AFM cantilevers are rectangular ("diving-board") and triangular.

AFM cantilevers are typically made either of silicon or silicon nitride, where silicon nitride is used for softer cantilevers with lower spring constants. The dimensions of the AFM cantilever are very important as they dictate its spring constant or stiffness; this stiffness is fundamental to governing the interaction between the tip and the sample and can result in poor image quality if not chosen carefully. The relationship between the cantilever's dimensions and spring constant, k, is defined by the equation:

$$k = \frac{Ewt^3}{4L^3}, \tag{4.1}$$

where w is cantilever width; t is cantilever thickness; L is cantilever length and E is Young's modulus of the cantilever material. Nominal spring constant values are typically provided by the vendor when buying the probes, but there can be significant variation in the actual values.

One more important concept to understand is feedback loop. In AFM, depending on the different modes, there is a parameter that serves as the set-point. For example, in static mode the feedback parameter is cantilever deflection while in the most common form of dynamic mode, the cantilever oscillation amplitude is the feedback parameter. The instrument is trying to keep this feedback parameter constant at its set-point value by adjusting the z piezo to move the cantilever probe up and down. The resulting z piezo movements provide the height information to create the surface topography.

The spring constant of the cantilever and deflection sensitivity of the system are important parameters to perform quantitative force spectroscopy. Conventionally, the spring constant is determined from a thermal tune spectrum fitted with a simple harmonic oscillator model to obtain the resonance frequency and quality or Q factor. The spring constant is calculated with the method that uses the top view cantilever dimensions from an database inside the AFM software.

For cantilevers in air the simple harmonic oscillator fit can also be applied on a frequency sweep to get the resonance frequency and quality factor of the cantilever oscillation. The Sader method only needs these two parameters from the resonance curve, in contrast to the equipartion theorem, which needs to know the calibrated area under the curve.

Consequently, the Sader method can be used with the data from a frequency sweep to calculate the spring constant. The difference between the two spring constant determinations is only 2%, thus within the absolute accuracy of the method.

Control of the feedback loop is done through the proportion-integral-derivative control, often referred to as the PID gains. These different gains refer to differences in how the feedback loop adjusts to deviations from the set-point value, the error signal. For AFM operation, the integral gain is most important and can have a most dramatic effect on the image quality. The proportional gain might provide slight improvement after optimization of the integral gain. The derivative gain is mainly for samples with tall edges. If gains are set too low, the PID loop will not be able to keep the set-point accurately. If the gains are chosen too high the result will be electrical noise in the image from interference from the feedback; the compensation for a deviation from the setpoint is larger than the error itself or noise gets amplified too strongly.

The other parameters that are important in feedback are the scan rate and the set-point. If the scan rate is too fast, the PID loop will not have sufficient time to adjust the feedback parameter to its set-point value and the height calculated from the z piezo movement will deviate from the true topography at slopes and near edges. Very slow scan rates are typically not an issue for the PID loop, but result in long acquisition times that can pose their own challenges such as thermal drift. Optimisation of the PID gains and the scan rate are necessary in order to optimise feedback loops. The set-point affects the interaction force or impulse between probe and sample. A set-point close to the parameter value out of contact feedback is most gentle for the sample, but tends to slow down the feedback.

4.3 Magnetic force microscopy

Magnetic force microscopy (MFM) works similarly as AFM, except magnetised tips are used to detect long-range magnetic forces. Firstly, a line of sample surface is scanned in in tapping mode same way as in the AFM mode. Then the tip is retracted from the surface to by a specified distance (e. g. 10nm, 50nm, 100nm) and the microscope moves the tip in tapping mode the same way as on the surface, but compensates for any surface features detected by previous AFM line scan by adjusting the tip height. This allows to detect any magnetised tip deflections solely due to magnetic forces acting

further away from the surface. When the tip finishes scanning at given distance from the surface, it is lowered down to the surface level and scans the next line in AFM mode which is followed by MFM and so on. The image is formed by detecting the tip oscillation phase change, therefore the formed image has units of degrees corresponding to magnetic property change. Same Veeco Instruments "Dimension 3100" atomic force microscope was used for imaging magnetic nanoparticles and complexes formed with them.

Key in MFM measurements is to separate the short-range van der Waals forces from the longer range electrical or magnetic forces. A lifting mechanism enables the probing of longer range electrical and magnetic forces, and de-convoluting them from the short-range van der Waals forces that are present during topographic imaging. The height that the tip is lifted over the sample is often a parameter that needs to be optimised by the user in order to have successful imaging of the magnetic or electrical properties and is typically in the few to hundreds of nanometer range.

The lifting can be done in so called single, interlaced and dual scan line modes. In a single-pass or constant height setup, the slope of the surface is measured from a completed topography image or line before the imaging of the long range interaction is started, and then the tip is scanned at a fixed height above the sample, compensating for the average slope.

Alternative to the single pass are the interlaced and dual pass imaging modes, providing the topographical information of the surface along with the functional signal. In interlaced mode the forward pass records the topography of a scan line and then the tip is lifted above the sample during the backward pass. In dual pass topography is measured forward and backward in the first pass and the long range signal in the forward and backward movement of the second pass. Dual scan provides the more accurate correlation between topography and long range signal, whereas the interlaced mode is faster.

4.4 Spectrophotometry

Spectrophotometry is a quantitative study of absorbed electromagnetic (EM) spectra of a chemical or biological substance. It is usually done in ultraviolet, visible and infrared regions of EM spectrum. A spectrophotometer works by recording EM wave that

passes through sample and comparing the intensity with a reference "blank" sample that does not contain sample in interest. Nanodrop 2000C spectrophotometer from Thermo Scientific, USA was used in the project to measure the absorption of the samples solutions in the UV-Visible EM spectrum.

4.5 Fluorospectrophotometry

Similarly like spectrophotometry, fluorospectrophotometry uses light and UV to analyse the samples. However, whereas in spectrophotometry the attenuated light intensity is compared to the reference sample, in fluorospectrophotometry a light source is present, that excites fluorescent species in the sample and collects emissive light. To avoid collecting excitation light, typically 90°set-up is used. The excitation light beam is perpendicular to the sample holder window, so that any remaining excitation light does not pass into the light detector and interfere with the signal (4.3). Shimadzu RF-5301PC fluorospectrophotometer was used for FRET experiments in this project. A xenon lamp installed in the instrument ensured ability to excite at any selected wavelength and the mirrors and slits allowed to scan through range of selected wavelengths for capturing the emissive data.

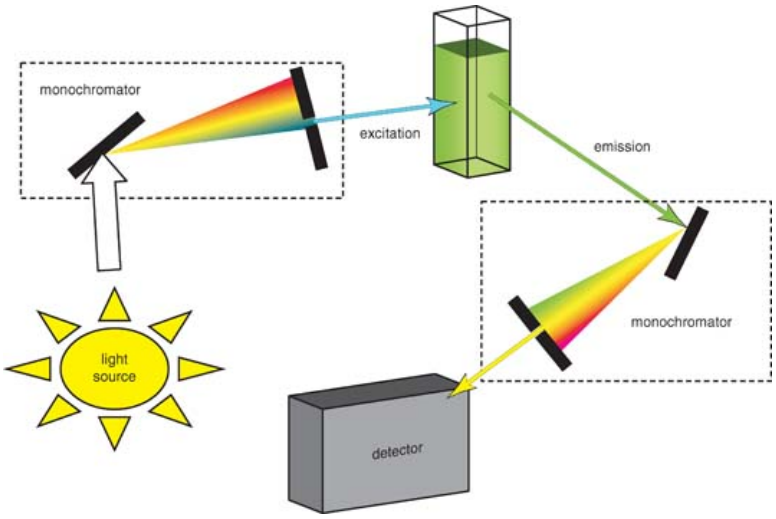

Figure 4.3: Working principles of fluorospectrophotometry

4.6 Confocal microscopy

Molecules have various states referred to as energy levels. Fluorescence spectroscopy is primarily concerned with electronic and vibrational states. Generally, the species being examined has a ground electronic state (a low energy state) of interest, and an excited electronic state of higher energy. Within each of these electronic states there are various vibrational states.

In fluorescence, the species is first excited, by absorbing a photon, from its ground electronic state to one of the various vibrational states in the excited electronic state. Collisions with other molecules cause the excited molecule to lose vibrational energy until it reaches the lowest vibrational state of the excited electronic state. This process is often visualized with a Jablonski diagram. The molecule then drops down to one of the various vibrational levels of the ground electronic state again, emitting a photon in the process. As molecules may drop down into any of several vibrational levels in the ground state, the emitted photons will have different energies, and thus frequencies. Therefore, by analysing the different frequencies of light emitted in fluorescent spectroscopy, along with their relative intensities, the structure of the different vibrational levels can be determined.

For atomic species, the process is similar; however, since atomic species do not have vibrational energy levels, the emitted photons are often at the same wavelength as the incident radiation. This process of re-emitting the absorbed photon is "resonance fluorescence" and while it is characteristic of atomic fluorescence, is seen in molecular fluorescence as well. In a typical fluorescence (emission) measurement, the excitation wavelength is fixed and the detection wavelength varies, while in a fluorescence excitation measurement the detection wavelength is fixed and the excitation wavelength is varied across a region of interest.

Confocal microscopy was also used for collecting the FRET data. A confocal microscope is a light microscope that excludes any light that does not form a focused plane of the image by using an aperture (4.4). A modern confocal microscope also uses a coherent light source instead of white light to have even more controlled data. The microscope used in the project used 488 nm, 515 nm and 561 nm excitation wavelength lasers, suitable for the selected fluorophores. The set-up uses adjustable dichroic mirrors and filters to split excitation and emission wavelengths into different channels which

can be captured independently. This allows monitoring both excitation and emission simultaneously over time.

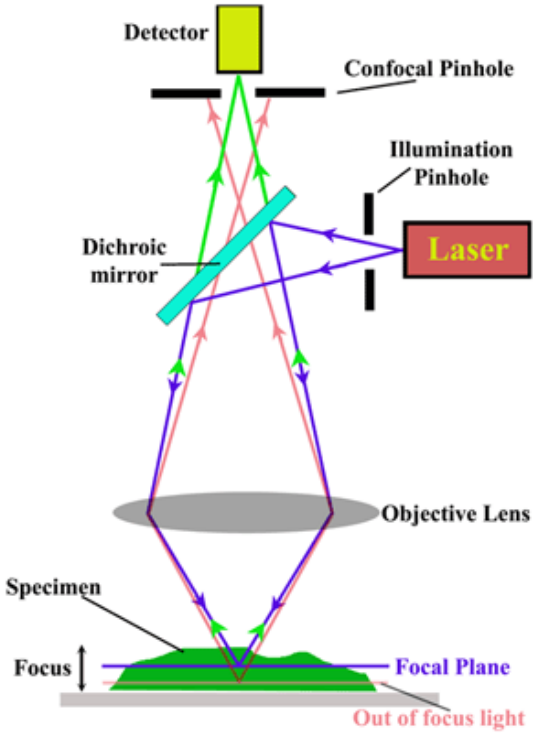

Figure 4.4: Working principles of a confocal microscope

4.7 Förster resonance energy transfer

Förster resonance energy transfer (or FRET, also commonly known as Fluorescence resonance energy transfer) is a molecular phenomenon and a technique used for measuring interactions and distances at a molecular scale, that involves a non-radiative transfer of electronic excitation from a donor molecule to an acceptor molecule. A molecule or a part of a molecule can demonstrate fluorescence if it can be excited electronically by a photon absorption, loose some of the absorbed energy through non-radiative means and finally emit a photon and subsequently come back to its ground state.

Such molecules are called fluorophores. Such a fluorescence event demonstrates a Stokes shift - the emitted photon has always a lower frequency (or a higher wavelength) and therefore lower energy than the absorbed photon and the difference in energy is

dissipated through vibrational relaxation to the surroundings. When two such fluorophores, having compatible excitation and emission energies are brought together, they may demonstrate FRET. In such case, the photon emission of one of the fluorophores (the donor) might not happen and the energy gets transferred non-radiatively to the other fluorophore (the acceptor) which subsequently emits a photon (Figure 4.5). The acceptor emitted photon usually will have even lower energy compared to the donor emitted photon so the event is distinguishable and measurable.

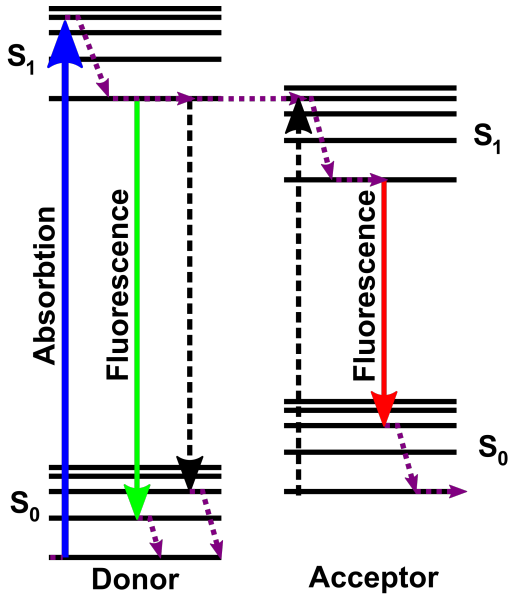

Figure 4.5: The Jablonski diagram for a FRET event. S_0 represent the ground states of a molecule and S_1 represent the excited states. The purple dashed purple lines represent non-radiative relaxation pathways for electrons. Dashed black lines represent pathways for radiative relaxation and excitation, taken by electrons if fluorophore are not close enough to interact.

One of the main fluorophore FRET compatibility criteria is the spectral overlap of donor emission and acceptor excitation spectra. This means that the donor emission vibrational energy levels must be comparable to acceptor emission vibrational energy levels. The other conditions on which FRET depends are the relative orientation of fluorophores and the distance between them. These requirements are summarised in Förster radius – the distance between two fluorophores, at which the energy transfer is

50%:

$$R_0 = [8.8 \times 10^{23} \kappa^2 n^{-4} Q Y_D J(\lambda)]^{\frac{1}{6}}, \tag{4.2}$$

where R_0 is given in Ångströms, κ is the the dipole orientation factor, n is the refractive index of the medium, QY_D is the quantum yield of the donor fluorophore and $J(\lambda)$ is the spectral overlap integral.

The FRET energy transfer between two fluorophores is inversely proportional to the sixth power of distance between them and typically works up to 10 nm distance. Therefore, attached fluorophores and the generated FRET signal are utilised for the interrogation of molecular interactions. FRET has been used to probe numerous molecular interactions, including protein – protein interactions *in vivo* [130], cell surface protein interactions [131] and protein folding [132].

This project used selected fluorophores attached to ends of ssDNA and dsDNA for investigating interaction kinetics of nucleoprotein filaments and dsDNA. FRET was detected and quatified by measuring fluorescence emission on a confocal microscope system as described in the previous section.

Chapter 5

Filament metallisation with gold and magnetic nanoparticles

5.1 Introduction

As discussed in the literature review chapter, the molecular biology tools for manipulating DNA are extensive and flexible. Different enzymes can be used to synthesise, cut, join and modify dsDNA. RecA can be used to fully cover the dsDNA or selectively patterned by forming a RecA nucleoprotein filament on a ssDNA and attaching it to the dsDNA in a selected region through the RecA filament homology search mechanism. The RecA patterning technique is a powerful tool for single-base specific DNA marking tool, however it does not add any functionality to DNA on its own. For the DNA toolkit and overall DNA framework construction to be useful in real life applications, the DNA constructs need to posses certain desired functionalities. The need for novel electronic device manufacturing techniques and viability of DNA technology to be suitable for it, suggests electronic functionality as the first development pursuit in DNA framework functionality. Electrical conduction is arguably the simplest and most important feature of any electronic device. Different methods for imparting electrical conduction to DNA were investigated as discussed before, however, the majority of them are either non-specific metallisation of the full length of the DNA or require extensive intrinsic modification of the DNA with long preparation times to achieve site-specific metallisation.

For RecA-patterned DNA systems to have site-specific conductivity, no intrinsic

DNA modification is required, since RecA is already used as a marker. Two strategies for metallising such a system can be taken: 1) selectively metallising the template DNA, but not the RecA-covered regions or 2) selectively metallising the RecA-patterned regions, but not the bare template DNA. This project is concerned with RecA-patterned region metallisation, since this has never been investigated before and it can give higher control on regions to be metallised. The approach taken to metallise the RecA-coated DNA combines well-established chemistry of protein modification and NP - thiol conjugation. Firstly, RecA bound to DNA is to be functionalised by derivatisation with thiols through a thiolating reagent. Secondly, gold NPs will be introduced to bind to derivatised constructs. Selected thiolating reagents are specific to interaction with proteins, which guarantees subsequent metallisation selectivity to RecA-coated regions only.

This chapter concerns itself only with establishment of metallisation methods on the simplest DNA-RecA construct – non-patterned dsDNA nucleoprotein filament, where RecA coats the whole length of the selected DNA. The overall goal of this chapter is to form conductive nanowires through metal NP deposition on thiolated filaments. To achieve that, the goal should be broken into smaller steps:

- dsDNA of a selected length needs to be synthesised using PCR;
- filament formation on the produced DNA needs to take place;
- the surface of the filament needs to be modified to introduce thiols;
- the filaments need to be purified from all the excess thiolating reagent;
- NPs can be introduced to react with the modified filament surface resulting in a nanowire formation.

For filament formation and subsequent modification, 3.5 kbp dsDNA as a fragment from λ-DNA was selected for all the work in this chapter. Filament formation on the DNA was done using ATPγS co-factor to produce a stable RecA-DNA complex. For filament thiolation, three different thiolating reagents were investigated: SATA, 2-IT and SPDP. All of them bind to lysines present on RecA at neutral or alkaline pH values. Because of that, formation of filaments is performed in an alkaline pH by using a solution buffering reagent.

A purification step is required because any excess thiolating reagent will interfere with filament-NP interaction by binding to the NP surface, saturating it and preventing filament thiol reaction with the NP.

5.1.1 Thiolation reagents

For RecA surface-exposed lysine modification three different thiolating reagents were used – SATA (N-succinimidyl S-acetylthioacetate, used in conjunction with hydroxylamine), 2-IT (2-iminothiolane) and SPDP (succinimidyl 3-(2-pyridyldithio)propionate).

SATA readily reacts with lysines exposed on the RecA surface adding a protected thiol group and releasing a N-hydroxysuccinimide (NHS) group (Figure 5.1). The protection is provided by an acyl group and allows storage of the modified proteins long-term without risk of thiol oxidation. SATA should be reacted with proteins at pH 7.2 - 8.0, because it is non-functional at acidic pH values and above pH 8.0 is unstable and hydrolyses, also loosing its function.

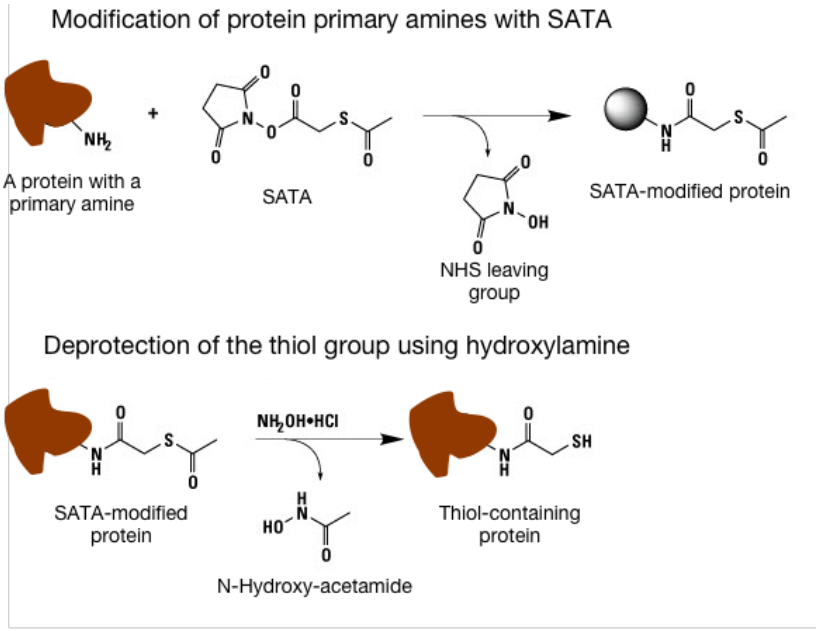

Figure 5.1: The working principle of protein primary amine modification using SATA.

SPDP is chemically similar to SATA (Figure 5.2). It reacts with a primary amine through NHS chemistry and leaves thiol protected in a disulfide form. A reducing agent, such as tris(2-carboxyethyl)phosphine (TCEP) or dithiothreitol (DTT) should be used

to obtain a reduced thiol group for later applications. SPDP is not readily soluble in water and needs to be initially dissolved in dimethyl sulfoxide (DMSO). Having the same NHS ester group as SATA, SPDP is functional at pH 7.2 - 8.0.

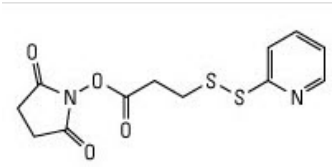

Figure 5.2: The structure of SPDP reagent.

2-IT, also known as Traut's reagent does not share structural similarity of an NHS ester with the previous two reagents. It contains a five-membered ring with a sulphur atom in it. When 2-IT reacts with a primary amine, the ring unfolds, then leaving sulphur atom exposed as a thiol (Figure 5.3). The working pH for 2-IT is also lightly alkaline (pH 7.0 - 9.0). The advantage of 2-IT is that it does not require an additional deprotecting reagent, readily exposing a thiol on the protein.

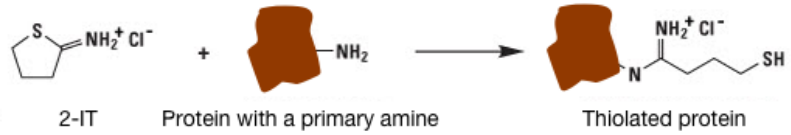

Figure 5.3: The working principle of protein primary amine modification using 2-IT.

5.2 Methods

5.2.1 Nucleoprotein filament formation

2 μl of RecA protein at 2 μg/ul, followed by 0.5 μl of ATPγS at 5 mM was added to a reaction tube containing 200ng of 3.5 kbp DNA at 30 mM TrisAc (Tris-Acetate) and 10 mM MgAc (Magnesium Acetate) in 20 μl of total volume. The sample was mixed subsequently and was incubated at 37 °C for 30mins.

Nucleoprotein filaments deposition on mica surface: 1 μl of the above sample in 19 μl of H_2O were deposited on a freshly cleaved mica substrate pre treated with 10 mM

$NiCl_2$ (nickel chloride) for 1min. After 5mins of sample incubation, the liquids were flicked off from the substrate and blow-dried with nitrogen gas.

5.2.2 SATA conjugation to filament proteins and subsequent thiol deprotection

To the mica substrate prepared above, 20 μl of 650 μM SATA (originally in dimethyl sulfoxide (DMSO) at 65 mM concentration, diluted to 650 μM with water) was placed and incubated for 30mins at room temperature. Finally, the sample if needed to image under AFM at this stage was then flicked off and the surface was blow-dried with nitrogen.

20 μl of 500 mM $NH_2OH \cdot HCl$ (hydroxylamine hydrochloride) solution was deposited onto the above prepared SATA-treated mica substrate with nucleoprotein filaments and incubated for 120mins at room temperature. Afterwards, the surface was dried with nitrogen.

5.2.3 Gold Nanoparticle visualisation under AFM

20 μl citrate-stabilised gold nanoparticles (diluted to 0.5 μM from a 9.5 μM stock solution with water) was placed on a freshly cleaved mica surface that was not pre treated with $NiCl_2$. Afterwards the surface was flicked off and dried with nitrogen.

5.2.4 Magnetic nanoparticle phase transfer (original protocol 1 (from Dr. Thanh)

5 ml of Fe_3O_4-Au supplied nanoparticles (from Dr. Thanh) in hexane solution were precipitated with 15 ml ethanol and were collected by a permanent magnet. The precipitate was washed two more times then redispered in 3 ml of 1M tetramethylammonium hydroxide (TMAOH) solution. Tri-sodium citrate (0.04g) was added and the pH of the resulting solution adjusted to pH = 6.5. The solution was sonicated for 15min, after which the Fe_3O_4-Au NP were collected using a magnet and re dispersed in 5 ml de ionised water and sonicated for a further 5mins.

Protocol 2: In a 2 ml reaction tube, 500 μl of molecular-biology grade ethanol was added to 20 μl of Fe_3O_4-Au supplied nanoparticles (from Dr. Thanh) in hexane solution. The solution colour changed from intense red to black. The reagents were

then mixed and placed on a magnetic rack for 5mins in order to precipitate the magnetic nanoparticles. While the tube was on the magnetic rack, the supernatant was collected and discarded. 400 μl of ethanol was then added to the precipitate. The sample was mixed using a vortex and then sonicated for 20mins. The nanoparticles were precipitated using a magnetic rack as previously, resuspended in fresh 400 μl ethanol and sonicated for 20mins. Finally, the nanoparticles were precipitated the same way and re-suspended in 400 μl of water. For AFM imaging, 20 μl of 1 in 20 dilution of the sample with water was deposited on the mica surface.

5.2.5 Deposition of magnetic and gold nanoparticles on thiolated nucleoprotein filaments

For gold nanoparticle deposition, 2 μl of gold NPs in 38 μl of H_2O was deposited on mica surface containing nucleoprotein filaments treated with SATA as earlier and deprotected for 30mins using hydroxylamine. The sample was incubated for 30mins at room temperature and then the mica substrate was dried under nitrogen. For magnetic nanoparticles deposition, 2 μl of Fe_3O_4-Au NPs (phase-transferred using protocol 2) in 38 μl of H_2O was used.

5.2.6 Comparing gold and magnetic NPs deposition on thiolated nucleoprotein filament on surface and in solution

On surface: for the gold nanoparticle treatment, nucleoprotein filaments were produced as earlier, except instead of Tris-Ac the reaction was carried out in 30 mM HEPES. 4 μl of the above sample in 20 μl H_2O was incubated on the $NiCl_2$-treated mica surface for 5mins. The surface was then washed thoroughly with deionised water and 50 μl of SATA at 1.3 mM concentration (diluted with H_2O from stock) was applied for 30mins at room temperature. After removing the excess liquid, 50 μl of 10 mM $NH_2OH \cdot HCl$ was applied for 30mins at room temperature. The mica substrate was then washed extensively with H_2O. To this, depending on the sample 0.05 μl, 0.5 μl, 1 μl or 2.5 μl (final concentrations = 9.5 nM, 0.1 μM, 0.2 μM and 0.5 μM respectively) of 9.5 mM Au NPs in 50 μl total volume (water) was applied and the surface was incubated further 30mins at room temperature. It was then washed twice with water and dried with nitrogen.

For magnetic NPs deposition on the filaments, 1 μl phase-transferred magnetic NPs (using protocol 2) were used instead of Au NPs.

In solution: For the solution chemistry, 1 μl of 65 mM SATA was added to the nucleoprotein filaments (in HEPES) solution and was incubated 30mins at 37 °C. To this, 1 μl of $NH_2OH \cdot HCl$ was added and further incubated for 30min. Finally, 1 μl or 0.5 μl (0.4 μM or 0.2 μM) of 9.5 μM Au NP solution was added to the reaction tube and incubated for 30mins. For AFM imaging, 4 μl of the above reaction with 16 μl of H_2O was deposited on a $NiCl_2$-treated mica substrate. The sample was incubated for 5mins and dried with nitrogen.

For magnetic NPs deposition on the nucleoprotein filaments in the solution, 0.1 μl or 1 μl of phase-transferred magnetic NPs, prepared using protocol 2 were used instead of Au NPs. Incubation times for nanoparticles were also varied - 30mins, 3h, 18h and 24h.

5.2.7 Nanoparticle size enhancement by gold reduction of gold and magnetic nanoparticles

For gold enhancement, Au^{3+} ions from chloroauric acid ($HAuCl_4$) were reduced to Au^0 using sodium borohydride ($NaBH_4$). For enhancing gold nanoparticles, a solution of 30 mM HEPES, 33 nM gold nanoparticles, 1 mM $HAuCl_4$ and 1 mM $NaBH_4$ was prepared ($HAuCl_4$ and $NaBH_4$ were added last). The sample was mixed and incubated for 30mins. 4 μl of the reaction mixed with 16 μl of H_2O were deposited on the mica surface, pre-treated with 10 mM $NiCl_2$ for 1min. After 5mins of sample incubation, the liquids were flicked off from the substrate and blow-dried with nitrogen gas. For gold enhancement on magnetic NPs, the sample was prepared as above, except 1 μl of phase-transferred magnetic NPs were used (prepared using protocol 2). For enhancing gold on magnetic NPs conjugated to thiolated filaments, the sample was prepared by adding 1 μl of phase-transferred magnetic NPs (prepared using protocol 2) to the filament tube prepared as per section 4.2.6 and incubating it for 30mins at room temperature. To this, 5 μl of 60 μM $HAuCl_4$ (final conc. 10 μM) and 1 μl of 300 μM $NaBH_4$ (final conc. 10 μM) were added. The tube was incubated for 5mins at room temperature. The sample was then prepared for AFM as described above.

5.2.8 Improving magnetic nanoparticle phase-transferring (protocol 3)

This protocol for phase-transferring magnetic nanoparticles is a modified version of a protocol that uses tetramethylammonium hydroxide (TMAOH) for stabilising similar magnetic particles.

100 μl of supplied magnetic nanoparticles in hexane were transferred to 2 ml a tube and topped up with 1.9 ml of molecular biology grade ethanol. The contents were mixed thoroughly and centrifuged at 5000 rpm for 1 min. The supernatant was discarded and 1.7 ml of 2.4 % TMAOH (diluted from stock with H_2O) was added to it. The tube was then inverted upside down several times and sonicated for 20mins. TMAOH washing was done two more times in the same way by centrifuging the nanoparticles, discarding the supernatant, adding fresh 1.7 ml 2.4 % TMAOH and sonicating it again. Finally, nanoparticles suspended in TMAOH were transferred to a new clean 2 ml tube. They were centrifuged again at 5000rpm for 1min and the supernatant was discarded. To this 1 ml of 0.02 % TMAOH was added and was sonicated for 20mins afterwards. The resulting nanoparticle suspension had a black colour.

To test the prepared NPs, 1 μl or 0.05 μl of prepared nanoparticles were added to the reaction tube prepared according to methods described in a later section.

5.2.9 Stable preparation (protocol 4) and fully coated nanowire formation

Protocol 3 was modified to obtain magnetic nanoparticles, which were stable for 4 days, before precipitating into big aggregates. The particles obtained in protocol 3 were kept in the fridge (4 C) for about 1 week, after which they had already started precipitating. The liquid had a colour gradient - black at the bottom, grey with a slight shade of pink and transparent at the top. Using a pipette, top and middle sections of the liquid were carefully collected (around 0.5 ml), avoiding the highly precipitated bottom part, and was transferred to a new 1.7 ml tube. The new nanoparticles had muddy, greyish pink colour and were stable for 1 - 2 weeks.

To deposit these particles on SATA modified and deprotected nucleoprotein filaments 1 μl of NPs were used in the protocol described in previous section.

5.2.10 Formation of fully stable magnetically-active nanoparticles (protocol 5)

100 μl of supplied magnetic nanoparticles in hexane were transferred to 2 ml a tube and topped up with 1.9 ml of molecular biology grade ethanol (from a new batch). The contents were mixed thoroughly and centrifuged at 5000rpm for 1min. The supernatant was discarded and 1.7 ml of 2.4 % TMAOH (diluted from stock with H_2O) was added to it. The tube was then inverted upside down several times and sonicated for 20mins. Afterwards, the tube was centrifuged at another 1min at 5000rpm. The red-coloured supernatant was collected and the remaining precipitate was resuspended in 2.4 % TMAOH by sonicating for 20mins and collected after centrifuging two more times.

In a separate set of experiment, 4.8 % and 10 % TMAOH was used in the above protocol for washing the nanoparticles.

5.2.11 Investigation on RecA-SATA interaction

Four samples with different concentrations (1.3 μM, 2.6 μM, 5.3 μM and 10.5 μM) of RecA protein were prepared in a 30 mM HEPES solution, with pH adjusted to pH 7.12. Afterwards, 10 μl of 65 mM SATA was added to each sample tube, which were mixed and were allowed to incubate for 21h at room temperature. The tube contents were then transferred into separate dialysis tubes and dialysed against 1l 30 mM HEPES solution for 19h at room temperature. The samples were collected and transferred to new tubes. 2 μl of 0.5M $NH_2OH \cdot HCl$ was added to deprotect thiols on SATA attached to the nucleoprotein filaments. Finally, 10 μl of 25 mM Ellman's reagent was added to each tube and incubated for 20mins before taking spectroscopic measurements.

5.2.12 Investigation on SATA-DTNB interaction

Samples with 6 different concentrations of DTNB (5,5'-dithiobis-(2-nitrobenzoic acid or Ellman's reagent) (0 μM, 132 μM, 263 μM, 562 μM, 1050 μM and 2100 μM) and 6 different SATA concentrations (0 μM, 132 μM, 263 μM, 562 μM, 1050 μM and 2100 μM), deprotected by 0.5M NH_2OH were prepared. Samples were reacted for 20mins before taking the readings with a spectrophotometer.

5.3 Results

5.3.1 Filament formation

A fully reproducible method for generating nucleoprotein filaments on a double-stranded DNA (dsDNA) was investigated. Nucleoprotein filaments were formed by polymerising protein RecA on 3.5 kbp DNA and characterised using AFM. As a control, the same sequence 3.5 kbp DNA was imaged with AFM and the results are shown in Figure 5.4. Long thin and curled structures were seen which is typical DNA morphology. Measurements on more straight string-like structures done using the AFM software showed length of around 1.2 μm. That is the expected length for 3.5 kbp DNA as the distance between two DNA bases is 0.34 nm.

For filament samples, elongated structures were seen (Figure 5.4). Although they were bent to some degree, however the observed structures were not curled up to the same level as the DNA strands. This indicates higher structure stiffness, which has been reported to be characteristic of nucleoprotein filaments formed on a dsDNA. The observed structures were typically 1.7 μm - 1.8 μm long and about 1.5 times longer than the original length of 3.5 kbp DNA. This is expected, because during the filament formation the DNA molecule gets extended 1.5 times from its native length by the RecA protein.

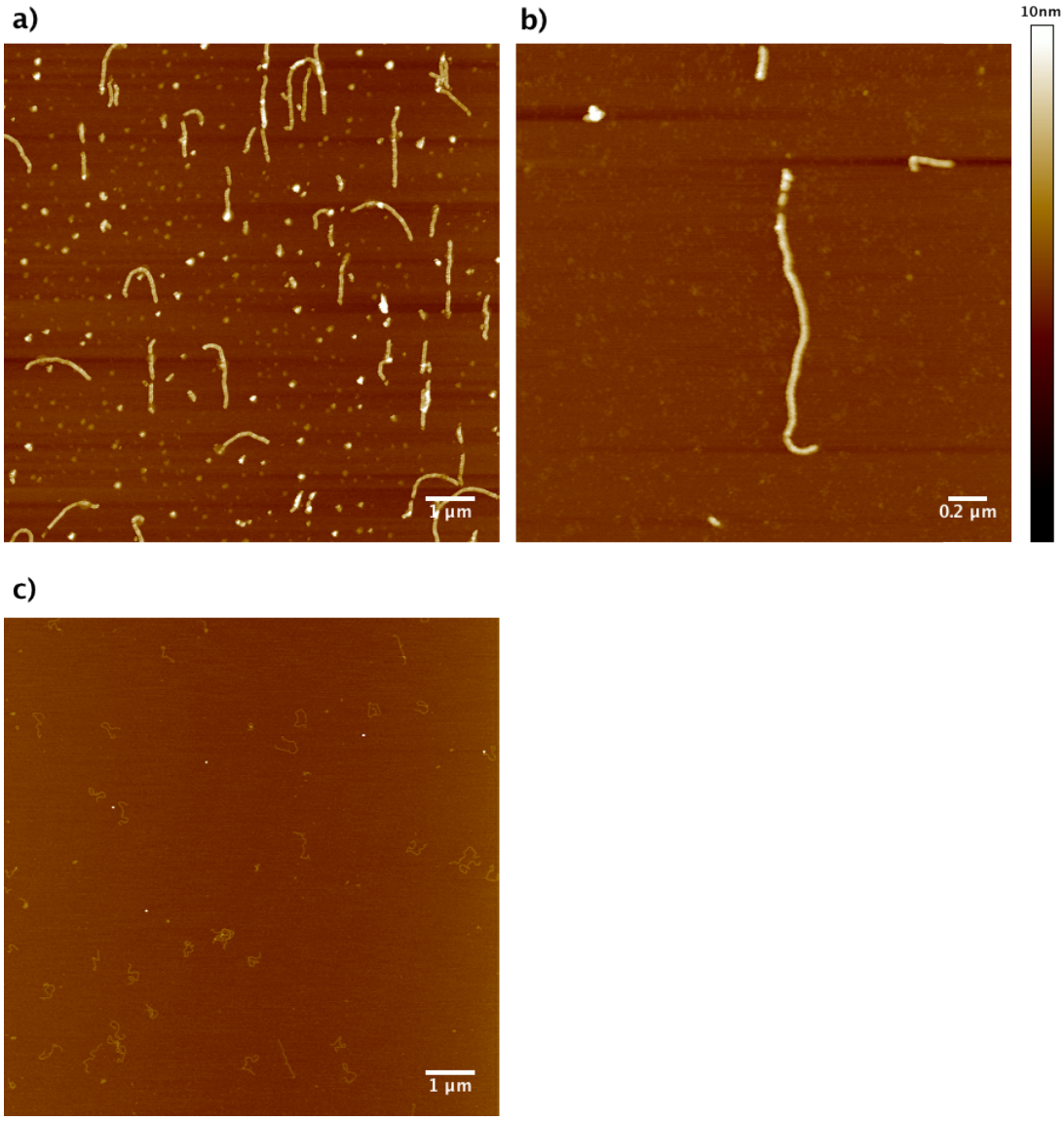

Figure 5.4: a) Nucleoprotein filaments formed on full length of 3.5 kbp DNA; b) single full length nucleoprotein filament; c) 3.5 kbp DNA without RecA proteins.

In addition to expected filamentous structures, shorter fragments, as well as single non-elongated 'dot' structures were present as well. The shorter fragments might represent a fraction of broken filaments, or filaments formed on short DNA strands, which might come from an incomplete PCR or due to a degraded DNA sample. Further-

more, the 'dot' structures could be the polymers of excess RecA formed which did not participate in the nucleoprotein filament formation. In the presence of higher Mg^{2+} concentration, RecA protein has been reported to self-polymerise resulting in short polymerised, filamentous structures.

A statistical analysis was done on the distribution of nucleoprotein filament length distribution as imaged with the AFM on mica surface (Figure 5.5). 30 different imaged sample areas from 5 samples of nucleoprotein filaments formed on 3.5 kbp DNA were collected and used for counting apparent filament length. The length was separated in ranges of 0.2 μm bins and frequency of each bin marked.

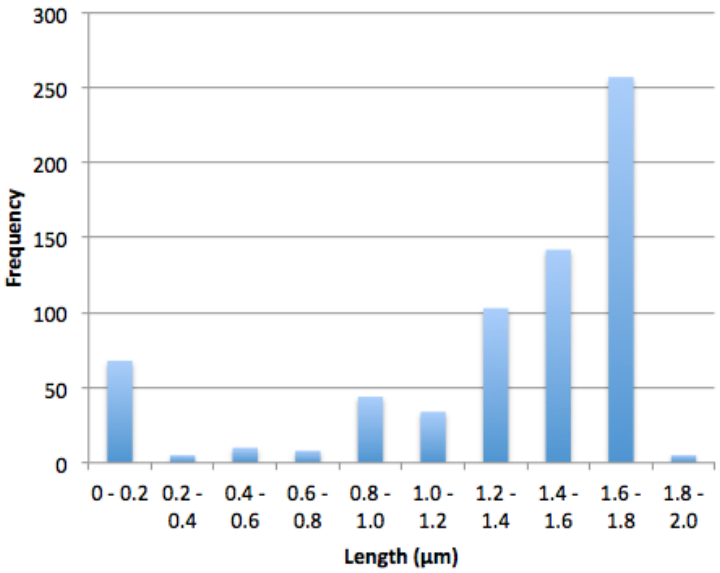

Figure 5.5: Distribution of lengths of the formed nucleoprotein filaments on 3.5 kbp DNA.

Length measurements showed that the bin with expected filament length (1.6 μm - 1.8 μ)m had the highest count of filaments in it. It contributed to 38 % of all the counted filaments. There were less than 1 % of filaments than 1.8 μm. Any such filaments could be an artefact of imaging, more than one filament counted as one full length filament, filament with extra RecA polymerisation at the ends or due to any extra reasons. Relative scarcity of such structures indicate good selected conditions for filament formation and imaging.

Filaments lengths between 0.8 μm and 1.6 μm were prevalent. They comprised 48 % of the counted filaments. This indicates non-full filament formation or possible filament breakage or both. This is corroborated by the fact that filaments of up to 0.2 μm length were also present in relatively large quantities (10 % of counted filaments). Such short filaments may be the broken fragments of longer filaments or RecA aggregate resulting from RecA agglomeration without any DNA present. Since the filaments are imaged with an AFM, the act of sample deposition can be responsible for the distribution of filament lengths. Drying the sample surface with a nitrogen gun or flicking the sample holder can impose stresses to the sample resulting in the observed filament lengths. Since a large amount of filaments with the right length were observed and they are to be modified chemically before they are deposited on the mica surface for imaging, no further concern was paid to the length distribution.

Besides the length, height and width measurements were carried out on formed structures (Figure 5.6). AFM image height profiles taken on three different regions of the potential filament with the average being 3.6 nm. Using the AFM software, filamentous structure width was measured to be 50 nm. The height and width should be both 10 nm - a value reported previously in [73]. The measured values are considerably different, nevertheless, this can be accounted by the effects of AFM tip potentially not being sharp enough, salts, electrostatic interactions between the filament and the tip and measurements on dry surface instead of more natural aqueous environment. Similar effects are seen for DNA samples, yet measured DNA strands are significantly smaller in height (2 nm) and width (8 nm) compared to filament structures.

The expected change in stiffness and dimensions lead to conclusion of successfully formed filaments. Filament formation and imaging was done more than 10 times afterwards with same results, indicating full reproducibility.

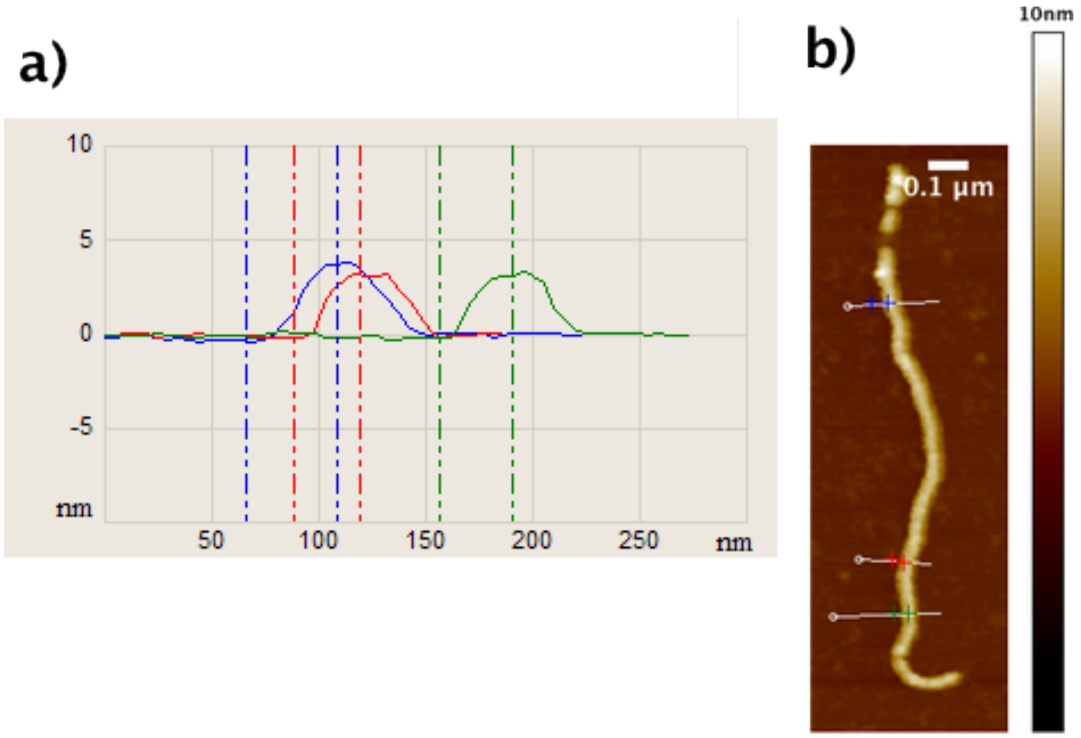

Figure 5.6: a) Graph of nucleoprotein filament height measurement at 3 different positions. Each colour indicates different measurement at different position on the filament. Vertical bars represent positions at which the difference in heights was measured - the background level and the top of filament; b) the corresponding positions on the filament at which the measurements were done.

5.3.2 Filament thiolation

After successful nucleoprotein filament formation, SATA treatment on filaments was investigated. Binding of SATA to biomolecules adds an acetyl-protected sulfhydryl group that, after deprotection with NH_2OH, exposes thiol for reaction with gold, silver or maleimide. Specifically in this case, thiol introduction is pursued for subsequent nanoparticle binding. SATA conjugation has been previously performed on different proteins for various applications and its chemistry is well described.

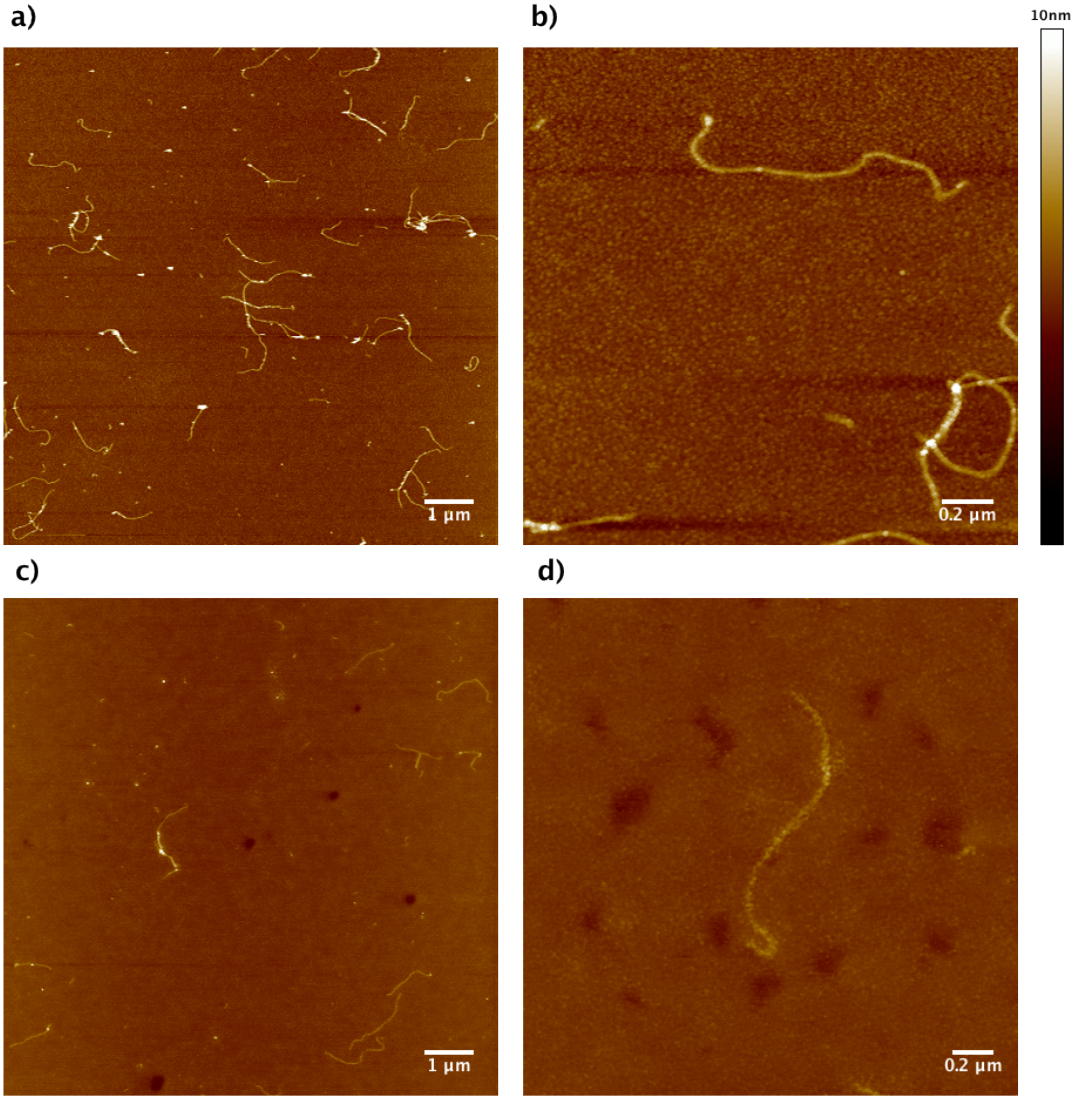

Figure 5.7: a), b) SATA-treated nucleoprotein filaments formed on 3.5 kbp DNA. c), d) SATA-treated filaments after deprotection with NH_2OH.

The main difference that can be seen after SATA conjugation to nucleoprotein filaments compared to unmodified filaments is the filament thickness. As seen in figure 5.7, filament height is decreased to average 2.1 nm and width to 15 nm - 30 nm. However, due to previously mentioned tip effects and possibility of a different tip use, the difference between height and width is not significant. Nevertheless, same filament

length and general morphology is fully preserved.

To fully expose thiols groups on the filament, sample SATA-treated filaments were reacted with NH_2OH. Deprotecting thiol groups with NH_2OH did not reveal any noticeable changes under AFM (Figure 5.7). Some pit-like structures were seen but they can be accounted by poor mica preparation, since later samples prepared by taking care during mica cleaving stage yielded clean surface.

In conclusion, thiol group introduction by SATA and NH_2OH chemistry did not affect filament morphology. No filament conformational change was expected with the SATA chemistry step because the effect SATA has on filaments is only on filament surface, not overall shape and SATA molecules are too small in size to be imaged individually.

5.3.3 Filament metallisation

When filaments are functionalised with thiols, they are fully ready to conjugate metallic nanoparticles, which on a continuous filament would enable electrical conduction and essentially produce a 'nanowire'. For that, two types of nanoparticles were used: gold nanoparticles and magnetic nanoparticles with a gold shell.

For the first set, when gold nanoparticles were investigated to conjugate filaments on surface, at high concentration of gold nanoparticles (0.2 μM, 0.5 μM), large structures, some of which were elongated were seen (Figure 5.8). Granular morphology suggested their particle nature. However, it is impossible to say for sure, that the structures were certainly templated by the filaments. Furthermore, the results varied greatly from sample to sample. Figure 5.8 reveals a bare DNA strand connecting two nanoparticle-formed structures. It is possible that RecA-coated, and subsequently SATA and hydroxylamine treated regions had a high affinity for conjugating gold nanoparticles and non-coated DNA was left to bridge two metallic regions, but judging from the lack of directionality and defined shape of the structure in figure 5.8, the metallisation seems to be chaotic, unpredictable and leaves gaps between nanoparticles.

Lowering nanoparticle sample concentration to 0.1 μM and below revealed recognisable filaments. However, they had no nanoparticles attached to them (figure 5.8), which together with previous results of clustered nanoparticles (figure 5.8) suggests that possible structure formation might be independent of nucleoprotein filaments in

this experiment. This leads to the conclusion, that gold nanoparticle conjugation on surface pre-deposited filaments is not efficient or does not work at all.

In the second set, when the reaction was done in solution with gold nanoparticles evenly dispersed nanoparticles were observed, after the sample was deposited on the mica surface (Figure 5.8). Nucleoprotein filaments were also seen, some of which appeared to be completely covered in nanoparticles, but most of them - only partially (Figure 5.8). This cannot be explained by the nanoparticles deficiency, as nanoparticle coverage in background is high enough to fully bind to all filaments in vicinity.

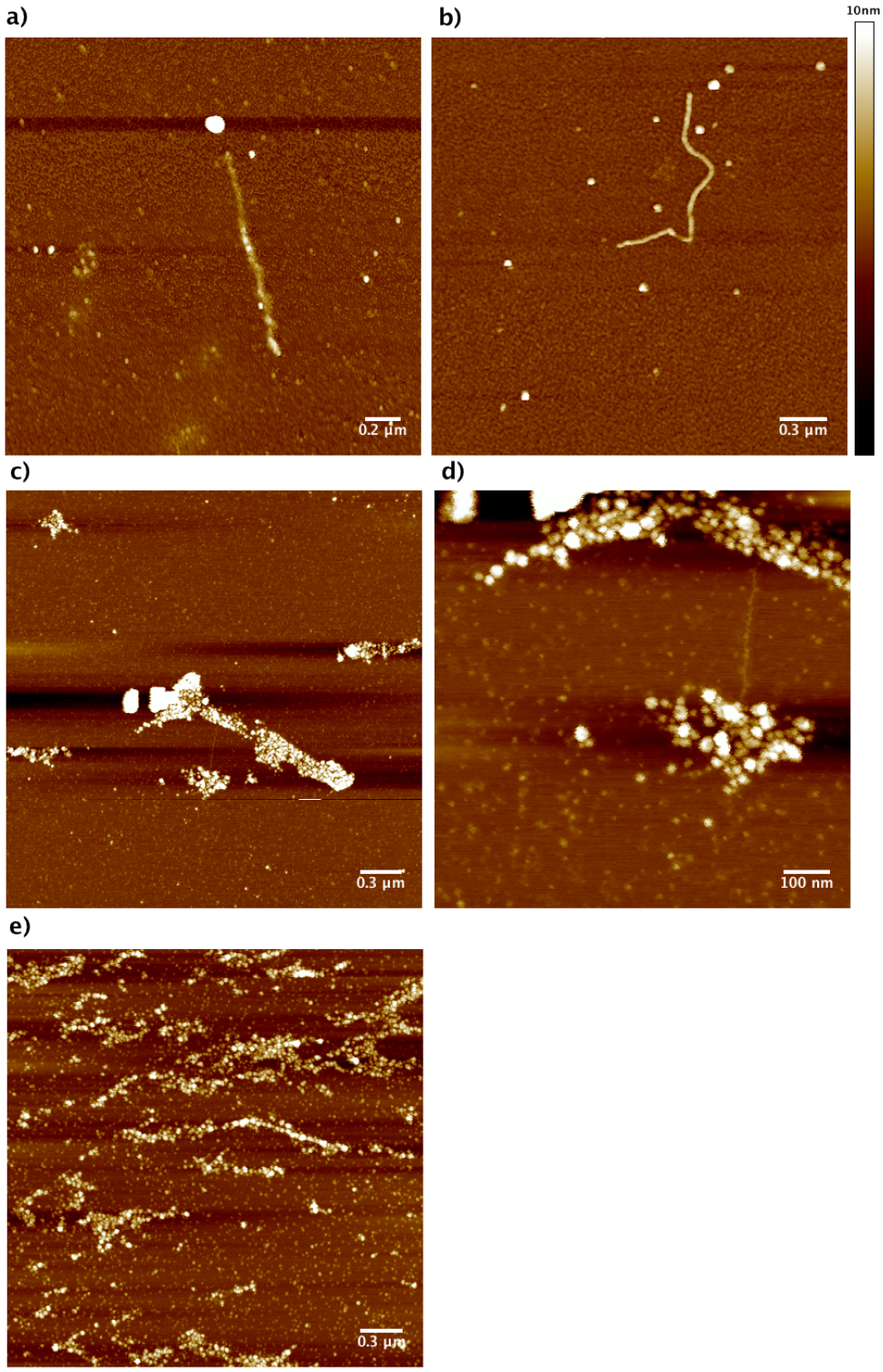

Figure 5.8: Gold nanoparticle treatment of surface-deposited nucleoprotein filaments (filament-SATA reactions done on already surface-deposited filaments as well); gold nanoparticle concentrations used: a) 0.01 μM, b) 0.1 μM, c), d) 0.2 μM, e) 0.5 μM.

5.3.4 Quantifying level of thiolation with SATA/NH2OH

It is not clear, how effective the SATA reaction and the hydroxylamine deprotection steps are, e. g. how does unreacted SATA affect nanoparticle deposition onto thiolated filaments. Furthermore, it was noticed that hydroxylamine hydrochloride acts as salt and promotes gold nanoparticle precipitation (data not included). As previously high amounts of $NH_2OH \cdot HCl$ were used to ensure excess for SATA deprotection that might have interfered with proper filament metallisation in some unaccounted ways.

To solve the aforementioned problems and elucidate on RecA modification, an experiment that eliminates excess reagents and quantifies the introduced thiols per single RecA protein, was designed. The RecA proteins are incubated with SATA overnight to ensure maximum number of thiol binding sites, dialysis was done overnight through a membrane, which has a smaller MWCO (molecular weight cut-off) value (6 kDa - 14 kDa) than the protein size (38 kDa), to remove any unreacted SATA and the collected sample was reacted with $NH_2OH \cdot HCl$ for exposing thiols. The quantification of thiols was done with Ellman's reagent, also known as 5,5'-dithiobis-(2-nitrobenzoic acid) or DTNB). Ellman's reagent reacts with the thiol groups producing 2-nitro-5-thiobenzoate (NTB-), which ionizes to NTB^{2-} in alkaline and neutral solutions. NTB^{2-} can be quantified by absorption at 412 nm using an extinction coefficient $\varepsilon(NTB^{2-})$=14,150 $M^{-1}cm^{-1}$. Because unreacted SATA was fully dialysed and one NTB^{2-} molecule is produced per one thiol, the thiols introduced onto RecA can be quantified with DTNB.

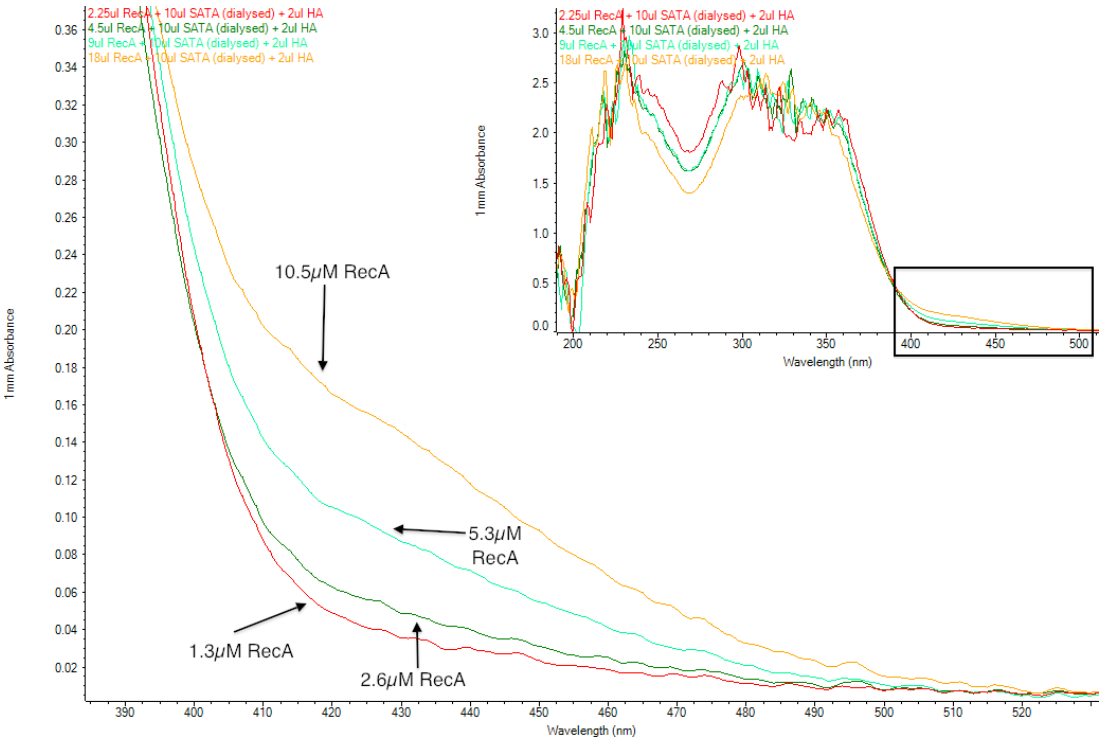

Figure 5.9: Spectra for quantifying thiol groups introduced to known amounts of protein RecA. The inset in the top right corner shows spectra at full wavelength range. The black rectangle represents position of the main graph on the inset graph position.

Four samples with different RecA concentrations were prepared. Quantification with DTNB revealed a correlation between absorption at 412 nm and RecA concentration used (figure 5.9), indicating RecA having exposed thiols, due to successful SATA chemistry. However, 412 nm peaks are most likely heavily influenced by much larger peaks at lower wavelengths (figure 5.9, inset). They are produced from excess unreacted DTNB, which has an absorption peak at 325 nm.

Nonetheless, the absorption values at 412 nm were used to calculate number of thiols per protein introduced. It was estimated that 11 thiol groups are produced per protein, which is a plausible figure as SATA binds onto primary amines - mainly lysine amino acids on proteins and lysine is numerous in proteins. It is possible that RecA becomes denatured during the incubation processes, exposing the cysteines (naturally thiol group containing amino acids), usually buried inside the protein structure, for

reaction with DTNB. To investigate that, a series of control samples with no modifications and dialysed will be prepared and reacted with DTNB in future work.

5.3.5 Investigation of SATA-DTNB interaction

Although the previous experiment established that SATA binds to RecA, the results were not very reliable due to unexpectedly large influence of unreacted DTNB peak. To determine the right amount of DTNB needed for reactions with thiols, a set of 36 samples were prepared. The samples had SATA and DTNB only at 6 different concentrations for each SATA ant DTNB. Spectra for these peaks were taken which indicated 4 different peaks, representing four different species in the solution: (i) NH_2OH, (ii) SATA, (iii) DTNB and (iv) NTB^{2-} (Figure 5.10).

The major trend noticed with all the samples was that with increase of SATA concentration, the SATA and NTB^{2-} peaks increase in height whereas DTNB decreases (Figure 5.10). To get more quantitative information, peak fitting on recorded spectral data points was performed using pro Fit 6.1.11 program. Standard Voigt peak function was used for each peak fitting in the spectral data. Each Voigt peak is defined as:

$$Voigt(A, x_0, sg, sl) = \sqrt{\frac{\pi}{2}} \cdot A \cdot \frac{sl}{sg} \cdot V\left(\frac{(x - x_0)}{\sqrt{2} \cdot sg}, \frac{sl}{\sqrt{2} \cdot sg}\right)$$

$$\text{with } V(X, Y) = \frac{Y}{\pi} \int_{-\infty}^{\infty} \frac{e^{-t^2}}{Y^2 + (X - t)^2} dt\,,$$

where A is peak amplitude, x0 - peak position on wavelength axis, sg - half width at half maximum of Gaussian part of the peak, sl - half width at half maximum of Lorentzian part of the peak. Initially, all four parameters (A, x0, sg, sl) were left free to be fit. After fitting all peaks in all 36 spectra, all four parameters for each plotted peaks were obtained and the average peak position (x0) was calculated from most of the spectra. Spectra with highest concentrations (>526 μM) of DTNB and SATA were not used for calculating x0, as the peaks were cut off due to spectrophotometer oversaturation. The NH_2OH peak was an exception as it had an apparent position shift with the increase of SATA concentration. The reason for NH_2OH peak shift was not known at the time. To compensate for the shift, NH_2OH peak positions determined by pro Fit were plotted against SATA concentration and a trend determined. Having

that, theoretical NH_2OH peak position for each SATA concentration was extracted and used subsequently.

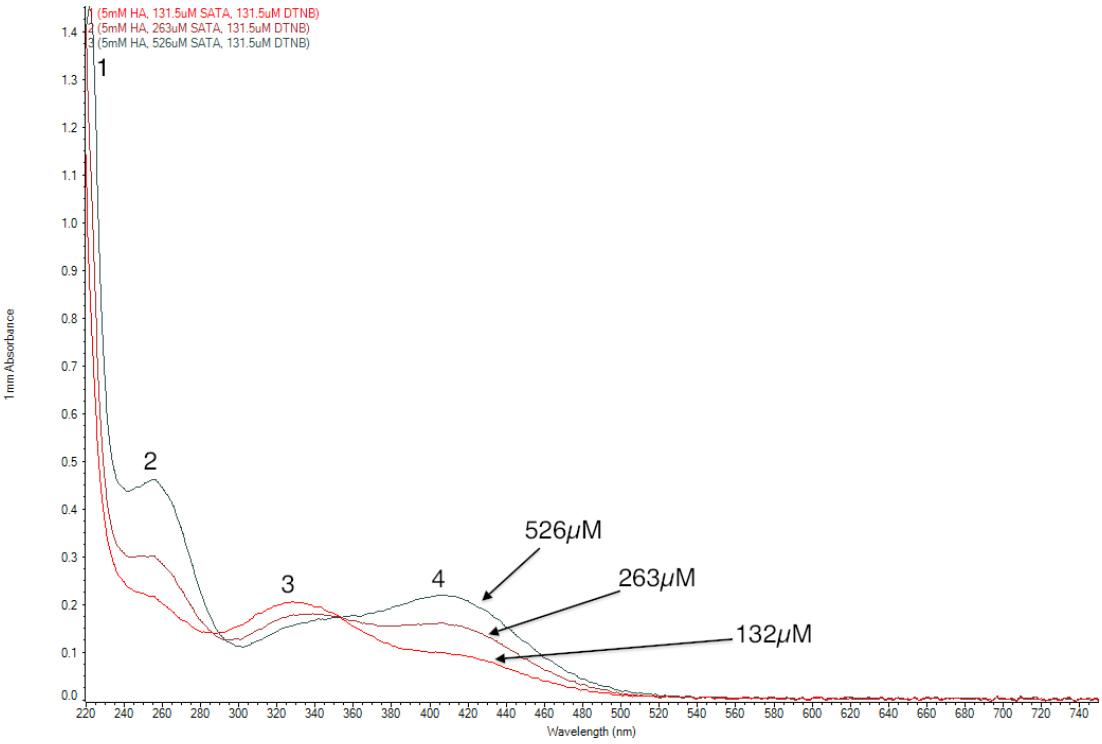

Figure 5.10: An example plot of three spectra of SATA-DTNB interaction at three different concentrations. Numbers 1 - 4 represent different species in the sample: 1 - NH_2OH, 2 - SATA, 3 - DTNB, 4 - NTB^{2-}. The labelled concentrations indicate different SATA concentrations for sample. All samples had DTNB at 132 μM concentration.

Next, pro Fit was used again to fit the peaks onto same spectral data but this time with peak positions fixed for each sample (different NH_2OH peak position for each SATA concentration). This assumption is reasonable as peak position is fixed by nature (except for the unusual cases, such as NH_2OH) and fixing it would allow obtaining more accurate data. The second set of peak shifts again yielded a new set of parameters. This time, the average sg and sl values for each peak were determined from all but the oversaturated peaks. sg and sl values are also intrinsic to the reaction so should not change. Finally, the third fit was done with only the peak amplitude as the only free parameter and the results were plotted against SATA concentration in

series of DTNB concentration used (Figure 5.11).

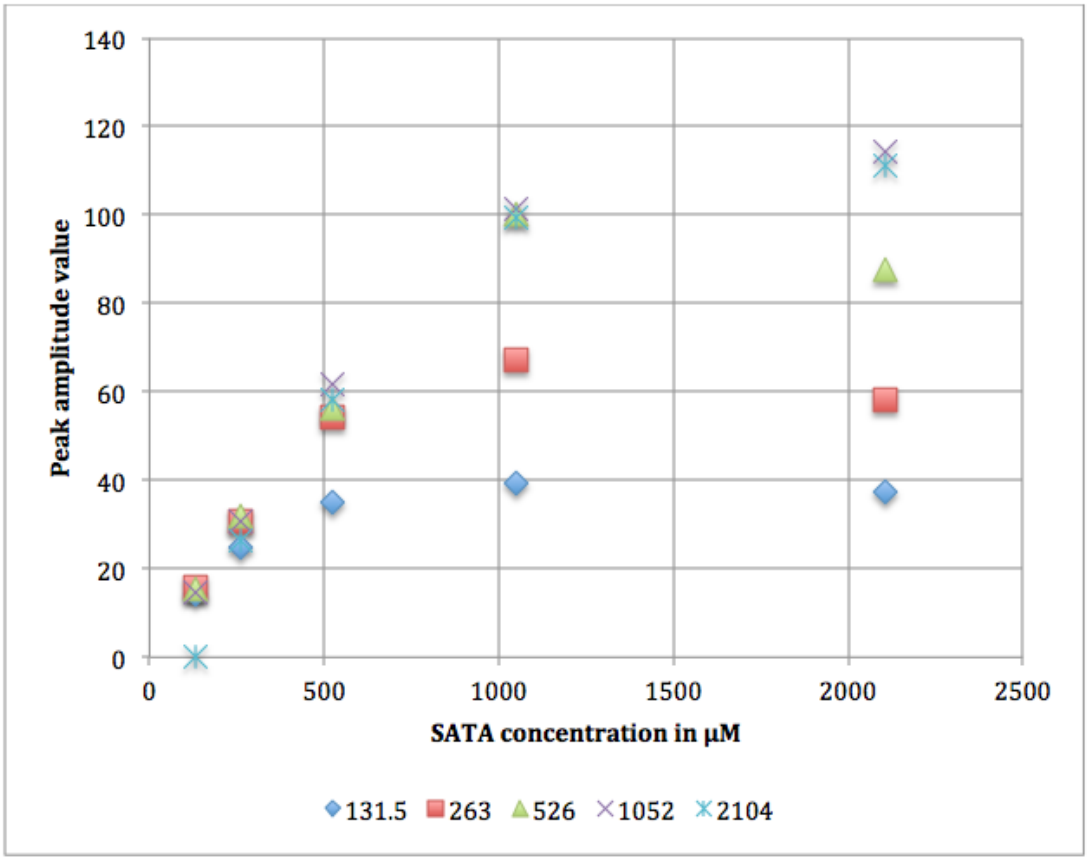

Figure 5.11: NBT2- peak amplitude (determined through third pro Fit fit) plotted against SATA concentration. The legend indicates DTNB concentration used for each set of data points.

The plot of NBT2- peak against added SATA indicates that with SATA concentration up to 526 μM, the absorption response is linear (Figure 5.11). However, with SATA concentrations in excess of 526 μM, the absorption trends saturate indicating that they cannot be trusted on determining thiol concentration above 500 μM. A plot of 132 μM DTNB concentration absorption peak values against increasing SATA concentration shows that there is a linear response for SATA thiol detection up to 526 μM SATA concentration. In theory, this is not possible because as discussed previously, the stoichiometric ratio of SATA to DTNB to NTB^{2-} is 1:1:1. Similar trends are no-

ticed with other DTNB concentration values. This suggests either that (i) SATA thiol binding efficiency is lower than 25 % or that (ii) NH_2OH deprotection is inefficient (0.5M, therefore high excess of it was used) or that (iii) thiols degrade or react with themselves (forming disulphide bonds) earlier than with DTNB or a combination of all three. However, the limiting step in the reactions is still availability of DTNB as the peak amplitude value plot against SATA concentration saturation level increases in value from 40 to 110 with the increase of DTNB concentration used (Figure 5.12).

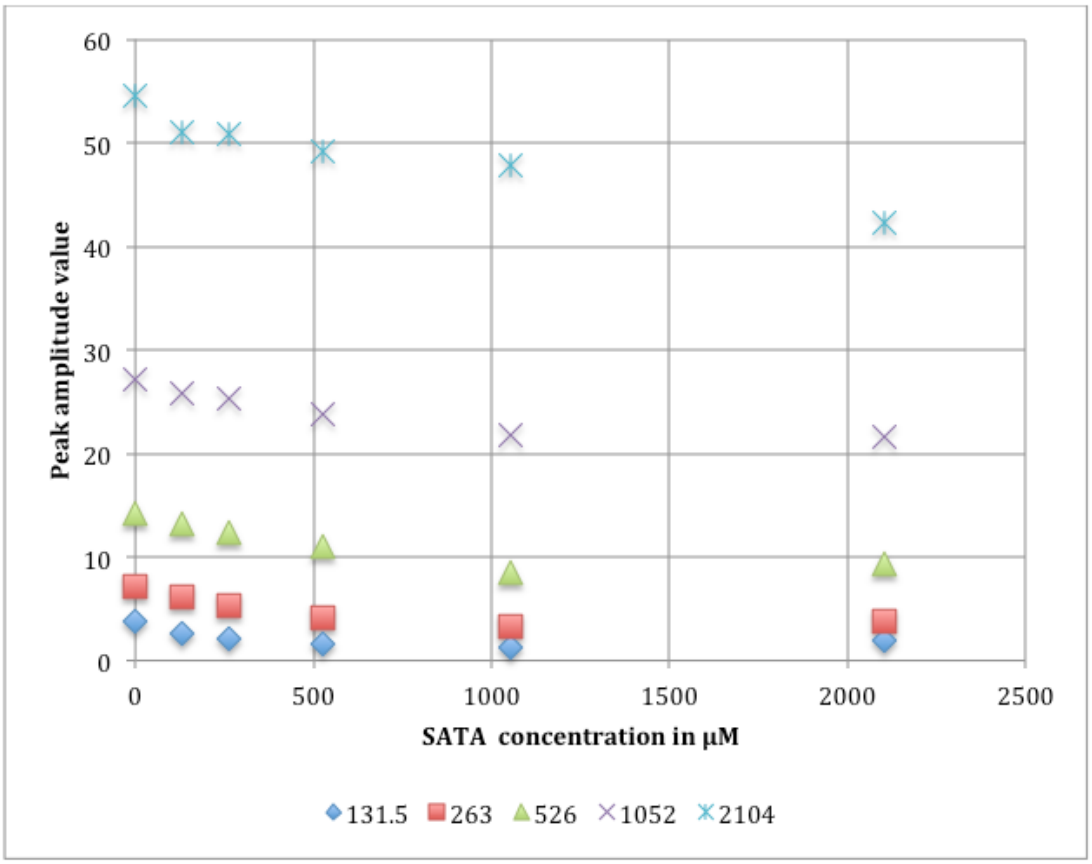

Figure 5.12: DTNB peak amplitude (determined through third pro Fit fit) plotted against SATA concentration. The legend indicates DTNB concentration used for each set of data points.

A separate plot of DTNB peak decrease with addition of SATA indicates that the peak amplitude decrease is not linear with the concentration, as one would expect (fig-

ure 5.12). The decrease in peak amplitude is linear initially for all six sets of samples with different concentration, but above 256 μM SATA concentration the peak amplitude values become constant irrespective of SATA concentration. The main difference between the trends is the offset on peak amplitude depending on the DTNB concentration used. This negates the previous assumption that availability of DTNB is the reaction-limiting step, as same trend is observed independent of SATA concentration added, and suggests that even though SATA is inefficient in binding to DTNB, some other interfering mechanism might be present. The only other reagent present in these reactions is NH_2OH, which already demonstrated an unusual behaviour with its peak shift. If NH_2OH is interfering with the SATA thiol-DTNB reaction, the exact mechanism is not yet understood and requires further investigation. The DTNB-SATA interaction samples indicated that absorption values could not be fully trusted as not yet understood trends are observed. If a single fixed DTNB concentration is used, thiol-containing samples can be compared between themselves, but quantitative determination should not be carried out. Further investigation of NH_2OH or any other interference should be done by comparing the results to corresponding reactions with same concentrations of DTNB and other readily thiol containing reagent, such as cysteamine or cystamine.

5.3.6 Filament metallisation with magnetic nanoparticles

When the reaction to bind magnetic nanoparticles to surface pre-deposited SATA- and NH_2OH-treated filaments was performed, similar results to gold nanoparticle treatment of surface pre-deposited filaments were observed. There was not a single nanoparticle bound to the filaments (Figure 5.13). This might be influenced by the lack of proper filament formation, as the imaged filaments were shorter and straight, probably indicating full-length filament fracturing.

The solution-based reaction incubated for 30mins did have some nanoparticles conjugated to the filaments, albeit the coverage was not continuous or extensive (figure 5.13). Only 5 - 15 nanoparticles were seen bound to each filament. When the reaction for conjugation was incubated for 18 - 24 h, similar level coverage of nanoparticle on the filaments was observed (figure 5.13). Only single nanoparticles (1 - 5 per filament) were bound to the filaments. However, on reducing the nanoparticle concentration ten times and incubating the reaction tube for 3 h at room temperature resulted in better binding.

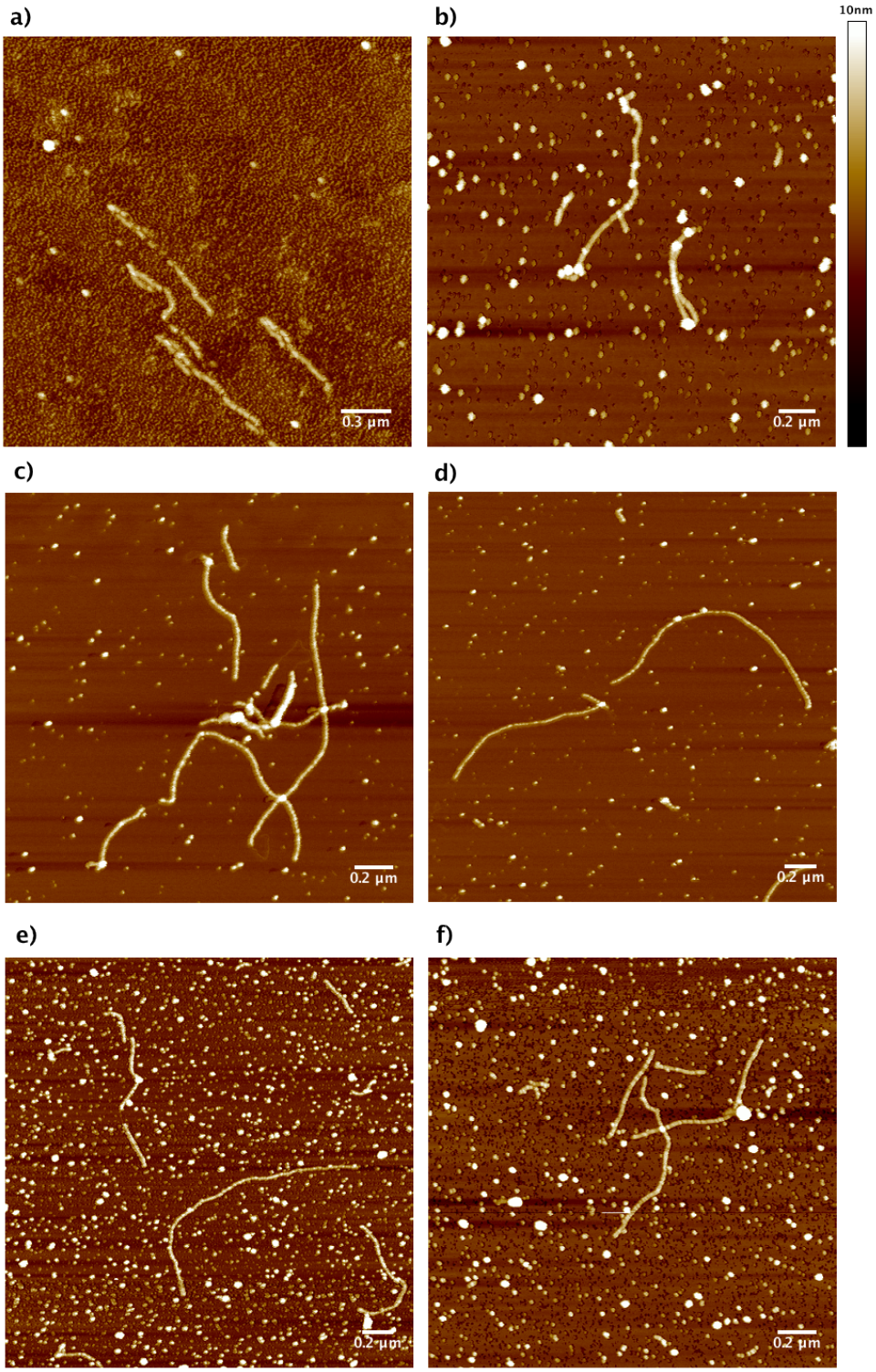

Figure 5.13: a) Treatment of thiolated filaments predeposited on the surface with 1 μl of magnetic nanoparticles; treatment of thiolated filaments in solution with 1 μl magnetic nanoparticles for 30 mins (b), 18 h (c), (d) and 24 h (e), (f).

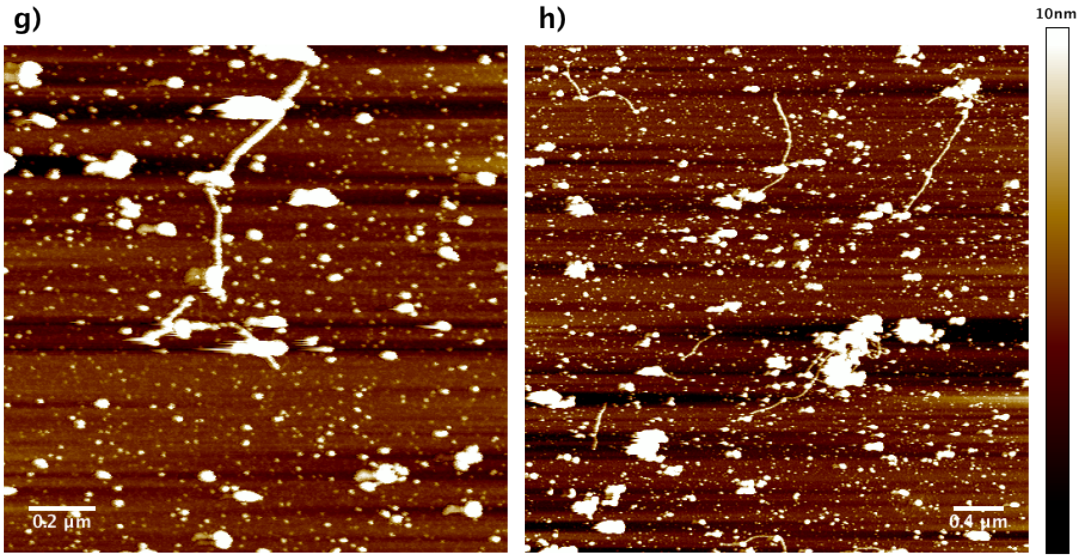

Figure 5.14: (cont.) g), h) treatment of thiolated filaments in solution with 0.1 μl magnetic nanoparticles for 3 h .a) Treatment of thiolated filaments predeposited on the surface with 1 μl of magnetic nanoparticles; treatment of thiolated filaments in solution with 1 μl magnetic nanoparticles for 30 mins (b), 18 h (c), (d) and 24 h (e), (f).

In addition to binding of particles the nanoparticles seemed to form agglomerates as well, as seen from figure 5.14. As the samples with 3h incubation period were prepared after the ones with 30mins, 18h and 24h incubation times and used same nanoparticle batch, it is possible that nanoparticles started to precipitate over time, leading to larger (10 - 30 times increase) average nanoparticle size which is observed for 3 h sample (Figure 5.14).

The reaction results do not seem to be consistent and predictable because they do not follow any obvious trend when concentration and incubation time are varied. This indicates, that the selected incubation time and concentration values do not influence nanoparticle binding and it might be due to other factors, or the nanoparticles are unstable and loose their ability to bind thiols over time. However, for this set of experiments, there is not enough of data to fully make conclusion on what influences nanoparticle binding.

Overall, it appeared that for both gold and magnetic nanoparticles, the conjugation to SATA and hydroxylamine treated filament results in better filament coverage

than on mica surface. Also, gold nanoparticles seemed to cover the filaments with higher efficiency than the magnetic ones (10 - 30 gold nanoparticles against 1 - 5 magnetic nanoparticles per filament). The difference could be attributed to the fact that magnetic nanoparticle level of stability is not well known. Reagent concentrations for phase-transferring magnetic nanoparticles to water were chosen arbitrarily as supplied magnetic nanoparticle concentration was unknown. This could have resulted in partial nanoparticle stabilisation and subsequent nanoparticle agglomeration which is suggested by one of the samples discussed previously Fiigure 5.14). Nevertheless, partial filament metallisation was still observed for both magnetic and gold nanoparticles albeit the coverage was not continuous.

5.3.7 Magnetic force microscopy imaging of nanoparticle-coated filaments

Although previous AFM results showed structures on filaments that resemble nanoparticles, it was not fully confirmed, if the structures are really nanoparticles. To confirm that observed structures are nanoparticles, MFM was used to image magnetic nanoparticle (phase-transferred using protocol 3) conjugated to thiolated filaments and to establish differences between nanoparticle-covered filaments and non-metallised regions. MFM was firstly tested by scanning areas on 3-inch floppy disk and a 20 GB hard disk. They showed defined regions of oppositely magnetised areas which were independent of surface features.

MFM images produced by scanning metallised filament samples were somewhat different from magnetic media references. While reference samples exhibit high lateral contrast changes independent of surface profile, nanoparticle and filament sample magnetic maps tend to strictly follow topographic surface features and show an AFM-like phase image component (indicated by arrows in figure 5.15). At lower scanning distances from surface, the MFM image resembles more a AFM phase image than MFM image. Therefore, it appears that surface forces still have an influence on MFM phase image even when scanning 10 nm - 30 nm above the sample surface.

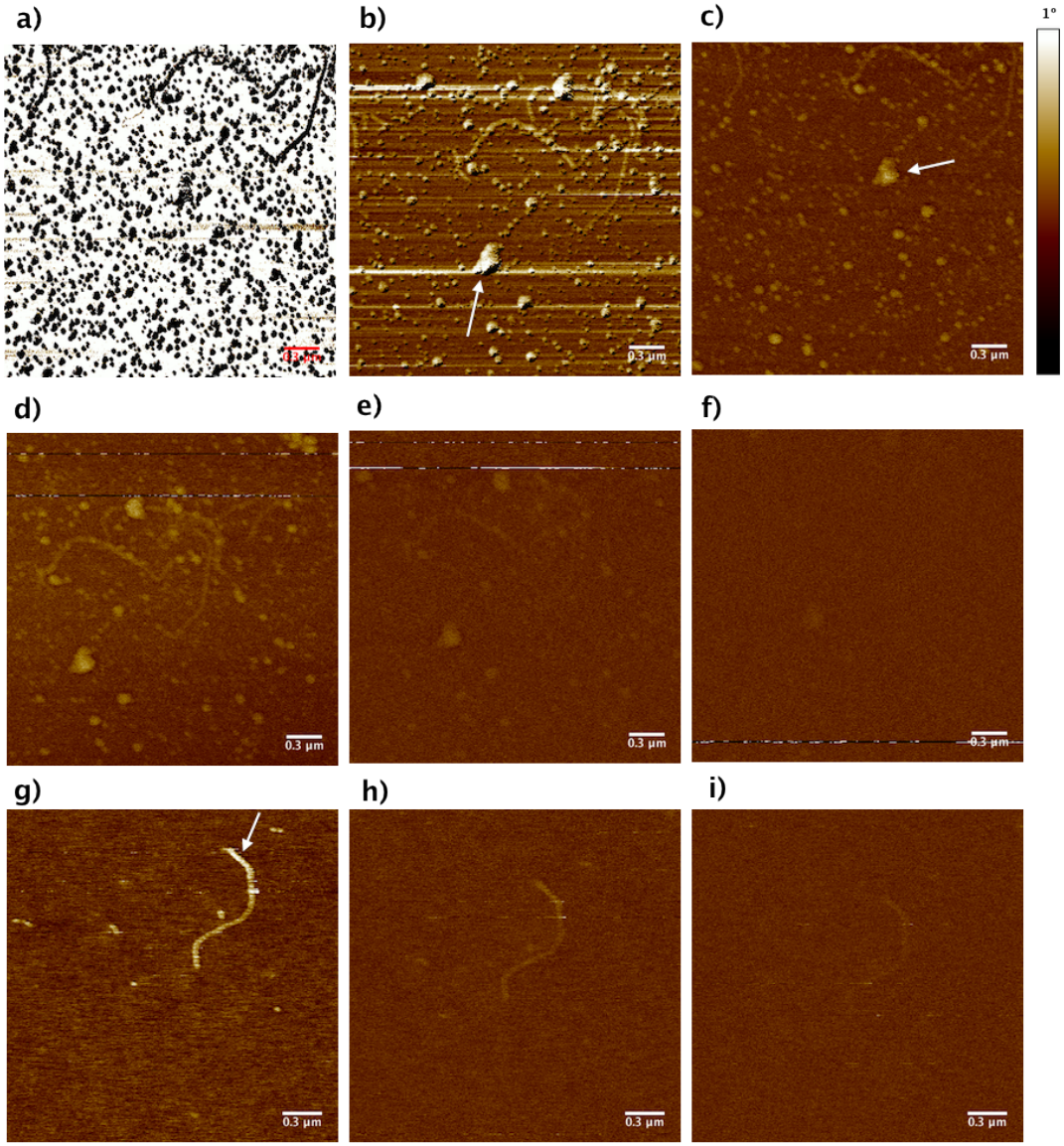

Figure 5.15: a) - f) MFM images of thiolated nucleoprotein filaments and magnetic nanoparticles formed by detecting tip vibrational phase change. g) - i) MFM phase images for nucleoprotein filaments. Phase images formed by scanning at a) 10 nm, b) 15 nm, c) 20 nm, d) 30 nm, e) 50 nm, f) 100 nm, g) 10 nm, h) 20 nm, i) 30 nm distance from surface.

This AFM phase component seems to decrease in strength with increase of scan-

ning distance from the surface, however it raises the question if the real magnetic map component is actually a true imaged magnetic moment map or a leftover distant interaction with the surface. Especially, as the control sample with filaments without any nanoparticles produced the same trend - a AFM phase image component with decreasing strength at larger scanning height distances and the same MFM component fading at higher distances (figure 5.15). And although the filament sample MFM image fades out at considerably lower surface distances (30 nm) than for thiolated filament and nanoparticle sample (100 nm), the fact that images exhibit the same features cannot be ignored.

Furthermore, control experiments with same type of magnetic tip, which was not magnetised prior to scanning, showed contradictory results (figure 5.16). Although only a contour of a filament for a 'filament-only' sample showed at 5 nm scan height, clear images for 'thiolated filament and nanoparticles' samples were formed with the same feature visibility, irrespective of scanning height (10 nm - 50 nm). This was not expected, as non-magnetised tip should not produce any magnetic map features.

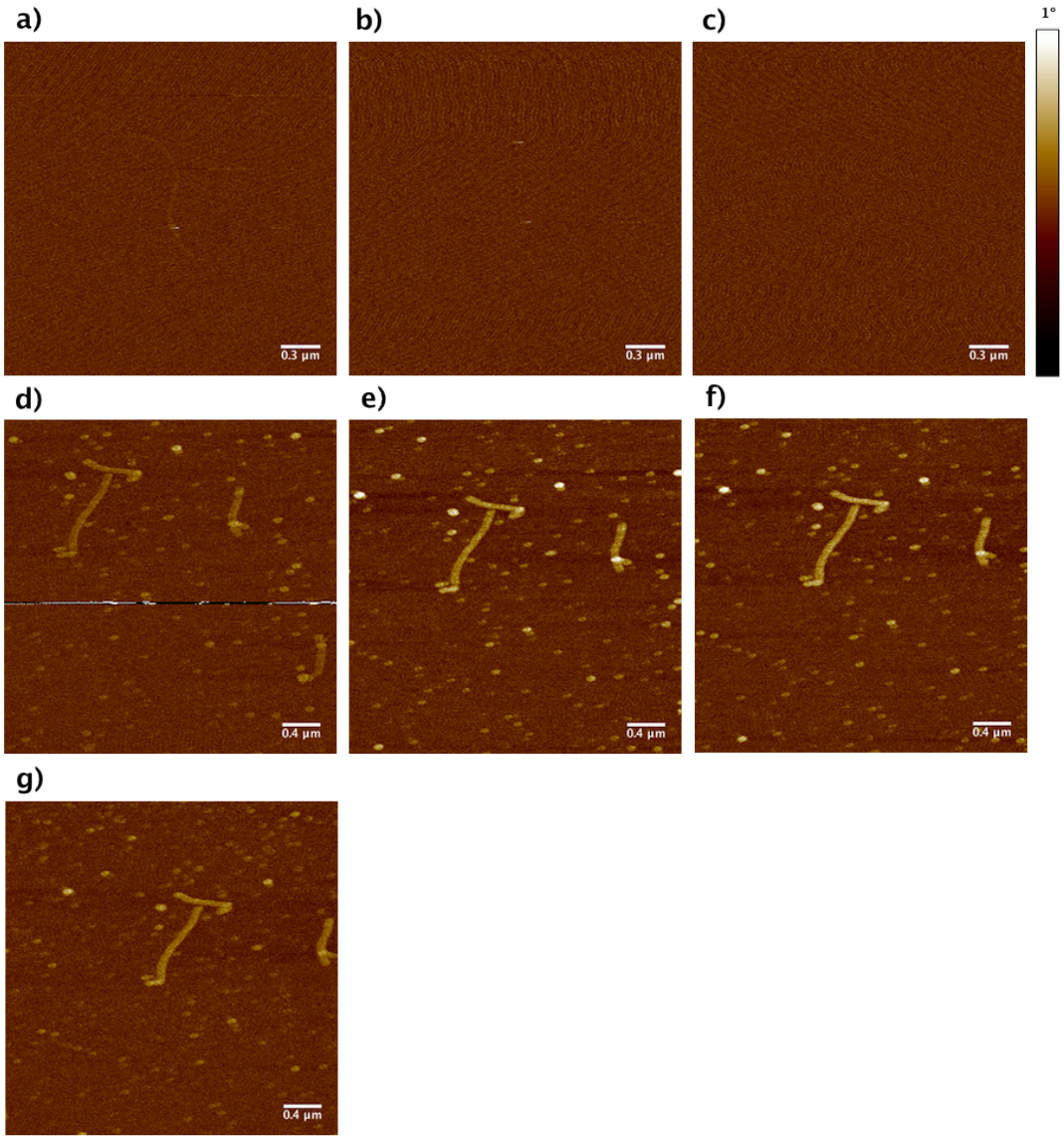

Figure 5.16: MFM phase images formed using a non-magnetised tip on a) - c) filament, d) - g) thiolated filament and magnetic nanoparticle samples. Images formed by scanning at a) 5 nm, b) 10 nm, c) 20 nm, d) 10 nm, e) 20 nm, f) 30 nm and g) 50 nm distance from surface.

To quantify the magnetic component's influence on phase change from the magnetic nanoaprticles, the magnetic nanoparticles phase change was compared to that of non-magnetic Au nanoparticles phase change at different distances from the surface. Both

types of nanoparticles were deposited on mica surface on separate samples and scanned in interleave mode with a magnetic tip. The resulting data showed no difference between magnetic and non-magnetic nanoparticles in phase change (Figure 5.17). Both samples retain same profile of phase difference decay over height. Both samples also display 1°of phase difference from the background at 10 nm distance from the surface scan height, but with a scan height of 30 nm, the phase difference becomes smaller than 0.2 °. This rapid decay in phase is comparable to the previous experiment of MFM imaging of filaments coated with magnetic nanoparticles and suggests that no magnetic properties can be observed of these magnetic NPs.

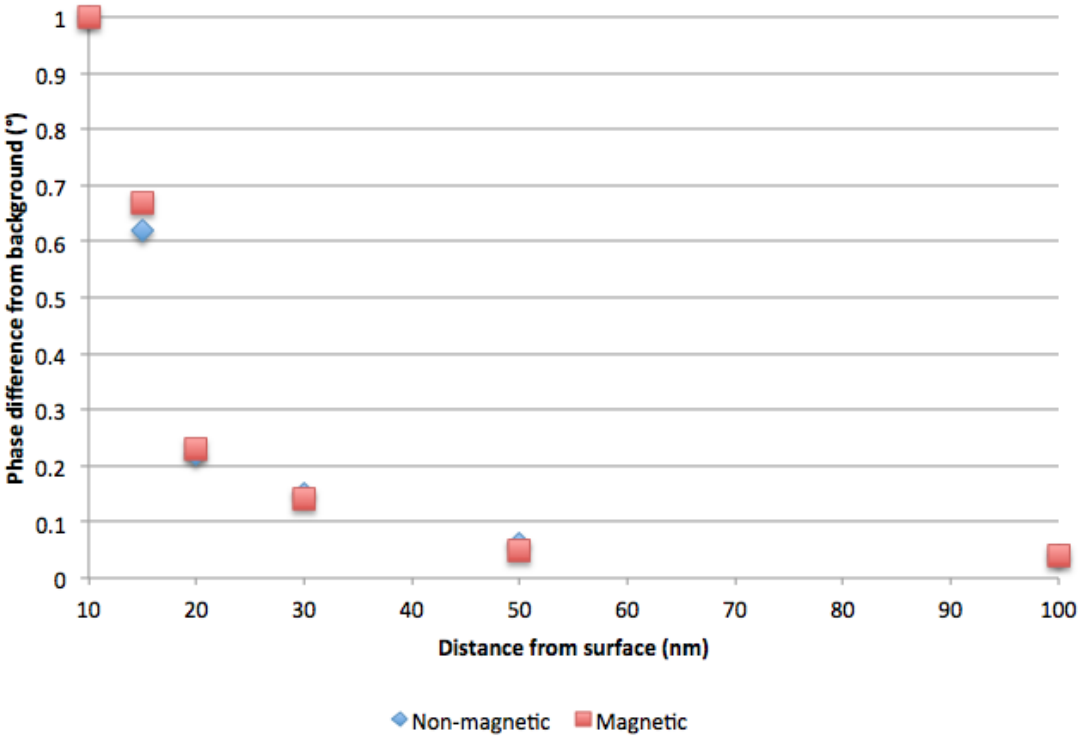

Figure 5.17: Phase change of 12nm Au (non-magnetic) NPs and magnetic NPs from background level when scanned under MFM with different distances from the surface.

Even though MFM worked for reference samples, attempt to investigate properties of magnetic nanoparticles was not successful. This might be due to several reasons - lateral feature size of nanoparticles smaller than MFM tip resolution, magnetic moments

in the nanoparticles being too small or thermal energy constantly switching magnetic moment direction - all of which are likely. Furthermore, it is not clear either whether the magnetic tip properties did not have an influence on the results. MFM was performed in tapping mode with a flexible (spring constant of 2.8 N/m) magnetic tip. It is not clear, at what amplitude the tip flexed, but if it was significantly larger than the distance from the surface at which MFM was performed, the tip would still interact with the sample surface forming an AFM phase image which was observed.

5.3.8 Fully coated nanowire formation using protocol 2

While constantly preparing new stock solutions of aqueous magnetic nanoparticles using the original protocol, it was noticed that older stocks when precipitating produce a gradient from transparent liquid at the top to full black solution at the bottom. It was decided to collect the non-precipitated particles (they are named protocol 2 nanoparticles). The collected particles had a greyish pink colour, indicating smaller particle size. Use of these nanoparticles in most of the cases yielded similar results to previous (data not included). However, in two attempts it was possible to achieve full nanoparticle coverage on thiolated filaments with relatively small background. Nanoparticles were not arranged in a straight, bead necklace-like fashion, but rather as a shell around a straight cylindrical core object. The granularity and specific arrangement highly suggests a nanowire formation. To fully confirm that, more extensive characterisation is needed. The coverage was full, except for regions, which were not polymerised by RecA (indicated by white arrows in figure 5.18) and subsequently, did not conjugate to nanoparticles. Nanoparticle lateral diameter was 10 nm - 35 nm.

Although these were the best nanowires formed and possess high enough integrity for measuring electrical conductivity and other properties, repeating the results was challenging. Various modifications (incubation times and concentrations for SATA, $NH_2OH \cdot HCl$ and nanoparticles) to the protocol were made to investigate if any of them might influence nanowire formation. However, no filaments with similar level of nanoparticle coverage were observed. The replication of successful nanowire is still to be investigated in the future work.

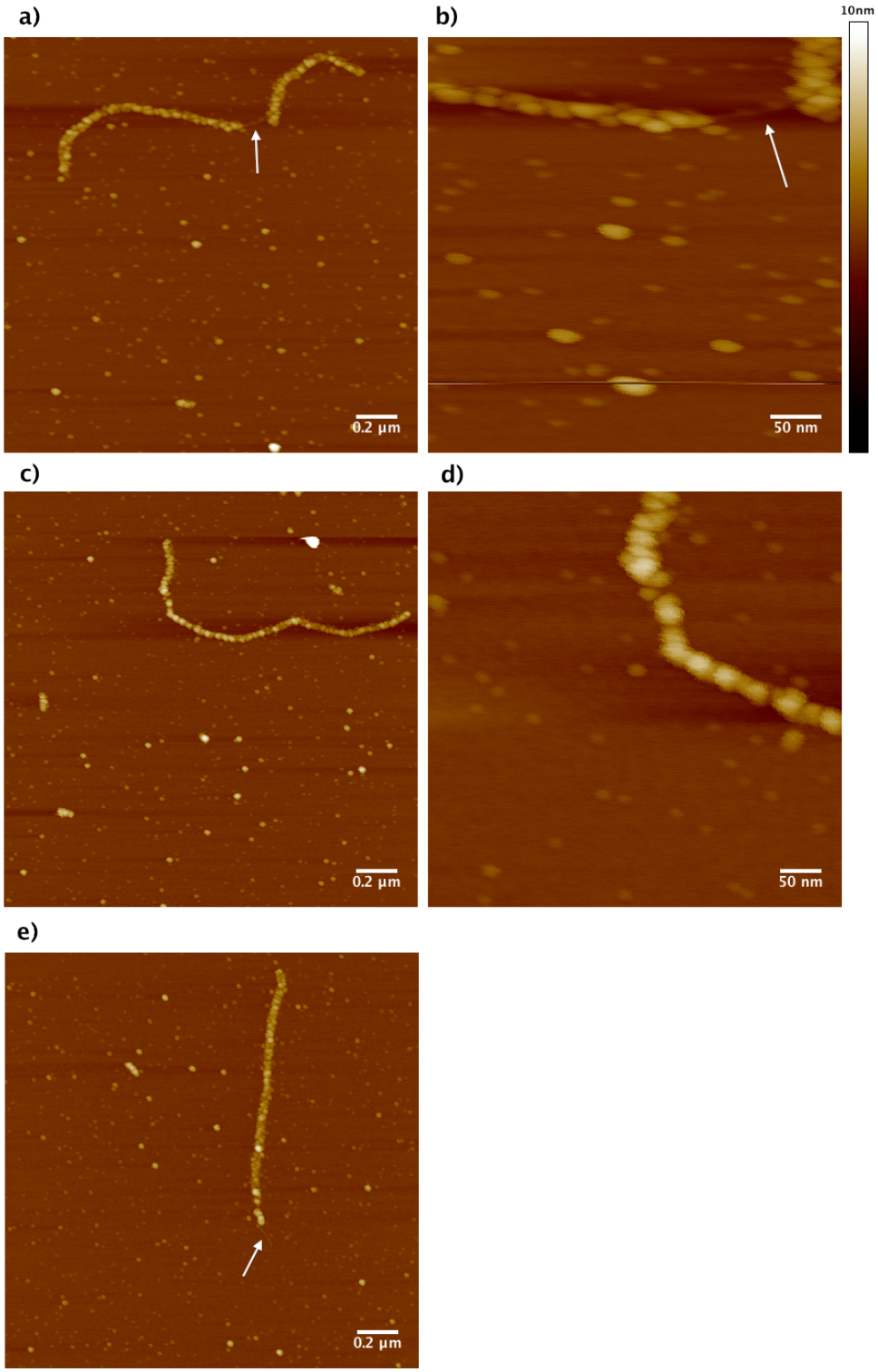

Figure 5.18: Thiolated nucleoprotein filaments fully metallised by magnetic nanoparticles purified using protocol 4. White arrows indicate bare DNA.

5.4 Filament purification

Protein spin desalting columns (PDSC) were selected to test purification of both monomeric modified RecA and thiolated nucleoprotein filaments. Although the columns are suited for globular proteins of 15 kDa or higher, nucleoprotein filaments being much larger (40 MDa) and having a stretched structure might still be purified using PDSC since the working principle of it is to retard the motion of the small molecules (ions, small organic molecules, inorganic compounds) and allow fast flow of large biomolecules. To test PDSC yield, bovine serum albumin (BSA) protein was used. The sample was added to the top of PDSC and spun. The eluted sample was collected and subjected to PDSC once again. Collected sample's 280 nm absorbance was measured using the spectrophotometer after the first and second elution. The decrease in absorption indicates loss of the protein and hence the yield of PDSC.

After the first purification step, 70% of the protein was retained. After the second purification step, 30% of protein was left, signifying large protein loss. However, this is yield specific to BSA and nucleoprotein filament complexes will have different and most likely larger yield, since they are larger molecules.

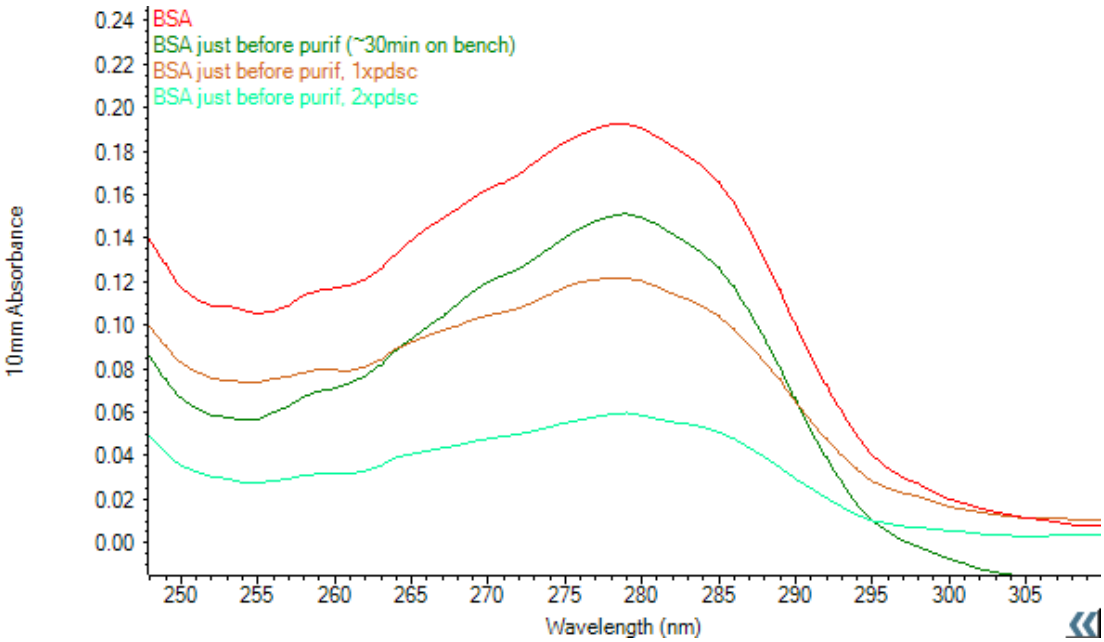

Figure 5.19: BSA purification

Afterwards, protein spin desalting columns were tested directly on RecA proteins, which were reacted with another thiolation reagent, 2-iminothiolane (2-IT). Three different samples (RecA, RecA reacted with 100x excess of 2-IT (RecA + 2-IT) and same concentration 2-IT (2-IT-only)) were purified twice with PDSCs and exposed to 4,4?-Dithiodipyridine (DTDP). DTDP is a thiol quantifying reagent, similar to DTNB and producing an absorption peak ant 324 nm after reaction with thiols. The samples' spectra were collected with a spectrophotometer (Figure 5.20) and compared.

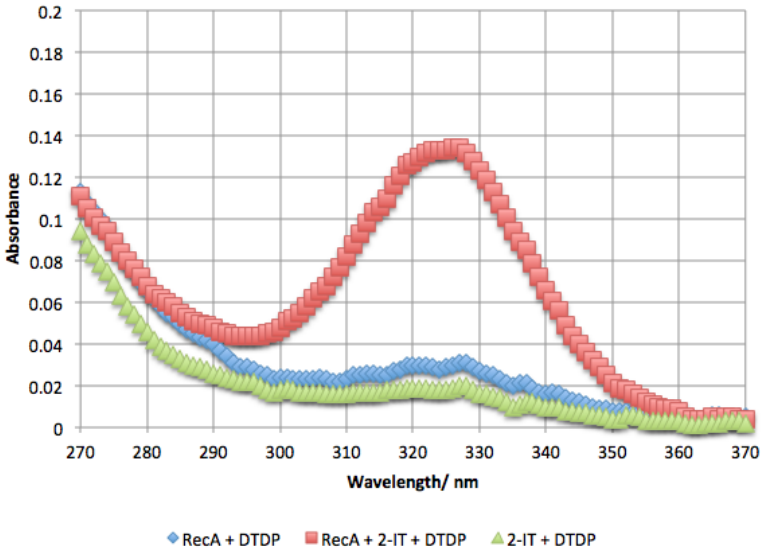

Figure 5.20: PDSC purification efficiency for RecA against unreacted 2-IT.

The resulting spectra revealed an absorption peak at 324 nm, indicating thiol presence for the RecA + 2-IT sample, but no significant absorption for the RecA sample or 2-IT-only sample (the ratio of absorbances of RecA + 2-IT sample to RecA or 2-IT sample was higher than 4). This indicates successful purification of RecA samples from excess 2-IT and successful reaction of 2-IT with RecA. From that point, both RecA and filaments were purified with PDSCs. The successful RecA thiolation with 2-IT was followed with attempts at 2-IT-modifiefd filament metallisation.

5.5 2-IT

With no full metallisation of RecA nucleoprotein filament with SATA, thiolation with 2-IT was investigated. Firstly, filaments were exposed to 100x excess (2-IT:RecA ratio) of 2-IT for 1 h and imaged under AFM. Filament integrity did not suffer from exposure to 2-IT (figure 5.21).

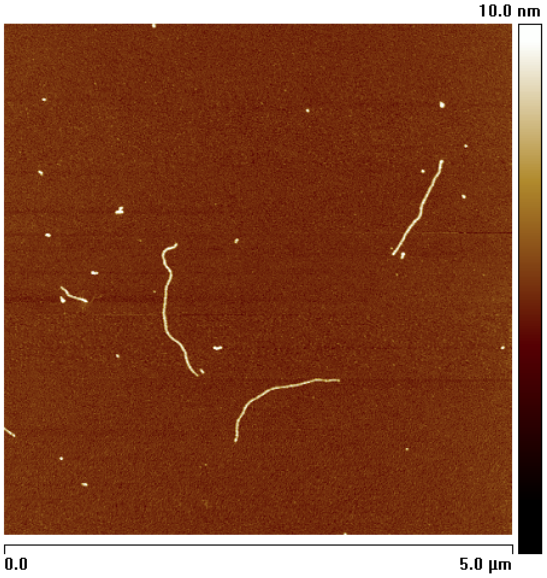

Figure 5.21: Filaments after modifications with 2-IT

Afterwards, filaments subjected to 100x excess 2-IT and purified with PDSCs twice were exposed to 26 nm NPs. The samples were deposited on mica surface and imaged with an AFM. Relatively large structures were observed (figures 5.22 and 5.23). The background was clear with no NPs or other artefacts. The large structures observed seemed to be composed of clustered NPs since the NP diameter was roughly consistent with 26 nm. The height of the structures was above 100 nm and lateral extent ranged in μms. Some linearity in the structures was observed, but no decisive evidence for proving that it was templated by the filaments was found.

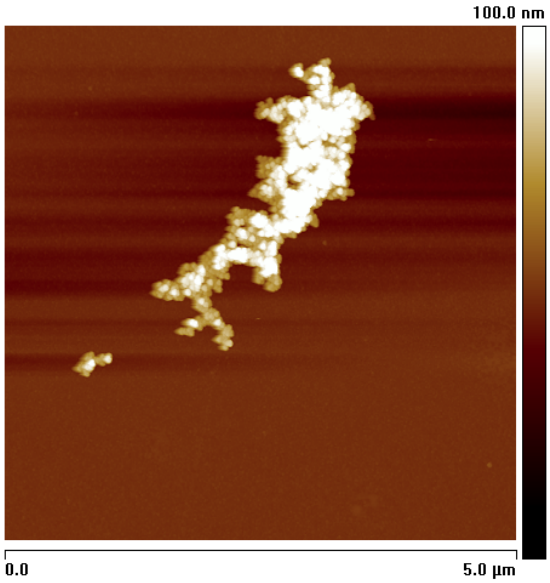

Figure 5.22: Filaments after modification with 2-IT and exposure to 26nm NPs

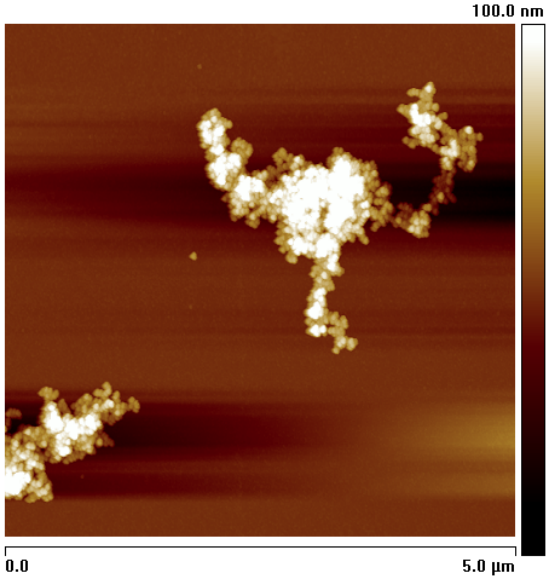

Figure 5.23: Filaments after modification with 2-IT and exposure to 26nm NPs (2)

After several repeats, same μm-sized agglomerated NPs were observed. However, certain samples showed partially non-metallised filaments that were present only between the clusters of agglomerated NPs and not anywhere else on the surface (Figures

5.24 and 5.25). This suggests that filaments template cluster formation, even though because of large agglomeration no linear features are observed.

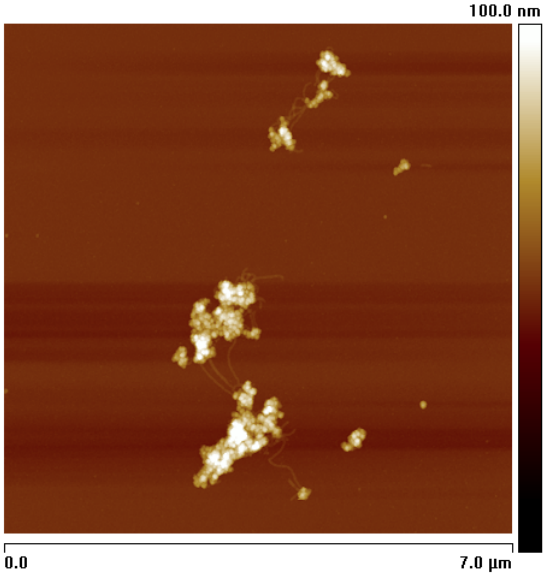

Figure 5.24: Filaments after modification with 2-IT and exposure to 26 nm NPs, demonstrating filament templating.

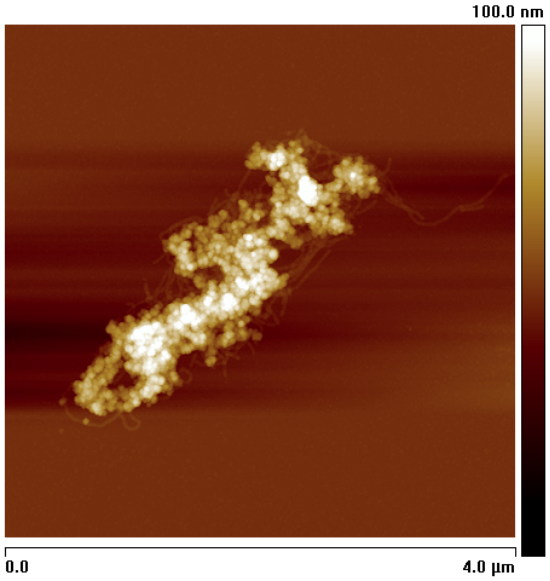

Figure 5.25: Filaments after modification with 2-IT and exposure to 26 nm NPs, demonstrating filament templating (2).

5.5.1 Filament metallisation using 2-IT on surface

An alternative method of thiolating and metallising filaments was investigated. Instead of performing thiolation and metallisation in solution, both steps were done after depositing the filaments on the surface. This surface metallisation method avoids the need for purification steps.

Formed filaments were deposited on mica surface and washed throughly with water. After that, they were exposed to 100x excess of 2-IT for 1 h and washed again. Finally, they were exposed to 12nm Au NPs and washed once more. Such method demonstrated to be a viable alternative to solution-based metallisation, since it did not cause any NP agglomeration, yet ensured thorough filament coverage. However, high background of NPs was also present, possibly indicating surface thiolation by 2-IT.

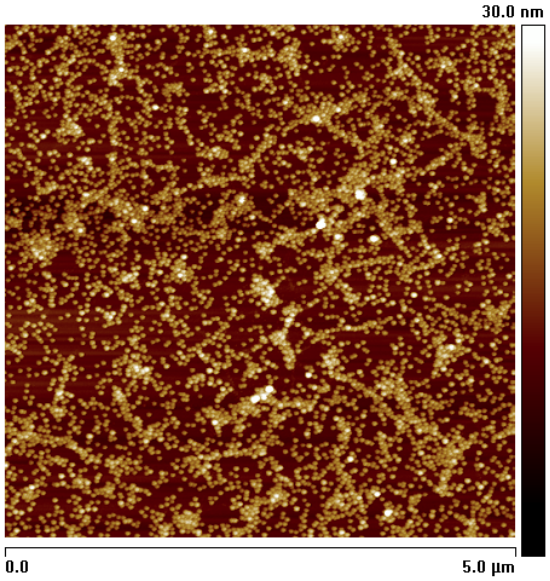

Figure 5.26: Filaments after deposition on the surface and subsequent modification with 2-IT and exposure to 12 nm NPs.

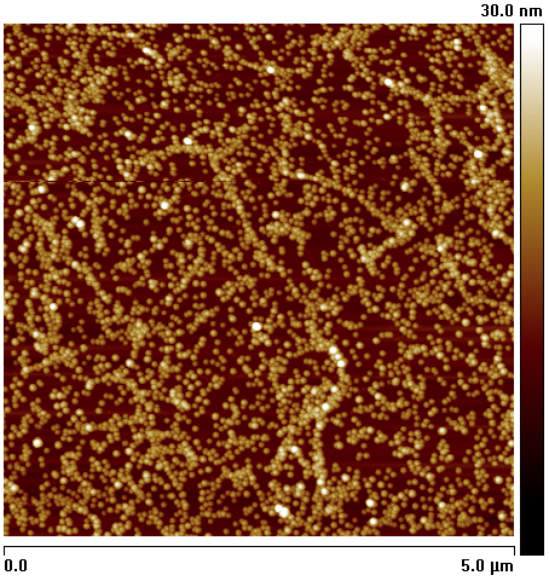

Figure 5.27: Filaments after deposition on the surface and subsequent modification with 2-IT and exposure to 12 nm NPs (2).

Surface metallisation method proved promising, yet the amount of background NPs was unsuitable for any further experimentation. To investigate 2-IT influence on mica surface, a control experiment with no filaments was performed. A clean mica surface was exposed to 100x excess equivalent of 2-IT for 1 h, washed and exposed to 12nm Au NPs as before. The resulting samples were investigated by AFM (Figure 5.28). The data showed excessive surface coverage by deposited nanoparticles. This indicates probable 2-IT reaction with the mica surface silicate. For any further filament metallisation on surface with 2-IT experiments, mica should be replaced with a different material.

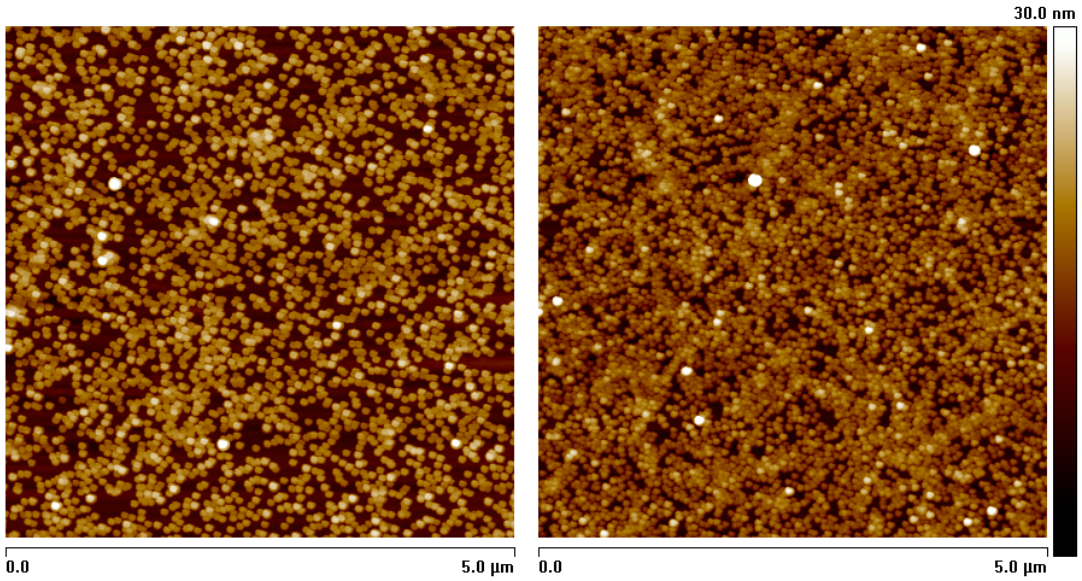

Figure 5.28: 12nm Au NPs deposited onto 2-IT-treated mica surface.

5.6 SPDP

Finally, as an alternative to 2-IT, SPDP was also investigated as a thiolating reagent for RecA-based filaments. Filaments were exposed to 100x excess of SPDP and purified with PDSCs twice followed by exposure to 12nm NPs. Afterwards, they were imaged with an AFM. Both filaments and single monomeric NPs were seen on the surface. However, the NP distribution on the surface was random and did not appear to exhibit any affinity towards the filaments. Furthermore, the results were indistinguishable from a control sample, where no SPDP was used for filament treatment.

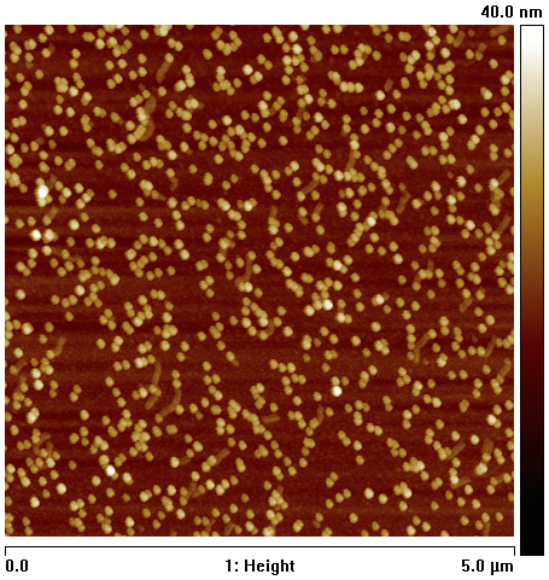

Figure 5.29: Filaments with no SPDP modification and exposure to 12 nm NPs (control sample)

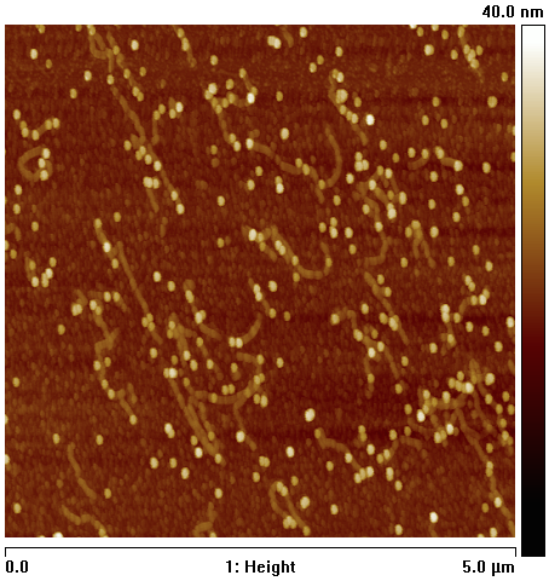

Figure 5.30: Filaments after modification with SPDP and exposure to 12 nm NPs

5.7 Conclusion

With three different thiolating reagents for lysines investigated, only 2-IT seemed to be relatively promising. Unfortunately, no protocol for reproducible nucleoprotein filament thiolation was developed. Metallisation performed on the mica surface seemed to work, but it is not very useful due to large nanoparticle deposition on the background and specific conditions of the mica surface which might not transfer to other, more important surfaces. Furthermore, even if a desirable protocol for metallisation on the surface was developed, by virtue of metallised filaments being on the surface, no post-metallisation modification can be done, e. g. through interaction with additional template DNA.

No certain reasons for difficulties in metallising thiolated filaments in the solution were found, but the suspected reason is large sensitivity of nanoparticles to solution conditions, such as the buffering agent and concentration of salts used.

Further work needs to be carried out before exact metallisation conditions can be found and successful and reproducible nucleoprotein filament metallisation can occur.

Chapter 6

Targeted single nanoparticle placement using patterning on DNA scaffold

6.1 Introduction

Having the ability to selectively metallise linear regions on a nanoscale framework is important, but not enough for any advanced applications. For features such as quantum devices or even simple transistors to be present on the RecA nucleoprotein filament - DNA template system, ability to place single NPs at well-defined positions is required. A simple way of achieving that is bioconjugating NPs to a template DNA framework with single, well determined thiol groups: if the thiol is present at a particular location of interest for binding the NP, it can accommodate only one NP, resulting in specific NP placement. Up until now, the strategy of introducing thiols was specific only to RecA nucleoprotein filament's outer surface. It does not target a specific location to nanometre or sub-nanometre scale and the statistical distribution of thiols per RecA monomer does not guarantee a single NP binding per thiol. To address this issue, a different approach of attaching NPs was investigated. The method in question still utilises RecA nucleoprotein filaments and thiol-gold chemistry, but instead of modifying lysines on RecA surface, it introduces single thiols at specific locations. To achieve that, ssDNA with a terminal thiol group is used to form a nucleoprotein filament. This filament, having a single thiol, can now bind to a gold NP. It can also be used to

pattern a dsDNA template. Combining both of the filament features leads to a specific NP placement.

There are two approaches for carrying out this technique. One is to firstly attach NPs to thiolated oligos, form nucleoprotein filaments on these oligos and then perform patterning with these bioconjugates on template DNA (named method A). The second one is to firstly perform the patterning of template DNA with the filament and then attach the NP (named method B).

Nucleoprotein patterning refers to the triple-stranded complex stabilised by RecA filament formation. It is produced by firstly forming a RecA filament on a ssDNA. The selected ssDNA must have a sequence that is complementary to one of the strands in a region on a equal length or longer dsDNA (called 'template'). To form a filament-patterned DNA, firstly a RecA filament is formed on the ssDNA using ATPγS as a non-hydrolysable cofactor for stability reasons. Secondly, the formed filament is mixed with template dsDNA and incubated at 37°C for 45 min. This allows RecA to perform the homology search between filament ssDNA and template dsDNA resulting in filament binding on template dsDNA in the right position [56].

DNA patterning can be verified by two methods – AFM imaging and restriction enzyme assay. In AFM imaging, after DNA patterning is performed, the sample is deposited on a mica surface and imaged with the AFM conventionally. Any patterned regions on dsDNA template will appear as heightened features at the expected position on the template DNA.

6.1.1 Restriction enzyme assay

The restriction enzyme assay is also used in this chapter to evaluate DNA patterning. Restriction enzyme assays are a common tool to measure activity of selected restriction enzymes [133].

Restriction enzymes (or endonucleases) are a class of enzymes that cut dsDNA at specific positions, known as 'recognition sites' or 'recognition sequences'. Naturally, bacteria and archaea use restriction enzymes as a defence mechanism against invading viruses by selectively cutting viral DNA preventing it from expression [133]. Host DNA remains unaffected by restriction enzyme because it is methylated by a methylation enzyme [133]. There are hundreds of different restriction enzymes, all of which have their own specific recognition site.

In this project, restriction enzymes are used as dsDNA patterning validation tool. When bare template dsDNA is mixed with a certain restriction enzyme that has enzyme's recognition site present in at least one position on template dsDNA, the enzyme will bind to the recognition site and cut (or 'cleave', 'digest') the template dsDNA at that position. If, however, a triple-stranded RecA complex is present on the restriction site, the restriction enzyme will not be able to fully displace the bound RecA and cleavage will not occur. Since RecA patterning sequences are longer than restriction enzyme sites, it is possible to use RecA to protect one of multiple restriction sites on the same template DNA.

As an example, consider a 130 bp dsDNA that has two recognition sites (GAATTC) of a common restriction enzyme *Eco*RI (Figure6.1). One of the restriction sites ('site 1') is 14 bp away from one of the DNA terminal ends, and the other one ('site 2') is 21 bp away from the opposite DNA terminus. If *Eco*RI is brought into proximity of the DNA, it will bind and cleave both of the restriction sites, resulting in 14 bp, 21 bp and 95 bp length DNA fragments. But if patterning is performed on any of those two sites with an appropriate RecA filament, the filament will protect the template DNA from digestion. If site 1 is patterned, only site 2 will be subject to cutting, resulting in DNA fragments of 109 bp and 21 bp lengths. If site 2 is patterned, only site 1 will be subject to digestion, leaving 14 bp and 116 bp length fragments. As a consequence, the resulting fragments after patterned or unpatterned DNA sample incubation with a restriction enzyme will yield different length dsDNA fragments.

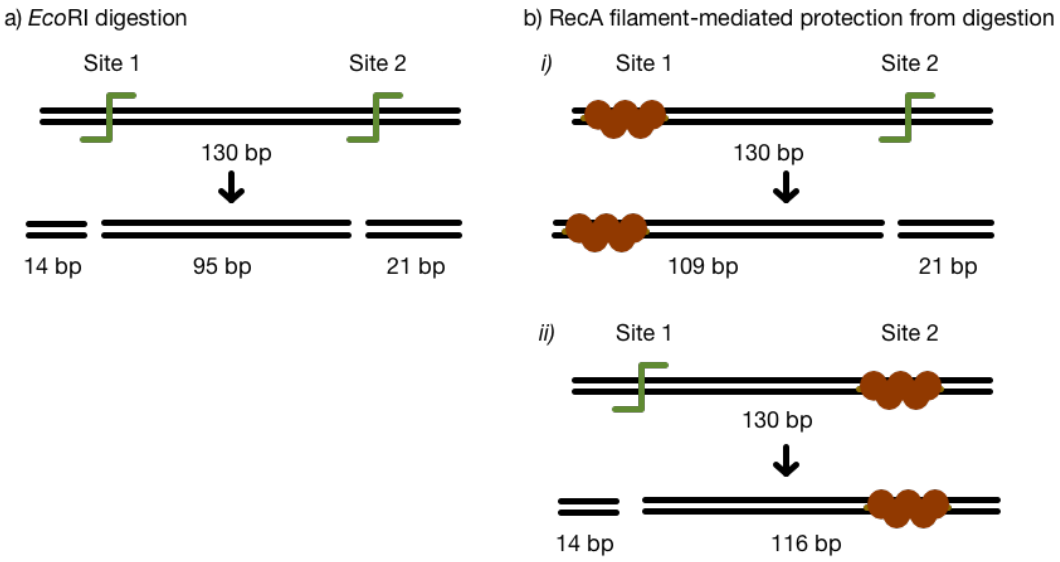

Figure 6.1: A schematic showing how restriction enzyme assay with *Eco*RI on 130bp dsDNA works. a) Two recognition sites on 130bp dsDNA are present and the restriction enzyme can cleave the DNA into 14 bp, 95 bp, and 21 bp fragments unhindered. b) i) RecA filament is bound onto dsDNA, fully covering site 1 and preventing *Eco*RI from digesting at that site. This results in dsDNA cleaved only at site 2 and 109 bp and 21 bp generated fragments. ii) RecA filament binds dsDNA on site 2, preventing digestion at that position and generating 14 bp and 116 bp long fragments.

The digestion can be stopped by introducing proteinase K (proK) - an enzyme that cleaves peptide bonds and eliminates any other proteins present, in this case RecA and *Eco*RI, stopping any further DNA fragment manipulation. Finally, the samples can be run on a polyacrylamide gel, which separates DNA by its length, allowing one to visualise and quantify the presence of various DNA fragments and deduce filament patterning efficiency.

6.1.2 Types of gels in electrophoresis

The types of gel most typically used are agarose and polyacrylamide gels. Each type of gel is well-suited to different types and sizes of analyte. Polyacrylamide gels are usually used for proteins, and have very high resolving power for small fragments of

DNA (5-500 bp). Agarose gels on the other hand have lower resolving power for DNA but have greater range of separation, and are therefore used for DNA fragments of usually 50 bp - 20 kbp in size. Polyacrylamide gels are run in a vertical configuration while agarose gels are typically run horizontally in a submarine mode. They also differ in their casting methodology, as agarose sets thermally, while polyacrylamide forms in a chemical polymerisation reaction.

Agarose gels are made from the natural polysaccharide polymers extracted from seaweed. Agarose gels are easily cast and handled compared to other matrices, because the gel setting is a physical rather than chemical change. Agarose gels do not have a uniform pore size, but are optimal for electrophoresis of proteins that are larger than 200 kDa. Agarose gel electrophoresis can also be used for the separation of DNA fragments ranging from 50 base pair to several megabases (millions of bases), the largest of which require specialised apparatus. The distance between DNA bands of different lengths is influenced by the percent agarose in the gel, with higher percentages requiring longer run times, sometimes days. Instead high percentage agarose gels should be run with a pulsed field electrophoresis (PFE), or field inversion electrophoresis. Most agarose gels are made with between 0.7% (good separation or resolution of large 5?10kb DNA fragments) and 2% (good resolution for small 0.2?1kb fragments) agarose dissolved in electrophoresis buffer. Up to 3% can be used for separating very tiny fragments but a vertical polyacrylamide gel is more appropriate in this case. Low percentage gels are very weak and may break when you try to lift them. High percentage gels are often brittle and do not set evenly.

Polyacrylamide gel electrophoresis (PAGE) is used for separating proteins ranging in size from 5 to 2,000 kDa due to the uniform pore size provided by the polyacrylamide gel. Pore size is controlled by modulating the concentrations of acrylamide and bis-acrylamide powder used in creating a gel. Care must be used when creating this type of gel, as acrylamide is a potent neurotoxin in its liquid and powdered forms. Typically resolving gels are made in 6%, 8%, 10%, 12% or 15%. Stacking gel (5%) is poured on top of the resolving gel and a gel comb (which forms the wells and defines the lanes where proteins, sample buffer and ladders will be placed) is inserted. The percentage chosen depends on the size of the protein that one wishes to identify or probe in the sample. The smaller the known weight, the higher the percentage that should be used.

Changes on the buffer system of the gel can help to further resolve proteins of very small sizes.

6.1.3 RNAstructure for DNA secondary structure analysis

For determining DNA secondary structure for oligonucleotides used, a program called "bifold" from a software set "RNAstructure" available as a web service was used [134]. The software was designed to be used for determining long complex RNA strand structures and parameters, however it is also suitable for ssDNA structure determination [135] [136]. "bifold" specifically predicts the lowest free energy structures containing two or one strands and is aware of intramolecular pairs. The algorithm for structure determination was derived from thermodynamical principles and developed over time. It uses comparative analysis, nearest neighbour rules and results from experimental data as the basis [135] [137].

6.2 Results

6.2.1 Method A (NP to oligo conjugation, filament formation, patterning)

The first method investigated is method A, where thiolated oligos are to be attached to Au NPs, nucleoprotein filaments formed on the attached oligos and the formed complexes used for patterning template DNA. To achieve that, the first step is to attach ssDNA with the terminal thiol to NPs. This has been done many times using both dsDNA and ssDNA [138] [139] [140]. The supplied oligos are shipped with thiols capped with a protective group (the thiol is in a disulfide configuration). Although Au-NP bond can in some cases be formed from disulfide bonds, it is a good practice to deprotect the thiols before exposing them to Au NPs for greater reactivity and avoidance of protective group binding to Au NPs.

Three different 60b oligos were selected and incubated with 12 nm Au NPs. Their sequences were: oligo 1 - 5' - GGG GTT CCG CGC ACA TTT CCC CGA AAA GTG CCA CCT GAT GCG GTG TGA AAT ACC GCA CAG 3'; oligo 2 - 5' - CCT CGC TCA CTG ACT CGC TGC GCT CGG TCG TTC GGC TGC GGC GAG CGG TAT CAG CTC ACT - 3'; oligo 3 - 5' - CCA CTC GTG CAC CCA ACT GAT CTT CAG CAT CTT TTA CTT TCA CCA GCG TTT CTG GGT GAG - 3'. Their possible

secondary structures at room temperature are given in Figure 6.2. Oligo 1 seems to have a higher probability for forming hairpin structures than the other two oligos, but this was not determined prior to their use.

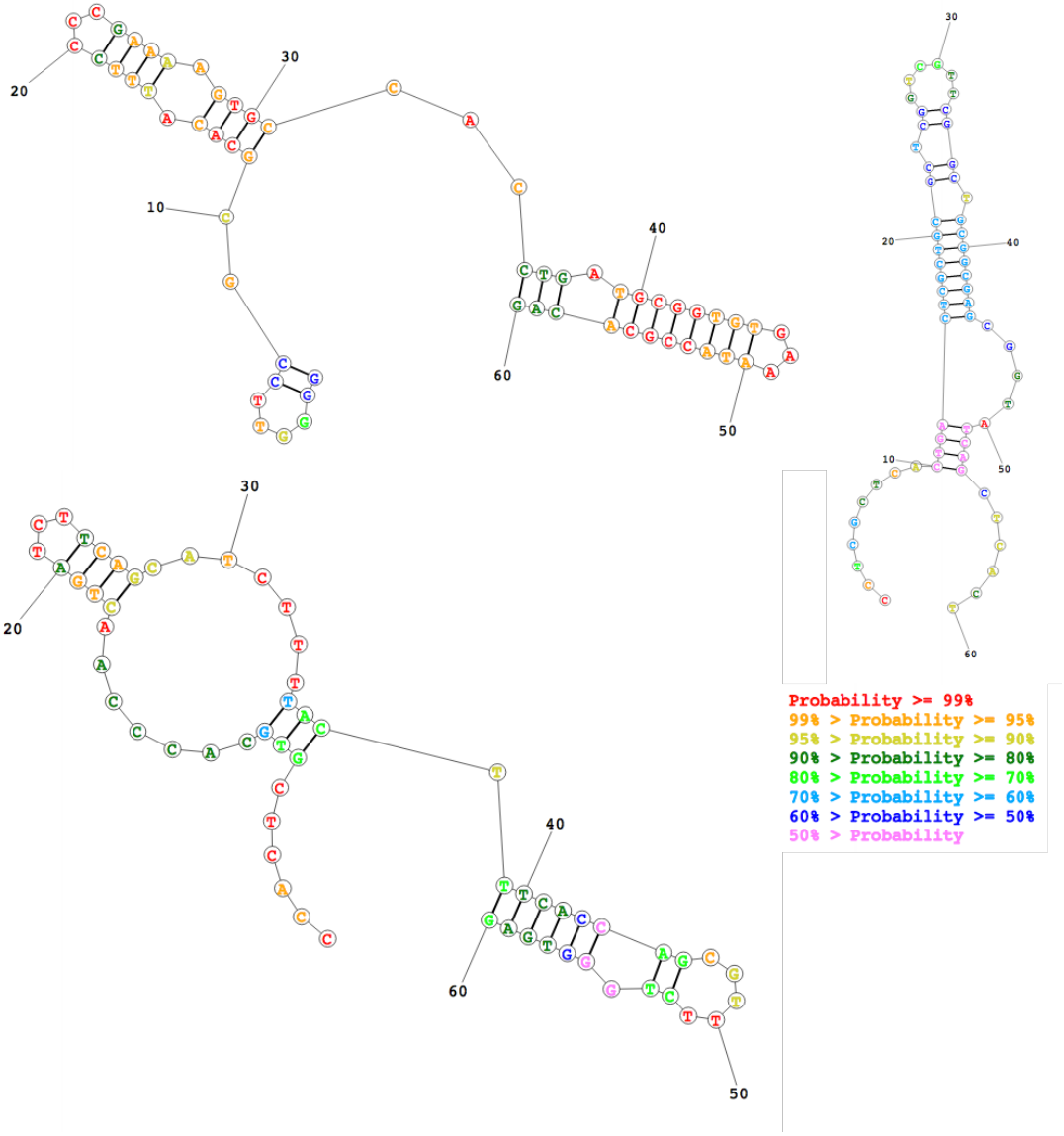

Figure 6.2: Three different oligo secondary structures formed at room temperature as determined with RNAstructure web server. Top left: oligo 1, top right: oligo 2, bottom left: oligo 3, bottom right: legend for the colours representing probability for the base being in the determined configuration.

When incubating with Au NPs, the oligos were either deprotected by exposing them to TCEP beforehand or not. Then then they were run on a gel and imaged (Figure 6.3).

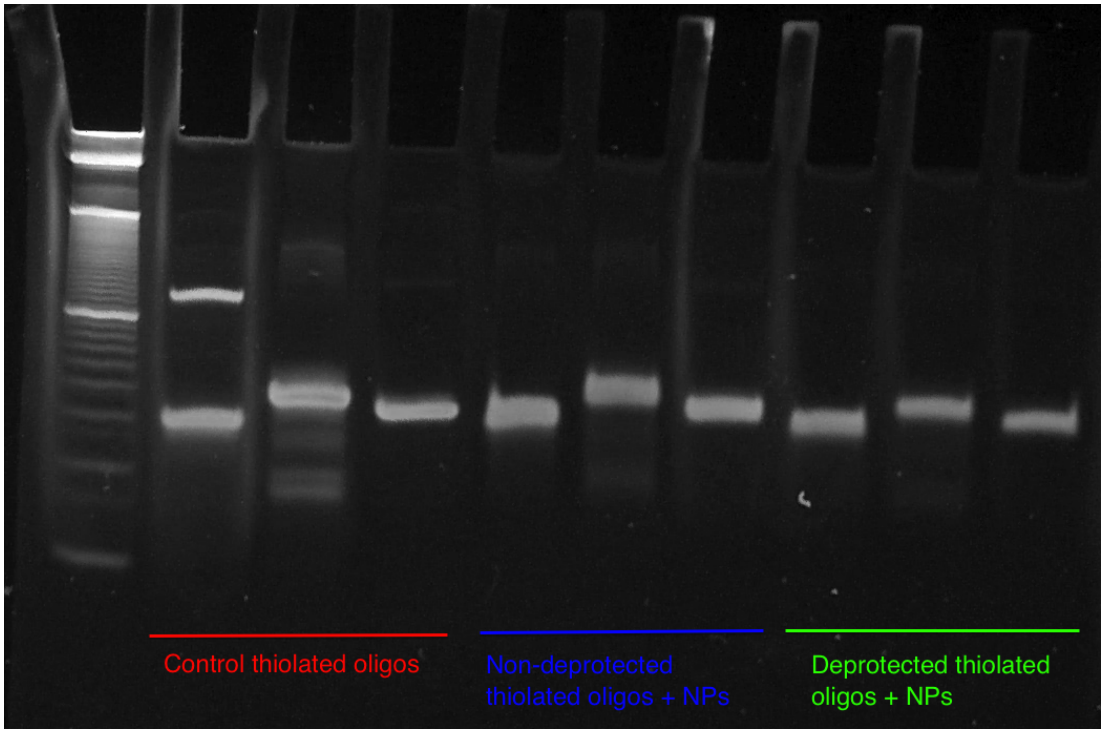

Figure 6.3: Thiol-terminated oligos after exposure to Au NPs (TCEP used for thiol deprotection). Lane 0 - 10 bp ladder; 1 - oligo 1; 2 - oligo 2; 3 - oligo 3; 4 - oligo 1+ NPs; 5 - oligo 2 + NPs; 6 - oligo 3 + NPs; 7 - oligo 1 + TCEP + Au NPs; 8 - oligo 2 + TCEP + Au NPs; 9 - oligo 3 + TCEP + Au NPs.

The first three lanes represent three different oligos run on the gel without any deprotection. Lanes 4 - 6 represent the same samples exposed to Au NPs without any deprotection as well. The last three lanes show the same samples exposed to TCEP and incubated with NPs afterwards.

As seen from the gel, each of three oligo bands are not in line with others, even though each oligo is 60b long. This is to be expected for ssDNA with varying sequences, since each unpaired base will interact with the running matrix to different degrees, depending on the base [139].

The bands, however, are consistently at the same heights for each of the same oligo sample, showing that neither length, shape or levels of interaction with the matrix has changed. As expected, there are no secondary bands for NP-bound oligos, since NPs are too large to enter polyacrylamide gel matrix.

Oligo 1 shows a relatively intense secondary band at higher molecular weights compared to the main band. Since the sample was treated exactly the same as all the other abundant secondary structures when run unmodified. This could be attributed to the higher possibility of hairpin structures for oligo 1, than other two oligos, as seen in Figure 6.2. Interestingly, this is not the case anymore when the same oligo is exposed to Au NPs. This could be explained by unfolding of a hairpin (or any other secondary) structure in the oligo after exposed nucleoside base interaction with the NPs ([139]).

The band intensity for oligos exposed to NPs and oligos exposed to both TCEP and NPs are similar for all three oligos. This is contrary to what is expected, since NPs should not be able to interact with NPs terminally through disulfides (or do that only to a small extent) resulting in the same intensity of the bands as control oligos, whereas TCEP-exposed oligos should be able to bind NPs tightly, resulting in fainter unconjugated oligo bands. The results suggest that either TCEP does not work as expected for reducing disulfides or gets consumed somehow else (for example, as adsorbant to NPs).

To investigate if TCEP is responsible for failed NP-oligo binding, it was replaced by DTT. A similar experiment was carried out where oligos were selectively exposed to DTT before reacting them with Au NPs. The resulting samples were run on a polyacrylamide gel (Figure 6.4) and an agarose gel (Figure 6.5).

It was observed, that the results of PAGE and agarose gels were quite different. Whereas nanoparticle conjugated to DNA did enter and move through the agarose gel, all of the red coloured sample, representing the nanoparticles. did not enter the polyacrylamide gel. This can be attributed to denser matrix in polyacrylamide gels, different running buffers and their influence on the nanoparticles. The following analysis of gels takes that into account and considers the lanes in PAGE gel lanes as containing only non-conjugated oligos, whereas agarose gels are considered to have DNA-NP conjugates.

Figure 6.5 shows clearly different results compared to previous attempt at deprotection with TCEP. Oligos exposed to DTT only do not run differently on the gel. Oligos

exposed to NPs only do have a reduced and somewhat less focused band. This is could be due to longer interaction with NPs through base-binding. However, exposure of oligos to NPs after DTT treatment heavily decrease the band intensity or fully eliminating it, signifying loss of oligos from the gel. This is a good indicator for oligo-NP conjugate formation.

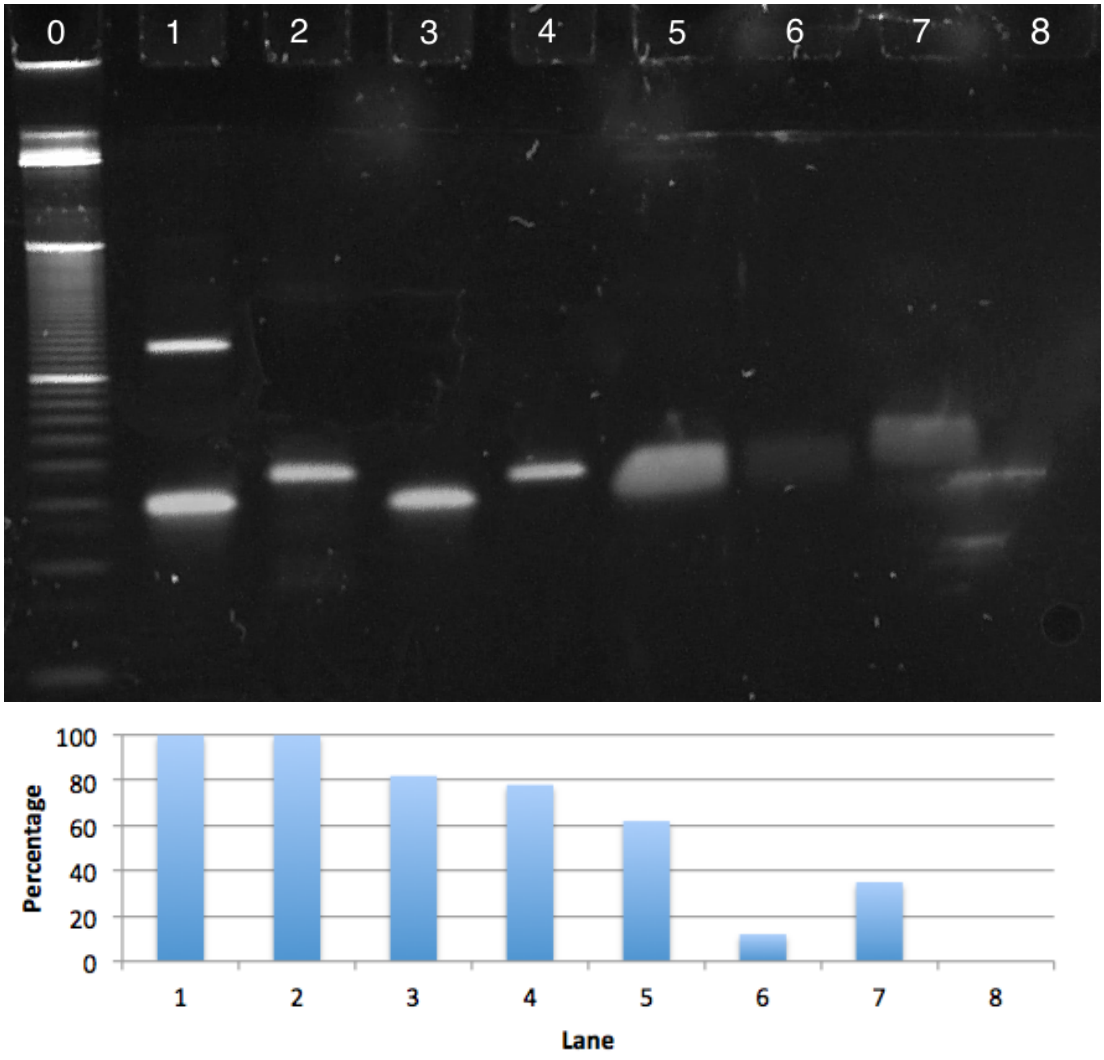

Figure 6.4: Top: thiol terminated oligos after exposure to Au NPs (DTT used for thiol deprotection). Lane 0 - 10 bp ladder, 1 - oligo 1; 2 - oligo 2; 3 - oligo 1 + DTT; 4 - oligo 2 + DTT; 5 - oligo 1 + NPs; 6 - oligo 1 + DTT + NPs; 7 - oligo 2 + NPs; 8 - oligo 2 + DTT + NPs. Bottom: normalised intensities for each oligo.

To see if this tentative NP-oligo conjugate formation affects NP mobility due to increased complex weight, similar samples were run on an agarose gel (Figure 6.5). Unmodified NPs did not migrate into the agarose gel and ended up diffusing from the loading well to the surrounding gel walls. NPs with unmodified oligos (either oligo 1 or 2) migrated into the gel and comparatively further than NPs with oligos 1 and 2, which were exposed to DTT prior to NPs. If DTT properly deprotects thiol groups and the oligos subsequently bind to NPs, the extra added negative charge from oligos to NPs would allow NPs to migrate to the gel, as seen in the results. However, the extra distance travelled for samples which were not deprotected prior to exposure to NPs indicate possibly a stronger binding effect of oligos to NPs. This is plausible, considering that oligos could be wrapping tightly around the NPs because of nucleoside base interaction with gold surface, adding considerable amount of negative charge to the nanoparticle due to oligo negative backbone. The deprotected oligos could be interacting through terminal thiols as well. Since terminal thiol interaction requires somewhat right angle of oligo to NP surface, this might considerably reduce the amount of free bases available to bind to NP surface but retaining the steric hindrance for additional oligo binding. This hypothesis can explain, why thiol-bound oligo-NP conjugates travel shorter distances than base-only-binding oligo-NP conjugates.

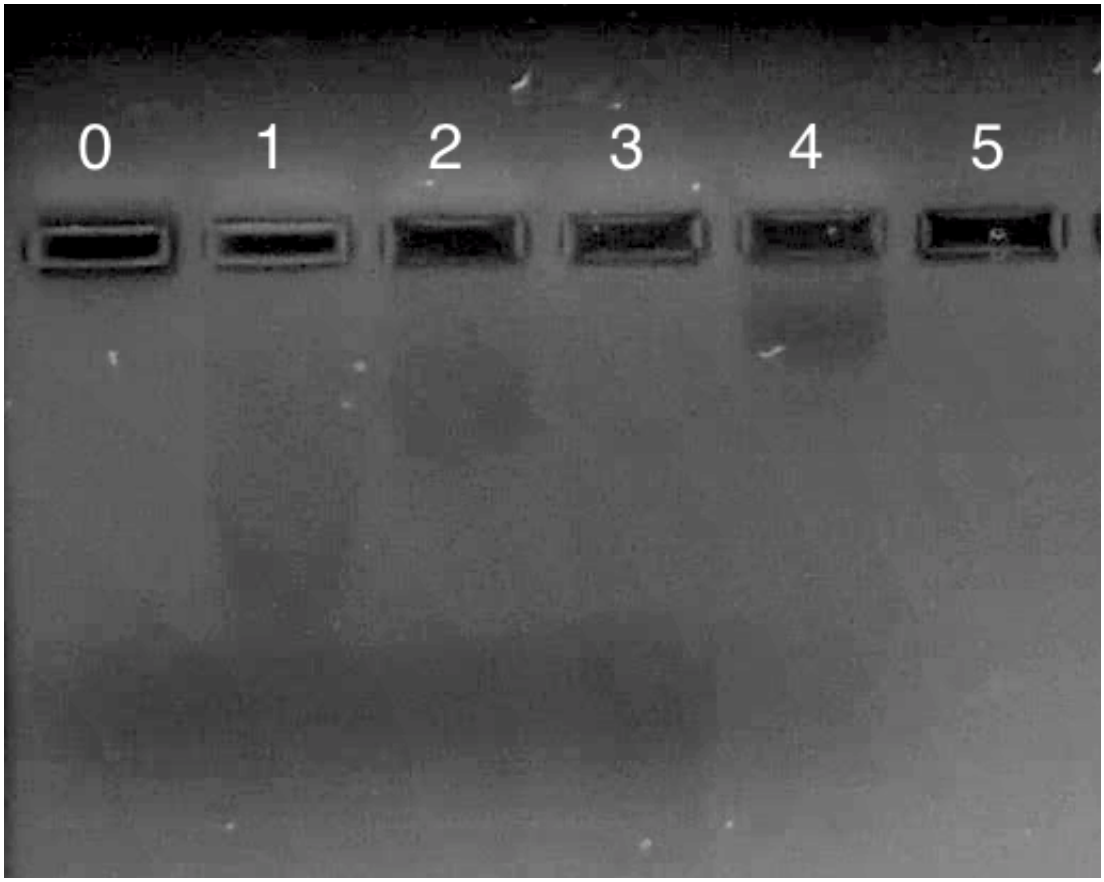

Figure 6.5: Thiol terminated oligos after exposure to Au NPs (DTT used for thiol deprotection, samples ran on an agarose gel). Lane 0 - control NPs, 1 - Oligo 1 + NPs; 2 - oligo 1 + DTT + NPs; 3 - oligo 2 + NPs; 4 - oligo 2 + DTT + NPs; 5 - empty well. The contrast of the image is enhanced for clarity.

Similar experiments of binding oligos to NPs were performed by another group as well [141]. They found that simple conjugation led to oligos wrapping around NPs and undesirable count of oligos bound to a single NP. To control this, they used a short, thiol-terminated alkane, namely 6-mercapto-1-hexanol (MCH). The alcohol was present on the opposite end for solubility reasons. The use of MCH allowed them to achieve precise NP-oligo conjugates with down to a single oligo per conjugate.

This research was adapted to work carried out in this project. Thiolated oligos were exposed to DTT, then NPs and finally extra MCH at varying concentrations was

added to decrease oligo base-binding to NP surface. The resulting samples were run on a polyacrylamide gel to investigate how MCH decreases oligo concentration in NP-oligo conjugates (Figure 6.6). The results show that even a small concentration of MCH affects NP surface availability to oligos. There is no difference in oligo band intensity for oligo-NP conjugates compared to oligo-NP conjugates, which were treated with a low concentration of MCH, suggesting that all of the bound oligos were displaced by MCH. Increasing MCH concentration ten-fold, increases the regained oligo concentration compared to even the sample of oligo + NP without any DTT deprotection, indicating that any base-bond oligos get fully displaced in such MCH-rich environment.

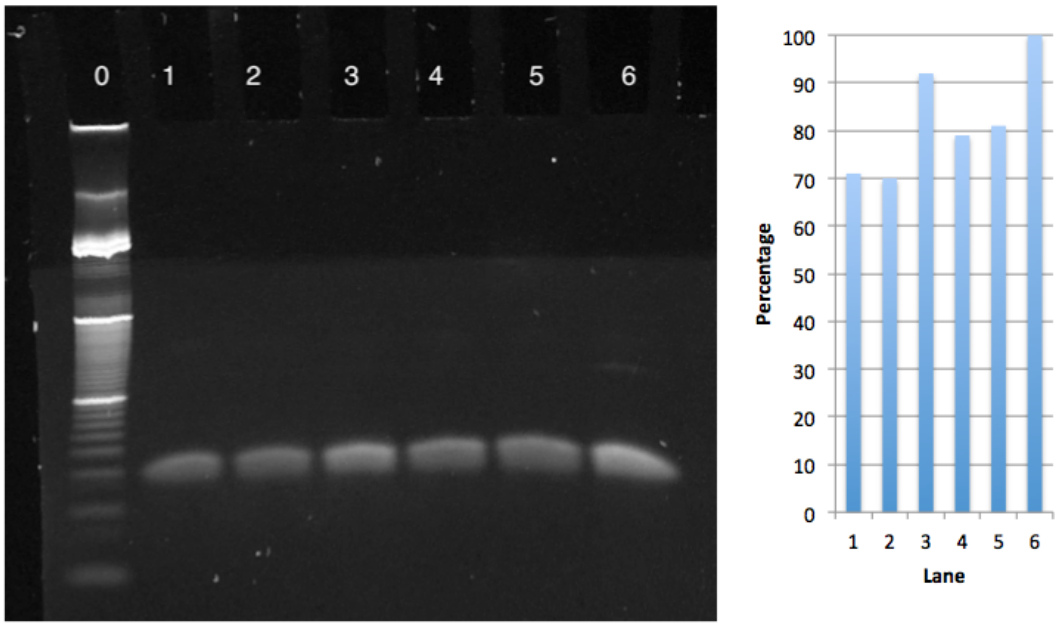

Figure 6.6: Left: oligo-NP conjugation experiment with MCH as mediator. Lane 0 - 10 bp ladder; 1 - oligos + NPs; 2 - oligos + NPs + MCH (low conc.), 3 - oligos + NPs + MCH (high conc.), 4 - oligos + DTT + NPs; 2 - oligos + DTT + NPs + MCH (low conc.), 3 - oligos + DTT + NPs + MCH (high conc.). Right: normalised intensities for each oligo band.

Furthermore, as seen on a true colour image of the same polyacrylamide gel, NPs in all the samples that contained MCH agglomerated and changed their colour. Since MCH does not have a charged group at the used alkaline pH, MCH adsorption to NP

surface and simultaneous displacement of charged species (citrate and oligos) decreases electrostatic charge of the NP, leading to the observed agglomeration.

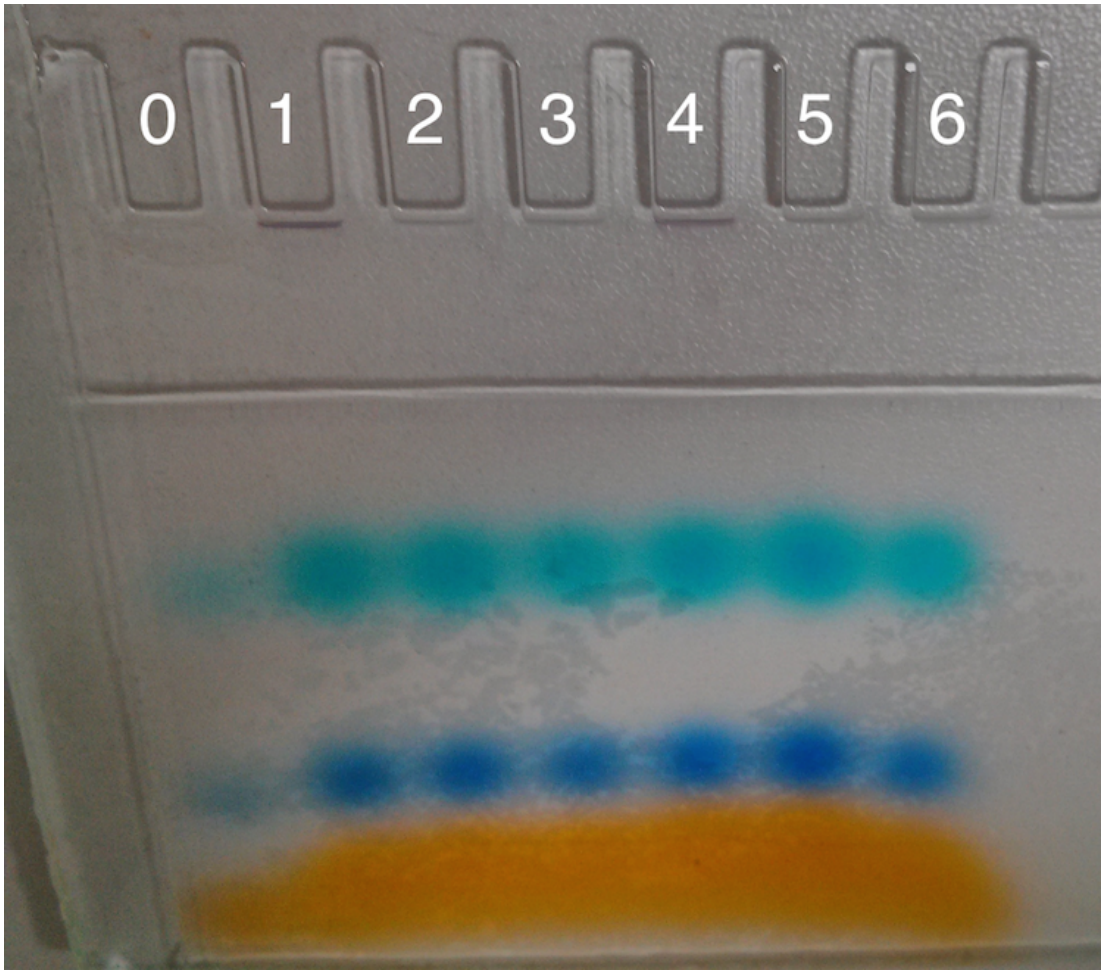

Figure 6.7: True colour image of the polyacrylamide gel with samples for oligo-NP conjugation mediated by MCH. Lane 0 - 10 bp ladder; 1 - oligos + NPs; 2 - oligos + NPs + MCH (low conc.), 3 - oligos + NPs + MCH (high conc.), 4 - oligos + DTT + NPs; 2 - oligos + DTT + NPs + MCH (low conc.), 3 - oligos + DTT + NPs + MCH (high conc.).

Since NPs were found to be sensitive to MCH concentration and MCH was found replacing negative NP surface charge for neutral, it was considered unsuitable for further investigation. Other suitable surface-mediating reagents were identified but due to lack

of time and higher perspectives of the method B, their investigation were not pursued. Instead, method B was examined.

6.2.2 Method B (filament formation, template patterning, NP attachment)

890bp restriction enzyme assay

The strategy of firstly patterning the template DNA and subsequently attaching gold NPs to the thiolated ends of the patterning filaments may seem more straightforward and easier than the previous method. Firstly, there is no need to purify NP-oligo conjugates with a single oligo in the conjugate. Secondly, there is no undesired wrapping of the oligo around the NP.

890bp dsDNA (section from λ-DNA) with three designated patterning sites was selected for performing the experiments of single NP targeted placement. The three patterning sites, each of 60b length, were located at one end, middle and the other end of 890bp template, named A, B and C sites, respectively. Oligos A, B and C were used, that cover these sites. Their sequences were: oligo A - 5' - GGG GTT CCG CGC ACA TTT CCC CGA AAA GTG CCA CCT GAT GCG GTG TGA AAT ACC GCA CAG -3' (same sequence as oligo 1 used in method A); oligo B - 5' - GAT GGC CCA CTA CGT GAA CCA TCA CCC TAA TCA AGT TTT TTG GGG TCG AGG TGC CGT AAA - 3'; oligo C - 5' - TGC GGC CAG TTC ATT CAG CGT ATA ATC ACT AGT GAA TTC GCG GCC GCC TGC AGG TCG ACC - 3'. The secondary structures for oligos B and C are given in Figure 6.8 (oligo A secondary structures are the same as oligo 1 in method A secion).

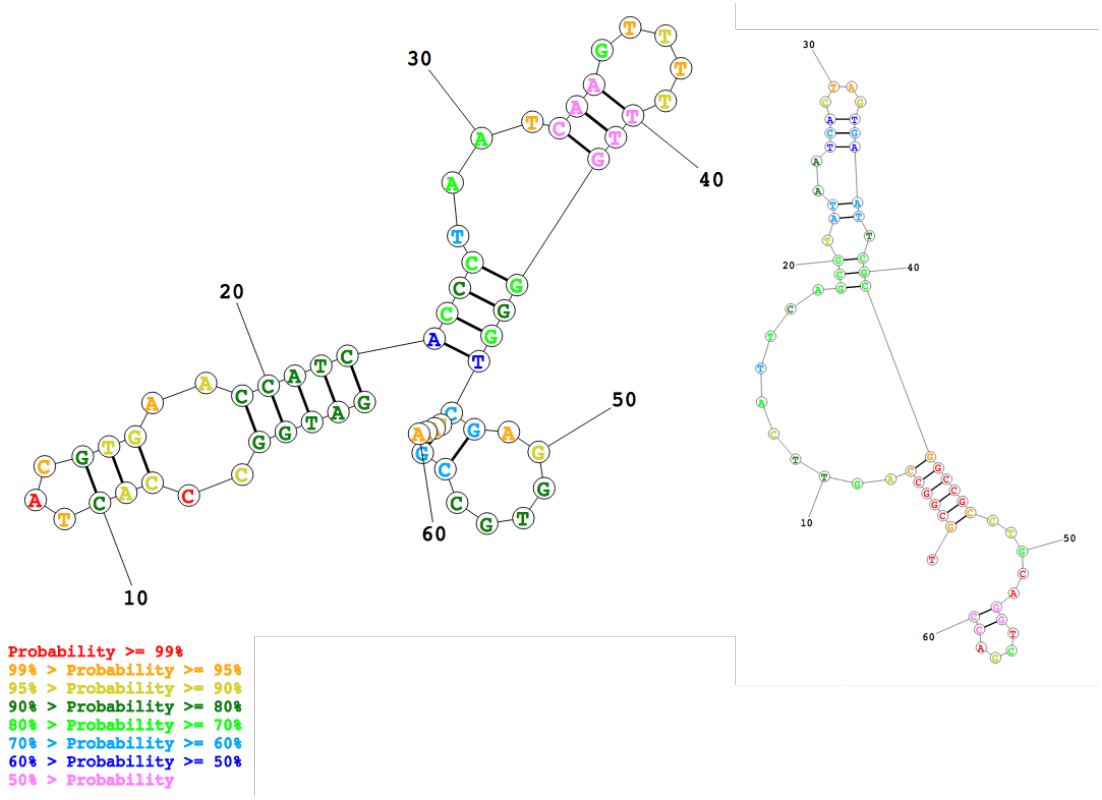

Figure 6.8: Two different oligo secondary structures formed at room temperature as determined with RNAstructure web server. Left: oligo B, right: oligo C, bottom: legend for the colours representing probability for the base being in the determined configuration.

A restriction enzyme assay with a ratio of 14:1 filament:template was performed on 890bp template DNA, testing patterning sites A and C (site B was not tested due to lack of suitable restriction enzyme). The results are shown in Figure 6.9. Both thiolated and non thiolated versions of oligos A and C were used.

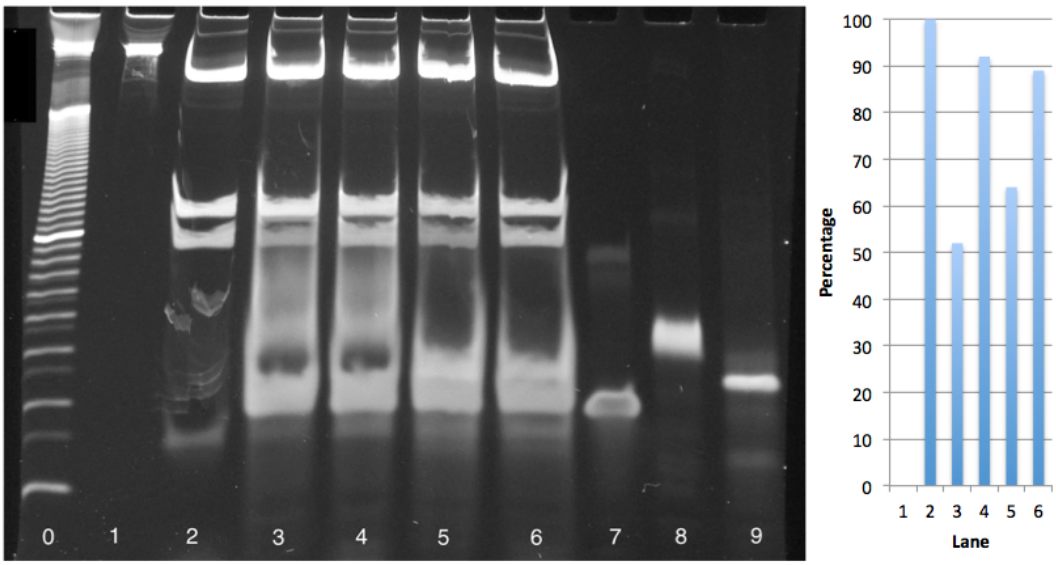

Figure 6.9: Left: 890bp restriction assay for oligo C and oligo A patterning. Lane 0 - 10 bp ladder; 1 - 890bp; 2 - fully digested 890bp; 3 - digestion with inactive RecA with oligo A patterning; 4 - digestion with oligo A patterning; 5 - digestion with inactive RecA with oligo C patterning; 6 - digestion with oligo C patterning; 7 - oligo A; 8 - oligo C; 9 - oligo B. Right: normalised intensities for bands signifying RecA patterning on the gel.

Due to large difference between cut and uncut fragments, the bands for smallest cut fragments are not too clear. However, even with present data, there is a difference in band intensity between filament-protected and non-protected regions. This is visible for both oligo A and oligo C patterning experiments.

To confirm the patterning on the 890bp template, AFM was performed on the patterned structures. In one experiment, patterning was performed with both oligos A and C simultaneously. The results indicated some tentative patterning present on 890bp template (Figure 6.10). In a separate experiment, oligo B was used to pattern the same template. Again, some more evidence was seen for successful patterning in the middle of the template DNA, as expected (Figure 6.11)

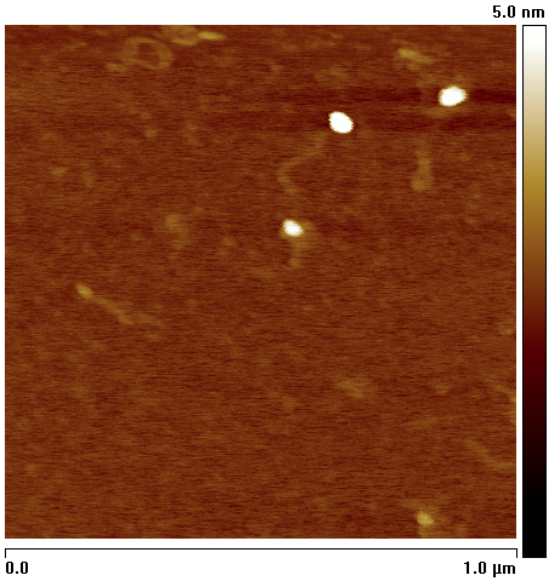

Figure 6.10: A and C site patterning on 890bp, AFM image

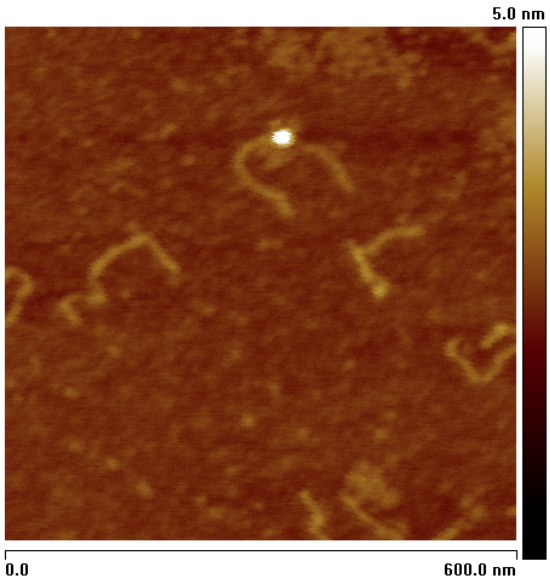

Figure 6.11: B site patterning on 890bp, AFM image

130bp restriction enzyme assay

To address the issue of cut and uncut fragment size disparity in the enzyme assay of long the 890bp template, a shorter, 130bp template was used for a similar restriction

assay. The 130bp template selected has exactly the same sequence as one of the ends of 890bp DNA. This renders it suitable for patterning it with the same oligo C at the exact position and test it with a restriction enzyme assay. This has been performed with much clearer results (Figure 6.12. Successful patterning can be inferred from the restriction assay, proving that oligo C patterning works.

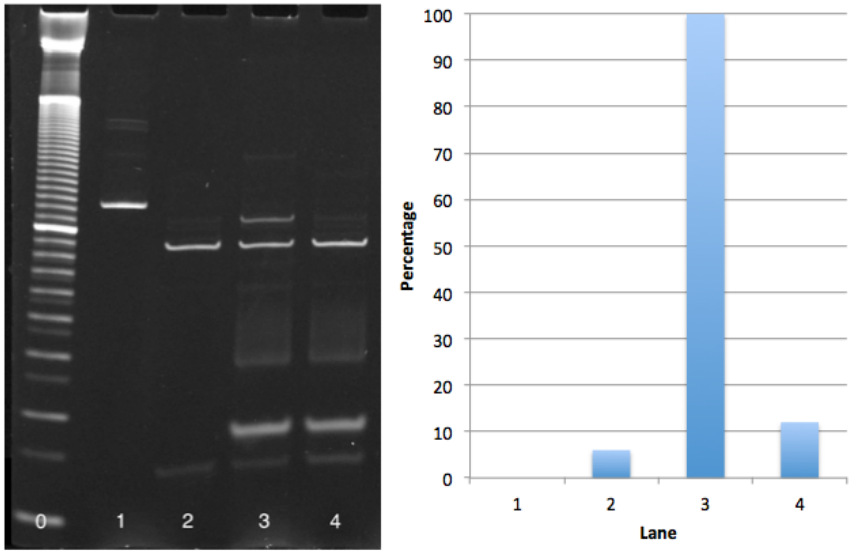

Figure 6.12: Left: 130bp restriction assay for oligo C patterning. Lane 0 - 10 bp ladder; 1 - 130bp; 2 - 130bp digested; 3 - 130bp digestion with oligo C patterning; 4 - 130bp digestion with inactive RecA and oligo C patterning. Right: normalised intensities for bands signifying RecA patterning on the gel.

6.2.3 Attaching NPs to specific position on patterned scaffold

The next step after successful filament patterning with terminal thiols is to introduce NPs. Since 130bp template DNA is too short to be imaged with AFM, 890bp template was used. Both single patterning site and simultaneous patterning of two patterning sites were carried out with subsequent exposure to NPs. However, only single patterning with subsequent conjugation showed some degree of success. Figure 6.13 depicts one such instance where two pieces of DNA are attached to one nanoparticle.

Subsequent measurement of nanoparticle-like structure showed structure height of 8 nm being in good agreement with used nanoparticle radius of 5 nm (6.14).

Unfortunately, only few successful cases of such structures were observed, showing that the multistep process of NP placement at precise position on the DNA scaffold needs to be optimised.

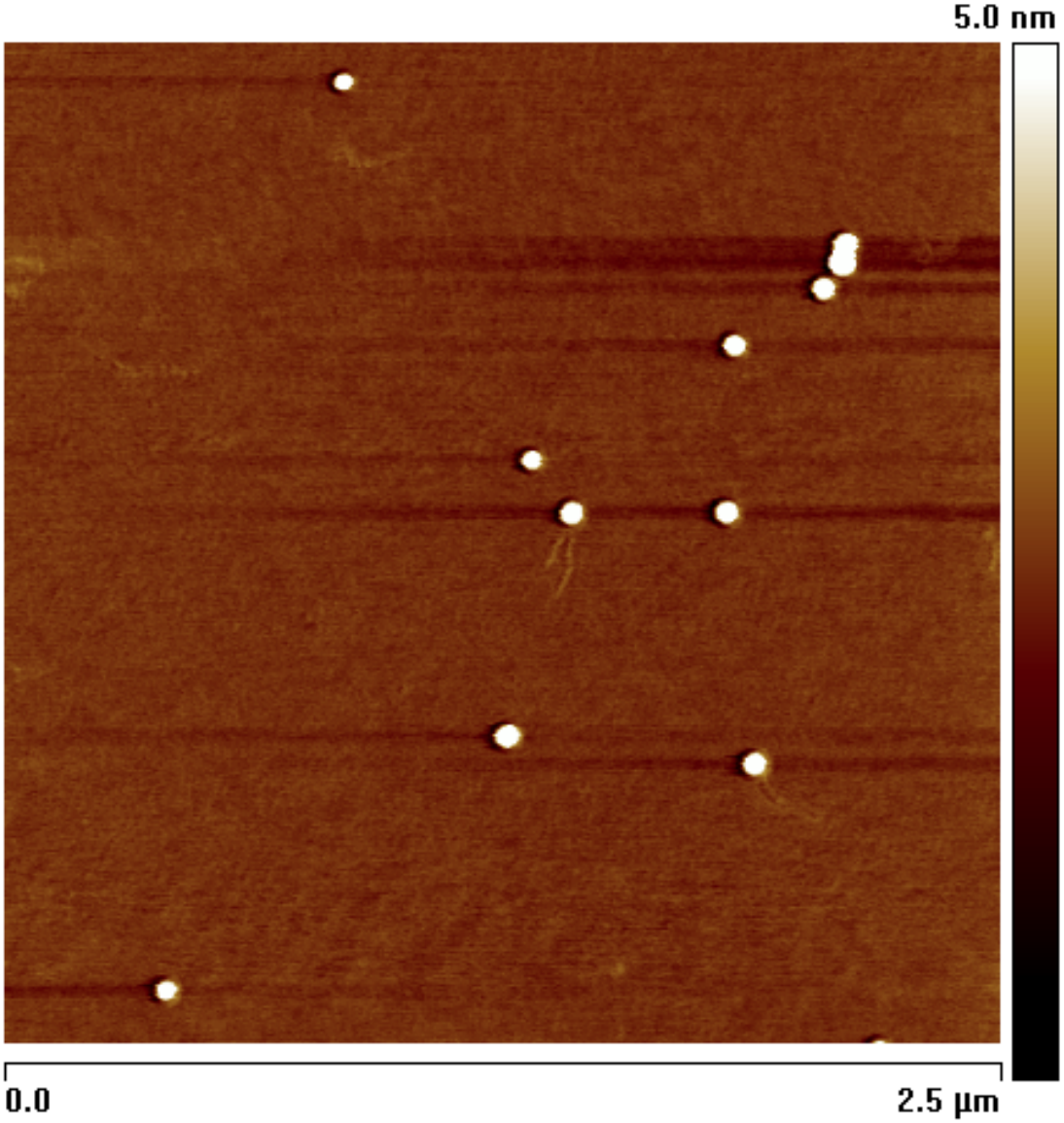

Figure 6.13: C site patterning on 890bp + NPs, AFM image

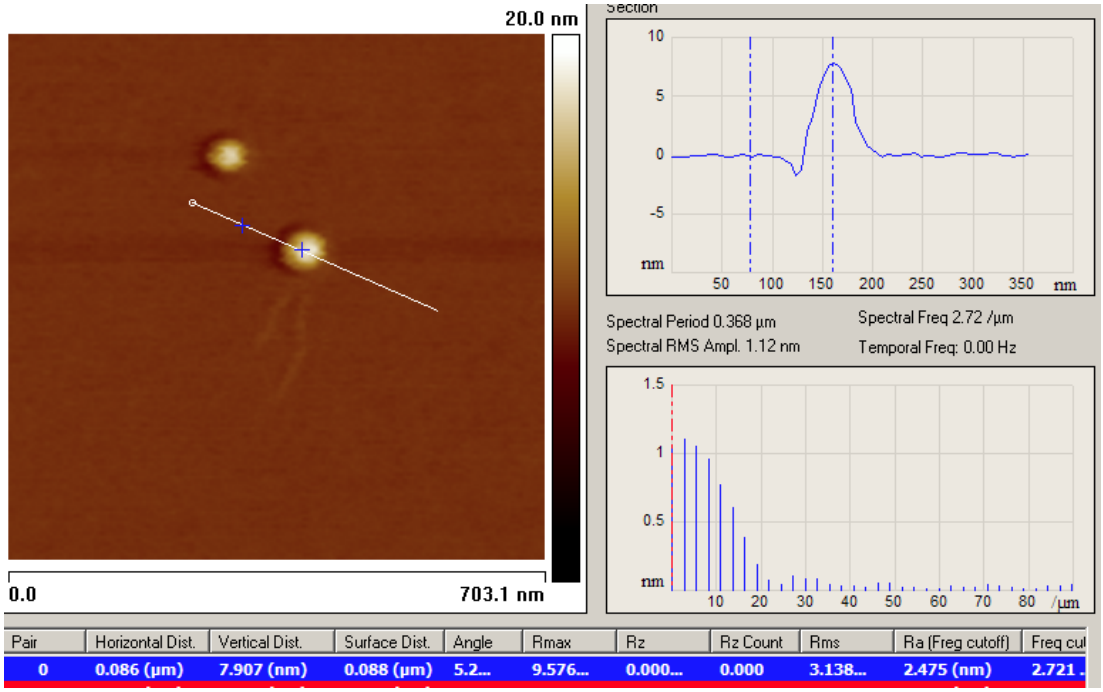

Figure 6.14: Height measurement of the NP for NP patterning on 890bp DNA.

6.3 Conclusion

Two different methods for binding single nanoparticles in well-defined, targeted manner were investigated and compared. Method A, which considers with oligo-NP interaction first, was found to be problematic due to NP sensitivity to any introduced reagents. Method B, where NPs are introduced at the last step, however, showed promise. More work needs to be done to both investigate method A's feasibility and method B's optimisation and scaling to larger structures.

Chapter 7

Investigation of nucleoprotein filament–dsDNA template interaction kinetics and complex stability through use of FRET

7.1 Introduction

Novel materials are typically seen having combined advanced functionality, whether it is electronic, optical or mechanical. However, these new materials are typically not composed of such simple building blocks as atoms or relatively small molecules. They are more likely to be built up from extensive number of large organic molecules, connected in complex ways. Due to the variety and nature of organic molecules, such systems can be fragile to environmental conditions: humidity, temperature, pH, solvent molecules, etc. For biological molecule-based systems, time-based stability is also important, since biomolecules evolved to interact with any other molecules mostly transiently. Contrary to that, materials should be stable on macroscopical level and therefore non-changing at nanoscale, unless the change is desired and enabled from outside. Therefore, it is necessary to properly investigate and optimise the stability of any novel system that is based on biomolecules.

To investigate filament-template interaction kinetics and formed complex stability, fluorescence resonance energy transfer system was designed and used. Two 60b oligos,

each complementary to other were selected and used for nucleportotein filament formation and patterning on 130 bp dsDNA template. The binding site for these oligos was at one of the ends of the template. One oligo (o-ATTO550) had an ATTO550 fluorophore on the terminal end that comes in proximity to the template end when patterning occurs. Similarly, the other oligo (o-Alexa647) had an Alexa647 fluorophore on the terminal end that also comes into proximity to the template end when patterning occurs, or it comes close to ATTO550 when bought of the oligos are hybridised. One of the template primers (p-ATTO488) also had a ATTO488 fluorophore, designed to come into contact with the precise fluorophores when patterning occurs. This system allows one to investigate interaction between all the strands of DNA during filament patterning through FRET signal change with ATTO488 working as a donor fluorophore, Alexa647 as a acceptor fluorophore and ATTO550 either as a donor or as an acceptor fluorophore.

The fluorophores were selected because of the optimal overlap between their spectral characteristics for FRET studies. Their spectra and structure are given in Figure 7.1.

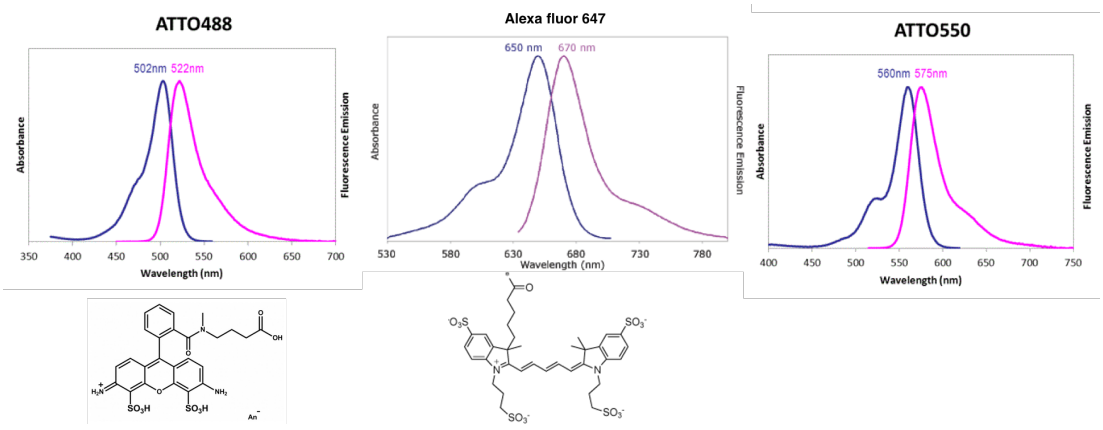

Figure 7.1: The selected fluorophores, their spectra and structure (below each spectral graph). Structure for ATTO550 is not known.

7.2 Results

7.2.1 Hybridisation of oligonucleotides with attached fluorophores for FRET testing

In order to establish the working of the FRET pairs of the selected fluorophores, oligonucleotides conjugated to the chosen fluorophores are exposed to each other. Since the oligonucleotides are selected to be complementary to each other, they will naturally hybridise and bring the fluorophores in close proximity. FRET has been used to follow DNA hybridisation before, hence the use of such technique to test FRET signal.

Oligos o-ATTO550 and o-Alexa647 were mixed together in 1:1 ratio and the intensity of both of their emissions was followed at 21°C. Here, o-ATTO550 works as a donor and o-Alexa647 works as an acceptor in a FRET pair. Only the donor was excited directly with a laser and he reaction was followed on the confocal microscope for 10 minutes with acceptor and donor emissions separated into two different data channels. The intensity of fluorescence was summed up throughout the whole captured image area for each channel and plotted on a single graph for comparison (Figure 7.2).

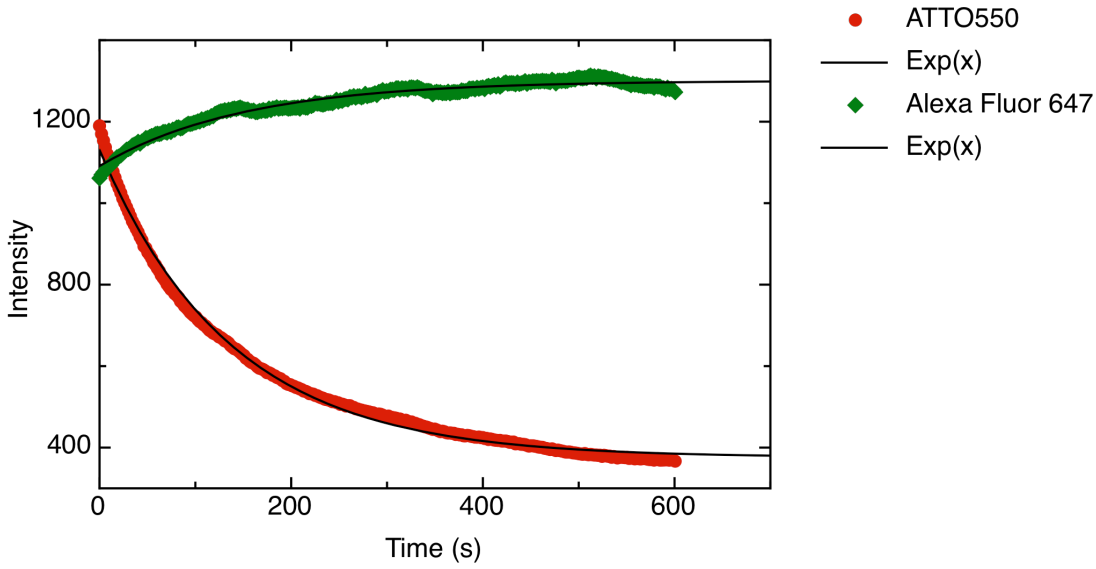

Figure 7.2: Hybridisation of o-ATTO550 and o-Alexa647 fluorophores

The donor fluorescence intensity exponentially decays over the measurement time, whereas the acceptor intensity rises in a similar fashion. The level of the acceptor

intensity rise is lower than of the the donor. This could be attributed to quantum efficiency of the FRET fluorophore coupling. Also, at the beginning of the reaction, acceptor intensity should be negligible, but here it starts at a 90% that of the donor. This can be explained by undesired direct acceptor excitation and spectral crosstalk: the acceptor channel registering light from the donor emission. Both of these effects increase the background level of the acceptor intensity. In 10min time of the reaction, donor emission decays to zero and the acceptor emission reaches a saturation level. The acceptor channel also demonstrates a certain level of intensity fluctuation over measurement time, which can be explained by excitation laser intensity time variations (see sections on p-ATTO488 and o-Alexa647 hybridisation and the control experiments for laser intensity fluctuation below). This inverse fluorophore intensity behaviour is expected in FRET and is a good indicator of fluorophores being brought together in close proximity through oligo hybridisation.

A general exponential function of the form

$$y = Ae^{-(\frac{x-x_0}{t_0})} + const \tag{7.1}$$

was used to fit the fluorescence data retrieved from the instruments where applicable. All of the variables were not fixed. t_0 is the time constant and was taken from each fit for the results. The time constants for for the fluorophores are t_0(o-ATTO550) = 136 s and t_0(o-Alexa647) = 150 s. Both are of similar size and suggest direct reaction between the oligos.

To test FRET interaction between ATTO488 and Alexa647 fluorophore pair, a similar hybridisation experiment was carried out on o-Alexa647 and the primer used to synthesise 130 bp DNA with ATTO488 fluorophore (p-ATTO488). The 20 base primer p-ATTO488 is complementary to o-Alexa647 and when both oligos interact, the fluorophores are brought into proximity and the FRET signal is observed. p-ATTO488 works as a FRET donor and o-Alexa647 is a FRET acceptor.

The oligos were reacted in 1:1 ratio and their emission was observed with the confocal microscope for 10min through two separate donor and acceptor channels at 21°C. As previously with o-ATTO550/o-Alexa647 FRET pair, fluorescence emission changes were observed for p-ATTO488/o-Alexa647 pair (Figure 7.3).

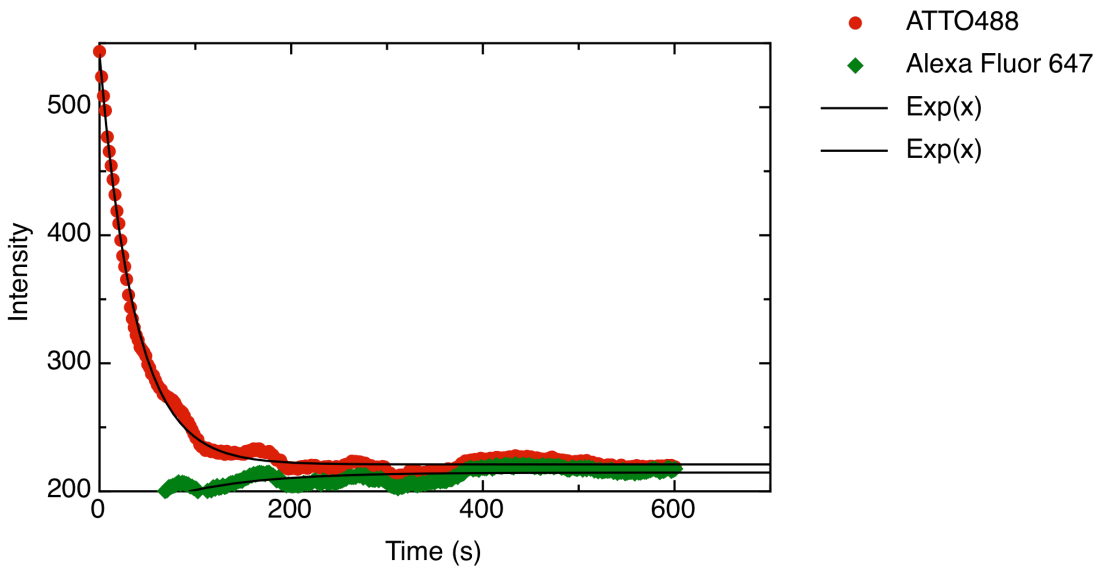

Figure 7.3: Hybridisation of p-ATTO488 and o-Alexa647.

In 3min time, the donor emission dropped down to a steady level and the acceptor emission level increased to a steady level. The donor emission did not drop to zero intensity because of residual direct laser light leakage to donor channel. The time constants for these oligos were t_0(p-ATTO488) = 37 s and t_0(o-Alexa647) = 85 s. The reason for shorter reaction time compared to the o-ATTO550/o-Alexa647 hybridisation is the shorter sequence of p-ATTO488. p-ATTO488 is only 20b long, whereas the other two oligos are 60b each. Hybridisation reaction time for 20b and 60b oligos is shorter than for 60b–60b oligo interaction because the recognition sequence is shorter and less time is needed for oligo sequence-probing (this is corroborated by the fact that a typical PCR reaction will have an primer annealing step of about 30s).

After 3min of reaction, some fluctuation of both donor and acceptor intensities are observed. These intensity fluctuation can be seen to correlate positively between the two channels. This rules out reaction-based instabilities since that would manifest as negative correlation just like initial intensity changes. The positive correlation indicates the change in intensity is coming not from FRET interaction, but from other sources, e. g. the non-steady laser intensity. A control experiment with stable single fluorophore excitation confirmed this.

The two hybridisation experiments cannot be compared with respect to the absolute intensity values. Although they were carried out with same oligo concentrations, a different laser wavelength was used to excite p-ATTO488 and o-ATTO550. Furthermore, each fluorophore pair had different spectral overlap, resulting in different FRET quantum efficiencies. However, both experiments demonstrated strong negative correlations between donor and acceptor intensities, indicating FRET taking place between the hybridising oligos.

7.2.2 Restriction enzyme assays for fluorophore-modified oligo use in patterning dsDNA

Having established that selected fluorophores successfully produce FRET signal through oligo hybridisation, the next step is to demonstrate filament patterning on dsDNA with filaments formed on the selected oligos with conjugated fluorophores. This is established through restriction enzyme assay of patterned dsDNA. The 130 bp DNA for restriction enzyme assay was engineered to have a two *Eco*RI digestion sites, one of which is embedded in the patterning site of a 60b filament. The patterning site ends flush with the template 130 bp DNA. The 130 bp region was selected so that the p-ATTO488 can be used as a primer to synthesise 130 bp. When the 130 bp DNA is synthesised with the fluorophore, the fluorophore aligns with the flush patterning end. Also, when the patterning is performed with either o-ATTO550 or o-Alexa647, the fluorophores of these oligos are oriented on the same flush patterning end. This allows for different patterning combinations with presence or absence of fluorophores on the template DNA and/or the patterning oligo.

While performing pilot FRET experiments on filament?dsDNA interaction, a dependance on MgAc concentration was noticed. It was found, that with typical concentrations of 20 mM MgAc used in filament patterning experiments for restriction enzyme assays cause visible solution agglomeration under confocal microscope. A series of experiments were performed, where fluorescence was observed for both donor and acceptor under confocal in samples with different concentrations of MgAc and different reagents. Samples that were examined were filaments, template DNA, filaments reacted with template DNA – all at varied MgAc concentrations. It was found, that template DNA does not cause any visible agglomeration of fluorescence signal at any

MgAc concentration. Filaments reacted with DNA and filaments on their own, however, do. The optimal concentration for reaction, avoiding majority of agglomeration was found to be 10 mM MgAc.

Reasons of visible agglomeration under 20 mM MgAc at which restriction assays perform well are not clear, but prolonged incubation and general RecA sensitivity to Mg^{2+} concentration might be the main reason. To avoid any agglomeration, 10mM MgAc was used for all the following FRET experiments.

To test if patterning with fluorophore-tagged oligos works and is not impeded by the fluorophore presence, a restriction enzyme assay with different combinations of oligos and template DNA was produced (Figure 7.4). The ratio of filaments to template DNA in these samples was 3 to 1 and the patterning reaction was carried out at 37°C.

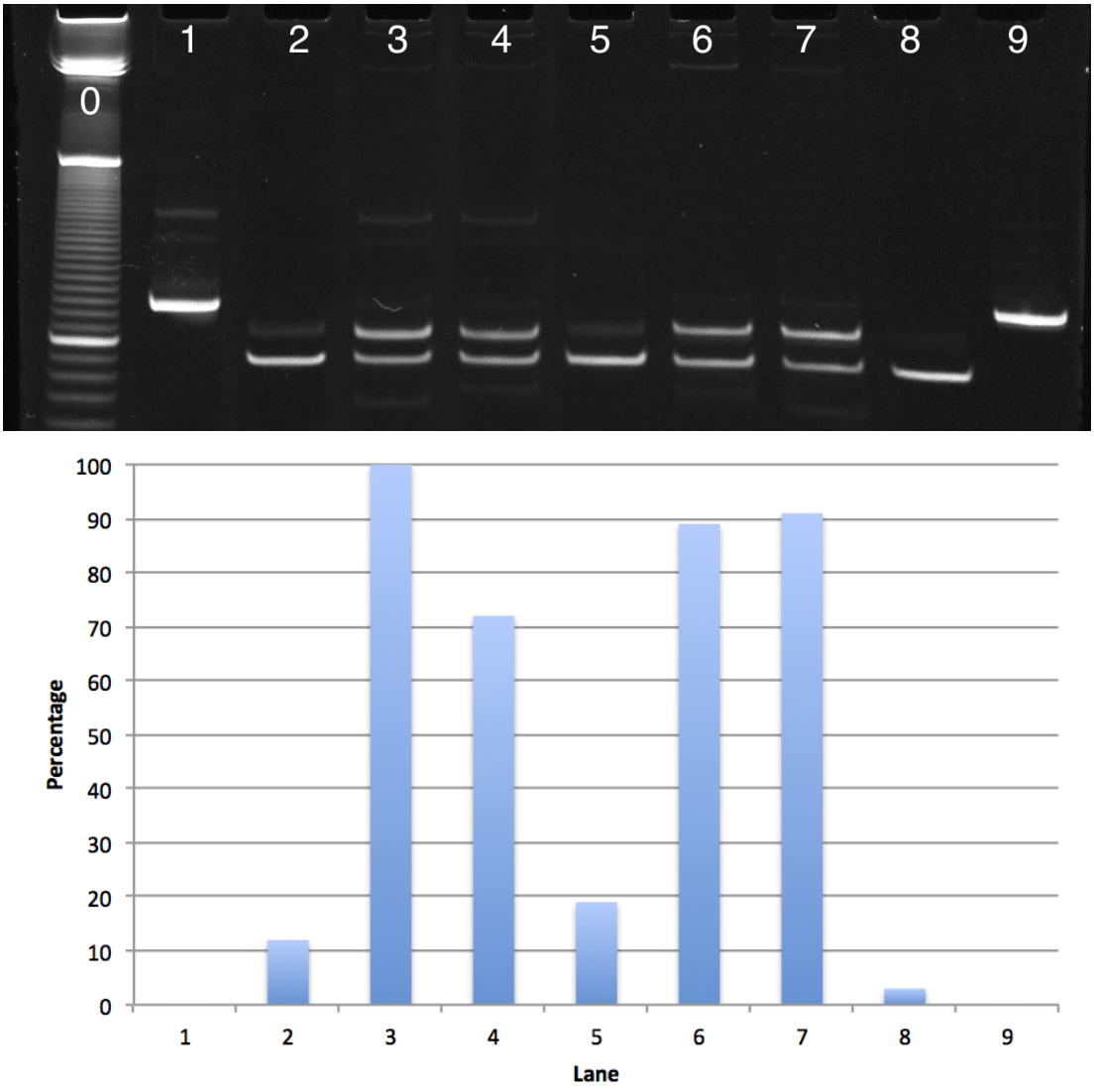

Figure 7.4: Restriction enzyme assay of 130 bp dsDNA patterned with 60b filament (ATTO488/ATTO550 pair); 3:1 filament:dsDNA ratio. Lane content: 1- 10bp dsDNA ladder; 2 - 130 bp template dsDNA; 3 - fully digested dsDNA; 4 - digestion after patterning with 60b filament; 5 - digestion after patterning with o-ATTO550 filament; 6 - digestion after patterning with 60b filament formed from inactivated RecA; 7 - digestion of dsDNA (synthesised with p-ATTO488) after patterning with o-ATTO550 filament; 8 - digestion of dsDNA (synthesised with p-ATTO488) after patterning with 60b filament; 9 - fully digested dsDNA (synthesised with p-ATTO488); 10 - dsDNA (synthesised with p-ATTO488). The graph below shows relative intensities of the bands of the protected fragment normalised to banground.

Lane 3 shows the bands visible after full digestion of 130 bp template DNA with EcoRI. Lane 4 and lane 5 show digestion of the same template DNA but in the presence of protecting filament formed on 60b oligo without a fluorophore and with a fluorophore (o-ATTO550), respectively. The high intensity bands in these lanes represent the larger remaining segments of partially digested template DNA (with filament protecting one of the digestion sites) and fully digested DNA (with filament failing to protect the digestion site). No significant difference is seen for the intensities of these two bands between lane 4 and lane 5 and the intensity ratio for the two bands is similar in both lanes. This suggests that using an oligo with an ATTO550 fluorophore attached to it for filament formation and patterning 60b region on dsDNA template does not impede the patterning efficiency.

Similarly, using template DNA tagged with ATTO488 fluorophore for patterning with untagged oligo (lane 8) or with o-ATTO550 (lane 7) does not affect the patterning efficiency as seen from the intensities of the same bands. This further shows that a combination of fluorophores present at the patterning end of the template DNA and the filament does not interfere with filament patterning at least 10 bases away from the fluorophore position, where the protected digestion site is located.

Since FRET measurements were to be performed at room temperature (21°C), an additional restriction enzyme assay for testing fluorophore patterning interference was produced where template DNA patterning was taking place at 21°C (Figure 7.5). The patterning efficiency will be reduced when done at lower than 37°C, therefore a sample with with filament to template DNA ratio of 3:1 and another sample with a ratio of 10:1 were used. The higher 10:1 ratio should compensate for reduced temperature and allow for high enough patterning efficiency to observe the respective DNA band. Both of the samples contained filaments produced on o-ATTO550 and the template DNA was synthesised with p-ATTO488.

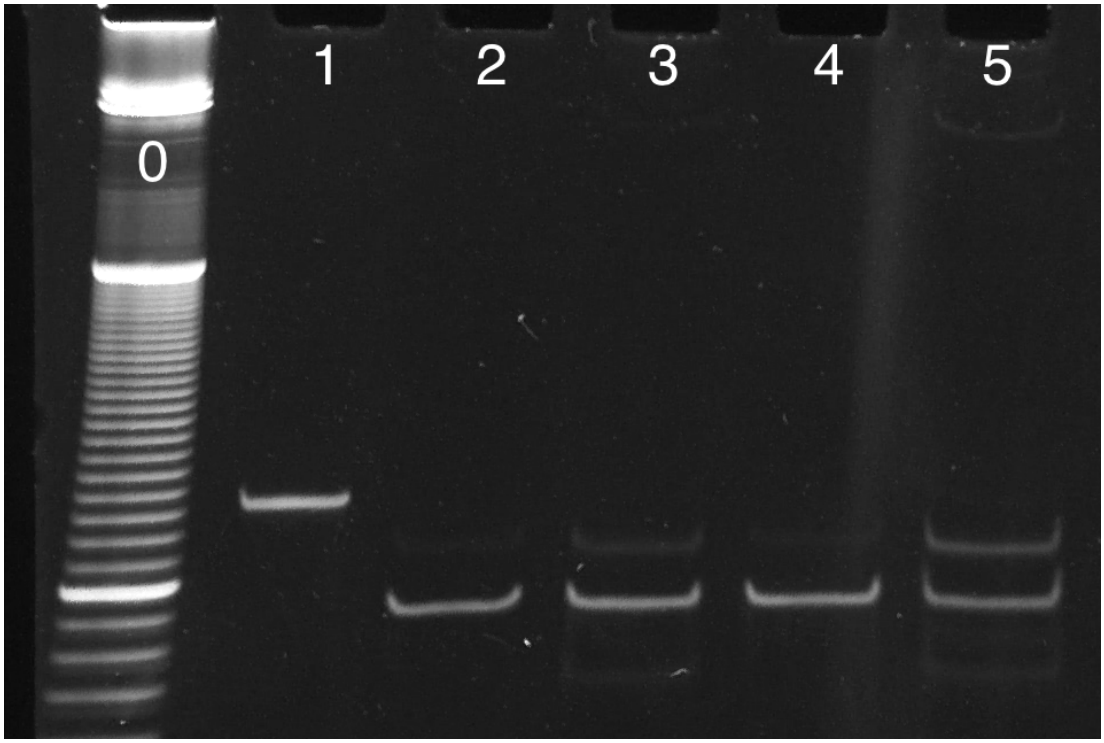

Figure 7.5: Restriction enzyme assay of 130 bp template DNA (synthesised with p-ATTO488) patterning with o-ATTO550 filament patterning performed at 21°C. Lane content: 1- 10bp dsDNA ladder; 2 - 130 bp template dsDNA; 3 - fully digested dsDNA; 4 - digestion after patterning with o-ATTO550 filament at 3:1 filament to template DNA ratio; 5 - digestion after patterning with o-ATTO550 filament formed from inactivate RecA at 3:1 ratio; 6 - same as lane 4, but filament to template DNA ratio is 10:1.

The bands in lane 4 and 6 in Figure 7.5 represent filament protection at 3:1 and 10:1 ratio, respectively. As expected, the band for the protected DNA in lane 4 is fainter than the equivalent bands in Figure 7.4, where the reaction temperature was 37°C. The bands in lane 6 reveal improved patterning efficiency over lane 4. Both of these lanes show that patterning is still possible at room temperature with fluorophore-tagged DNA.

With the filament patterning of template DNA established as not dependant on attached fluorophores, the next step is to evaluate the kinetics of filament patterning. Although FRET through the attached fluorophores is the main tool for establishing kinetic values, certain investigation can be carried out with restriction enzyme assays

as well. A series of samples incubated for different amounts of time at the patterning stage in the restriction enzyme assay allows for varied filament protection levels. Such an assay was produced, where each sample was incubated at the patterning stage for 5min – 60min (Figure 7.6). Lane 3 to 8 contain the sample with patterning at 37°C for 5min, 10min, 20min, 30min, 45min, 60min (in that order). With the top band progressively becoming more intense and the bottom one fainter throughout the lanes, gradual increase in the fraction of filament-protected template DNA is observed. These time snapshots of patterning show that only 5min of patterning time is enough for a significant fraction of template DNA to be protected by the filaments.

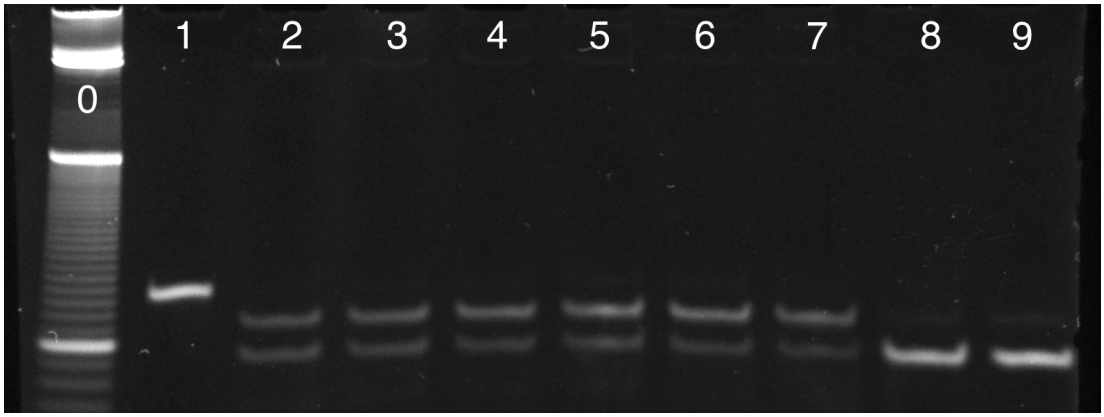

Figure 7.6: Restriction enzyme assay of 130 bp template DNA (synthesised with p-ATTO488) patterning with o-ATTO550 filaments. Patterning was done at 37°C for varied amounts of time: lane 3 - 5min, lane 4 - 10min, lane 5 - 20min, lane 6 - 30min, lane 7 - 45min, lane 8 - 60min. Other lane contents: lane 1 - 10bp dsDNA ladder; lane 2 - 130 bp template dsDNA; lane 9 - patterning with inactive RecA filaments; lane 10 - fully digested template DNA.

The relative fraction of filament protection can be expressed as the intensity of the digested band divided by the sum of both digested and digestion-protected band intensities. Using this method, fractional filament protection from Figure 7.6 were quantified and plotted as time series (Figure 7.7). The data shows that filament protection reaches its maximum efficiency after 20min.

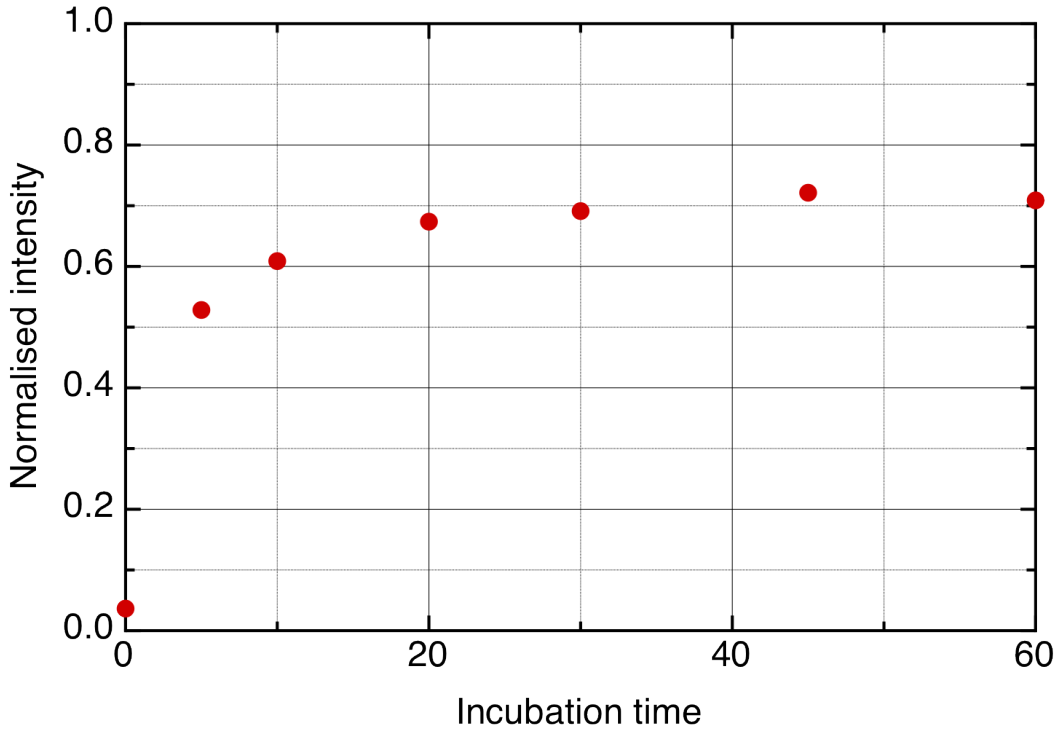

Figure 7.7: Graph for restriction enzyme assay from figure 7.6. The data is normalised as the intensity of the digested fragment band divided by the sum of the intensities of digested and digestion-protected fragment bands.

7.2.3 ATTO488/Alexa647

After investigating binding kinetics of 130 bp template DNA and filament formed on o-ATTO550, binding of o-Alexa647 filament onto the same 130 bp template DNA was looked into. In this case, o-Alexa647 is complementary to the template DNA strand with the ATTO488 fluorophore. After triple-stranded fragment formation, if full or partial strand-exchange happens, both fluorophores should be brought together closer than in the previous system of template DNA and o-ATTO550 filament and FRET signal should be observed. To test that, o-Alexa647 filament patterning was followed with a fluorospectrophotomer by observing fluorescence spectra of the mixture solution over defined time intervals for 40min at 21°C with filament:template DNA ratio of 3:1. The fluorescence values for donor emission wavelength (522 nm) and acceptor emission wavelength (670 nm) were plotted as time series (Figures 7.8 and 7.9, respectively). The

donor emission decreased over the reaction time and the acceptor emission increased – signifying filament patterning and FRET. The acceptor emission showed a saturation curve typical to binding kinetics, whereas the donor emission decreased more linearly over time. This can be explained by the large baseline value for donor emission coming from remaining unfiltered excitation beam. No t_0 was calculated for the donor data and the t_0 of the acceptor was found to be 179 s - substantially higher than oligo-oligo interactions.

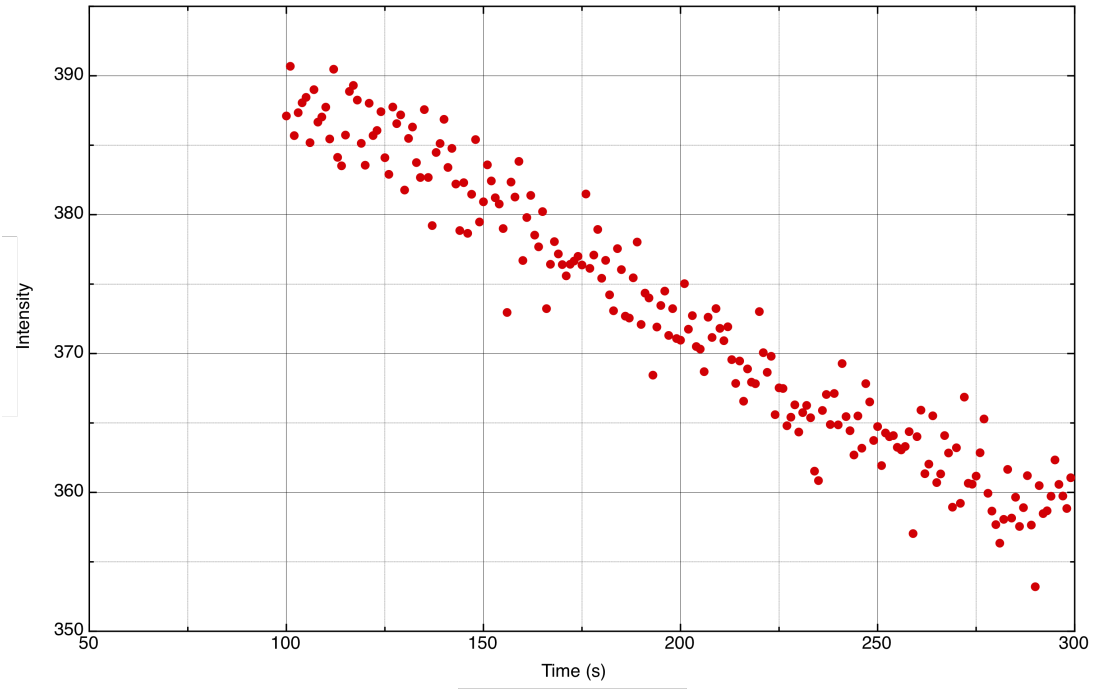

Figure 7.8: o-Alexa647 filament patterning on 130 bp DNA template at 21°C, followed with Shimadzu fluorospectrophotomer; 3:1 filament:template DNA ratio; donor emission at 522 nm wavelength.

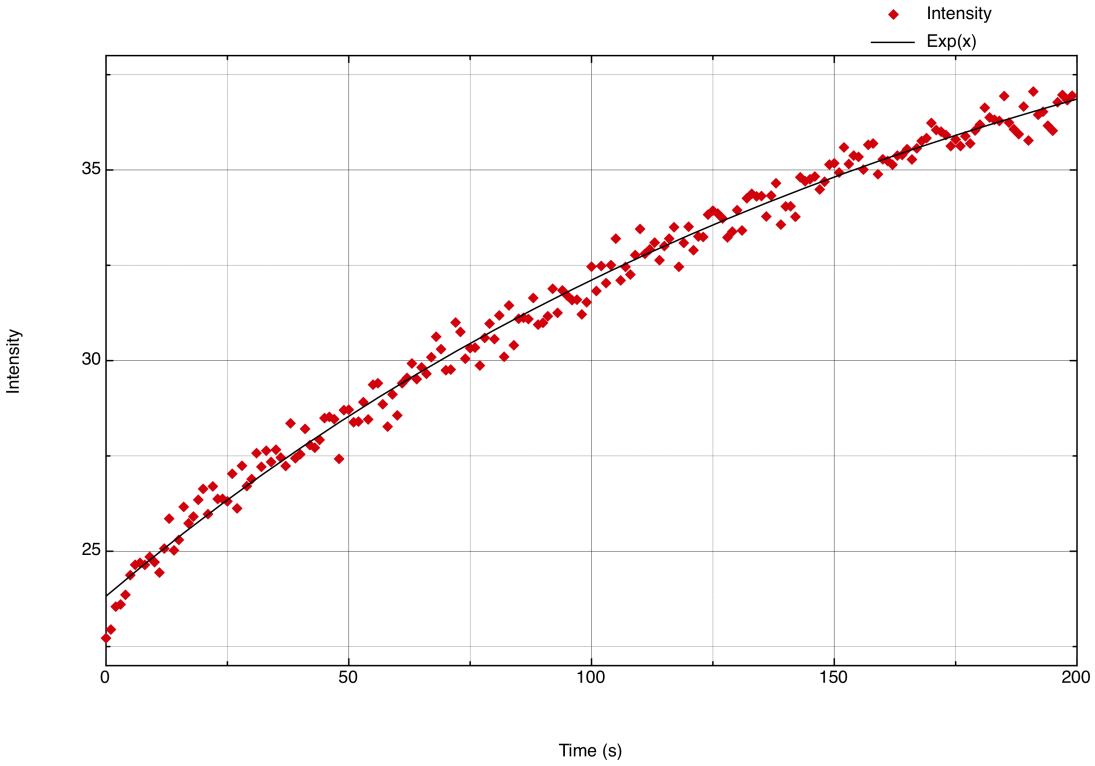

Figure 7.9: o-Alexa647 filament patterning on 130 bp DNA template at 21°C, followed with Shimadzu fluorospectrophotomer; 3:1 filament:template DNA ratio; acceptor emission at 670 nm wavelength.

The same experiment was repeated on a confocal microscope. The binding of o-Alexa647 filament onto template DNA at a ratio of 3:1 of filaments:template DNA was followed for 210min at 21°C. The data reveal FRET signal that is in agreement with the previous fluorospectrophotometer results (Figure 7.10). The time constant for the fitted curve in this experiment was $t_0 = 123$ s.

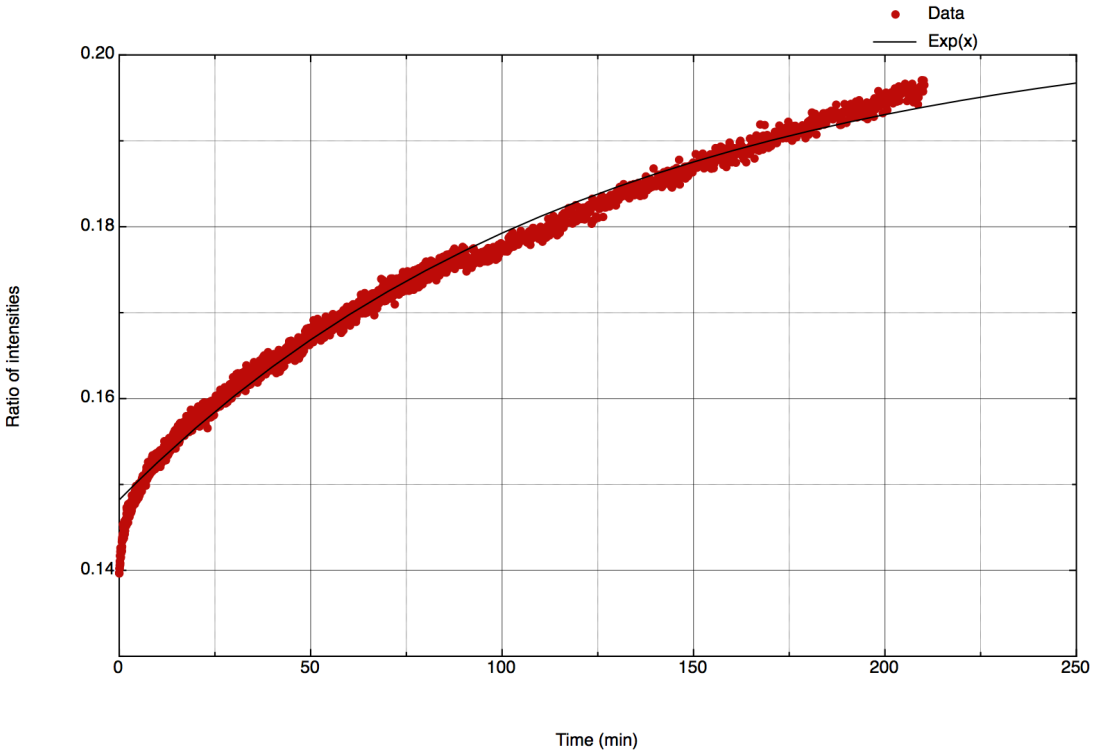

Figure 7.10: o-Alexa647 filament patterning on 130 bp DNA template at 21°C, followed with a confocal microscope; 3:1 filament:template DNA ratio; acceptor intensity values divided by donor intensity values.

The exact same experiment was performed with 1:1 ratio of filaments:template DNA, showing similar trend (Figure 7.11). The time constant in 1:1 ratio experiment was slightly slower ($t_0 = 143$ s) than in the previous 3:1 experiment. This was expected, as the 3:1 filament to template ratio sample had more optimal ratio for quick reaction.

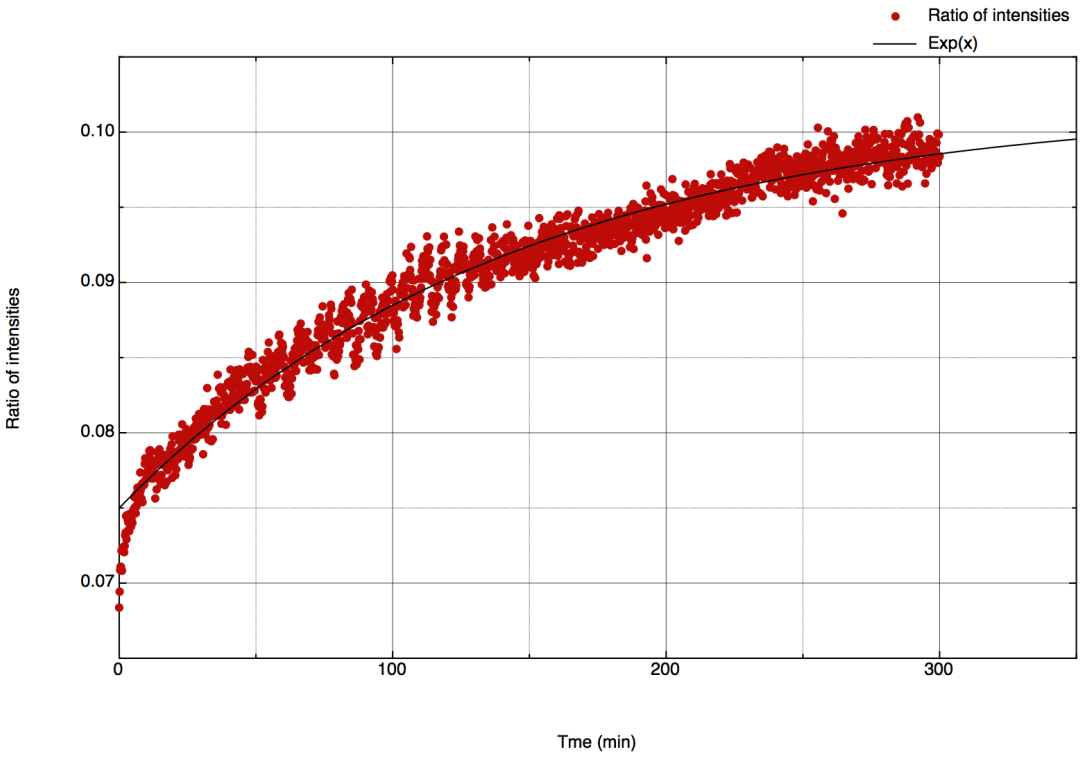

Figure 7.11: Confocal 488-647, 1:1, acceptor divided by donor

7.2.4 Outcompetition

With binding constants determined for different ratios of filaments to template DNA, dissociation constants are still needed for Kd determination. Since there is no way to guarantee 100 % of interacting molecules being filament-template complexes at the initial time of the experiment, an experiment design that takes this into account was devised. The method for determining filament-template dissociation constant is based on adding excess outcompeting template that affects the FRET signal. The experiments would start as with the binding constant determination method, where fluorophore-labelled filament and template would be allowed to interact for certain amount of time. When all or the majority of the filament-template complexes are formed, unlabelled template dsDNA that is 10 times in excess to the initial template is introduced. If filaments transiently fully detach from the labelled template, this should be observable with gradual decrease in FRET signal due to higher likelihood of filaments binding to

10 times more prevalent unlabelled template than the labelled one.

The initial outcompetition experiment used 10x higher unlabelled dsDNA template after 3 hours of incubation of ATTO488-labelled template DNA and filament formed on o-Alexa647 at 3:1 (filament:template) ratio. The sample for outcompetition was incubated for 5 hours after adding the excess unlabelled DNA. The measurements were performed on the Shimadzu fluorospectrophotometer. Both wavelength intensities of the donor and the acceptor were recorded (Figures 7.12, figure 7.13).

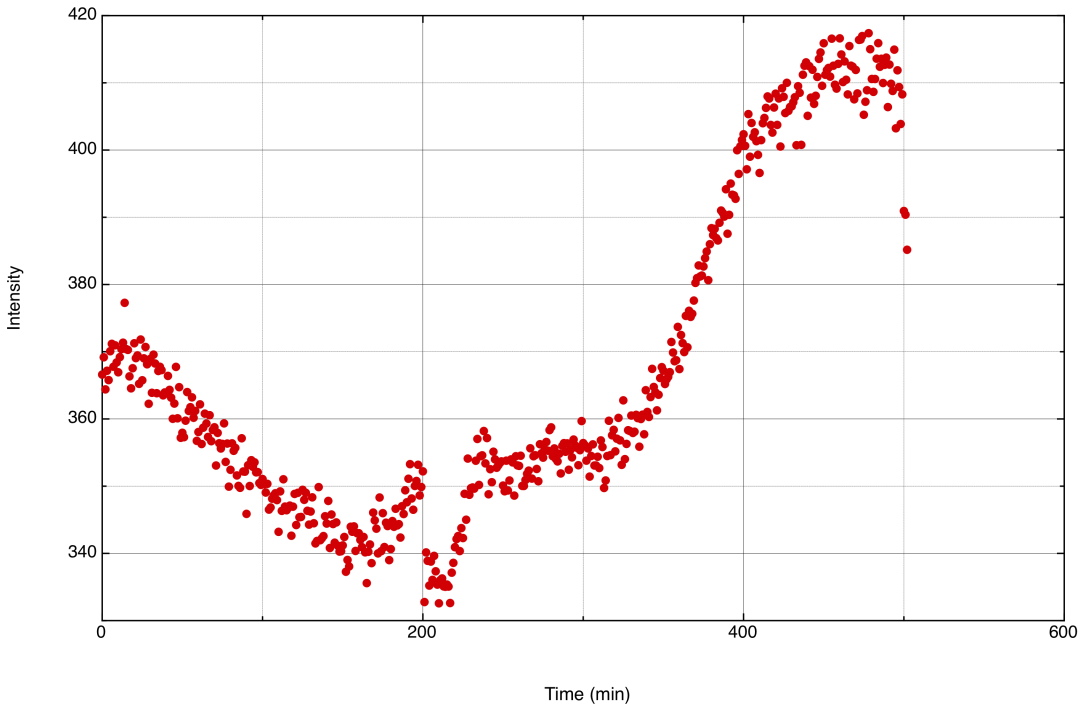

Figure 7.12: Shimadzu 488-647 outcompetition with 10x excess untagged dsDNA, donor emission

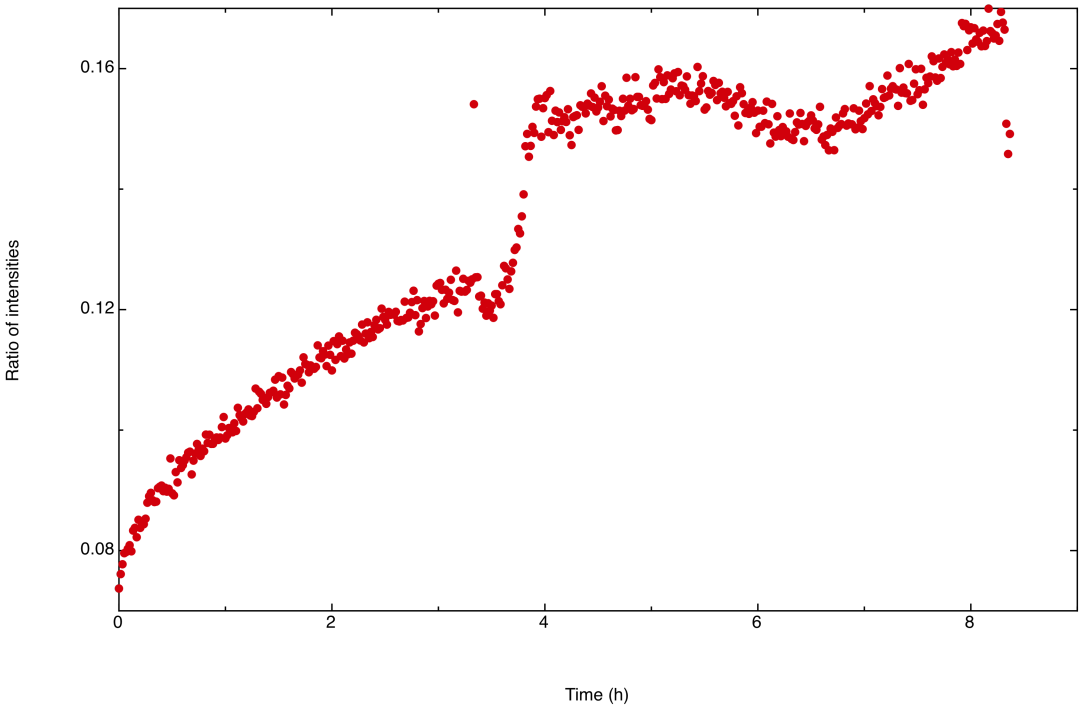

Figure 7.13: Shimadzu 488-647 outcompetition with 10x excess untagged dsDNA, acceptor emission

As can be seen from the figures, a clear decrease in fluorescence intensity in the donor channel and an increase in the acceptor channel were registered for the first 3h of incubation, where filament-template binding occured. However, after that a slight dip with sharp increase, followed by slower increase that correlates with both channels was observed. Since the result follows the same trend with both of the channels, it is most likely that it does not represent the actual reaction, but an instrumental error or an unexpected phenomenom in the solution, such as a possible agglomeration. No exact conclusion from these data on outcompetition success can be drawn.

To minimise possible filament crosslinking, the same experiment was repeated with 10 times decreased concentration of the reactants (initial labelled template DNA, filament and additional unlabelled DNA). The results are visible in figures 7.14 and 7.15.

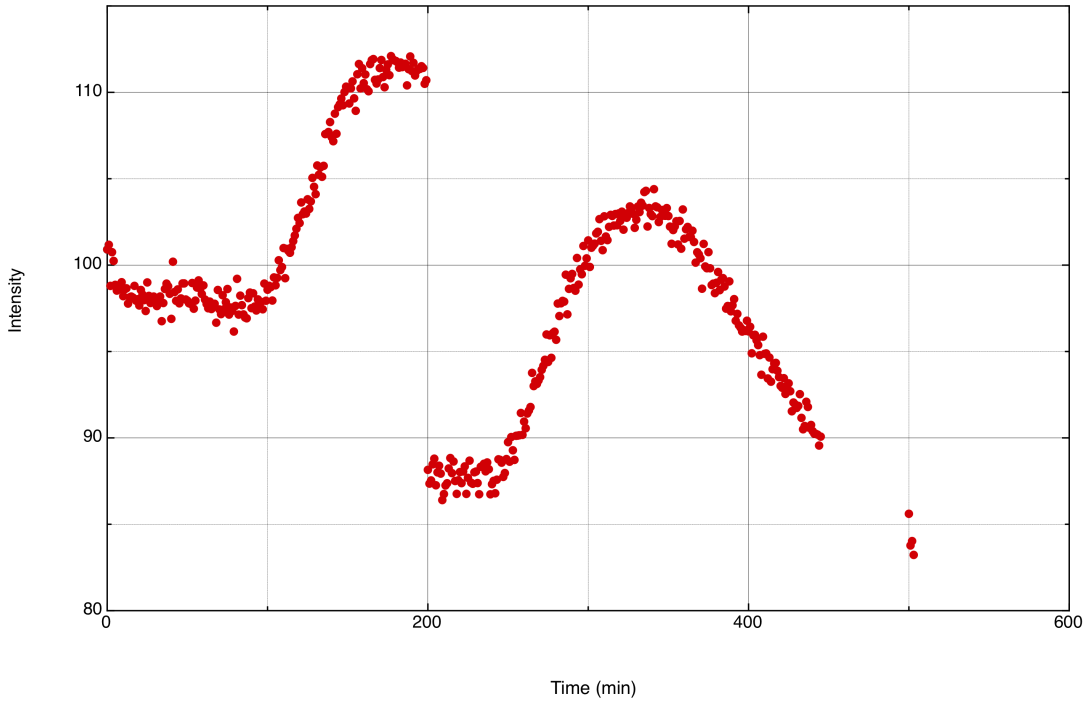

Figure 7.14: Shimadzu 488-647 outcompetition with 10x excess untagged dsDNA, donor emission (reagents 10x diluted)

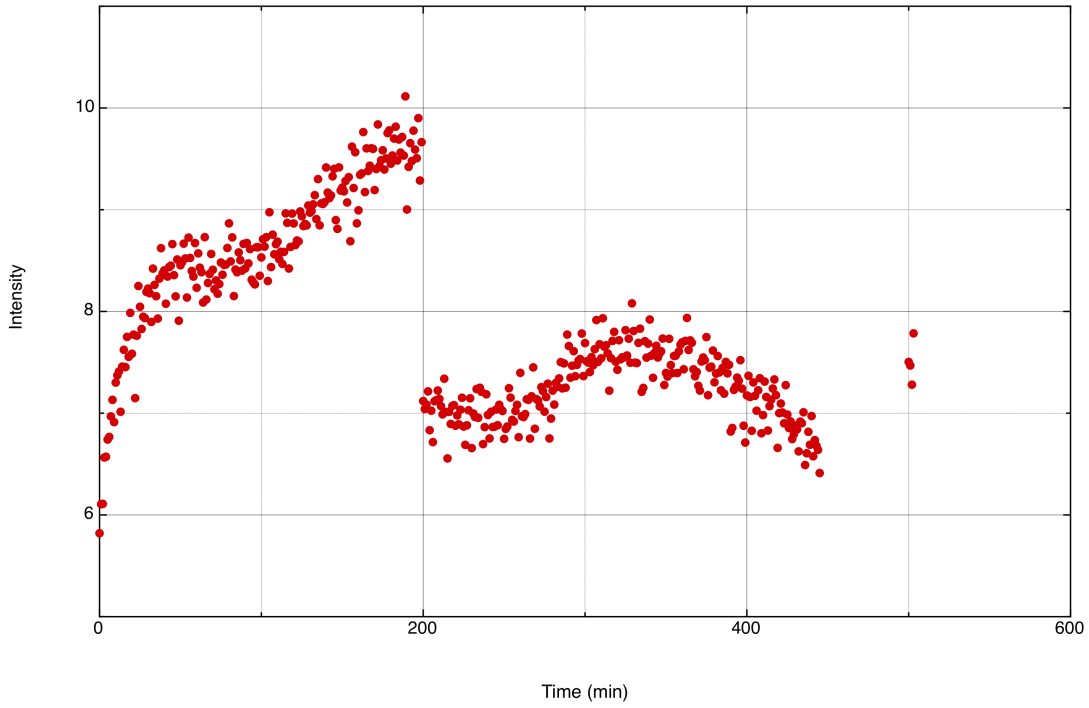

Figure 7.15: Shimadzu 488-647 outcompetition with 10x excess untagged dsDNA, acceptor emission (reagents 10x diluted)

A decrease in donor intensity and an increase in acceptor intensity are visible in the first 30 minutes of the experiment, but a channel-correlated increase in intensity is seen for the rest of incubation until outcompeting DNA was added. This again indicates a systematic error, not related to the actual reaction. After the addition of the outcompeting template DNA, a sudden drop in fluorescence for both channels is observed. And through the rest of 5 hours of incubation a gradual increase and later decrease for both channels were observed. Again, these phenomena indicate that the observed large gradual shifts in the intensity are not part of the reaction and come from the set-up of the experiment.

To eliminate the possibility of an instrumental error for the previous experiments, similar tests were carried out on the confocal microscope. The same samples were tested at 3:1 ratio of filaments:template for the original concentration and the 10 times diluted version (Figures 7.17 and 7.16). As before, results are plotted as acceptor

channel intensities divided by the donor channel intensities to reduce instrumental error.

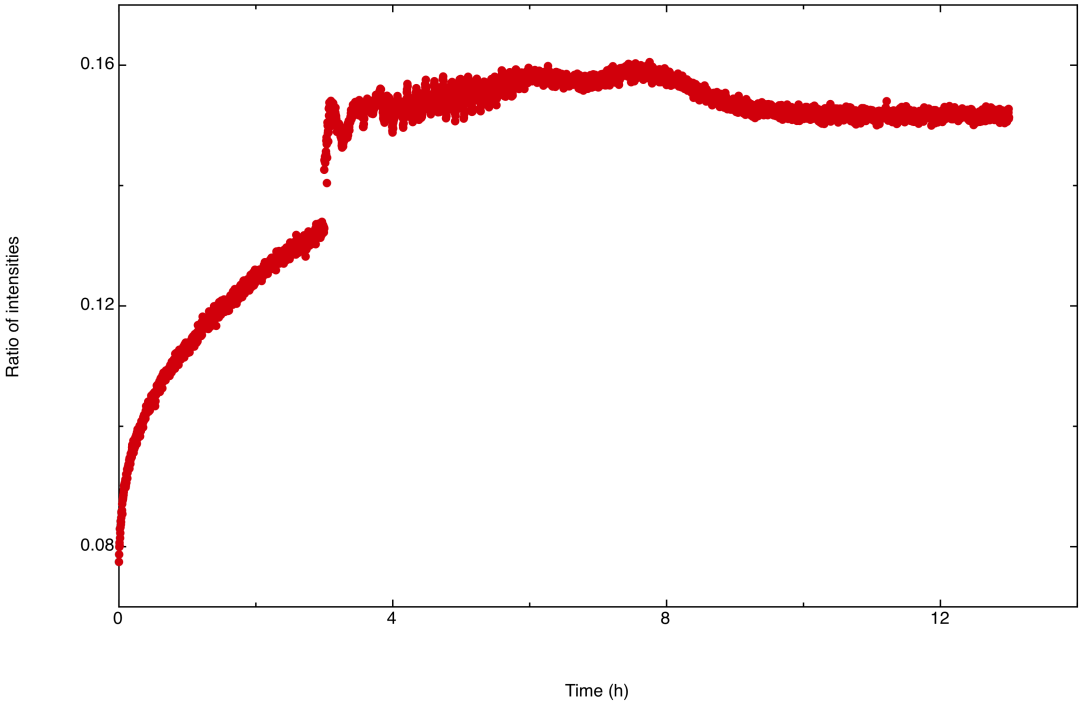

Figure 7.16: Confocal 488-647, 3:1 ratio, outcompetition with 10x excess untagged dsDNA, acceptor by donor

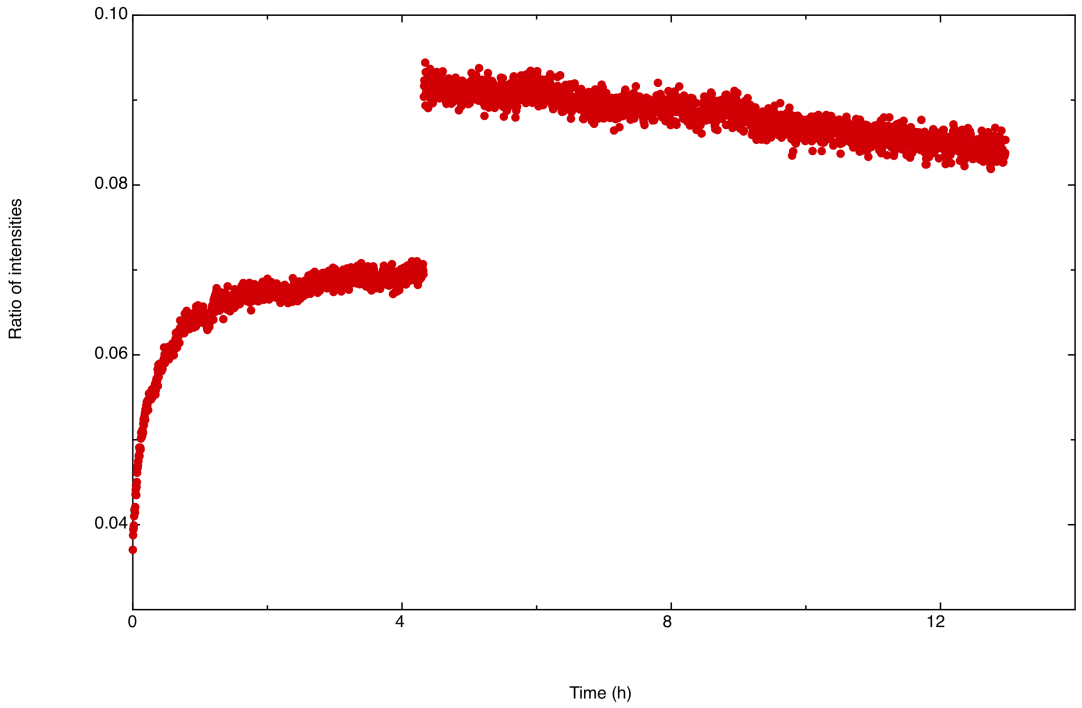

Figure 7.17: Confocal 488-647, 3:1 ratio, outcompetition with 10x excess untagged dsDNA, acceptor by donor (reagents 10x diluted)

The resulting curves show expected FRET signal increase for both of the samples for initial filament-template incubation. However, addition of the outcompeting template resulted in abrupt change in intensities for both of the samples, increasing the ratio of acceptor to donor signal even more. Since the instrumental error is cancelled out mathematically, the abrupt change in intensity could only be explained by a sample-related phenomenon. As argued before, the exact reason for it is unknown, but partial agglomeration is a possible explanation.

Incubation with outcompeting template DNA showed a much smaller variation in intensity over time than on the Shimadzu fluorospectrophotometer. The first sample showed certain intensity instability for the first 2 hours, but after that stabilised and remained constant. The sample with 10 diluted reagents revealed constantly decreasing FRET signal. However, the signal decrease was linear and not exponential, as expected for a dissociation reaction. The exact reason for the discrepancy between the results of these two samples is not known. However, since abrupt changes in intensity are most

likely caused by the sample and not the instrument, it is possible that any instabilities observed at the outcompetition stage are also a result of sample specifics.

Since the outcompetition stage does not have any component of exponential decrease in intensity, it is safe to assume that filament dissociation is either non-existent in the given time scale or too low to be detected by the two instruments used.

7.3 Conclusion

The work in this chapter successfully demonstrated binding of nucleoprotein filament to template dsDNA through patterning mechanism through FRET signal change. Interestingly, FRET signal is noticeable only when the bound filament oligo is complementary to the strand on template DNA that has the second fluorophore. This reaffirms that exact state of triple-stranded complex is not well understood and is not stable with respect to strands being locked-in to their position. As other groups have suggested, linear filament motion along the template DNA and relative "kick-out" of replaced strand by filament is possible and might indicate lack of FRET signal in that case [142]. The "sliding" of filament during the homology sarch or partial detachment of the exchanged strand would cause the fluorophores to separate and FRET signal to diminish.

The designed outcompetition experiments were not suitable for the selected FRET system due to instability of the solution over longer periods of time, possibly due to degradation of filament-template complexes or ATPγS hydrolysis. However, with certain experiments it was shown that there is some tentative suggestion that with long incubation times, filaments stay fully bound to the template DNA until ATPγS hydrolysis. This suggests that filament-template complex is temporally stable system in the range of hours, which should be enough for subsequent metallisation to be carried out.

Dependence on MgAc was found to be different in these experiments in comparison to the restriction enzyme assays and other published experiments [143] [144]. Knowing RecA sensitive dependence on Mg^{2+} concentration and different roles it undertakes at different concentrations, it is not surprising that with longer incubation times visible agglomeration of filaments was observed.

Chapter 8

Conclusion and future work

With the constant scaling of electronic component size in the electronics industry, fundamental physical limits are already manifesting themselves as manufacturing issues. To negate them, researchers are iteratively improving the conventional lithographical apporach by changing the materials and optimising the processes, however it is clear, that to advance the industry any further, changes in the whole process and manufacturing approach is needed.

The literature review demonstrated that DNA and proteins are flexible and versatile biomolecules able to interact with each other and create advanced structures that are either static or dynamic, controlled via various extrinsic stimuli, such as pH change, light or salt concentration. Furthermore, their possession of self-assembly as a property and ability to be synthesised on massive scales promises a possibility in constructed structure upscaling. The selected biomolecules have excellent potential to create novel materials and connect the living world with human ability to monitor and interact. However, the lack of any reliable electronic properties in these biomolecules raised questions if any of the designed structures will be used via electric manipulation.

The work done in this project investigated the possibility of using a specific biomolecular system, namely RecA nucleoprotein filament patterned template DNA as a novel framework for future nanometre scale electronic and material engineering. The investigation performed here focused on a specific method for imparting electrical properties to the DNA scaffolds – one of the most important aspects for future electronic devices. It also looked into filament-template stability and kinetics. However, these are not the only questions to be answered for successful DNA-RecA scaffold utilisation. Issues,

such as scaffold size scaling, out-of-solution degradation and integration with external environment need to be investigated as well before pursuing any fully developed devices.

8.1 Work conclusions

The previous work done by Sharma *et al.* demonstrated controlled ability of patterning template dsDNA with RecA nucleoprotein filaments formed on template dsDNA [56]. It was shown, that filaments as long as 60 bases and as short as 6 bases are able to pattern template DNA. The ability to change the patterning length and patterning site by changing the DNA sequence is a powerful tool for marking regions of DNA for further modification. Combined with the ability for multiple patterning, the technique lays foundations for DNA as a backbone onto which additional functionality can be introduced.

The work of this PhD was to investigate whether patterned DNA regions can be functionalised with Au NPs, introducing the desired electronic properties to the DNA scaffold. To do that, conventional gold-thiol chemistry and protein modification through primary amines were used. The second goal of the project was to investigate if single NPs can be placed with nanometre or sub-nanometre precision for exact control of electronic properties. Lastly, the stability of bound nucleoprotein filaments to template DNA was investigated. Patterned structure stability is a desired feature since unstable scaffolds would prove hard or impossible to modify in the more advanced scenarios required for device production.

8.1.1 Full filament coverage with NPs

One of the most straightforward questions for using the developed RecA-DNA system to ask is if the patterned regions can be fully metallised for imparting simple electrical conduction. Due to their universality, controlled size and ease of synthesising, Au NPs were selected for deposition onto RecA-coated regions. Since Au NPs do not readily bind to proteins, three different reagents that mediate NP-protein interaction were investigated: SATA, 2-IT and SPDP. All of them bind to primary amines present on the proteins and expose a thiol for Au NP attachment. All of the three reagents were successfully used to introduce thiols onto nucleoprotein filaments. The thiols per RecA

introduced were quantified using DTNB and DTDP reagents and subsequently exposed to Au and magnetic NPs.

The control of NP binding to thiolated filaments proved to be somewhat challenging. The most successful results were achieved with 2-IT. When filament thiolation and NP conjugation was performed in the solution, large clusters of NPs templated by the filaments were obtained. The clusters were hundreds of nanometres in size and did not follow filament shape anymore. This was speculated to result from salts, residual unreacted thiolating reagents and other species in the filament solution, which cannot be removed without destabilising the filament structure. Some of it might be removed through protein spin desalting columns, dialysis or magnetic bead capture technique, but these methods tend to lower filament quantity or not purify the unwanted species well enough. Alternatively, filament modification and metallisation can be performed after the filaments are deposited on a surface. This allows to wash any unwanted reagents off the surface and introduce thiolating reagent and NPs without mixing the solutions and compromising the reagents. Good filament metallisation with NPs without NP agglomeration was achieved using this method, but the samples also retained high levels of NPs on the background. Furthermore, modification and metallisation of filaments on the surface is not a suitable technique, since not all the surfaces might be suitable for exposure to reagents. It was shown, that mica surface, in particular, is not suitable for work with 2-IT – one of the most promising thiolation reagents.

The work demonstrated the potential for NP binding to nucleoprotein filaments and challenges needed to overcome for controlled and even metallisation.

8.1.2 Single NP precise positional attachment

For the RecA-DNA system to be useful for novel devices, ability to place single nanometre-scale entities, such as single biomolecules or NPs is needed. Patterning template DNA with nucleoprotein filaments formed on terminally-modified oligos could allow that. If the terminal modification is a thiol, a single NP can be attached to the end of the oligo without the chance of it binding anywhere else on the framework.

Two approaches of attaching single NPs through terminal thiols were investigated. In the first one, thiolated oligos were introduced to NPs for conjugation and later filament formation and patterning. The approach proved problematic at the first step with oligos binding non-specifically to NPs through unpaired base interaction. To

alleviate the effect, a small NP surface-binding molecule (MCH) for partially covering the NP surface was used to interfere with ssDNA base-NP surface interaction. This would allow for control of oligos per NP and keep the oligos away from NP surface for filament formation. However, it was demonstrated that MCH is hard to control for NP surface modification because MCU removes electrostatic stabilisation on the NP and leads to NP agglomeration.

The alternative method of performing RecA filament patterning on template ds-DNA, where the filament is formed on the thiol-terminated oligo, followed by introduction of NPs guarantees single NP binding to a single site since the all the thiols of interest are pre-located in their correct positions. Successful formation of filaments on thiol-terminated oligos together with their binding onto template dsDNA was demonstrated using restriction enzyme assays and AFM data. Additionally, it was shown that the formed patterned structures with exposed thiols can be successfully used to attach Au NPs. This proves the feasibility of localising single NPs to a base pair resolution on a DNA template and paves the way of using RecA-patterned DNA scaffolds for Au NP arrangement for novel materials and devices.

8.1.3 Filament-template DNA stability investigation through FRET

With successful demonstration of filament metallisation and single NP positioning on template dsDNA in simple set-ups, the interest lies in transferring the methods to more advanced DNA geometries. Since this might require sequential metallisation of patterned regions on the template dsDNA, stability of patterned regions is essential. To determine how well the filaments stay bound to the template DNA, FRET set-ups were designed for investigating filament-template interaction kinetics. Restriction enzyme assays revealed that fluorophore-terminated oligos are suitable for RecA filament formation and patterning on a template dsDNA. Restriction assay method was also successfully used to demonstrate time progression of patterning efficiency.

Since restriction assays are limited for use of following biomolecular kinetics, the designed FRET system was used to monitor binding and unbinding of filament to template dsDNA. It was demonstrated, that if the filament-forming ssDNA having the fluorophore is complementary to the coupling fluorophore-carrying strand on the template dsDNA, a FRET signal is observed and the association kinetics can be followed over time. However, if the filament ssDNA is complementary to a strand that is not

carrying a fluorophore on the template dsDNA, the fluorophore interaction is not visible. This suggests a more complicated structure than a stable triple-stranded complex when RecA filament patterning occurs, with the invading filament ssDNA possibly competing with the sequence-equivalent DNA strand in the template dsDNA for the complementary strand.

To test filament-template dissociation, excess unlabelled template dsDNA was used after complexes were formed. However, because of instrument or solution instability in periods of over 6 hours, no decisive results on filament-template dissociation were obtained, but there is no reproducible evidence for diminishing FRET signal over time either, possibly suggesting stable complexes.

Finally, it was found that filament-template complexes and filaments in general are sensitive to high salt concentration in the solution and optimal conditions need to be selected for complex formation.

8.2 Immediate future work

RecA nucleoprotein filament patterning on template dsDNA as a viable tool for self-assembly-based structures has been demonstrated in previous works. Now, with the demonstrated ability to metallise RecA filaments, certain immediate short-term interests are in focus.

Firstly, both solution and surface-based metallisation methods need to be optimised for producing metallisation without any NP agglomeration, with thin nanowires, having a metal sheath thickness of as few as one NP. This would allow much more well defined metallised DNA nanostructures, reduce their size and manufacturing tolerances. Different solution conditions, such as buffers, Mg^{2+} salts and pH values should be investigated, as well as NPs with various sizes and stabilising agents. An optimum combination will guarantee selective DNA metallisation techniques suitable for novel material and device development.

The work in this project proved that because of particular RecA filament structure, purification of post-modified complexes is challenging. Typical protein purification techniques are not ideal due to small yields or incubation times and larger structure purification methods, like virus purification or filtration are not suitable because of formed complex stability. Purification methods sought after should be suitable for

purifying short filaments formed on oligos, patterned structures on kilobases-long DNA or large branched templates with multiple patterning sites. These methods should be able to eliminate out small ionic compounds for changing the solution conditions, small organic molecules after RecA or DNA modification and larger compounds, such as used filaments, DNA or unincorporated NPs. Because of high demands for the purification system, it most likely would consist of several independent purification steps, covering various conditions.

Furthermore, the formed nanowires need to be characterised. For electrical applications, the Au NP-based nanowires should be able to demonstrate appreciable electrical conduction. The successfully produced nanowires in this project had irregular shape and therefore unpredictable precipitation out of the solution characteristics. The surface-based nanowires were formed on a mica surface which is not suitable for deposition of electrode contacts for subsequent nanowire conduction probing. Both methods should be suitable for depositing expected nanowires on surfaces like doped silicon for electrical characterisation.

The formed magnetic nanowires need to be also investigated with regard to their magnetic properties. Basic MFM proved to be insufficient for NPs with such small magnetic domains, so MFM with an external magnetic field should be suitable for demonstrating the magnetism in the nanowires.

When suitable nanowires can be manufactured and characterised, the next step is to form them on patterned DNA structures. This would finally allow to construct basic electronic devices with controlled insulating gaps between the nanowire fragments and measure the device characteristics with deposited contacts.

Considering single NP placement, the performed work could be translated to positioning single NPs at multiple sites along the template dsDNA. The distance between NPs would allow characterisation of NP properties, such as SPR signal change, single electron transfer or magnetic domain changes.

With regards to filament-template interaction and stability, the same system based on FRET can be used to investigate many other interesting issues. Firstly, fluorescence stability issues over long periods of time need to be identified and eliminated. This will open the possibility to properly follow the dissociation kinetics of filament-template complexes and establish a dissociation constant. Secondly, the FRET system could be used to research progressively shorter filaments in the filament-template complex.

Such work would allow to establish formed complex stability dependance on the filament length.

8.3 Long-term future work

The next level for DNA-RecA-based metallised scaffolds would be to develop non-linear, branched structures. The linear nature of DNA should not limit use of the developed DNA techniques to simplistic devices. In combination with the previously discussed work in the literature review chapter on complex two-dimensional and three-dimensional shapes of DNA, selective DNA metallisation could scale to more advanced devices, where multiple electrode contacts, nanowires and single NPs can be integrated to form electronic circuitry. NP SPR signals could also be manipulated in large long-range assemblies for optical effects and magnetic NPs would give way for magnetic properties.

The DNA-RecA system is not limited to traditional physics-based devices only. Since DNA and RecA are biological molecules, they readily interact with many other biomolecules. Other DNA-binding proteins, such as single-strand DNA-binding protein, histones, zinc fingers or transcription factors enlarge the molecular toolkit and open paths for previously described uses to be integrated with biomolecular or medical applications. The biological nature of the nanostructures would be able to interact with such systems as DNA transcription and expression, epigenetic modification, drug delivery and response, cell homeostasis and the physical side of the engineered structures would allow for precise monitoring, expression and regulation of the biological parameters.

Chapter 9

Appendix

9.0.1 chapter 7

Figure 9.1: Confocal 488-647 3to1 acceptor

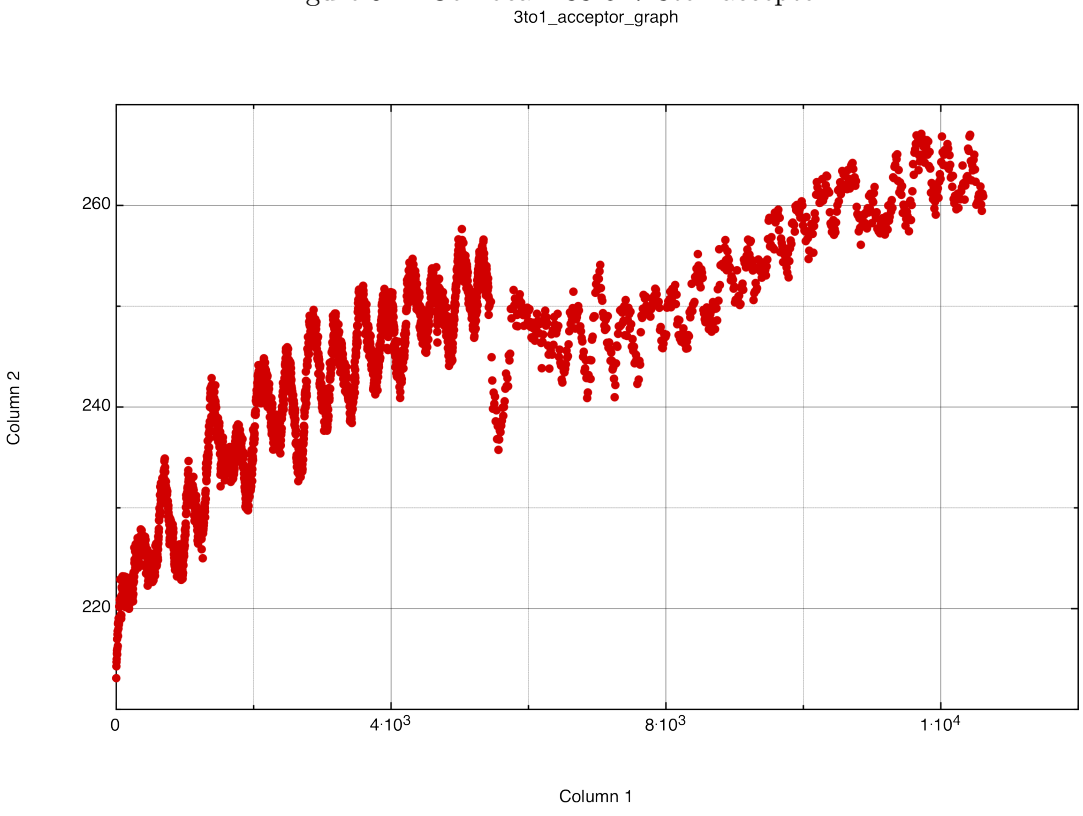

Figure 9.2: Confocal 488-647 3to1 donor

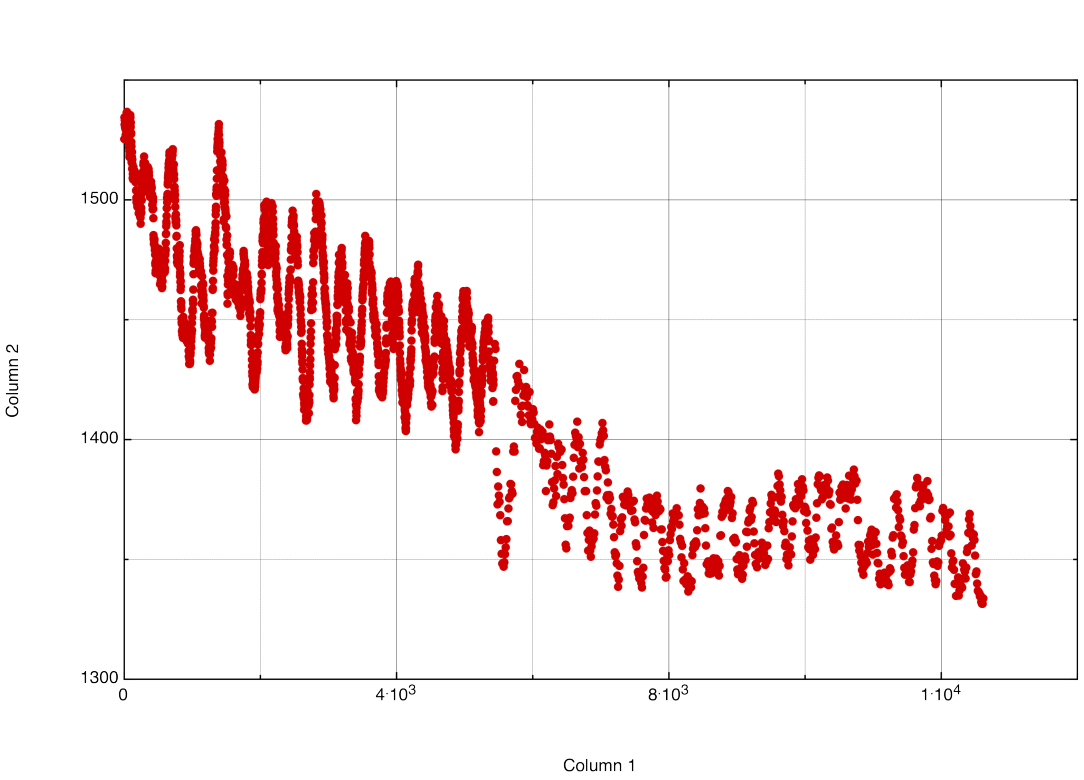

Figure 9.3: Confocal 488-647 1to1 acceptor

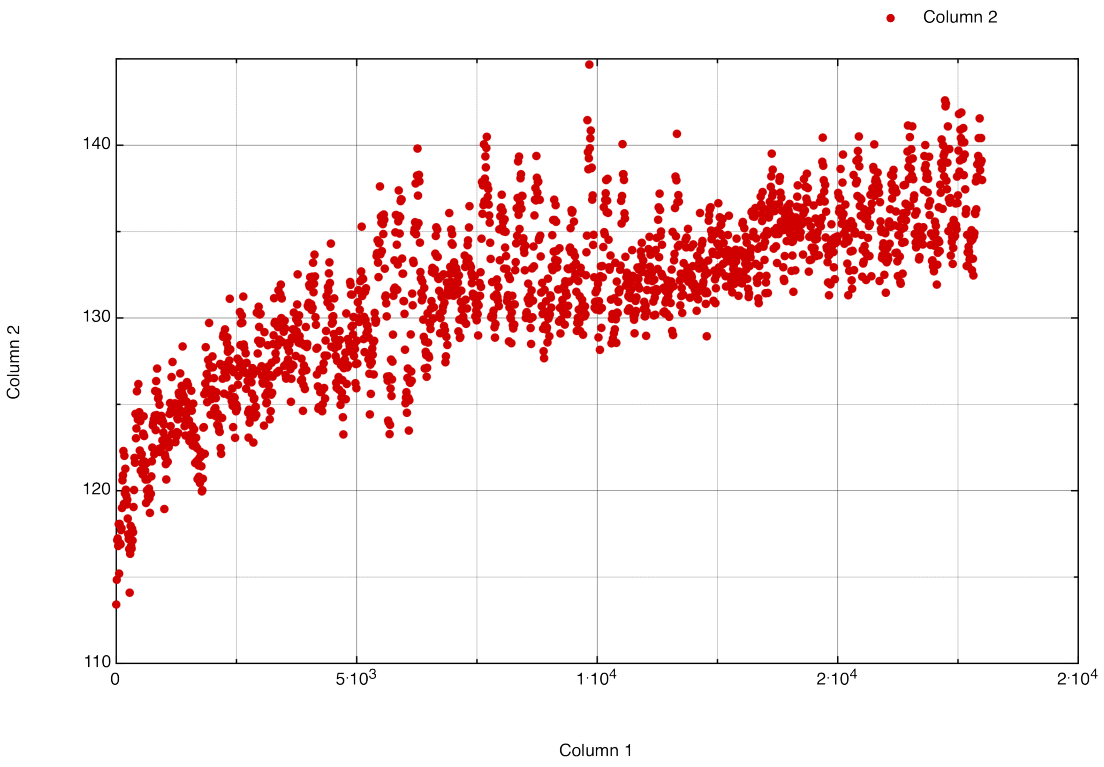

Figure 9.4: Confocal 488-647 1to1 donor

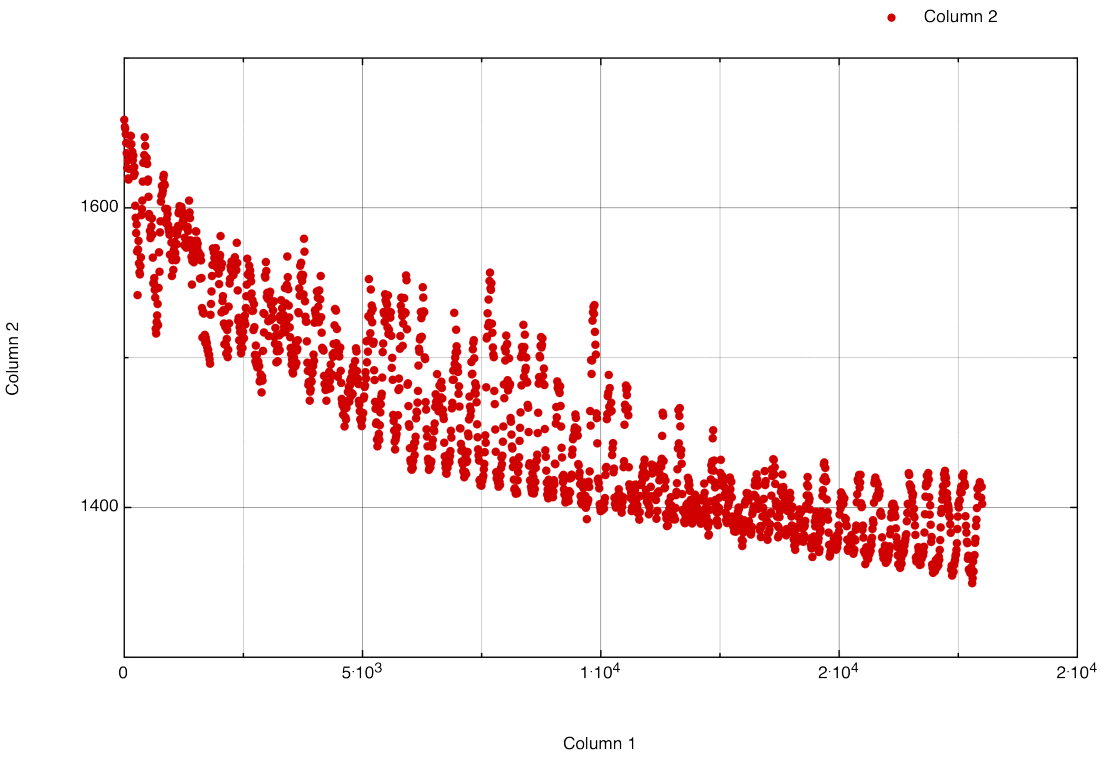

Figure 9.5: Shimadzu 488-647 outcompetition w/ 10x XS untagged dsDNA, donor emission divided by baseline (reagents 10x diluted)

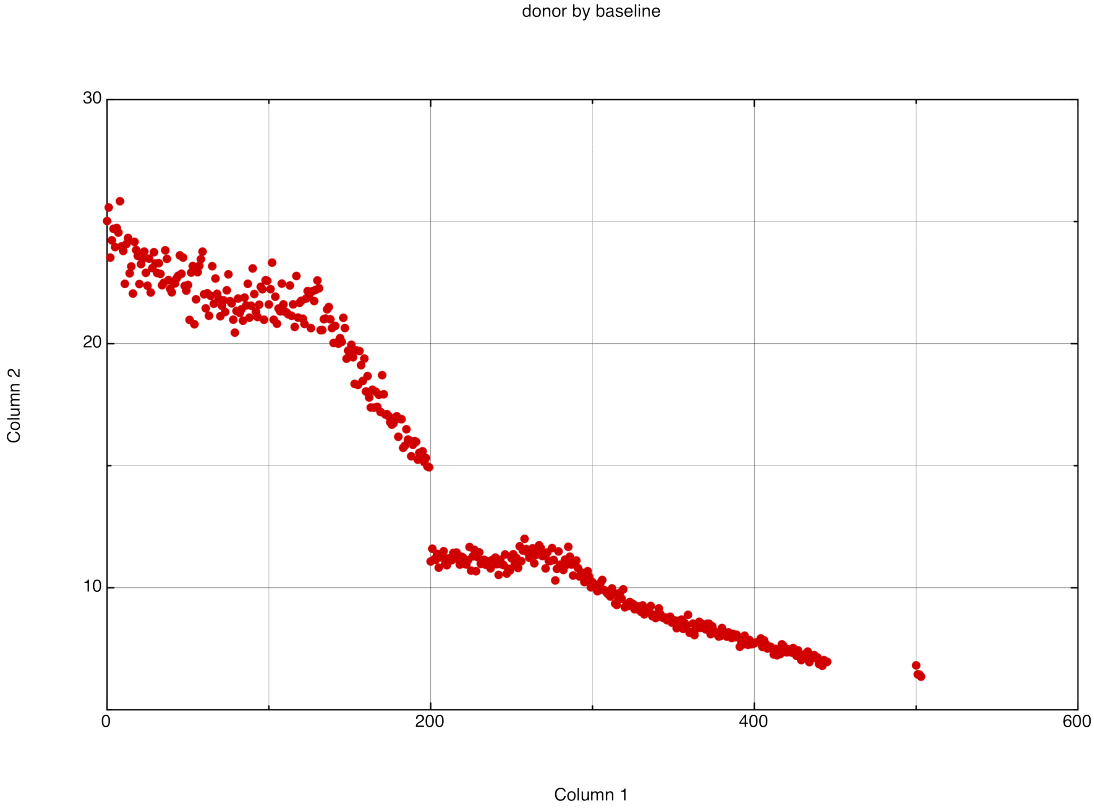

Figure 9.6: Shimadzu 488-647 outcompetition w/ 10x XS untagged dsDNA, acceptor emission divided by baseline (reagents 10x diluted)

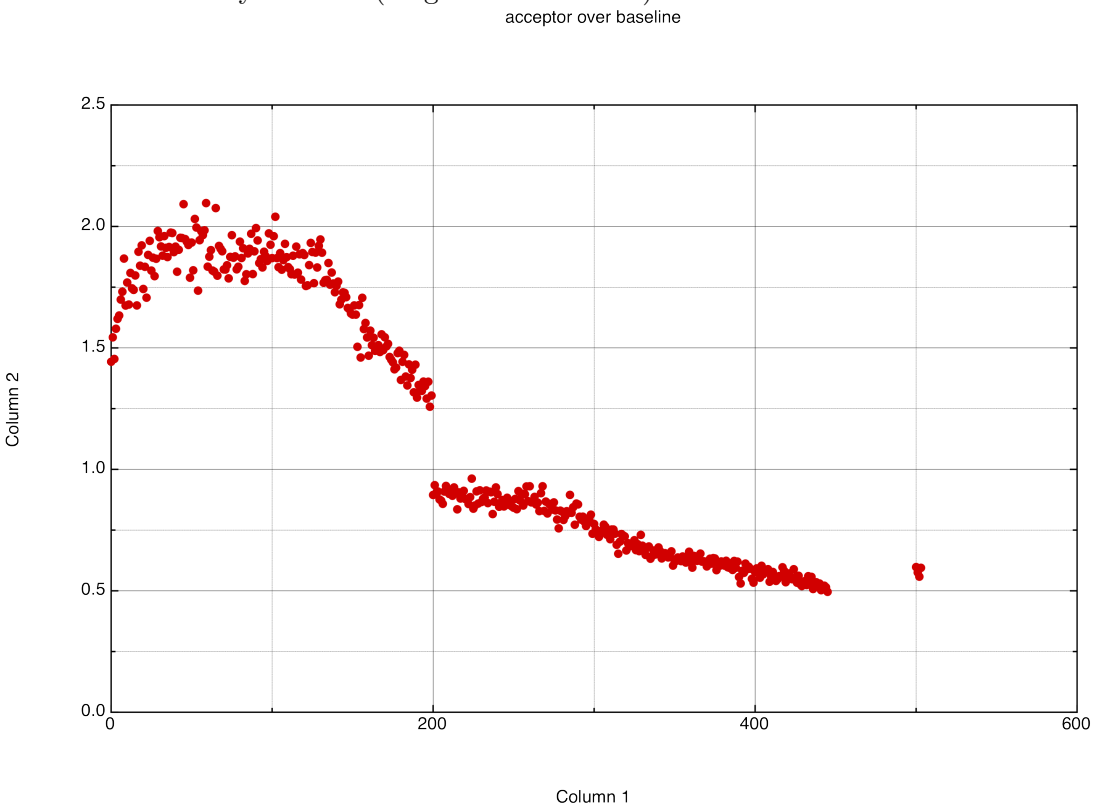

Figure 9.7: Confocal 488-647 1to1 10x dil outcompeting donor

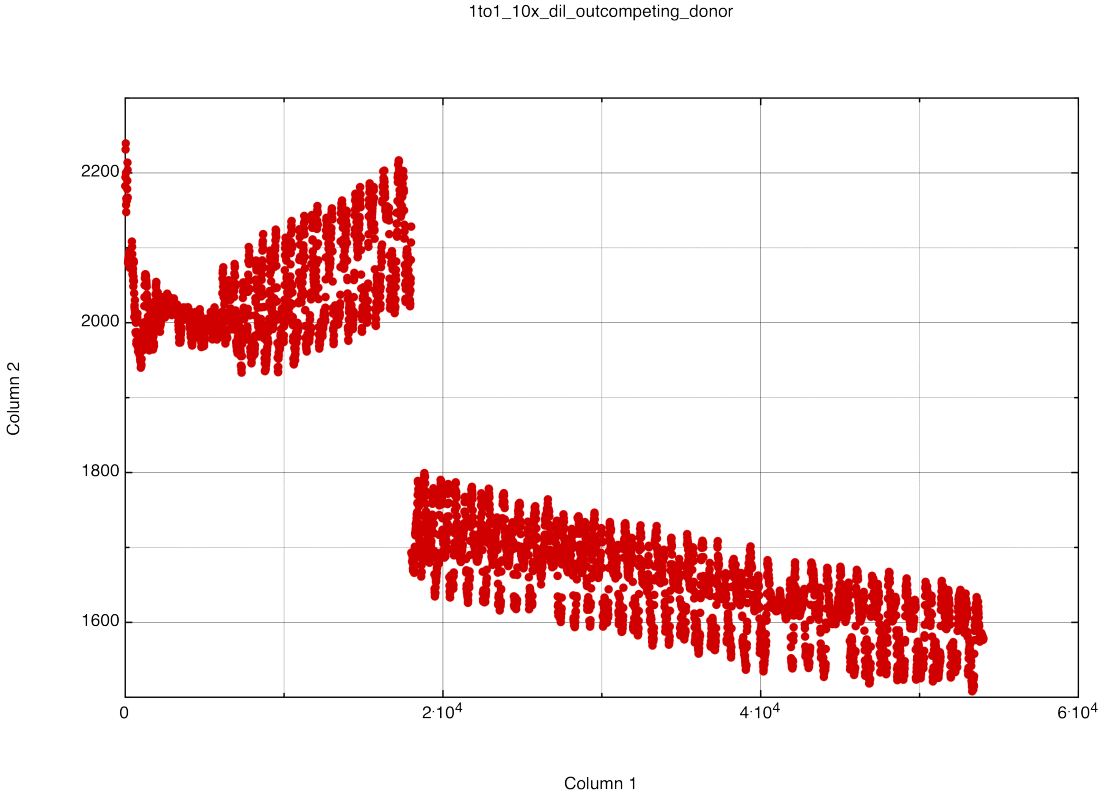

Figure 9.8: Confocal 488-647 1to1 10x dil outcompeting acceptor

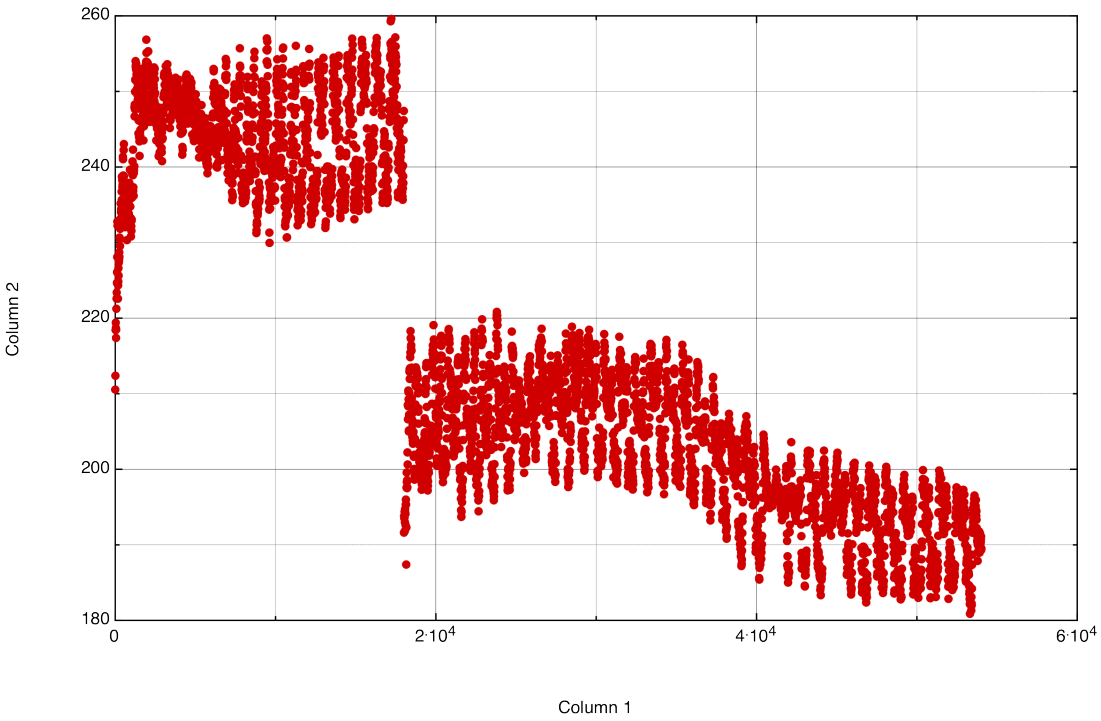

Figure 9.9: Confocal, 488-647 3:1, outcompeting, donor

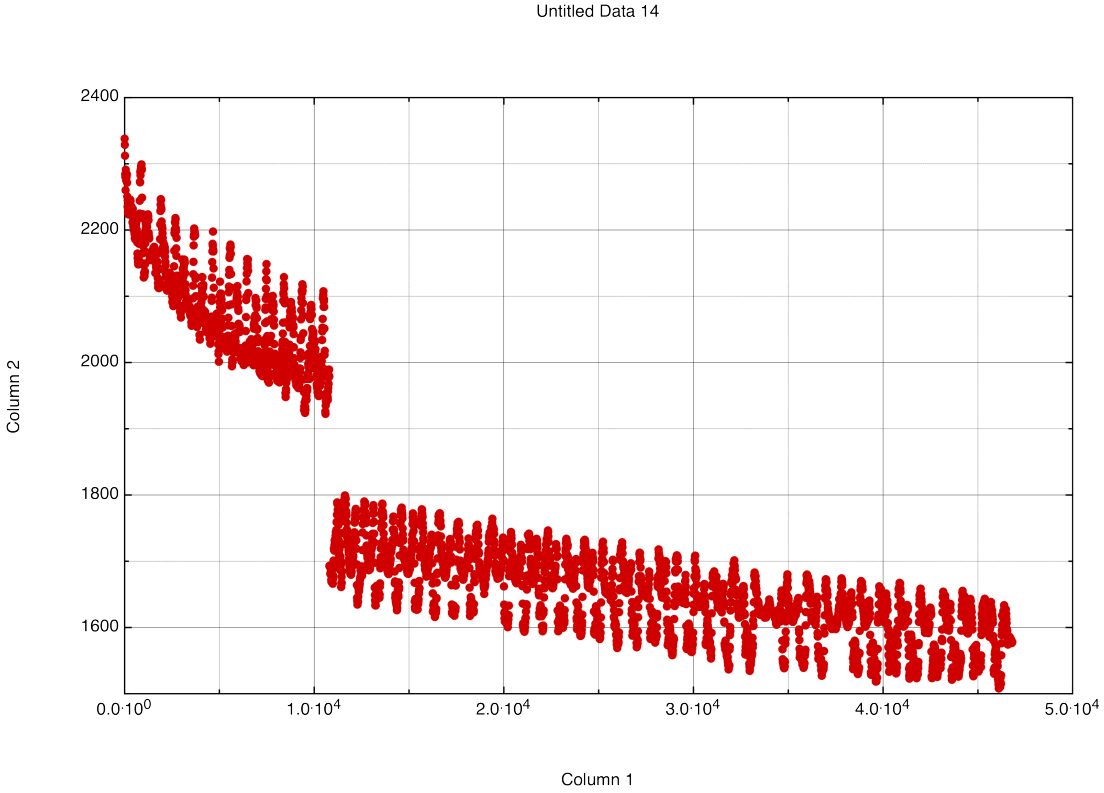

Figure 9.10: Confocal, 488-647 3:1, outcompeting, acceptor

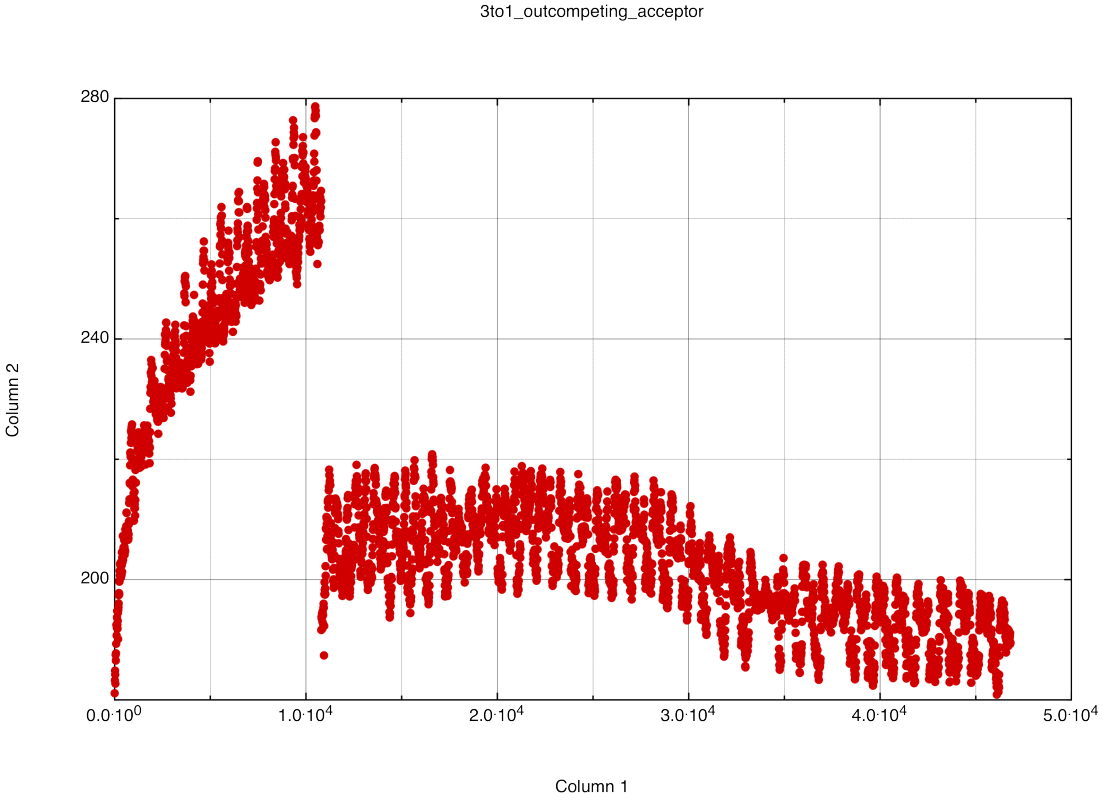

Figure 9.11: Confocal, 5prcnt laser power, 3to1 488-647, donor channel

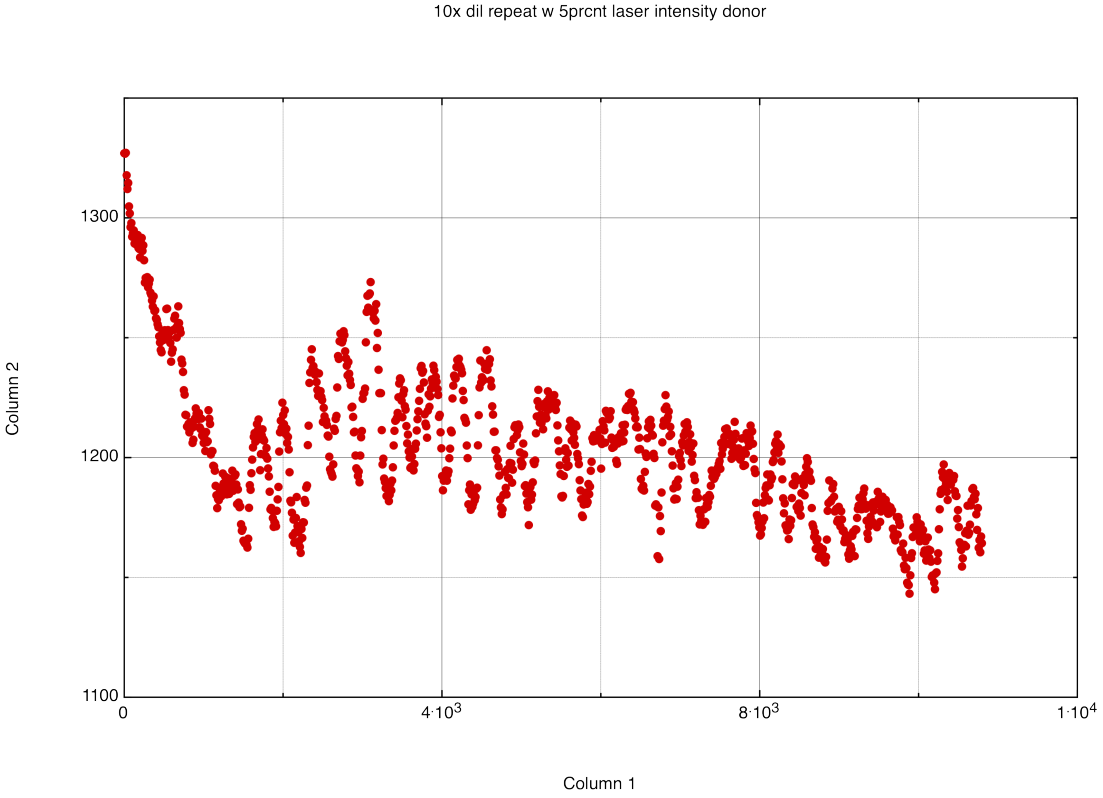

Figure 9.12: Confocal, 5prcnt laser power, 3to1 488-647, acceptor channel

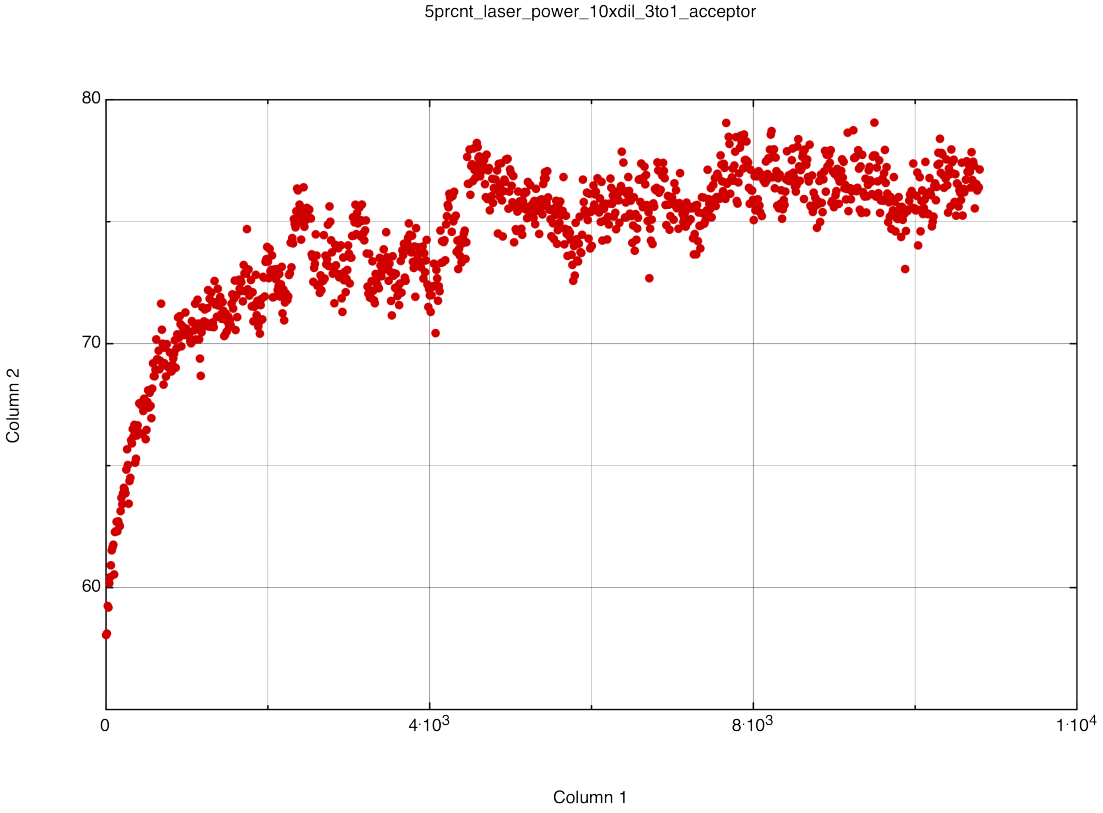

References

[1] Peter Robin Morris. *A History of the World Semiconductor Industry*. Number 12 in IEE History of technology. Peter Peregrinus Ltd. on behalf of the Institution of Electrical Engineers, 1990.

[2] S. Y. Chang and Simon M. Sze. *ULSI Devices*. John Wiley & Sons, Inc., 2000.

[3] Shyam P. Murarka and Martin C. Peckerar. *Electronic Materials: Science and Technology*. Academic Press, Inc., 1989.

[4] Chris Mack. *Fundamental Principles of Optical Lithography: The Science of Microfabrication*. John Wiley & Sons Ltd., 2007.

[5] Gordon E. Moore. Cramming more components onto integrated circuits. *Electronics*, 38(8), 1965.

[6] K. Schuegraf, M.C. Abraham, A Brand, M. Naik, and R. Thakur. Semiconductor Logic Technology Innovation to Achieve Sub-10 nm Manufacturing. *Electron Devices Society, IEEE Journal of the*, 1(3):66–75, March 2013.

[7] Shekhar Borkar. Design Perspectives on 22nm CMOS and Beyond. In *Proceedings of the 46th Annual Design Automation Conference*, DAC '09, pages 93–94, New York, NY, USA, 2009. ACM.

[8] R.W. Keyes. Fundamental limits of silicon technology. *Proceedings of the IEEE*, 89(3):227–239, March 2001.

[9] Sima Dimitrijev. *Principles of Semiconductor Devices*. The Oxford Series in Electrical and Computer Engineering. Oxford University Press, 2006.

[10] Neil Savage. Materials science: Super carbon. *Nature*, 483(7389):S30–S31, March 2012.

[11] Matthew J. Allen, Vincent C. Tung, and Richard B. Kaner. Honeycomb Carbon: A Review of Graphene. *Chemical Reviews*, 110(1):132–145, January 2010.

[12] A. K. Geim and K. S. Novoselov. The rise of graphene. *Nature Materials*, 6(3):183–191, March 2007.

[13] Shanshan Chen, Qingzhi Wu, Columbia Mishra, Junyong Kang, Hengji Zhang, Kyeongjae Cho, Weiwei Cai, Alexander A. Balandin, and Rodney S. Ruoff. Thermal conductivity of isotopically modified graphene. *Nature Materials*, 11(3):203–207, March 2012.

[14] Jesse D. Fowler, Matthew J. Allen, Vincent C. Tung, Yang Yang, Richard B. Kaner, and Bruce H. Weiller. Practical Chemical Sensors from Chemically Derived Graphene. *ACS Nano*, 3(2):301–306, February 2009.

[15] F. V. Kusmartsev, W. M. Wu, M. P. Pierpoint, and K. C. Yung. Application of Graphene within Optoelectronic Devices and Transistors. *arXiv:1406.0809 [cond-mat]*, June 2014.

[16] Frank Schwierz. Graphene transistors. *Nature Nanotechnology*, 5(7):487–496, July 2010.

[17] Mark S. Gudiksen, Jianfang Wang, and Charles M. Lieber. Synthetic Control of the Diameter and Length of Single Crystal Semiconductor Nanowires. *The Journal of Physical Chemistry B*, 105(19):4062–4064, May 2001.

[18] Matt Law, Joshua Goldberger, and Peidong Yang. Semiconductor Nanowires and Nanotubes. *Annual Review of Materials Research*, 34(1):83–122, 2004.

[19] Jonathan S. Lindsey. Self-assembly in synthetic routes to molecular devices. Biological principles and chemical perspectives: A review. *New J. Chem*, 15(2-3):153–179, 1991.

[20] Reginald H. Garrett and Charles M. Grisham. *Biochemistry*. Brooks/Cole, Belmont, CA, 4th edition, December 2008.

[21] Lyndsey M. Greig and Douglas Philp. Applying biological principles to the assembly and selection of synthetic superstructures. *Chemical Society Reviews*, 30(5):287–302, January 2001.

[22] Barbara Saccà and Christof M. Niemeyer. DNA Origami: The Art of Folding DNA. *Angewandte Chemie International Edition*, 51(1):58–66, January 2012.

[23] Jonathan Bath and Andrew J. Turberfield. DNA nanomachines. *Nature Nanotechnology*, 2(5):275–284, 2007.

[24] Paul W. K. Rothemund. Folding DNA to create nanoscale shapes and patterns. *Nature*, 440(7082):297–302, March 2006.

[25] Yonggang Ke, Luvena L. Ong, William M. Shih, and Peng Yin. Three-Dimensional Structures Self-Assembled from DNA Bricks. *Science*, 338(6111):1177–1183, November 2012.

[26] Dongran Han, Suchetan Pal, Jeanette Nangreave, Zhengtao Deng, Yan Liu, and Hao Yan. DNA Origami with Complex Curvatures in Three-Dimensional Space. *Science*, 332(6027):342–346, April 2011.

[27] Nadrian C. Seeman. DNA NANOTECHNOLOGY: Novel DNA Constructions. *Annual Review of Biophysics and Biomolecular Structure*, 27(1):225–248, 1998.

[28] Ebbe S. Andersen, Mingdong Dong, Morten M. Nielsen, Kasper Jahn, Ramesh Subramani, Wael Mamdouh, Monika M. Golas, Bjoern Sander, Holger Stark, Cristiano L. P. Oliveira, Jan Skov Pedersen, Victoria Birkedal, Flemming Besenbacher, Kurt V. Gothelf, and Jørgen Kjems. Self-assembly of a nanoscale DNA box with a controllable lid. *Nature*, 459(7243):73–76, May 2009.

[29] Chuan Zhang, Cheng Tian, Xiang Li, Hang Qian, Chenhui Hao, Wen Jiang, and Chengde Mao. Reversibly Switching the Surface Porosity of a DNA Tetrahedron. *Journal of the American Chemical Society*, 134(29):11998–12001, July 2012.

[30] Georg Seelig, David Soloveichik, David Yu Zhang, and Erik Winfree. Enzyme-Free Nucleic Acid Logic Circuits. *Science*, 314(5805):1585–1588, August 2006.

[31] Ji Youn Lee, Soo-Yong Shin, Tai Hyun Park, and Byoung-Tak Zhang. Solving traveling salesman problems with DNA molecules encoding numerical values. *Biosystems*, 78(1–3):39–47, December 2004.

[32] Lulu Qian, Erik Winfree, and Jehoshua Bruck. Neural network computation with DNA strand displacement cascades. *Nature*, 475(7356):368–372, July 2011.

[33] Jong-Shik Shin and Niles A. Pierce. A Synthetic DNA Walker for Molecular Transport. *Journal of the American Chemical Society*, 126(35):10834–10835, September 2004.

[34] Kyle Lund, Anthony J. Manzo, Nadine Dabby, Nicole Michelotti, Alexander Johnson-Buck, Jeanette Nangreave, Steven Taylor, Renjun Pei, Milan N. Stojanovic, Nils G. Walter, Erik Winfree, and Hao Yan. Molecular robots guided by prescriptive landscapes. *Nature*, 465(7295):206–210, May 2010.

[35] Derek N. Woolfson and Zahra N. Mahmoud. More than just bare scaffolds: Towards multi-component and decorated fibrous biomaterials. *Chemical Society Reviews*, 39(9):3464–3479, August 2010.

[36] Janos H. Fendler. Chemical Self-assembly for Electronic Applications. *Chemistry of Materials*, 13(10):3196–3210, October 2001.

[37] B. Amir Parviz, Declan Ryan, and George M. Whitesides. Using self-assembly for the fabrication of nano-scale electronic and photonic devices. *IEEE Transactions on Advanced Packaging*, 26(3):233–241, August 2003.

[38] C. Dekker and M.A. Ratner. Electronic properties of DNA. *Phys. World*, 14(8):29–33, 2001.

[39] T. Gregory Drummond, Michael G. Hill, and Jacqueline K. Barton. Electrochemical DNA sensors. *Nature Biotechnology*, 21(10):1192–1199, October 2003.

[40] Jens Müller. Chemistry: Metals line up for DNA. *Nature*, 444(7120):698–698, July 2006.

[41] Zhaoxiang Deng and Chengde Mao. DNA-Templated Fabrication of 1D Parallel and 2D Crossed Metallic Nanowire Arrays. *Nano Letters*, 3(11):1545–1548, November 2003.

[42] H. Kudo and M. Fujihira. DNA-templated copper nanowire fabrication by a two-step process involving electroless metallization. *IEEE Transactions on Nanotechnology*, 5(2):90 –92, March 2006.

[43] Fernando Patolsky, Yossi Weizmann, and Itamar Willner. Actin-based metallic nanowires as bio-nanotransporters. *Nature Materials*, 3(10):692–695, 2004.

[44] Michael Mertig, Lucio Colombi Ciacchi, Ralf Seidel, Wolfgang Pompe, and Alessandro De Vita. DNA as a Selective Metallization Template. *Nano Letters*, 2(8):841–844, August 2002.

[45] Jianfei Liu, Yanli Geng, Elisabeth Pound, Shailendra Gyawali, Jeffrey R. Ashton, John Hickey, Adam T. Woolley, and John N. Harb. Metallization of Branched DNA Origami for Nanoelectronic Circuit Fabrication. *ACS Nano*, 5(3):2240–2247, March 2011.

[46] Subhadeep Roy, Magdalena Olesiak, Shiying Shang, and Marvin H. Caruthers. Silver Nanoassemblies Constructed from Boranephosphonate DNA. *Journal of the American Chemical Society*, April 2013.

[47] Mato Knez, Alexander M. Bittner, Fabian Boes, Christina Wege, Holger Jeske, E. Maiβ, and Klaus Kern. Biotemplate Synthesis of 3-nm Nickel and Cobalt Nanowires. *Nano Letters*, 3(8):1079–1082, August 2003.

[48] Erez Braun, Yoav Eichen, Uri Sivan, and Gdalyahu Ben-Yoseph. DNA-templated assembly and electrode attachment of a conducting silver wire. *Nature*, 391(6669):775–778, February 1998.

[49] Marie-Christine Daniel and Didier Astruc. Gold Nanoparticles: Assembly, Supramolecular Chemistry, Quantum-Size-Related Properties, and Applications toward Biology, Catalysis, and Nanotechnology. *Chemical Reviews*, 104(1):293–346, January 2004.

[50] Susie Eustis and Mostafa A. El-Sayed. Why gold nanoparticles are more precious than pretty gold: Noble metal surface plasmon resonance and its enhancement of the radiative and nonradiative properties of nanocrystals of different shapes. *Chemical Society Reviews*, 35(3):209–217, February 2006.

[51] O. V. Salata. Applications of nanoparticles in biology and medicine. *Journal of Nanobiotechnology*, 2(1):3, April 2004.

[52] F. Einar Kruis, Heinz Fissan, and Aaron Peled. Synthesis of nanoparticles in the gas phase for electronic, optical and magnetic applications—a review. *Journal of Aerosol Science*, 29(5–6):511–535, June 1998.

[53] Partha Ghosh, Gang Han, Mrinmoy De, Chae Kyu Kim, and Vincent M. Rotello. Gold nanoparticles in delivery applications. *Advanced Drug Delivery Reviews*, 60(11):1307–1315, August 2008.

[54] Eugenii Katz and Itamar Willner. Integrated Nanoparticle–Biomolecule Hybrid Systems: Synthesis, Properties, and Applications. *Angewandte Chemie International Edition*, 43(45):6042–6108, November 2004.

[55] S. C. Kowalczykowski, D. A. Dixon, A. K. Eggleston, S. D. Lauder, and W. M. Rehrauer. Biochemistry of homologous recombination in Escherichia coli. *Microbiological Reviews*, 58(3):401–465, January 1994.

[56] R. Sharma, A. G. Davies, and C. Wälti. Nanoscale programmable sequence-specific patterning of DNA scaffolds using RecA protein. *Nanotechnology*, 23(36):365301, September 2012.

[57] Edward H. Egelman and Andrzej Stasiak. Structure of helical RecA-DNA complexes: II. Local conformational changes visualized in bundles of RecA-ATPγS filaments. *Journal of Molecular Biology*, 200(2):329–349, March 1988.

[58] Evangelina Pensa, Emiliano Cortés, Gastón Corthey, Pilar Carro, Carolina Vericat, Mariano H. Fonticelli, Guillermo Benítez, Aldo A. Rubert, and Roberto C. Salvarezza. The Chemistry of the Sulfur–Gold Interface: In Search of a Unified Model. *Accounts of Chemical Research*, 45(8):1183–1192, August 2012.

[59] Hannu Häkkinen. The gold-sulfur interface at the nanoscale. *Nature Chemistry*, 4(6):443–455, June 2012.

[60] Greg T. Hermanson. *Bioconjugate Techniques*. Academic Press, January 1996.

[61] Bernard A. Connolly and Peter Rider. Chemical synthesis of oligonucleotides containing a free sulphydryl group and subsequent attachment of thiol specific probes. *Nucleic Acids Research*, 13(12):4485–4502, June 1985.

[62] K. C. Gupta, P. Sharma, P. Kumar, and S. Sathyanarayana. A general method for the synthesis of 3′-sulfhydryl and phosphate group containing oligonucleotides. *Nucleic Acids Research*, 19(11):3019–3026, November 1991.

[63] J H Ojeda, M Pacheco, and P A Orellana. An array of quantum dots as a spin filter device by using Dicke and Fano effects. *Nanotechnology*, 20(43):434013, October 2009.

[64] Di Zhang, Jia-ning Ma, Hua Li, Shu-fang Fu, and Xuan-Zhang Wang. Antiresonance of electron tunneling through a four-quantum-dot ring with two side-coupled quantum dots. *Physics Letters A*, 372(17):3085–3088, April 2008.

[65] János Szöllosi, Sándor Damjanovich, and László Mátyus. Application of fluorescence resonance energy transfer in the clinical laboratory: Routine and research. *Cytometry*, 34(4):159–179, August 1998.

[66] Ralf Dahm. Discovering DNA: Friedrich Miescher and the early years of nucleic acid research. *Human Genetics*, 122(6):565–581, January 2008.

[67] J. D. Watson and F. H. C. Crick. Molecular Structure of Nucleic Acids: A Structure for Deoxyribose Nucleic Acid. *Nature*, 171(4356):737–738, April 1953.

[68] Christopher K. Mathews, Kensal E. van Holde, and Kevin G. Ahern. *Biochemistry*. Life Sciences and Chemistry. Addison Wesley Longman, third edition, 1999.

[69] Christian Hertweck. Biosynthesis and Charging of Pyrrolysine, the 22nd Genetically Encoded Amino Acid. *Angewandte Chemie International Edition*, 50(41):9540–9541, October 2011.

[70] J M Adams and M R Capecchi. N-formylmethionyl-sRNA as the initiator of protein synthesis. *Proceedings of the National Academy of Sciences of the United States of America*, 55(1):147–155, January 1966.

[71] Gregory Petsko and Dagmar Ringe. *Protein Structure and Function*. OUP Oxford, London; Sunderland, MA; Oxford, May 2008.

[72] Randall M. Story and Thomas A. Steitz. Structure of the recA protein–ADP complex. *Nature*, 355(6358):374–376, January 1992.

[73] Xu Xing and Charles E. Bell. Crystal Structures of Escherichia coli RecA in a Compressed Helical Filament. *Journal of Molecular Biology*, 342(5):1471–1485, October 2004.

[74] Zhucheng Chen, Haijuan Yang, and Nikola P. Pavletich. Mechanism of homologous recombination from the RecA–ssDNA/dsDNA structures. *Nature*, 453(7194):489–494, May 2008.

[75] S. Datta, M. M. Prabu, M. B. Vaze, N. Ganesh, Nagasuma R. Chandra, K. Muniyappa, and M. Vijayan. Crystal structures of Mycobacterium tuberculosis RecA and its complex with ADP–AlF4: Implications for decreased ATPase activity and molecular aggregation. *Nucleic Acids Research*, 28(24):4964–4973, December 2000.

[76] J. Rajan Prabu, G. P. Manjunath, Nagasuma R. Chandra, K. Muniyappa, and M. Vijayan. Functionally important movements in RecA molecules and filaments: Studies involving mutation and environmental changes. *Acta Crystallographica Section D Biological Crystallography*, 64(11):1146–1157, November 2008.

[77] Rakhi Rajan and Charles E. Bell. Crystal Structure of RecA from Deinococcus radiodurans: Insights into the Structural Basis of Extreme Radioresistance. *Journal of Molecular Biology*, 344(4):951–963, December 2004.

[78] Edward H. Egelman and Andrzej Stasiak. Structure of helical RecA-DNA complexes: Complexes formed in the presence of ATP-gamma-S or ATP. *Journal of Molecular Biology*, 191(4):677–697, October 1986.

[79] S. C. West, E. Cassuto, and P. Howard-Flanders. recA protein promotes homologous-pairing and strand-exchange reactions between duplex DNA molecules. *Proceedings of the National Academy of Sciences*, 78(4):2100–2104, January 1981.

[80] Catherine J. Murphy, Tapan K. Sau, Anand M. Gole, Christopher J. Orendorff, Jinxin Gao, Linfeng Gou, Simona E. Hunyadi, and Tan Li. Anisotropic Metal Nanoparticles: Synthesis, Assembly, and Optical Applications. *The Journal of Physical Chemistry B*, 109(29):13857–13870, July 2005.

[81] Igor L. Medintz, H. Tetsuo Uyeda, Ellen R. Goldman, and Hedi Mattoussi. Quantum dot bioconjugates for imaging, labelling and sensing. *Nature Materials*, 4(6):435–446, June 2005.

[82] J. Kimling, M. Maier, B. Okenve, V. Kotaidis, H. Ballot, and A. Plech. Turkevich Method for Gold Nanoparticle Synthesis Revisited. *The Journal of Physical Chemistry B*, 110(32):15700–15707, August 2006.

[83] Ying Jiang, Hong Zhao, Ningning Zhu, Yuqing Lin, Ping Yu, and Lanqun Mao. A Simple Assay for Direct Colorimetric Visualization of Trinitrotoluene at Picomolar Levels Using Gold Nanoparticles. *Angewandte Chemie*, 120(45):8729–8732, 2008.

[84] Nidhi Nath and Ashutosh Chilkoti. A Colorimetric Gold Nanoparticle Sensor To Interrogate Biomolecular Interactions in Real Time on a Surface. *Analytical Chemistry*, 74(3):504–509, February 2002.

[85] Ivan H. El-Sayed, Xiaohua Huang, and Mostafa A. El-Sayed. Surface Plasmon Resonance Scattering and Absorption of anti-EGFR Antibody Conjugated Gold Nanoparticles in Cancer Diagnostics: Applications in Oral Cancer. *Nano Letters*, 5(5):829–834, May 2005.

[86] Nadrian C Seeman and Philip S Lukeman. Nucleic acid nanostructures: Bottom-up control of geometry on the nanoscale. *Reports on Progress in Physics*, 68(1):237–270, January 2005.

[87] Rong-Ine Ma, Neville R. Kallenbach, Richard D. Sheardy, Mary L. Petrillo, and Nadrian C. Seeman. Three-arm nucleic acid junctions are flexible. *Nucleic Acids Research*, 14(24):9745–9753, September 1986.

[88] Mary L. Petrillo, Colin J. Newton, Richard P. Cunningham, Rong-Ine Ma, Neville R. Kallenbach, and Nadrian C. Seeman. The ligation and flexibility of four-arm DNA junctions. *Biopolymers*, 27(9):1337–1352, 1988.

[89] Junghuei Chen and Nadrian C. Seeman. Synthesis from DNA of a molecule with the connectivity of a cube. *, Published online: 18 April 1991; | doi:10.1038/350631a0*, 350(6319):631–633, April 1991.

[90] Erik Winfree, Furong Liu, Lisa A. Wenzler, and Nadrian C. Seeman. Design and self-assembly of two-dimensional DNA crystals. *Nature*, 394(6693):539–544, August 1998.

[91] Jianping Zheng, Jens J. Birktoft, Yi Chen, Tong Wang, Ruojie Sha, Pamela E. Constantinou, Stephan L. Ginell, Chengde Mao, and Nadrian C. Seeman. From molecular to macroscopic via the rational design of a self-assembled 3D DNA crystal. *Nature*, 461(7260):74–77, September 2009.

[92] Dage Liu, Mingsheng Wang, Zhaoxiang Deng, Richard Walulu, and Chengde Mao. Tensegrity: Construction of Rigid DNA Triangles with Flexible Four-Arm DNA Junctions. *Journal of the American Chemical Society*, 126(8):2324–2325, March 2004.

[93] William M. Shih, Joel D. Quispe, and Gerald F. Joyce. A 1.7-kilobase single-stranded DNA that folds into a nanoscale octahedron. *Nature*, 427(6975):618–621, February 2004.

[94] Yu He, Tao Ye, Min Su, Chuan Zhang, Alexander E. Ribbe, Wen Jiang, and Chengde Mao. Hierarchical self-assembly of DNA into symmetric supramolecular polyhedra. *Nature*, 452(7184):198–201, March 2008.

[95] R. P. Goodman, I. a. T. Schaap, C. F. Tardin, C. M. Erben, R. M. Berry, C. F. Schmidt, and A. J. Turberfield. Rapid Chiral Assembly of Rigid DNA Building Blocks for Molecular Nanofabrication. *Science*, 310(5754):1661–1665, September 2005.

[96] Bernard Yurke, Andrew J. Turberfield, Allen P. Mills, Friedrich C. Simmel, and Jennifer L. Neumann. A DNA-fuelled molecular machine made of DNA. *Nature*, 406(6796):605–608, August 2000.

[97] Peng Yin, Hao Yan, Xiaoju G. Daniell, Andrew J. Turberfield, and John H. Reif. A Unidirectional DNA Walker That Moves Autonomously along a Track. *Angewandte Chemie International Edition*, 43(37):4906–4911, 2004.

[98] Rahul Chhabra, Jaswinder Sharma, Yan Liu, and Hao Yan. Addressable Molecular Tweezers for DNA-Templated Coupling Reactions. *Nano Letters*, 6(5):978–983, May 2006.

[99] Hongzhou Gu, Jie Chao, Shou-Jun Xiao, and Nadrian C. Seeman. A proximity-based programmable DNA nanoscale assembly line. *Nature*, 465(7295):202–205, May 2010.

[100] Akimitsu Okamoto, Kazuo Tanaka, and Isao Saito. DNA Logic Gates. *Journal of the American Chemical Society*, 126(30):9458–9463, August 2004.

[101] Xingping Su and Lloyd M. Smith. Demonstration of a universal surface DNA computer. *Nucleic Acids Research*, 32(10):3115–3123, May 2004.

[102] Milan N. Stojanovic and Darko Stefanovic. A deoxyribozyme-based molecular automaton. *Nature Biotechnology*, 21(9):1069–1074, 2003.

[103] Joanne Macdonald, Yang Li, Marko Sutovic, Harvey Lederman, Kiran Pendri, Wanhong Lu, Benjamin L. Andrews, Darko Stefanovic, and Milan N. Stojanovic. Medium Scale Integration of Molecular Logic Gates in an Automaton. *Nano Letters*, 6(11):2598–2603, November 2006.

[104] B.G. Maiya and T. Ramasarma. DNA, a molecular wire or not-The debate continues. *CURRENT SCIENCE-BANGALORE-*, 80(12):1523–1530, 2001.

[105] T. Požar. Electronic properties of DNA.

[106] D. Porath, A. Bezryadin, S. de Vries, and C. Dekker. Direct measurements of electrical transport through DNA molecules. *AIP Conference Proceedings*, 544(1):452–456, November 2000.

[107] Hans-Werner Fink and Christian Schönenberger. Electrical conduction through DNA molecules. *Nature*, 398(6726):407–410, April 1999.

[108] Lintao Cai, Hitoshi Tabata, and Tomoji Kawai. Self-assembled DNA networks and their electrical conductivity. *Applied Physics Letters*, 77(19):3105–3106, November 2000.

[109] A. Yu Kasumov, M. Kociak, S. Guéron, B. Reulet, V. T. Volkov, D. V. Klinov, and H. Bouchiat. Proximity-Induced Superconductivity in DNA. *Science*, 291(5502):280–282, December 2001.

[110] K. W. Hipps. It's All About Contacts. *Science*, 294(5542):536–537, October 2001.

[111] Jason D. Slinker, Natalie B. Muren, Sara E. Renfrew, and Jacqueline K. Barton. DNA charge transport over 34 nm. *Nat Chem*, 3(3):228–233, March 2011.

[112] Sarah Delaney and Jacqueline K. Barton. Long-Range DNA Charge Transport. *The Journal of Organic Chemistry*, 68(17):6475–6483, August 2003.

[113] Haim Weizman and Yitzhak Tor. 2,2‘-Bipyridine Ligandoside: A Novel Building Block for Modifying DNA with Intra-Duplex Metal Complexes. *Journal of the American Chemical Society*, 123(14):3375–3376, April 2001.

[114] Kentaro Tanaka and Mitsuhiko Shionoya. Synthesis of a Novel Nucleoside for Alternative DNA Base Pairing through Metal Complexation. *The Journal of Organic Chemistry*, 64(14):5002–5003, July 1999.

[115] Glenn A. Burley, Johannes Gierlich, Mohammad R. Mofid, Hadar Nir, Shay Tal, Yoav Eichen, and Thomas Carell. Directed DNA Metallization. *Journal of the American Chemical Society*, 128(5):1398–1399, February 2006.

[116] Palok Aich, Shaunivan L. Labiuk, Les W. Tari, Louis J.T. Delbaere, William J. Roesler, Kennneth J. Falk, Ronald P. Steer, and Jeremy S. Lee. M-DNA: A complex between divalent metal ions and DNA which behaves as a molecular wire. *Journal of Molecular Biology*, 294(2):477–485, November 1999.

[117] Dage Liu, Sung Ha Park, John H. Reif, and Thomas H. LaBean. DNA nanotubes self-assembled from triple-crossover tiles as templates for conductive nanowires. *Proceedings of the National Academy of Sciences of the United States of America*, 101(3):717–722, January 2004.

[118] Qun Gu and Donald T. Haynie. Palladium nanoparticle-controlled growth of magnetic cobalt nanowires on DNA templates. *Materials Letters*, 62(17–18):3047–3050, June 2008.

[119] Qun Gu, Chuanding Cheng, Shivashankar Suryanarayanan, Kun Dai, and Donald T. Haynie. DNA-templated fabrication of nickel nanocluster chains. *Physica E: Low-dimensional Systems and Nanostructures*, 33(1):92–98, June 2006.

[120] Hector A. Becerril, Paul Ludtke, Barry M. Willardson, and Adam T. Woolley. DNA-Templated Nickel Nanostructures and Protein Assemblies. *Langmuir*, 22(24):10140–10144, November 2006.

[121] Khoa Nguyen, Miguel Monteverde, Arianna Filoramo, Laurence Goux-Capes, Sébastien Lyonnais, Pascale Jegou, Pascal Viel, Marcelo Goffman, and Jean-Philippe Bourgoin. Synthesis of Thin and Highly Conductive DNA-Based Palladium Nanowires. *Advanced Materials*, 20(6):1099–1104, 2008.

[122] Joseph M. Kinsella and Albena Ivanisevic. DNA-Templated Magnetic Nanowires with Different Compositions: Fabrication and Analysis. *Langmuir*, 23(7):3886–3890, March 2007.

[123] Joseph M. Kinsella and Albena Ivanisevic. Enzymatic Clipping of DNA Wires Coated with Magnetic Nanoparticles. *Journal of the American Chemical Society*, 127(10):3276–3277, March 2005.

[124] Kinneret Keren, Rotem S. Berman, and Erez Braun. Patterned DNA Metallization by Sequence-Specific Localization of a Reducing Agent. *Nano Letters*, 4(2):323–326, February 2004.

[125] Kinneret Keren, Michael Krueger, Rachel Gilad, Gdalyahu Ben-Yoseph, Uri Sivan, and Erez Braun. Sequence-Specific Molecular Lithography on Single DNA Molecules. *Science*, 297(5578):72–75, May 2002.

[126] David Hopwood. The reactions of glutaraldehyde with nucleic acids. *The Histochemical Journal*, 7(3):267–276, May 1975.

[127] Colin J. Loweth, W. Brett Caldwell, Xiaogang Peng, A. Paul Alivisatos, and Peter G. Schultz. DNA-Based Assembly of Gold Nanocrystals. *Angewandte Chemie International Edition*, 38(12):1808–1812, 1999.

[128] Robert Schreiber, Jaekwon Do, Eva-Maria Roller, Tao Zhang, Verena J. Schüller, Philipp C. Nickels, Jochen Feldmann, and Tim Liedl. Hierarchical assembly of metal nanoparticles, quantum dots and organic dyes using DNA origami scaffolds. *Nature Nanotechnology*, 9(1):74–78, January 2014.

[129] Camilla Russell, Ken Welch, Jonas Jarvius, Yixiao Cai, Rimantas Brucas, Fredrik Nikolajeff, Peter Svedlindh, and Mats Nilsson. Gold Nanowire Based Electrical DNA Detection Using Rolling Circle Amplification. *ACS Nano*, 8(2):1147–1153, February 2014.

[130] Kevin Truong and Mitsuhiko Ikura. The use of FRET imaging microscopy to detect protein–protein interactions and protein conformational changes in vivo. *Current Opinion in Structural Biology*, 11(5):573–578, September 2001.

[131] Damien Maurel, Laëtitia Comps-Agrar, Carsten Brock, Marie-Laure Rives, Emmanuel Bourrier, Mohammed Akli Ayoub, Hervé Bazin, Norbert Tinel, Thierry Durroux, Laurent Prézeau, Eric Trinquet, and Jean-Philippe Pin. Cell-surface protein-protein interaction analysis with time-resolved FRET and snap-tag technologies: Application to GPCR oligomerization. *Nature Methods*, 5(6):561–567, June 2008.

[132] Benjamin Schuler and William A Eaton. Protein folding studied by single-molecule FRET. *Current Opinion in Structural Biology*, 18(1):16–26, February 2008.

[133] W Arber and S Linn. DNA Modification and Restriction. *Annual Review of Biochemistry*, 38(1):467–500, 1969.

[134] RNAstructure, rna.urmc.rochester.edu/RNAstructureWeb/.

[135] Jessica S Reuter and David H Mathews. RNAstructure: Software for RNA secondary structure prediction and analysis. *BMC Bioinformatics*, 11:129, March 2010.

[136] Stanislav Bellaousov, Jessica S. Reuter, Matthew G. Seetin, and David H. Mathews. RNAstructure: Web servers for RNA secondary structure prediction and analysis. *Nucleic Acids Research*, 41(Web Server issue):W471–W474, July 2013.

[137] D. H. Mathews, J. Sabina, M. Zuker, and D. H. Turner. Expanded sequence dependence of thermodynamic parameters improves prediction of RNA secondary structure. *Journal of Molecular Biology*, 288(5):911–940, May 1999.

[138] T. Andrew Taton. Preparation of Gold Nanoparticle–DNA Conjugates. In *Current Protocols in Nucleic Acid Chemistry*. John Wiley & Sons, Inc., 2001.

[139] Linette M. Demers, Chad A. Mirkin, Robert C. Mucic, Robert A. Reynolds, Robert L. Letsinger, Robert Elghanian, and Garimella Viswanadham. A Fluorescence-Based Method for Determining the Surface Coverage and Hybridization Efficiency of Thiol-Capped Oligonucleotides Bound to Gold Thin Films and Nanoparticles. *Analytical Chemistry*, 72(22):5535–5541, November 2000.

[140] Haley D. Hill, Jill E. Millstone, Matthew J. Banholzer, and Chad A. Mirkin. The Role Radius of Curvature Plays in Thiolated Oligonucleotide Loading on Gold Nanoparticles. *ACS Nano*, 3(2):418–424, February 2009.

[141] Sunho Park, Katherine A. Brown, and Kimberly Hamad-Schifferli. Changes in Oligonucleotide Conformation on Nanoparticle Surfaces by Modification with Mercaptohexanol. *Nano Letters*, 4(10):1925–1929, October 2004.

[142] Kaushik Ragunathan, Cheng Liu, and Taekjip Ha. RecA filament sliding on DNA facilitates homology search. *eLife*, 1, December 2012.

[143] Donna M. Budzynski, Xinhao Gao, and Albert S. Benight. Isolation, characterization, and magnesium-induced self-association kinetics of discrete aggregates of RecA protein from Escherichia coli. *Biopolymers*, 38(4):471–491, 1996.

[144] Shelley L. Lusetti, Jeffrey J. Shaw, and Michael M. Cox. Magnesium Ion-dependent Activation of the RecA Protein Involves the C Terminus. *Journal of Biological Chemistry*, 278(18):16381–16388, February 2003.